Electrical Engineering Theses   Electrical Engineering

Fall 8-15-2012

Modeling, Control and Characterization of Aircraft Electric Power Systems

Hadi Ebrahimi

MODELING, CONTROL AND CHARACTERIZATION OF AIRCRAFT ELECTRIC
POWER SYSTEMS

by

HADI EBRAHIMI

A thesis submitted in partial fulfillment
of the requirements for the degree of
Master of Science in Electrical Engineering
Department of Electrical Engineering

Hassan El-Kishky, Ph.D., Committee Chair

College of Engineering and Computer Science

The University of Texas at Tyler
May 2012

The University of Texas at Tyler

Tyler, Texas

This is to certify that the master's thesis of
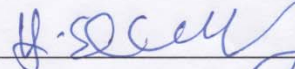
HADI EBRAHIMI
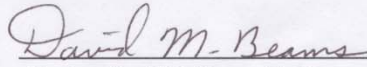
has been approved for the thesis requirement on
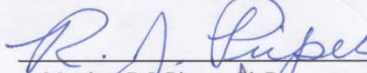
May 18, 2012

for the Master of Science Degree in Electrical Engineering

Approvals:

_____

Thesis Chair: Hassan El-Kishky, Ph.D.

_____

Member: David M. Beams, Ph.D.

_____

Member: R J. Pieper , Ph.D.

_____

Chair and Graduate Coordinator: Mukul V.
Shirvaikar, Ph. D.

_____

Dr. James K. Nelson, Jr., Ph.D., P.E.,
Dean, College of Engineering and Computer Science,
Brazzel Professor of Engineering

Acknowledgements

Table of Contents

List of Figures

List of Tables

Abstract

MODELING, CONTROL AND CHARACTERIZATION OF AIRCRAFT ELECTRIC
POWER SYSTEMS

Hadi Ebrahimi

Thesis Chair: Hassan El-Kishky, Ph.D.

The University of Texas at Tyler

May 2012

This thesis presents modeling, characterization and stability assessment of the
Advanced Aircraft Electric Power System (AAEPS) with Auxiliary Power Unit (APU).
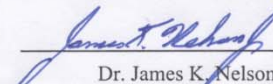The hybrid system under study contains a battery/fuel cell unit as a backup system for the
case of emergency or failure of the aircraft Synchronous Generator (SG) system. A
comprehensive model is developed in PSIM9 (commercial software developed for power
electronic circuit analysis) environment using the Boeing767 aircraft electric structure as
a study model [5]. The transient and steady-state performance of the system are studied
where the battery and fuel cell stack operate as a hybrid system. The dynamic
characteristics of the aircraft integrated system are captured and analyzed at major nodes
of ac/dc main buses. Also, power quality of the system is investigated where different
types of loads (linear and non-linear) contribute harmonics to the grid. Furthermore, a
complete set of mathematical models corresponding to the aircraft system and sub-system
has been developed to obtain the key dynamic features of the system main profiles at
major nodes by applying the Generalized State Space Averaging (GSSA) technique.
Estimation of the averaging state variables (state vectors) includes both transient and
steady-state behaviors of the critical signals that significantly determine system's
performance and characteristics in terms of continuity in secure operation and stability
under chaotic conditions. In a sense, this effort brings the capability of monitoring the

important dynamics of the whole aircraft electric system where simulation time, cost constraints and limitation of computer resources are of prime concern.

Bifurcation analysis has been employed to find the equilibrium solutions of the system's differential equations. Multi-variable parameters (so-called "bifurcation parameters") are considered to verify the stability of the aircraft electric power system under study. While applying variations to the control parameters and loading configurations, bifurcation diagrams are utilized to determine the stability margins of the system and sub-systems at different operating conditions. The present effort on modeling and performance characterization of the system can be effectively used in more secure and reliable design topologies for the APU-based AAEPS under various operation conditions, such as; chaos, over loading and other kinds of unexpected events. Models introduced may open windows into future studies, dealing with system stability assessment, system observability, automatic control parameters updates, and real-time control parameter estimation (Proportional Integrator (PI) parameter generation) to keep the system's operation within standard limits [7].

Chapter One

Introduction

1.1 Motivation

The More Electric Aircraft (MEA) has been proposed by many authors in the recent past and is becoming a viable alternative to the commercial aircraft with mechanical energy structures. It has been found that aircraft with more electric energy resources reduce fuel consumption and improve reliability as a result of fault-tolerant electrically-operated flight control actuators and elimination of the hydraulic system. Moreover, reduced design complexity, reduced flight test hours, less tooling, reduced performance testing time and simplification or elimination of the hydraulic system, (which has a deleterious impact on the environment) are considered to be other benefits of the advanced aircraft system [1-3]. Also, the electrical power system does not require a heavy infrastructure and is very flexible compared with the conventional mechanical systems [4]. On the other hand, conventional civil aircraft architecture consists of a combination of systems dependent on mechanical, pneumatic, hydraulic and electrical sources. These systems have drawbacks such as low efficiency and difficulty in detecting leaks in pneumatic system, using many gearboxes for mechanical system, heavy, inflexible piping and the potential leakage of dangerous and corrosive fluids from hydraulic system. The major concerns of using MEA are: lower power density than hydraulic power and higher risk of fire in case of a short circuit [5,8]. The concept of the "all-electric aircraft" and the "more electric aircraft" (MEA) have been introduced to overcome some of the drawbacks found in conventional architectures and bring more attractive advantages, such as improved fuel consumption, and lower maintenance and operation costs. This implies an increase in electrical load and power electronic equipment, higher consumption of electrical energy, more demand for generated power, power quality and stability problems [8].

1.2 Previous Work

The topic "Advanced Aircraft Electric Power System" and "All-electric Airplane" was originally proposed by the author of [6] in 1983. The same author claims that a broad

range of concepts from the "evolutionary to the revolutionary" are inspired by the above mentioned topics and the revolutionary developments are exciting to the research and development community. However, the author believed that there was little encouragement or acceptance from the side of airframe developers, whose objective was to build an advanced technology airplane using merely "off-the-shelf, proven equipment". He continued with the following quotation: "we know how bad the current situation is, but we have learned to live with it. We have only your vision of how good an advanced system will be and fear to chance it". Since that time, so many efforts have been made on pushing the technology forward to replace some of the aircraft's mechanical components with electric equipment. There is no argument that their diligence has led to many encouraging results, strengthening the hope in designers that having aircraft with a clean and reliable source of energy is quite feasible and may be achieved in the near future. The MEA concept is found as a fast growing trend in modern aircraft family, which is along with advancement in power electronic circuits, electric/electronic loads, Flexible AC Transmission Systems (FACTS) devices, which are used for power quality and power factor improvement. Also advanced control techniques will be introduced for robust control of the aircraft electric system under investigation. Subsequently, use of electrical power onboard is remarkably increasing within the areas of communications, surveillance and general systems, such as radar, cooling, landing gear or actuators systems [7]. Hence, advanced aircraft integrated system has been viewed and investigated from different angles and large number of research studies are reported on system performance and analysis. Also, extensive research has been done on modeling and characterization of More Electric Aircraft (MEA) during past few decades and much attention has been paid to continuity and security of operation of the system as well as reliable performance under various conditions. It is obvious that aircraft system is classified as a highly secure system. Therefore, very reliable system operation is of prime importance. On the other hand, costs and efficiency are remarkably taken into account in the system design. The research studies reported in recent years cover a broad area of modeling and simulation of the system/sub-systems, dealing with major components and critical profiles of the system's operation. The performance characteristics and power quality analysis of Variable Speed Constant Frequency (VSCF) AAEPS using Active

Power Filters (APF) are accomplished by the authors of [8,10]. In these articles, the representative model of AAEPS is developed and the system performance and power quality of the electric grid is characterized via several case studies. Modeling and simulation of the aircraft electric system with a fuel cell-equipped APU connected at the network's HVDC main bus is performed by [11] and the dynamic and steady-state behaviors of the system are analyzed. Also, the performance analysis of one-cycle control method for high power factor rectifiers in aircraft electric power system is carried out by the authors of [12]. Furthermore, the application and challenges of power electronics for Variable Frequency Aircraft Electric Power System (VFAEPS) of MEA is addressed in [13]. There are great efforts done on developing the mathematical models for fundamental frequencies and harmonics approximation for Active Power Filters (APF) applications in the AAEPS [14,15]. Also, time-saving methods are developed for modeling and simulation of the AEPS by [16-18].

1.3 Thesis Objectives

The aim of this thesis is modeling, characterization and stability performance analysis of the hybrid fuel cell/battery-based AAEPS and its dynamic behaviors under various conditions. The following issues are addressed in this thesis:

- Mathematical modeling corresponding to the aircraft electric system, including multi-level power electronic system, ac/dc and dc/ac converters, dynamic loads and harmonics filters, is developed using the Generalized State Space Averaging (GSSA) approach. Also, the proposed models are utilized to capture the dynamical behaviors of the aircraft electric grid under various conditions, and the accuracy of the obtained results is compared with the real-time simulations from a study model developed in PSIM9 environment.

- Transient and steady-state performance of the APU is studied and the amount of distortion contributed by the hybrid system is investigated via several case studies.

- The stability problems of the system are assessed by applying Bifurcation analysis. In this section, the AAEPS network stability and robustness are studied

with respect to variation of system parameters, also called "bifurcation parameters". Therefore, the effort made in this section would introduce the range of reliable operation for the system under study and provide a better design scheme.

- Finally, the quality of delivered power is studied for various loading scenarios. Both active and passive power filtering methods are applied to the electric network to measure the effectiveness and applicability of each technique.

1.4 Research Questions

- What are the all benefits of modeling, characterization and performance analysis of the AAEPS?
- Do the system's profiles meet military/IEEE standards?
- Can the power quality problems be solved by using harmonic-reduction devices?
- What factors affect the stability of AAEPS under investigation?
- How the stability margins of the system can be predicted for a reliable design?

1.5 Thesis Structure

- Chapter 2 includes the mathematical modeling of AAEPS along with obtained simulation results.
- Chapter 3 presents the performance and characteristics of the APU-based system under the consideration of several case studies.
- Chapter 4 introduces the aircraft system's stability using Bifurcation analysis.
- Chapter 5 covers the power quality analysis of the system at the presence of harmonics filters.
- Chapter 6 contains a concise discussion associated with the results and future work.

Chapter Two

Mathematical Modeling of AAEPS with the GSSA Technique

2.1 Overview

In an advanced aircraft electric system comprised of multi-converters, several types of loads, harmonic filters and other kinds of switching components [19], the continuity of performance and security of operation is of prime concern. The system is in the normal condition if there are no overloads, no overvoltages, no undervoltages, and specific standards are met by the system's profiles (e.g., voltages, currents, harmonic contents...,etc). The control center of the system should maintain the system securely by continuous observation of system performance. For security as well as control purposes, the control center must have a complete set of data and information associated with the electric components and power electronic network in AAEPS, which should be updated automatically in real time if any rapid change occurs in system's profiles. There is, consequently, a need to monitor system activity. However, measuring all the necessary signals may be impossible or may not be economically feasible. In addition, measurements may contain errors and be corrupted noise. As a result, there is a need to obtain the complete set of necessary information from incomplete noisy set of real time measurements for the control center. This can be recognized as the advantages of state estimation of the aircraft electric system [20]. Time-domain simulation of an advanced aircraft with complex electric components including nonlinear loads and switching modules demands substantial number of facilities and is time-consuming process. The GSSA method would facilitate the data acquisition of the entire aircraft electric system and components under investigation, leading to a considerable reduction in computer processing requirements and time. The use of the GSSA method was originally introduced by the author of [21] and has subsequently been applied to describe the dynamic behaviors of multi-level dc/dc converters in [22,23]. The main restrictions of using State Space Averaging (SSA) method with consideration of small variations in the state variables has been compensated using the large-signal model proposed by the GSSA approach [28,29]. The advantages of this method over state space averaging estimation used for switching-based circuits with small variations have been discussed in [21,24].

The authors of [24,25] have utilized the GSSA technique to develop models of quasi-resonant converter systems. In [26,27] the applicability of this method has been demonstrated to describe the discontinuous conducting mode in various types of Switching Power Converters (SPC) and the dynamic behaviors of Neutral Point Diode Clamped (NPC) converters, respectively.

2.2 VSCF AAEPS Structure and Electrical Components

The schematic model depicted in Fig. 2.1 represents the electric power system of a Boeing 767. aircraft system, proposed in [30]. The main power source of the single channel model is a Synchronous Generator (SG), and the aircraft electric network is comprised of several components as follows:
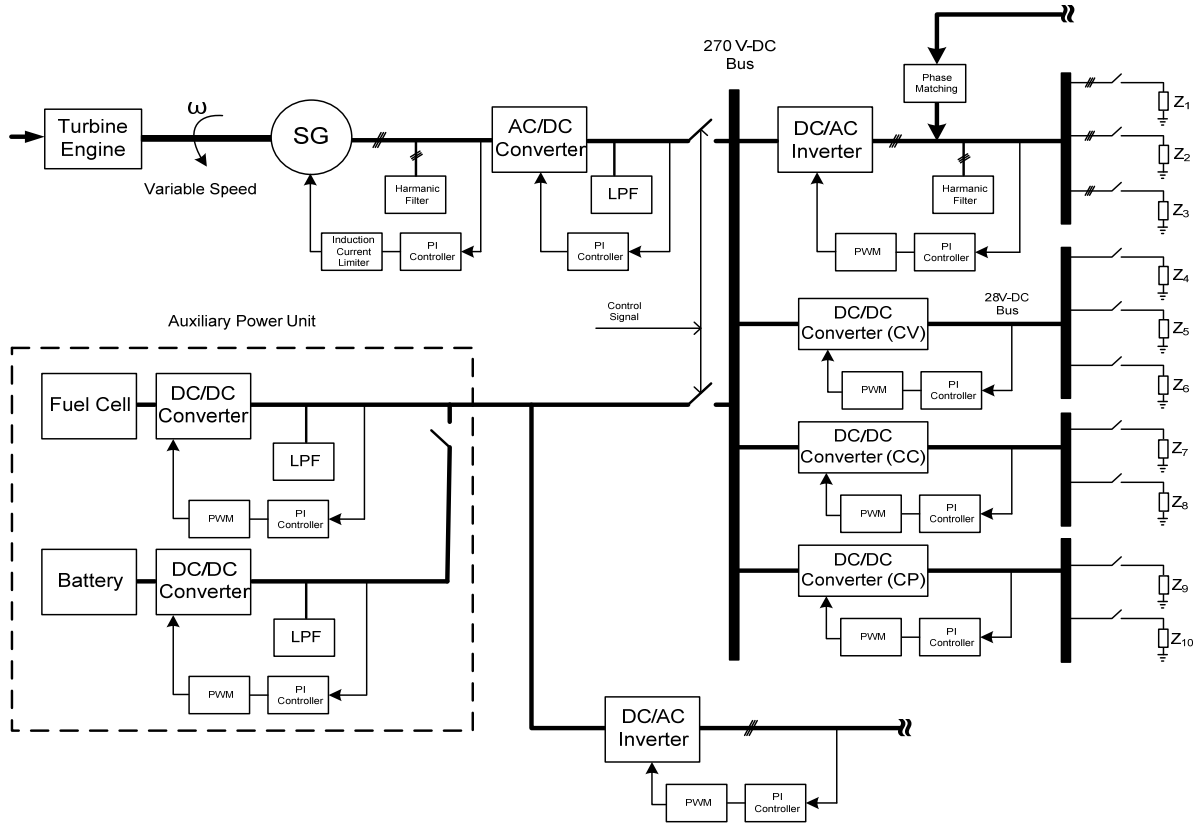
Fig. 2.1: Schematic diagram of AAEPS with APU system.

2.2.1 Generating System

The generating system is comprised of starter/generators, a voltage control unit and a feedback control system from the dc-link. In the VSCF Synchronous Generator (SG), the rated operating frequency is 400 Hz, although the frequency may vary in the range of 400 Hz to 800 Hz to compensate for engine speed changes. A feedback proportional-integral (PI) control strategy regulates the voltage of the 270V-dc bus by appropriately modifying the field excitation current of the SG.

2.2.2 Rectifier Unit

Connected to the generator is a transformer rectifier unit (TRU) with a passive 12-pulse rectifier unit. This configuration ensures the cancellation of low-order harmonics. Moreover, to implement the 30° phase shift required to obtain 12-pulse operation, a Y/Y/D transformer is employed.

2.2.3 DC/AC Loads

Various types of controlled dc and ac loads are distributed throughout the aircraft electric system. Depending on the operation conditions (e.g., normal operation or abnormal situations), the loading configurations change on different time scale. The dc non-linear loads are classified as constant power (CP), constant current (CC), and constant voltage (CV) loads. Also, passive and dynamic loads are considered in an AAEPS at different power ratings. In this paper, lumped circuit elements of series RL, as a representation of ac passive loads are modeled, with a minimum load power factor of 0.85 lagging [30,34].

2.2.4 Power Inverter

A voltage source inverter (VSI) is also connected to the 270V-dc bus, consisting of two 6-pulse switching bridge inverters. A feedback proportional-integral (PI) controller regulates the modulation index of the SPWM inverter to maintain a constant phase voltage of 115Vrms (200Vrms line-to-line) at the main 400Hz ac bus. A Y/Y/Δ transformer applies the necessary 30° phase shift to combine the signals from each output phase of the 6-pulse inverters. The combination of the signals produces the required 115V/200V rms, 400Hz line voltage at the main ac bus.

2.3 Mathematical Representation of the System Dynamics

In this section, sets of mathematical equations are extracted from the representative circuits of the aircraft electric system under study. These state space equations are used to model the system's performance in both transient and steady-state condition.

2.3.1 Mathematical Modeling of the SG with Harmonic Filter

Fig.2.2 shows the circuit model representation of the main generating system with harmonic filter. The time-domain differential equations describing the single channel generating system with Band Pass Harmonics Filter (BPHF) are presented as follows:
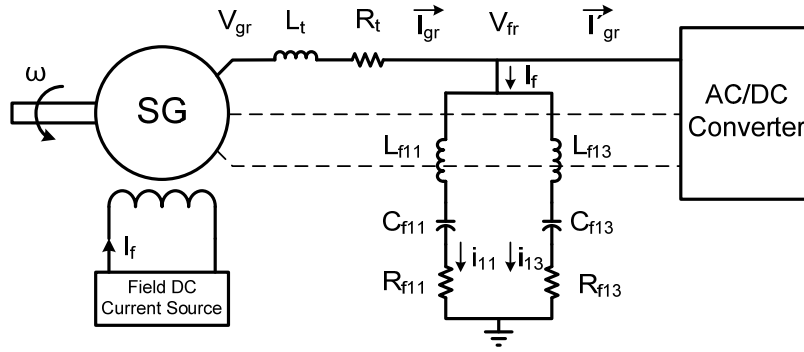
Fig. 2.2: Circuit representation of the generating system with BPHF.

$$
\begin{cases}
V_{gr} = V_m \sin\left(\omega t + \delta + \frac{\pi}{2}\right) \\
V_{gs} = V_m \sin\left(\omega t + \delta - \frac{\pi}{6}\right) \\
V_{gt} = V_m \sin\left(\omega t + \delta - \frac{5\pi}{6}\right)
\end{cases}
\tag{1}
$$

$$
\begin{cases}
V_{fr} = V_{gr} - R_t I_{gr} + L_t \frac{dI_{gr}}{dt} \\
V_{fs} = V_{gs} - R_t I_{gs} + L_t \frac{dI_{gs}}{dt} \\
V_{ft} = V_{gt} - R_t I_{gt} + L_t \frac{dI_{gt}}{dt}
\end{cases}
\tag{2}
$$

$$
r_g + r_l = R_t
\tag{3}
$$

$$
l_g + l_l = L_t
\tag{4}
$$

Assuming V_{gr}, V_{gs} and V_{gt} represent 3-phase open-circuit voltages at the SG terminals, and V_m is the peak value of phase voltage. V_{fr}, V_{fs} and V_{ft} introduce 3-phase voltage

profile at the harmonic filter terminals, ω denotes the angular frequency of the generating system. $l_l + l_g$ and $r_l + r_g$ represent the combined effect of the transmission cable and SG leakage inductances and resistances, respectively. Also, I_{gr}, I_{gs} and I_{gt} are the synchronous generator 3-phase currents flowing through the transmission line after filtering, and I'_g represents the current through TRU at ac side. According to the schematic circuit depicted in Fig.2.2, one comes to the differential equation identifying voltage and current profiles at the single phase harmonic filter's terminals as follows:

$$
\begin{cases}
L_{f11}\frac{d^2 i_{f11}}{dt} + r_f \frac{di_{f11}}{dt} + \frac{1}{C_{f11}} i_{f11} = \frac{dV_{fr}}{dt} = \\
\quad L_{f13}\frac{d^2 i_{f13}}{dt} + r_f \frac{di_{f13}}{dt} + \frac{1}{C_{f13}} i_{f13} \\
\quad i_{f11} + i_{f13} = I_{fr} = I'_{gr} - I_{gr}
\end{cases}
\tag{5}
$$

where L_{f11}, C_{f11} and L_{f13}, C_{f13} represent the inductors and capacitors of each branch in the BPHF tuned for harmonics mitigation. i_{f11} and i_{f13} are the currents through filter branches tuned for the order of 11th and 13th of the reference current, respectively. Also, R_{f11} and R_{f13} represent the filter's resistances. Equation (5) can be rearranged in the form of a differential state-space equation given by (6), (7)

$$
\begin{bmatrix} \dot{\chi}_1 \\ \dot{\chi}_2 \end{bmatrix} = \begin{bmatrix} 0 & 1 \\ \frac{-1}{L_{f11}C_{f11}} & \frac{-R_{f11}}{L_{f11}} \end{bmatrix} \begin{bmatrix} \chi_1 \\ \chi_2 \end{bmatrix} + \begin{bmatrix} \frac{1}{L_{f11}} \\ \frac{-R_{f11}}{L_{f11}^2} \end{bmatrix} V_{fr}
\tag{6}
$$

$$
\begin{bmatrix} \dot{\chi}_3 \\ \dot{\chi}_4 \end{bmatrix} = \begin{bmatrix} 0 & 1 \\ \frac{-1}{L_{f13}C_{f13}} & \frac{-R_{f13}}{L_{f13}} \end{bmatrix} \begin{bmatrix} \chi_3 \\ \chi_4 \end{bmatrix} + \begin{bmatrix} \frac{1}{L_{f13}} \\ \frac{-R_{f13}}{L_{f13}^2} \end{bmatrix} V_{fr}
\tag{7}
$$

where $\chi_1 = i_{f11}$ and $\chi_3 = i_{f13}$ are selected as state variables. The full expression of (6), (7) describing the harmonics filter characteristics is given by a state space matrix equation as

$$
\dot{\chi} = \Psi \chi + \Gamma u
\tag{8}
$$

where the state vector χ is given by (9). In this vector, χ_2 and χ_4 represent the derivative of χ_1 and χ_3. The state matrix Ψ as a representation of the filter's characteristics is expressed in (10). Moreover, the input profile is introduced by (11).

9

$$\chi = \begin{bmatrix} \chi_1 \\ \chi_2 \\ \chi_3 \\ \chi_4 \end{bmatrix} \tag{9}$$

$$\Psi = \begin{bmatrix} 0 & 1 & 0 & 0 \\ \frac{-1}{L_{f11}C_{f11}} & \frac{-R_{f11}}{L_{f11}} & 0 & 0 \\ 0 & 0 & 0 & 1 \\ 0 & 0 & \frac{-1}{L_{f13}C_{f13}} & \frac{-R_{f13}}{L_{f13}} \end{bmatrix} \tag{10}$$

$$\Gamma = \begin{bmatrix} \frac{1}{L_{f11}} \\ \frac{-R_{f11}}{L_{f11}^2} \\ \frac{1}{L_{f13}} \\ \frac{-R_{f13}}{L_{f13}^2} \end{bmatrix} \quad , \quad \mathrm{u} = V_{fr}(\omega, t) \tag{11}$$

In the state space vector given by (9), χ_1 and χ_3 represent the harmonic currents through two branches of the BPHF, which are tuned for harmonic mitigation of the order of 11th and 13th of the fundamental frequency component, generated by 12-pulse rectifier unit. Using these variables, the filter current can be estimated as

$$I_{fr} = \chi_1 + \chi_3 \tag{12}$$

2.3.2   Non-linear Description of TRU with Low Pass Filter (LPF)

Suppose the currents flowing through TRU (I'_{gr}, I'_{gs}, I'_{gt}) are continuous and the semiconductor diodes used in full-bridge rectifier are ideal. Fig. 2.3 can be used to represent a current-fed full-bridge power supply with LPF, proposed by [30,34].
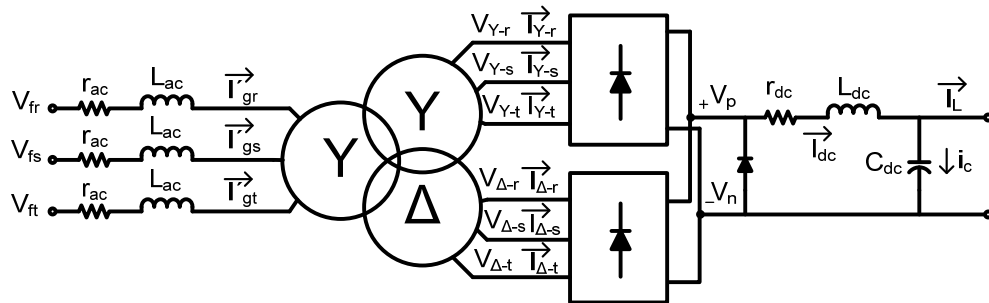
Fig. 2.3: Circuit configuration of the TRU with LPF.

10

As the diode bridge network of the rectifier unit simply converts the voltage and current directions between the ac input side and the main dc link in each cycle, the relationship between the ac and dc side, considering a naturally commutated full bridge diode, can be described by the following non-linear differential equations. Assume the 3-phase input voltages (measured respect to neutral) of the rectifier unit are given by

$$\begin{cases} V_{fr} = V'_m \sin\left(\omega t + \frac{\pi}{2}\right) \\ V_{fs} = V'_m \sin\left(\omega t - \frac{\pi}{6}\right) \\ V_{ft} = V'_m \sin\left(\omega t - \frac{5\pi}{6}\right) \end{cases} \tag{13}$$

where V'_m is the peak phase voltage of the BPHF. Assuming the transformer ratio of the rectifier unit be equal to unity, then the rectifier's upper and lower bridge input voltages (measured respect to neutral) can be stated as

$$\begin{cases} V_{Y-r} = V_{fr} = V'_m \sin\left(\omega t + \frac{\pi}{2}\right) \\ V_{Y-s} = V_{fs} = V'_m \sin\left(\omega t - \frac{\pi}{6}\right) \\ V_{Y-t} = V_{ft} = V'_m \sin\left(\omega t - \frac{5\pi}{6}\right) \end{cases} \tag{14}$$

$$\begin{cases} V_{\Delta-r} = V'_m \sin\left(\omega t + \frac{\pi}{2} + \frac{\pi}{6}\right) = V'_m \sin\left(\omega t + \frac{2\pi}{3}\right) \\ V_{\Delta-s} = V'_m \sin\left(\omega t - \frac{\pi}{6} + \frac{\pi}{6}\right) = V'_m \sin(\omega t) \\ V_{\Delta-t} = V'_m \sin\left(\omega t - \frac{5\pi}{6} + \frac{\pi}{6}\right) = V'_m \sin\left(\omega t - \frac{2\pi}{3}\right) \end{cases} \tag{15}$$

In an AAEPS with the power rating of 90-kW [30,34,38], the dc load current is relatively low. Therefore, the commutation angle (μ) may be considered less than $\pi/6$, and the commutation intervals in the upper and lower bridges do not overlap, hence the circuit dynamics can be expressed by [36,39]

1) during commutation interval $\alpha \leq \theta < \mu$

$$\begin{cases} L_{ac} \frac{dI_{\Delta-r}}{dt} = -r_{ac}I_{\Delta-r} + V_{\Delta-r} - V_p \\ L_{ac} \frac{dI_{\Delta-s}}{dt} = -r_{ac}I_{\Delta-s} + V_{\Delta-s} - V_n \\ L_{ac} \frac{dI_{\Delta-t}}{dt} = -r_{ac}I_{\Delta-t} + V_{\Delta-t} - V_n \end{cases} \tag{16}$$

$$\begin{cases} L_{ac}\dfrac{dI_{Y-r}}{dt} = -r_{ac}I_{Y-r} + V_{Y-r} - V_p \\ L_{ac}\dfrac{dI_{Y-s}}{dt} = -r_{ac}I_{Y-s} + V_{Y-s} - V_n \end{cases} \tag{17}$$

$$\begin{cases} I_{\Delta-r} = -(I_{\Delta-s} + I_{\Delta-t}) \\ \quad I_{Y-r} = -I_{Y-s} \\ \quad I_{Y-t} = 0 \\ \quad I_{Y-r} + I_{\Delta-r} = I_{dc} \end{cases} \tag{18}$$

where $\theta = \omega t$ and α represent the starting commutation angle. I_Y, I_Δ correspond to the upper and lower bridge input current per phase, L_{ac} and r_{ac} model the effect of the TRU leakage inductance and resistance, respectively. Also, V_p, V_n denote the positive and negative nodes of the dc link voltages.

2) during conduction interval $\mu \leq \theta < \alpha + \dfrac{\pi}{6}$

$$\begin{cases} L\dfrac{dI_{\Delta-r}}{dt} = -r_{ac}I_{\Delta-r} + V_{\Delta-r} - V_p \\ L\dfrac{dI_{\Delta-t}}{dt} = -r_{ac}I_{\Delta-t} + V_{\Delta-t} - V_n \end{cases} \tag{19}$$

$$\begin{cases} L\dfrac{dI_{Y-r}}{dt} = -r_{ac}I_{Y-r} + V_{Y-r} - V_p \\ L\dfrac{dI_{Y-s}}{dt} = -r_{ac}I_{Y-s} + V_{Y-s} - V_n \end{cases} \tag{20}$$

$$\begin{cases} I_{\Delta-r} = -I_{\Delta-t} \\ \quad I_{\Delta-s} = 0 \\ \quad I_{Y-r} = -I_{Y-s} \\ \quad I_{Y-r} + I_{\Delta-r} = I_{dc} \\ \quad I_{Y-r} = I_{\Delta-r} = \dfrac{1}{2}I_{dc} \\ \quad I_{Y-t} = 0 \end{cases} \tag{21}$$

From (16), (17), (18) and (19), (20), (21) one comes to

$$\begin{cases} V_p - V_n = \dfrac{6}{7}V_{\Delta-r} + \dfrac{3}{7}(V_{Y-r} - V_{Y-s}) \\ \quad -\dfrac{6}{7}r_{ac}I_{dc} - \dfrac{6}{7}L_{ac}\dfrac{dI_{dc}}{dt} \qquad \alpha \leq \theta < \mu \\ V_p - V_n = \dfrac{1}{2}(V_{\Delta-r} - V_{\Delta-t}) + \dfrac{1}{2}(V_{Y-r} - V_{Y-s}) \\ \quad -r_{ac}I_{dc} - L_{ac}\dfrac{dI_{dc}}{dt} \qquad \mu \leq \theta < \alpha + \dfrac{\pi}{6} \end{cases} \tag{22}$$

Substituting (14) and (15) into (22) yields

12

$$\begin{cases} V_p - V_n = \frac{6+3\sqrt{3}}{7}V'_m \sin\left(\theta + \frac{2\pi}{3}\right) - \frac{6}{7}r_{ac}I_{dc} \\ \quad -\frac{6}{7}L_{ac}\frac{dI_{dc}}{dt} \qquad\qquad\qquad\qquad \alpha \le \theta < \mu \\ V_p - V_n = \frac{1}{2}\{\sqrt{3}V'_m \cos(\theta) + \sqrt{3}V'_m \sin\left(\theta + \frac{2\pi}{3}\right)\} \\ \quad -r_{ac}I_{dc} - L_{ac}\frac{dI_{dc}}{dt} \qquad\qquad \mu \le \theta < \alpha + \frac{\pi}{6} \end{cases} \tag{23}$$

where I_{dc} is the current of the rectifier's dc side. Also, the dynamic characteristics of the net dc voltage, corresponding to the dc current and load currents can be expressed by

$$r_{dc}I_{dc} + L_{dc}\frac{dI_{dc}}{dt} = \left(V_p - V_n\right) - V_{dc} \tag{24}$$

$$I_{dc} = C_{dc}\frac{dV_{dc}}{dt} + I_{Load} \tag{25}$$

where r_{dc} is the total resistance of the main dc bus, L_{dc}, C_{dc} represent the inductance and capacitance of the rectifier's output filter, respectively. Substituting (24), (25) into (23), the steady-state dynamics of the system's dc main bus can be described by the following periodic non-liner equation:

$$V_{dc} + R_2 C_{dc}\frac{dV_{dc}}{dt} + L_2 C_{dc}\frac{d^2V_{dc}}{dt} = \frac{6+3\sqrt{3}}{7}V'_m \sin\left(\theta + \frac{2\pi}{3}\right) - R_2 I_{Load} - L_2 \frac{dI_{Load}}{dt}$$

$$-\frac{\pi}{4} \le \theta < \mu - \frac{\pi}{4} \tag{26}$$

$$V_{dc} + R_2 C_{dc}\frac{dV_{dc}}{dt} + L_2 C_{dc}\frac{d^2V_{dc}}{dt} = \frac{1}{2}\{\sqrt{3}V'_m \sin\left(\theta + \frac{\pi}{2}\right) + \sqrt{3}V'_m \sin\left(\theta + \frac{2\pi}{3}\right)\} - R_2 I_{Load} -$$

$$L_2 \frac{dI_{Load}}{dt} \quad \mu - \frac{\pi}{4} \le \theta < -\frac{\pi}{12} \qquad\qquad (27)$$

where

$$R_1 = r_{dc} + \frac{6}{7}r_{ac} \tag{28}$$

$$L_1 = L_{dc} + \frac{6}{7}L_{ac} \tag{29}$$

$$R_2 = r_{dc} + r_{ac} \tag{30}$$

$$L_2 = L_{dc} + L_{ac} \tag{31}$$

For further simplicity, equations (26) and (27) can be combined as

$$L_2 C \frac{d^2 V_{dc}}{dt} + R_2 C \frac{dV_{dc}}{dt} + V_{dc} = -\{R_2 I_{Load} + L_2 \frac{dI_{Load}}{dt}\} + h(\theta,\mu)\frac{6+3\sqrt{3}}{7} V_m \sin\left(\theta + \frac{2\pi}{3}\right) + (1-$$

$$h(\theta,\mu))\frac{1}{2}\{\sqrt{3}V_m \cos(\theta) + \sqrt{3}V_m \sin\left(\theta + \frac{2\pi}{3}\right)\} \tag{32}$$

where the commutation function $h(\theta,\mu)$ is defined by

$$h(\theta,\mu) = \begin{cases} 1 & if \quad 2n\pi - \frac{\pi}{4} \le \theta < 2n\pi + \mu - \frac{\pi}{4} \\ 0 & if \quad 2n\pi + \mu - \frac{\pi}{4} < \theta < 2n\pi - \frac{\pi}{12} \end{cases} \tag{33}$$

In which n is an integer number and the periodic function $h(\theta,\mu)$ repeats every $\frac{\pi}{6}$ cycle. Moreover, the differential state space representation of the equation (32) is obtained as follows

$$\begin{bmatrix} \dot{X}_v \\ \dot{X}_c \end{bmatrix} = \begin{bmatrix} 0 & \frac{1}{C} \\ -\frac{1}{L_2} & -\frac{R_2}{L_2} \end{bmatrix} \begin{bmatrix} X_v \\ X_c \end{bmatrix} + \begin{bmatrix} -\frac{1}{C} & 0 \\ 0 & \frac{1}{L_2} \end{bmatrix} \begin{bmatrix} I_{Load} \\ f_v \end{bmatrix} \tag{34}$$

where the filter capacitance voltage ($X_v = V_{dc}$) and dc link current ($X_c = I_{dc}$) are selected as state variables, also, f_v represents the following term

$$f_v = f_v(V'_m, \theta, \mu) = h(\theta,\mu)\frac{6+3\sqrt{3}}{7} V'_m \sin\left(\theta + \frac{2\pi}{3}\right) + (1-h(\theta,\mu))\frac{\sqrt{3}}{2}\{V'_m \cos(\theta) +$$

$$V'_m \sin\left(\theta + \frac{2\pi}{3}\right)\} \tag{35}$$

2.3.3 Dynamic Model Expression of the Multi-Converter System in AAEPS

Buck converters have been traditionally used in a variety of applications, such as; spacecraft, aircraft electric power systems, More Electric Ship Power Systems (MESPS), More Electric Vehicles (MEVs), electric and hybrid electric cars, and medical electronics application. The use of dc/dc converters is very common in the multiconverter power electronic system in an APU-based advanced aircraft [30,34,37,38]. As illustrated in Fig. 2.4, various types of buck converters interact with the dc main bus while providing a tightly regulated voltage, current, and constant power (CV, CP, CC) to the available dc loads. In this study, load profiles vary versus time. Depending on loading conditions, the dynamic behavior of the converter may change accordingly. A wide operating profile of the dc loads may cause the current drawn from the power supply to vary over a wide range. The load changes from one profile to another often take place in a very short time,

usually accompanied by a rapid change of the current demand. Hence, both transient and steady-state performance of the multiconverter at major nodes is highly affected by loading condition. In this section, differential equations describing the system's dynamics are developed assuming that the buck converters shown in Fig. 2.4 operate based on pulse width-modulation (PWM) technique; also, converters are considered to be operating in continuous conduction mode, with switching period T and duty cycle d_t. The value of T is determined by the PWM switching frequency and is considered to be constant; however, d_t varies from one loading condition to another (time-varying loads (TVL)).
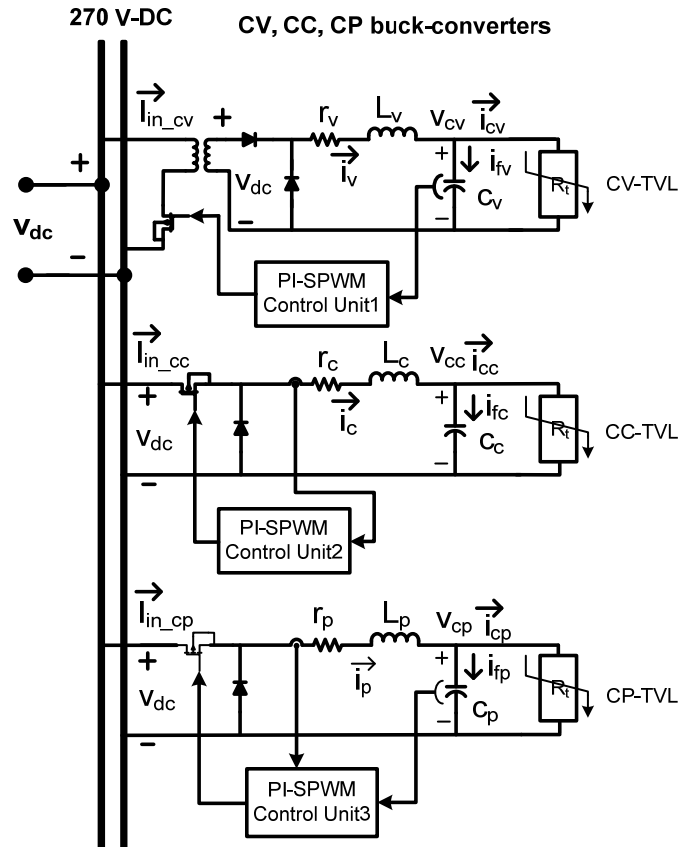
Fig. 2.4: A representative circuit model of the dc-dc converters used in an AAEPS.

1) ***CV-buck converter with Time Varying Load (TVL)***

The representation circuit model has been traditionally used by many authors [21,22,39,40]. Continuous conduction-mode operation of the buck converter can be described by the following set of differential equations

15

$$\begin{cases} \frac{dI_v}{dt} = h(t, T_v) \frac{V_{dc(t)}}{L_v} - r_v \frac{I_{v(t)}}{L_v} - \frac{V_{cv(t)}}{L_v} \\ \frac{dV_{cv}(t)}{dt} = \frac{I_v(t)}{C_v} - \frac{V_{cv(t)}}{C_v R_t} \\ I_{in\_cv} = h(t, T_v) I_v(t) \end{cases} \tag{36}$$

where I_{in_cv} represents the buck input current. Line current I_v and output voltage of the filter V_{cv} are selected as state variables. r_v, L_v, C_v represent line resistance, inductance and capacitance of the buck converter's filter, respectively. Also, the dc time varying load is introduced by R_t. The commutation function describing circuit switching control is defined as

$$h(t, T_v) = \begin{cases} 1 & 0 \leq t \leq d_t T_v \\ 0 & d_t T_v \leq t \leq T_v \end{cases} \tag{37}$$

where T_v corresponds to the time period of PWM switching frequency, and d_t is determined according to the loading condition.

2)   CC-buck converter with TVL

The CC-buck converter's steady-state characteristics can be represented in a manner similar to those of the CV-buck converter given by (36). The only difference is the frequency of PWM control signal that varies from one type of converter to another represented in this study.

3)   CP-buck converter with TVL

The dynamic performance of CP-buck converter can be similarly derived using equations similar to (36). Also, the current through converter I_p and filter's output voltage V_{cp} may be used to estimate the constant power rating, as follows

$$P(t) = V_{cp}(t) I_p(t) \tag{38}$$

2.3.4   DC/AC Inverter in the Multi-Converter System

Fig. 5 depicts a circuit representation of the 12-pulse voltage source inverter (VSI) with SPWM control strategy used in an AEPS. By selecting the line currents and filter's output as state variables, one comes to the differential equations describing inverter's dynamics as follows
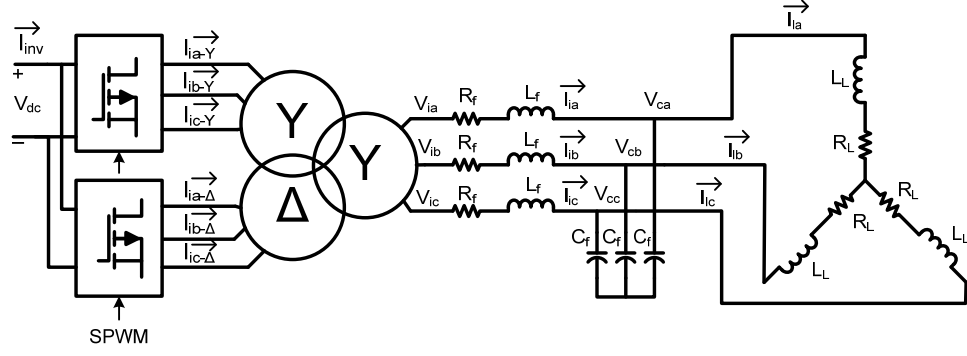
Fig. 2.5: PWM 12-pulse voltage source inverter with RL load

$$
\begin{cases}
\dfrac{dI_{ia}}{dt} = -\dfrac{R_f}{L_f}I_{ia} - \dfrac{1}{L_f}v_{ca} + \dfrac{1}{L_f}v_{ia} \\[2mm]
\qquad \dfrac{dI_{la}}{dt} = -\dfrac{R_L}{L_L}I_{la} + \dfrac{v_{ca}}{L_L} \\[2mm]
\qquad\quad \dfrac{dv_{ca}}{dt} = \dfrac{I_{ia}}{C_f} - \dfrac{I_{la}}{C_f} \\[2mm]
\dfrac{dI_{ib}}{dt} = -\dfrac{R_f}{L_f}I_{ib} - \dfrac{1}{L_f}v_{cb} + \dfrac{1}{L_f}v_{ib} \\[2mm]
\qquad \dfrac{dI_{lb}}{dt} = -\dfrac{R_L}{L_L}I_{lb} + \dfrac{v_{cb}}{L_L} \\[2mm]
\qquad\quad \dfrac{dv_{cb}}{dt} = \dfrac{I_{ib}}{C_f} - \dfrac{I_{lb}}{C_f} \\[2mm]
\dfrac{dI_{ic}}{dt} = -\dfrac{R_f}{L_f}I_{ic} - \dfrac{1}{L_f}v_{cc} + \dfrac{1}{L_f}v_{ic} \\[2mm]
\qquad \dfrac{dI_{lc}}{dt} = -\dfrac{R_L}{L_L}I_{lc} + \dfrac{v_{cc}}{L_L} \\[2mm]
\qquad\quad \dfrac{dv_{cc}}{dt} = \dfrac{I_{ic}}{C_f} - \dfrac{I_{lc}}{C_f}
\end{cases}
\tag{39}
$$

where V_{ia}, V_{ib}, V_{ic} are the ac voltages respect to neutral, I_{ia}, I_{ib} and I_{ic} represent current of the VSI for a 3-phase balanced system, respectively, R_f, L_f, C_f correspond to the harmonics filter, R_l, L_l and i_{la}, i_{lb}, i_{lc} model series RL passive load and corresponding load currents for the described 3-phase system. Also, V_{ca}, V_{cb} and V_{cc} introduce the ac voltages respect to neutral, for phases a, b and c, measured at the LPF terminals. Furthermore, the inverter's output voltage can be obtained by [41]

$$
\begin{bmatrix} V_{ia} \\ V_{ib} \\ V_{ic} \end{bmatrix} = \frac{N_s}{N_p}\frac{V_{dc}}{3}\begin{bmatrix} 2 & -1 & -1 \\ -1 & 2 & -1 \\ -1 & -1 & 2 \end{bmatrix}\begin{bmatrix} s_{11} \\ s_{12} \\ s_{13} \end{bmatrix}
\tag{40}
$$

where s_{11}, s_{12}, s_{13} introduce the SPWM switching function for output voltage control and frequency regulation purposes of the SVI, V_{dc} represents the input dc voltage, and $\dfrac{N_s}{N_p}$

17

corresponds to windings turn ratio of the transformer connected to the VSI. By applying $30°$ phase shift to the described switching functions, the control signals corresponding to the upper row of the $\Delta - Y$ rectifying bridge can be introduced as s_{31}, s_{32}, s_{33}. Using this set of switching functions, the relationship between input current and inverter's output ac currents can be expressed by the following equation

$$I_{inv} = S_{11}I_{ia-Y} + S_{12}I_{ib-Y} + S_{13}I_{ic-Y} + S_{31}I_{ia-\Delta} + S_{32}I_{ib-\Delta} + S_{33}I_{ic-\Delta} \tag{41}$$

where I_{inv} represents the input current of the 12-pulse PWM inverter. Also, the relations between ac currents at two sides of the transformer are given by

$$I_{ia-Y} = \frac{I_{ia}}{2}, \quad I_{ib-Y} = \frac{I_{ib}}{2}, \quad I_{ic-Y} = \frac{I_{ic}}{2} \tag{42}$$

$$I_{ia-\Delta} = \frac{I_{ia(30°)}}{2}, \quad I_{ib-Y} = \frac{I_{ib(30°)}}{2}, \quad I_{ic-Y} = \frac{I_{ic(30°)}}{2} \tag{43}$$

2.4 Modeling and Analysis of the AAEPS Using the GSSA Method

2.4.1 Basic Principles of the GSSA

The main concept of the GSSA (Generalized State Space Averaging) [21] modeling is to replace the real time-domain variables with their complex Fourier coefficients over a desired time interval. The GSSA method is derived from Fourier transform of non-periodic signals [21,24,28]. In fact, each signal $x(\tau)$ as a function of time (τ) can be approximated using finite number of time-dependant Fourier coefficients $\langle x \rangle_k(\tau)$. For each τ within the time period $[t - T, t]$, the approximated signal can be given by

$$x(\tau) = \sum_{k=-\infty}^{\infty} \langle x \rangle_k(\tau) e^{jk\omega\tau} \tag{44}$$

where T is the time period (T is defined for periodic signals) and $\omega = \frac{2\pi}{T}$ is the angular frequency. The complex Fourier time dependent coefficients $\langle x \rangle_k(\tau)$ are given by

$$\langle x \rangle_k(\tau) = \frac{1}{T} \int_{t-T}^{t} x(\tau) e^{-jk\omega\tau} d\tau \tag{45}$$

Reconstructing $x(\tau)$ from its Fourier coefficients, equation (44) becomes

$$x(\tau) = \langle x \rangle_0 + 2 \sum_{k=1}^{\infty} \{\Re \langle x \rangle_k \cos(k\omega\tau) - \Im\langle x \rangle_k \sin(k\omega\tau)\} \tag{46}$$

Also, the precision of estimation is increased with considering more Fourier coefficients. In fact, required degree of accuracy can be achieved by choosing appropriate value of the

harmonics order k [21,28]. In a practical transformation, the following basic operations on the complex Fourier coefficients are normally required:

$$\frac{d}{dt}\langle x(\tau)\rangle_k = -jk\omega\langle x(\tau)\rangle_k + \langle\frac{dx(\tau)}{dt}\rangle_k \tag{47}$$

$$\langle x(\tau)y(\tau)\rangle_k = \sum_{i=-\infty}^{\infty}\langle x(\tau)\rangle_{k-i}\langle y(\tau)\rangle_i \tag{48}$$

$$\langle x(\tau) + y(\tau)\rangle_k = \langle x\rangle_k(\tau) + \langle y\rangle_k(\tau) \tag{49}$$

where x and y are time domain functions and $\langle x(\tau)\rangle_k$, $\langle y(\tau)\rangle_k$ denote their k^{th} order complex Fourier coefficients. Moreover, the proposed approximated models in next sections overcome the difficulties of applying conventional SSA models with the following limitations [24]:

(i)   *the PWM switching frequency is assumed to be much greater than the highest natural frequency of the buck converter in each switching cycle of the operation mode, and*

(ii)   *the input voltage to the converter in each switching cycle must remain constant, or slow time varying variables compared to the switching frequency*

2.4.2 *The GSSA Representation of the BC interacting with 12-Pulse Rectifier*

1) CV-buck converter with TVL

In this set of equations, generalized state space averaged model of the buck converter with output constant voltage time varying loads (TVLs) is developed using first-order Fourier approximation. In this model the actual state space variables describing system's dynamics are obtained from the Fourier coefficients of the circuits state variables I_v, V_{cv} , given by (36). Moreover, the state variable is constructed with a dc coordinate and an oscillating term, which correspond to the parameter $k = -1, 0, +1$ from (44). Using the first-order approximation of Fourier coefficients, I_v, v_{cv} can be obtained using the following state variables

$$\begin{cases} \langle I_v\rangle_0 = q_1 \\ \langle v_{cv}\rangle_0 = q_2 \\ \langle I_v\rangle_1 = q_3 + jq_4 \\ \langle v_{cv}\rangle_1 = q_5 + jq_6 \end{cases} \tag{50}$$

19

since I_v, v_{cv} are real values, then

$$\begin{cases} \langle I_v \rangle_{-1} = \langle I_v \rangle_1^* \\ \langle v_{cv} \rangle_{-1} = \langle v_{cv} \rangle_1^* \end{cases} \tag{51}$$

where * represents the conjugate of a complex number. By applying the time derivative properties of the Fourier coefficients in (36) and further substituting the first-order Fourier coefficients of the switching function $h(t, T_v)$

$$\langle h(t, T_v) \rangle_0 = d_t, \quad \langle h(t, T_v) \rangle_1 = \frac{1 - e^{-j2\pi d_t}}{2\pi j} \tag{52}$$

one comes to the following equations

$$\dot{q}_1 = d_t \frac{V_{dc}}{L_v} - r_v \frac{q_1}{L_v} - \frac{q_2}{L_v} + \frac{\langle V_{dc}(t) h(t, T_v) \rangle_0}{L_v} \tag{53}$$

$$\dot{q}_2 = \frac{q_1}{C_v} - \frac{q_2}{C_v R_t} \tag{54}$$

$$\dot{q}_3 = \frac{-r_v}{L_v} q_3 + \omega_v q_4 - \frac{1}{L_v} q_5 + \Re \frac{\langle V_{dc}(t) h(t, T_v) \rangle_1}{L_v} \tag{55}$$

$$\dot{q}_4 = -\omega_v q_3 - \frac{r_v}{L_v} q_4 - \frac{1}{L_v} q_6 + \Im \frac{\langle V_{dc}(t) h(t, T_v) \rangle_1}{L_v} \tag{56}$$

$$\dot{q}_5 = \frac{1}{C_v} q_3 - \frac{1}{R_t C_v} q_5 + \omega_v q_6 \tag{57}$$

$$\dot{q}_6 = \frac{1}{C_v} q_4 - \omega_v q_5 + \frac{1}{R_t C_v} q_6 \tag{58}$$

By applying the averaged product property of the Fourier coefficients in (48) to $V_{dc} * h(t, T_v)$, the dc and first order oscillating component can be obtained as follows

Assume

$$\langle V_{dc}(t) \rangle_0 = X_1, \quad \langle V_{dc}(t) \rangle_{1(cv\_bc)} = X_7 + j X_8 \tag{59}$$

then

$$\langle V_{dc}(t) h(t, T_v) \rangle_0 = X_1 d_t + 2(X_7 \frac{\sin(2\pi d_t)}{2\pi} + X_8 \frac{\cos(2\pi d_t) - 1}{2\pi} \tag{60}$$

$$\langle V_{dc}(t) h(t, T_v) \rangle_1 = X_1 \frac{\sin(2\pi d_t)}{2\pi} + d_t X_7 + j(d_t X_8 + X_1 \frac{\cos(2\pi d_t) - 1}{2\pi}) \tag{61}$$

where $\langle V_{dc}(t)\rangle_{1(cv\_bc)}$ represents the Fourier coefficient corresponding to the fundamental harmonic component appears on the 12-pulse rectifier's dc voltage, due to interaction with the cv-buck converter. These types of oscillating components will be explained in more detail in the next sections. Also, the matrix representation of the state variables can be expressed subsequently as

$$
\begin{bmatrix} \dot{q}_1 \\ \dot{q}_2 \\ \dot{q}_3 \\ \dot{q}_4 \\ \dot{q}_5 \\ \dot{q}_6 \end{bmatrix} = \begin{bmatrix} \frac{-r_v}{L_v} & \frac{-1}{L_v} & 0 & 0 & 0 & 0 \\ \frac{1}{C_v} & \frac{-1}{R_tC_v} & 0 & 0 & 0 & 0 \\ 0 & 0 & \frac{-r_v}{L_v} & \omega_v & \frac{-1}{L_v} & 0 \\ 0 & 0 & -\omega_v & \frac{-r_v}{L_v} & 0 & \frac{-1}{L_v} \\ 0 & 0 & \frac{1}{C_v} & 0 & \frac{-1}{R_tC_v} & \omega_v \\ 0 & 0 & 0 & \frac{1}{C_v} & -\omega_v & \frac{1}{R_tC_v} \end{bmatrix} * \begin{bmatrix} q_1 \\ q_2 \\ q_3 \\ q_4 \\ q_5 \\ q_6 \end{bmatrix} + \begin{bmatrix} \frac{X_1 d_t + 2(X_7\frac{\sin(2\pi d_t)}{2\pi}+X_8\frac{\cos(2\pi d_t)-1}{2\pi})}{L_v} \\ 0 \\ \frac{X_1\sin(2\pi d_t)}{2\pi L_v} + \frac{d_t X_7}{L_v} \\ \frac{X_1(\cos(2\pi d_t)-1)}{2\pi L_v} + \frac{d_t X_8}{L_v} \\ 0 \\ 0 \end{bmatrix} \tag{62}
$$

Equation (62) also can be rewritten as following state space differential equation

$$
\dot{q} = \Omega(t)q + U(t) \tag{63}
$$

In equation (62) d_t is a time-dependant quantity and varies according to the loading conditions, and R_t models the time-dependent dc loads. Using the real-time state variables approximation of (62) and substituting in equation (46), I_v, c_{cv} can be obtained as

$$
\begin{cases} I_v(t) = q_1 + 2q_2\cos(\omega_v t) - 2q_4\sin(\omega_v t) \\ v_{cv}(t) = q_2 + 2q_5\cos(\omega_v t) - 2q_6\sin(\omega_v t) \end{cases} \tag{64}
$$

where $\omega_v = \frac{2\pi}{T_v}$, and T_v represents the time period of PWM operating frequency for the constant voltage buck converter. Furthermore, using the multiplying property in (48), zeroth and first-order Fourier coefficients corresponding to input current of the buck converter can be approximated as

$$
\langle I_{in\_cv}\rangle_0 = \langle h(t, T_v)I_v(t)\rangle_0 = d_t q_1 + 2(q_3\frac{\sin(2\pi d_t)}{2\pi} + q_4\frac{(\cos(2\pi d_t)-1)}{2\pi}) \tag{65}
$$

$$
\langle I_{in\_cv}\rangle_1 = \langle h(t, T_v)I_v(t)\rangle_1 = q_1\frac{\sin(2\pi d_t)}{2\pi} + d_t q_3 + j(q_1\frac{(\cos(2\pi d)-1)}{2\pi} + q_4 d_t) \tag{66}
$$

Also, substituting (64), (65) into (46) yields

$$I(t)_{in\_cv} = d_t q_1 + 2\left(q_3 \frac{sin(2\pi d_t)}{2\pi} + q_4 \frac{(cos(2\pi d_t)-1)}{2\pi}\right) + 2\left[\left(q_1 \frac{sin(2\pi d_t)}{2\pi} + d_t q_3\right)\cos(\omega_v t) - \right.$$
$$\left(q_1 \frac{(cos(2\pi d_t)-1)}{2\pi} + q_4 d_t\right)sin(\omega_v t) \tag{67}$$

1) *CP-buck converter with TVL*

For the constant power buck-converter with time varying loads, the GSSA model previously derived for the cv-converter is valid and can be employed to describe the system's characteristics for various loading conditions. Suppose $I_p(t)$ and $v_{cp}(t)$ are selected as time-domain state variables identifying cp-buck converter's dynamics. Using these two variables to describe active power consumed by cp-type dc loads, the averaged value as well as fundamental oscillating component of the power can be generated via first-order Fourier coefficients approximation as following

Assume

$$\begin{cases} \langle I_p(t)\rangle_0 = a_1 \\ \langle v_{cp}(t)\rangle_0 = a_2 \\ \langle I_p(t)\rangle_1 = a_3 + ja_4 \\ \langle v_{cp}\rangle_1 = a_5 + ja_6 \end{cases} \tag{68}$$

By applying the multiplying property of (48) into (38), the zeroth and first-order Fourier coefficient is respectively given by

$$\langle P(t)\rangle_0 = \langle V_{cp}(t)I_p(t)\rangle_0 = a_1 a_2 + 2(a_3 a_5 + a_4 a_6) \tag{69}$$

$$\langle P(t)\rangle_1 = \langle V_{cp}(t)I_p(t)\rangle_1 = a_1 a_5 + a_2 a_3 + j(a_1 a_6 + a_2 a_4) \tag{70}$$

Also, equation (62) may be used to calculate the state variables of the cp buck converter introduced by (68). Furthermore, real-time large-signal representation of the constant power consumption is achieved by using (69), (70) and further substituting into (46) as expressed by

$$P_{cp}(t) = a_1 a_2 + 2(a_3 a_5 + a_4 a_6) + 2[(a_1 a_5 + a_2 a_3)\cos(\omega_p t) - (a_1 a_6 + a_2 a_4)\sin(\omega_p t)] \tag{71}$$

where ω_p introduces the main harmonic frequency corresponding to the oscillating component in the approximate constant power waveform.

2.4.3 *The GSSA Modeling of the 12-Pulse PWM VSI*

In this section, the GSSA method is applied to model the dynamic behaviors of the 12-pulse switching inverter with RL passive loads, which is connected to the main dc link at the output of 12-pulse diode rectifier's harmonics filter. The Fourier coefficients as representation of the circuit's state variables can be derived from the equations introduced by (39)-(43). Assume a 3-phase system with zero dc offset as

$$\begin{cases} \langle I_{ia} \rangle_0, \langle I_{la} \rangle_0, \langle V_{ca} \rangle_0 = 0 \\ \langle I_{ia} \rangle_1 = p_1 + j p_2 \\ \langle I_{la} \rangle_1 = p_3 + j p_4 \\ \langle V_{ca} \rangle_1 = p_5 + j p_6 \\ \langle s_{11} \rangle_0 = s_{dc}, \langle s_{11} \rangle_1 = s_i + j s_j \end{cases} \tag{72}$$

$$\langle V_{ia} \rangle_0 = 0, \langle V_{ia} \rangle_1 = \frac{1}{3} \langle (2 V_{dc} s_{11} - V_{dc} s_{12} - V_{dc} s_{13}) \rangle_1 \tag{73}$$

where the dc and first-order Fourier components of a signal x are shown with $\langle x \rangle_0$ and $\langle x \rangle_1$, respectively. By applying the Fourier coefficient properties from (48), (49) into (72), (73), and further substituting into equations (39), (40), (41), one gets to the first-order Fourier representation of the inverter's output profile, described by a differential state space matrix equation as follows

$$\begin{bmatrix} \dot{p}_1 \\ \dot{p}_2 \\ \dot{p}_4 \\ \dot{p}_5 \\ \dot{p}_5 \\ \dot{p}_6 \end{bmatrix} = \begin{bmatrix} \frac{-R_f}{L_f} & \omega_i & 0 & 0 & \frac{-1}{L_f} & 0 \\ -\omega_i & \frac{-R_f}{L_f} & 0 & 0 & 0 & \frac{-1}{L_f} \\ 0 & 0 & \frac{-R_L}{L_L} & \omega_i & \frac{1}{L_L} & 0 \\ 0 & 0 & -\omega_i & \frac{-R_L}{L_L} & 0 & \frac{1}{L_L} \\ \frac{1}{C_f} & 0 & \frac{-1}{C_f} & 0 & 0 & \omega_i \\ 0 & \frac{1}{C_f} & 0 & \frac{-1}{C_f} & -\omega_i & 0 \end{bmatrix} \begin{bmatrix} p_1 \\ p_2 \\ p_4 \\ p_5 \\ p_5 \\ p_6 \end{bmatrix} + \begin{bmatrix} X_1 \frac{s_i \cos(\varphi) - s_j \sin(\varphi)}{L_f} \\ X_1 \frac{s_i \sin(\varphi) + s_j \cos(\varphi)}{L_f} \\ 0 \\ 0 \\ 0 \\ 0 \end{bmatrix} \tag{74}$$

where ω_i is the operating frequency of the ac main bus, φ corresponds to initial phase angle of the switching function s_{11} and X_1 represents the averaged dc value of the preceding 12-pulse rectifier's output voltage (V_{dc}), which we will discuss with more detail in next sections. The GSSA model also can be used to approximate the characteristics of a 3-phase imbalanced system with the following state equation

$$\begin{bmatrix} \dot{P}_a \\ \dot{P}_b \\ \dot{P}_c \end{bmatrix} = \begin{bmatrix} A_a & 0 & 0 \\ 0 & A_b & 0 \\ 0 & 0 & A_c \end{bmatrix} \begin{bmatrix} P_a \\ P_b \\ P_c \end{bmatrix} + \begin{bmatrix} U_a \\ U_b \\ U_c \end{bmatrix} \tag{75}$$

23

where P_a, P_b, P_c introduce the state variable vectors per phase, which previously derived in (74), A_a, A_b, A_c represent the state matrices for each phase, and U_a, U_b, U_c correspond to the input matrices, operating with $120°$ phase shift respect to each other, representing the 3-phase balanced system under study. Using the state variables given by (74), the time-domain representation of the inverter's output voltage and current profiles can be reconstructed as

$$I_{ia}(t) = 2p_1 \cos(\omega_i t + \alpha_i) - 2p_2 \sin(\omega_i t + \alpha_i) \tag{76}$$

$$I_{la}(t) = 2p_3 \cos(\omega_i t + \alpha_l) - 2p_4 \sin(\omega_i t + \alpha_l) \tag{77}$$

$$V_{ca}(t) = 2p_5 \cos(\omega_i t + \alpha_c) - 2p_6 \sin(\omega_i t + \alpha_c) \tag{78}$$

where $\alpha_i, \alpha_l, \alpha_c$ introduce the phase angle corresponding to I_{ia}, I_{la}, V_{ca} , respectively. Furthermore, the averaged value of the inverter's input current described by (41)-(43) may be similarly derived as

$$\langle I_{inv} \rangle_0 = \langle S_{11} \tfrac{I_{ia}}{2} + S_{12} \tfrac{I_{ib}}{2} + S_{13} \tfrac{I_{ic}}{2} + S_{31} \tfrac{I_{ia(30°)}}{2} + S_{32} \tfrac{I_{ib(30°)}}{2} + S_{33} \tfrac{I_{ic(30°)}}{2} \rangle_0 \tag{79}$$

By applying the Fourier coefficient properties in (48), (49) and further substituting the state variables of (72) into (79) with $120°$ phase shift consideration for the 3-phase system, one comes to

$$\langle I_{inv} \rangle_0 = 12 \left[\cos(\gamma) \left(s_i p_1 + s_j p_2 \right) - \sin(\gamma)(s_j p_1 - s_i p_2) \right] \tag{80}$$

where γ denotes the phase angle corresponding to power factor (PF) of the lumped circuit elements of series RL as a representation of ac passive loads, described previously in section 2.2. As was mentioned earlier, one of the approximations of the GSSA method is neglecting high order harmonics, which depends on the required degree of accuracy. Therefore, the fundamental oscillating component of I_{inv}, representing the inverter's input current main characteristics can be developed using first-order Fourier coefficient approximation yields the following sequence of equations

$$\langle I_{inv} \rangle_{1(inv)} = \langle S_{11} \tfrac{I_{ia}}{2} + S_{12} \tfrac{I_{ib}}{2} + S_{13} \tfrac{I_{ic}}{2} + S_{31} \tfrac{I_{ia(30°)}}{2} + S_{32} \tfrac{I_{ib(30°)}}{2} + S_{33} \tfrac{I_{ic(30°)}}{2} \rangle_{1(inv)} \tag{81}$$

where $\langle I_{inv} \rangle_{1(inv)}$ represents the dominant oscillating component in the dc-side current of the 12-pulse inverter. Now let us consider higher term harmonics in the 6-pulse bridge inverter's phase currents expressed by following equation

$$\begin{cases} I_x = \frac{I_{ia}}{2(6k\pm1)}\sin[(6k\pm1)\omega_i t + \beta_x] \\ x = a, b, c \qquad k = 1, 2, \dots \end{cases} \qquad (82)$$

where I_x corresponds to the phase current flows through each branch of the 6-pulse inverter bridge. By substituting (82) into (81) and applying the convolution property from time-domain product to frequency domain transfer and further using product property in Fourier series (48) one gets to the dominant oscillating component appearing in the current waveform at dc-side of the 12-pulse VSI as follows

$$\langle I_{inv} \rangle_{5\omega_i} = \frac{3}{5}[s_{dc} * \frac{I_{ia}}{2j}]e^{j\gamma} \qquad (83)$$

2.4.4 *12-Pulse Diode Rectifier Interacting with BC and 12-Pulse PWM VSI*

In this section, through the application of the GSSA in modeling and characterization of AAEPS, the interaction of 12-pulse diode rectifier connected to the PWM-VSI and three different types of dc/dc buck converters are presented. The interconnected complex system as an integrated multi-converter system is large-signally modeled (GSSA) via first-order Fourier approximation. Throughout the development of averaging model of the system under study, it has been assumed that the PWM switching frequencies of the buck-converters, as well as 12-pulse inverter are much higher than the natural frequency of the 12-pulse diode rectifier. In the set of equations of the generalized state space average model, V_{dc} and I_{dc} are selected as representation of circuit's state variables. Moreover, the actual state-space variables describing system's transient and steady-state performance are produced via Fourier coefficients as following

Suppose the average values of V_{dc}, I_{dc} ($k = 0$) are given by

$$\begin{cases} \langle V_{dc} \rangle_0 = X_1 \\ \langle I_{dc} \rangle_0 = X_2 \end{cases} \qquad (84)$$

Also, twenty other state-space variables may be produced to represent the fundamental frequency components appearing on the main dc-link voltage and current waveforms, due to interactions with switching non-linear dc/dc converters, as well as 12-pulse PWM source voltage inverter, shown in Fig. 2.6.
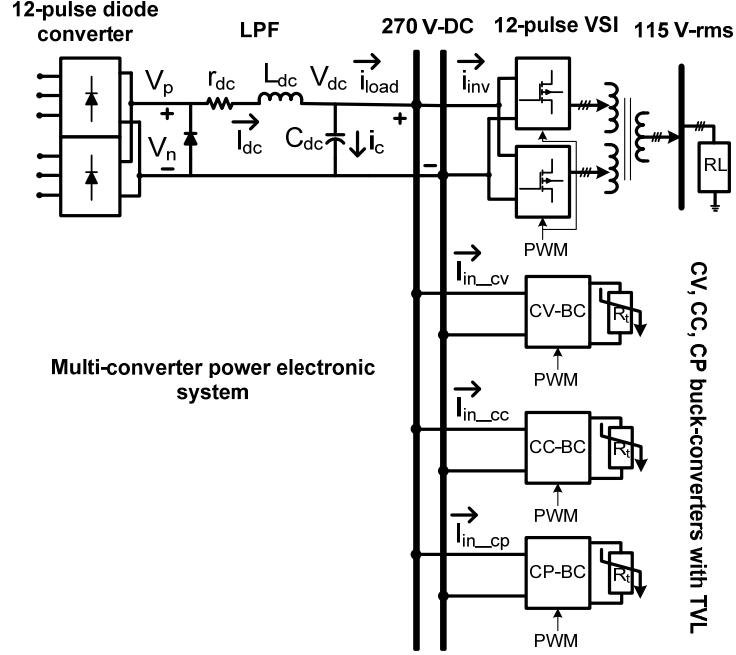
Fig. 2.6: Circuit representation of the integrated multi-converter system in AAEPS

These first-order Fourier coefficients, describing the dc voltage and current profile are expressed by

$$\begin{cases} \langle V_{dc} \rangle_{1(rec)} = X_3 + jX_4 \\ \langle I_{dc} \rangle_{1(rec)} = X_5 + jX_6 \end{cases} \tag{85}$$

$$\begin{cases} \langle V_{dc} \rangle_{1(cv\_bc)} = X_7 + jX_8 \\ \langle I_{dc} \rangle_{1(cv\_bc)} = X_9 + jX_{10} \end{cases} \tag{86}$$

$$\begin{cases} \langle V_{dc} \rangle_{1(cc\_bc)} = X_{11} + jX_{12} \\ \langle I_{dc} \rangle_{1(cc\_bc)} = X_{13} + jX_{14} \end{cases} \tag{87}$$

$$\begin{cases} \langle V_{dc} \rangle_{1(cp\_bc)} = X_{15} + jX_{16} \\ \langle I_{dc} \rangle_{1(cp\_bc)} = X_{17} + jX_{18} \end{cases} \tag{88}$$

$$\begin{cases} \langle V_{dc} \rangle_{1(inv)} = X_{19} + jX_{20} \\ \langle I_{dc} \rangle_{1(inv)} = X_{21} + jX_{22} \end{cases} \tag{89}$$

where $\langle V_{dc} \rangle_1$, $\langle I_{dc} \rangle_1$ with the relevant subscripts; (rec), (cv_bc), (cc_bc), (cp_bc) and (inv) represent the fundamental oscillating components of the voltage and current waveforms, generated by 12-pulse diode bridge rectifier, constant voltage, constant

current and constant power buck-converters, as well as switching PWM inverter, respectively. Since V_{dc}, I_{dc} are real values, then;

$$\begin{cases} \langle V_{dc} \rangle_{-k} = \langle V_{dc} \rangle_k^* \\ \langle I_{dc} \rangle_{-k} = \langle I_{dc} \rangle_k^* \\ k = 0, 1, 2 \ldots \end{cases} \tag{90}$$

where the operator * represents the conjugate of a complex number. Taking the differentiation of the Fourier coefficients in (82)-(87) with respect to time, using time-derivative property in (47) and further substituting in (34), we obtain

$$\dot{X}_1 = \frac{1}{C_{dc}} X_2 - \frac{1}{C_{dc}} \langle I_{Load} \rangle_0 \tag{91}$$

$$\dot{X}_2 = -\frac{1}{L_2} X_1 - \frac{R_2}{L_2} X_2 + \frac{1}{L_2} \langle f_v \rangle_0 \tag{92}$$

$$\dot{X}_3 + j\dot{X}_4 = -j\omega_1 X_3 + \omega_1 X_4 + \frac{1}{C_{dc}} X_5 + j\frac{1}{C_{dc}} X_6 - \frac{1}{C_{dc}} \langle I_{Load} \rangle_{1(rec)} \tag{93}$$

$$\dot{X}_5 + j\dot{X}_6 = -j\omega_1 X_5 + \omega_1 X_6 - \frac{1}{L_2} X_3 - j\frac{1}{L_2} X_4 - \frac{R_2}{L_2} X_5 - j\frac{R_2}{L_2} X_6 + \frac{1}{L_2} \langle f_v \rangle_{1(rec)} \tag{94}$$

$$\dot{X}_7 + j\dot{X}_8 = -j\omega_2 X_7 + \omega_2 X_8 + \frac{1}{C_{dc}} X_9 + j\frac{1}{C_{dc}} X_{10} - \frac{1}{C_{dc}} \langle I_{Load} \rangle_{1(cv\_bc)} \tag{95}$$

$$\dot{X}_9 + j\dot{X}_{10} = -j\omega_2 X_9 + \omega_2 X_{10} - \frac{1}{L_2} X_7 - j\frac{1}{L_2} X_8 - \frac{R_2}{L_2} X_9 - j\frac{R_2}{L_2} X_{10} + \frac{1}{L_2} \langle f_v \rangle_{1(cv\_bc)} \tag{96}$$

$$\dot{X}_{11} + j\dot{X}_{12} = -j\omega_3 X_{11} + \omega_3 X_{12} + \frac{1}{C_{dc}} X_{13} + j\frac{1}{C_{dc}} X_{14} - \frac{1}{C_{dc}} \langle I_{Load} \rangle_{1(cc\_bc)} \tag{97}$$

$$\dot{X}_{13} + j\dot{X}_{14} = -j\omega_3 X_{13} + \omega_3 X_{14} - \frac{1}{L_2} X_{11} - j\frac{1}{L_2} X_{12} - \frac{R_2}{L_2} X_{13} - j\frac{R_2}{L_2} X_{14} + \frac{1}{L_2} \langle f_v \rangle_{1(cc\_bc)} \tag{98}$$

$$\dot{X}_{15} + j\dot{X}_{16} = -j\omega_4 X_{15} + \omega_4 X_{16} + \frac{1}{C_{dc}} X_{17} + j\frac{1}{C_{dc}} X_{18} - \frac{1}{C_{dc}} \langle I_{Load} \rangle_{1(cp\_bc)} \tag{99}$$

$$\dot{X}_{17} + j\dot{X}_{18} = -j\omega_4 X_{17} + \omega_4 X_{18} - \frac{1}{L_2} X_{15} - j\frac{1}{L_2} X_{16} - \frac{R_2}{L_2} X_{17} - j\frac{R_2}{L_2} X_{18} + \frac{1}{L_2} \langle f_v \rangle_{1(cp\_bc)} \tag{100}$$

$$\dot{X}_{19} + j\dot{X}_{20} = -j\omega_5 X_{19} + \omega_5 X_{20} + \frac{1}{C_{dc}} X_{21} + j\frac{1}{C_{dc}} X_{22} - \frac{1}{C_{dc}} \langle I_{Load} \rangle_{1(inv)} \tag{101}$$

$$\dot{X}_{21} + j\dot{X}_{22} = -j\omega_5 X_{21} + \omega_5 X_{22} - \frac{1}{L_2} X_{19} - j\frac{1}{L_2} X_{20} - \frac{R_2}{L_2} X_{21} - j\frac{R_2}{L_2} X_{22} + \frac{1}{L_2} \langle f_v \rangle_{1(inv)} \tag{102}$$

Since the output voltage of the 12-pulse diode rectifier f_v does not include any harmonic components at the PWM frequency of CVBC, CCBC, CPBC and VSI; hence one may get to the following

$$\langle f_v \rangle_{1(cv_{bc})} = \langle f_v \rangle_{1(cc_{bc})} = \langle f_v \rangle_{1(cp\_bc)} = \langle f_v \rangle_{1(inv)} = 0 \qquad (103)$$

Accordingly, matrix representation of the generalized state space averaging differential equation of the reduced-order system under full interaction is a 22×22 dimensional matrix (See Appendix A.1). Here we have developed the matrix representation of the GSSA equation corresponds to the interaction of 12-pulse rectifier with the CVBC.

$$
\begin{bmatrix} \dot{X}_1 \\ \dot{X}_2 \\ \dot{X}_3 \\ \dot{X}_4 \\ \dot{X}_5 \\ \dot{X}_6 \\ \dot{X}_7 \\ \dot{X}_8 \\ \dot{X}_9 \\ \dot{X}_{10} \end{bmatrix} =
\begin{bmatrix}
0 & \frac{1}{C_{dc}} & 0 & 0 & 0 & 0 & 0 & 0 & 0 & 0 \\
\frac{-1}{L_2} & \frac{-R_2}{L_2} & 0 & 0 & 0 & 0 & 0 & 0 & 0 & 0 \\
0 & 0 & 0 & \omega_1 & \frac{1}{C_{dc}} & 0 & 0 & 0 & 0 & 0 \\
0 & 0 & -\omega_1 & 0 & 0 & \frac{1}{C_{dc}} & 0 & 0 & 0 & 0 \\
0 & 0 & \frac{-1}{L_2} & 0 & \frac{-R_2}{L_2} & \omega_1 & 0 & 0 & 0 & 0 \\
0 & 0 & 0 & \frac{-1}{L_2} & -\omega_1 & \frac{-R_2}{L_2} & 0 & 0 & 0 & 0 \\
0 & 0 & 0 & 0 & 0 & 0 & 0 & \omega_2 & \frac{1}{C_{dc}} & 0 \\
0 & 0 & 0 & 0 & 0 & 0 & -\omega_2 & 0 & 0 & \frac{1}{C_{dc}} \\
0 & 0 & 0 & 0 & 0 & 0 & \frac{-1}{L_2} & 0 & \frac{-R_2}{L_2} & \omega_2 \\
0 & 0 & 0 & 0 & 0 & 0 & 0 & \frac{-1}{L_2} & -\omega_2 & \frac{-R_2}{L_2}
\end{bmatrix} *
\begin{bmatrix} X_1 \\ X_2 \\ X_3 \\ X_4 \\ X_5 \\ X_6 \\ X_7 \\ X_8 \\ X_9 \\ X_{10} \end{bmatrix} +
$$

$$
\begin{bmatrix}
-\frac{1}{C_{dc}}\left\{ d_t q_1 + 2(q_3 \frac{\sin(2\pi d_t)}{2\pi} + q_4 \frac{(\cos(2\pi d_t)-1)}{2\pi}) \right\} \\
\frac{1}{L_2}\left\{ 0.7905 V_m - 1.4 V_m \cos\left(\mu + \frac{5\pi}{12} \right) - 1.654 V_m \sin\left(\mu - \frac{\pi}{4} \right) \right\} \\
0 \\
0 \\
\hline
\left\{ \frac{1}{L_2}\{ -0.0538 V_m \cos\left(13\mu - \frac{31\pi}{12} \right) + 0.0636 V_m \cos\left(-11\mu + \frac{41\pi}{12} \right) - \right. \\
\left. 0.0636 V_m \sin\left(13\mu - \frac{13\pi}{4} \right) + 0.0751 V_m \sin\left(11\mu - \frac{11\pi}{4} \right) + 0.0055 V_m \} \right\} \\
\hline
\left\{ \frac{1}{L_2}\{ -0.0637 V_m \sin\left(-11\mu + \frac{41\pi}{12} \right) - 0.0539 V_m \sin\left(13\mu - \frac{31\pi}{12} \right) + \right. \\
\left. 0.0636 V_m \cos\left(13\mu - \frac{13\pi}{4} \right) + 0.0752 V_m \cos\left(11\mu - \frac{11\pi}{4} \right) + 0.0204 V_m \} \right\} \\
\hline
-\frac{1}{C_{dc}}\left\{ q_1 \frac{\sin(2\pi d_t)}{2\pi} + d_t q_3 \right\} \\
-\frac{1}{C_{dc}}\left\{ q_1 \frac{(\cos(2\pi d_t)-1)}{2\pi} + q_4 d_t \right\} \\
0 \\
0
\end{bmatrix} \qquad (104)
$$

2.4.5 AC-Side Profile Approximation with Averaged DQ0 Transformation

By considering the non-linear equations of commutation and conduction states for the input currents through upper and lower bridge rectifier correspond to the TRU, previously introduced in (18) and (21), one comes to the following algebraic equations describing the dynamic performance of the voltage and current profiles at the SG ac side. The DQ0 transform approach has been employed to translate the three phase system to a two-dimensional equivalent system with less complexity. The DQ0 representative equations for both upper and lower bridge rectifier's input currents average value over the time interval $T_{dq0} = \frac{\pi}{3}\frac{1}{\omega}$ may be calculated as

$$\begin{cases} I_{dq_0}(Y) = T I_Y \\ I_{dq_0}(\Delta) = T I_\Delta \end{cases} \tag{105}$$

where

$$I_Y = \begin{bmatrix} I_{Y-r} \\ I_{Y-s} \\ I_{Y-t} \end{bmatrix} \quad , \quad I_\Delta = \begin{bmatrix} I_{\Delta-r} \\ I_{\Delta-s} \\ I_{\Delta-t} \end{bmatrix} \tag{106}$$

and the DQ0 operator matrix is expressed by the following equation

$$T = \sqrt{\frac{2}{3}} * \begin{bmatrix} \cos(\theta) & \cos\left(\theta - \frac{2\pi}{3}\right) & \cos\left(\theta + \frac{2\pi}{3}\right) \\ \sin(\theta) & \sin\left(\theta - \frac{2\pi}{3}\right) & \sin\left(\theta + \frac{2\pi}{3}\right) \\ \frac{\sqrt{2}}{2} & \frac{\sqrt{2}}{2} & \frac{\sqrt{2}}{2} \end{bmatrix} \tag{107}$$

Performing the equation (103) by applying the non-linear conditional equations from (18) and (21), the averaged values of the input currents in DQ0 axis may be calculated as

$$\begin{cases} I_D(Y) = \frac{\sqrt{3}}{\pi} X_1 \cos\left(\mu + \frac{\pi}{6}\right) + \frac{3V_m}{\pi\omega_1 L}\left(\frac{1}{4}\cos\left(2\mu + \frac{\pi}{6}\right)\right. \\ \qquad\qquad \left. -\cos\left(\mu + \frac{\pi}{6}\right) - \frac{\mu}{4} + \frac{3\sqrt{3}}{8}\right) \\ I_Q(Y) = -\frac{\sqrt{3}}{\pi} X_1 \sin\left(\mu + \frac{\pi}{6}\right) - \frac{3V_m}{\pi\omega_1 L}\left(\frac{1}{4}\sin\left(2\mu + \frac{\pi}{6}\right)\right. \\ \qquad\qquad \left. -\sin\left(\mu + \frac{\pi}{6}\right) + \frac{\mu\sqrt{3}}{4} + \frac{3}{8}\right) \end{cases} \tag{108}$$

$$\begin{cases} I_D(\Delta) = \frac{\sqrt{3}}{\pi} X_1 \cos(\mu) + \frac{3V_m}{\pi\omega_s L}\left(\frac{1}{4}\cos(2\mu) - \cos(\mu) + \frac{3}{4}\right) \\ I_Q(\Delta) = -\frac{\sqrt{3}}{\pi} X_1 \sin(\mu) - \frac{3V_m}{\pi\omega_s L}\left(\frac{1}{4}\sin(2\mu) - \sin(\mu) + \frac{1}{2}\mu\right) \end{cases} \tag{109}$$

where X_1 represents the average value for the inductor's current at HVDC link, and the commutation angle μ can be obtained from the following expression (the simplified equation is derived assuming a very small value for r_{ac}; hence, neglecting it)

$$\mu = cos^{-1}(1 - \frac{2\omega L_{ac}}{\sqrt{3}V_m}X_1) \tag{110}$$

By considering the $30°$ phase shift corresponding to the $Y - \Delta$ transformer in TRU and performing the vector sum of above equations (Phasor description), the primary I_{DQ0} at the SG ac side can be developed as

$$\begin{cases} \vec{I}_{DQ_0} = \vec{I}_{dq_0}(Y) + \vec{I}_{dq_0}(\Delta) \\ I_D = \frac{1}{\sqrt{3}}(I_D(\Delta) + \frac{\sqrt{3}}{2}I_D(Y) - \frac{1}{2}I_Q(Y) \\ I_Q = \frac{1}{\sqrt{3}}(I_Q(\Delta) + \frac{1}{2}I_D(Y) - \frac{\sqrt{3}}{2}I_Q(Y) \end{cases} \tag{111}$$

Applying the inverse matrix T^{-1} to equation (108), the averaged representation of the TRU 3-ph input currents at SG ac side can be described as

$$\begin{bmatrix} I'_{gr} \\ I'_{gs} \\ I'_{gt} \end{bmatrix} = T^{-1}\begin{bmatrix} I_D \\ I_Q \\ 0 \end{bmatrix} = T^{-1}I_{DQ0} \tag{112}$$

Let us now identify the SG ac side profiles, using the equations extracted from the DQ0 transform, further applying the GSSA method. The GSSA representative differential equation corresponding to equation (8) can be expressed as follows

$$\begin{cases} \langle \dot{v} \rangle_{12k\pm1} = -j(12k \pm 1)\omega\langle v \rangle_{12k\pm1} + [\Psi\langle v \rangle_{12k\pm1} + \Gamma\langle V_{fr} \rangle_{12k\pm1}] \\ \langle I_{fr} \rangle_{12k\pm1} = \langle v_1 + v_3 \rangle_{12k\pm1} \end{cases} \tag{113}$$

Applying equation (2) for a single channel model, and by considering the averaged DQ0 representation of the SG ac side current and further substituting into equation (2), one comes to the following expression describing the voltage and current profiles at SG main bus harmonics filter

$$\{L_t\begin{bmatrix} 1 \\ 0 \\ 1 \\ 0 \end{bmatrix}^T \Gamma_{4\times1} + 1\}\langle V_{fr} \rangle_{12k\pm1} = \begin{bmatrix} 1 \\ 0 \\ 1 \\ 0 \end{bmatrix}^T \langle L_t\dot{T}^{-1} + R_tT^{-1} \rangle_{12k\pm1}I_{DQ0}$$

$$- \begin{bmatrix} 1 \\ 0 \\ 1 \\ 0 \end{bmatrix}^T \{R_tI_{4\times4} + L_t\Psi_{4\times4}\}\langle v_{4\times1} \rangle_{12k\pm1} + \frac{V_m}{2j} \tag{114}$$

where

$$\langle V_{gr} \rangle_{12k \pm 1} = \frac{V_m}{2(12k \pm 1)j} \tag{115}$$

Now, substituting equation (111) into (110) for the averaged value of filter's voltage $\langle V_{fr} \rangle_{12k \pm 1}$, one comes to the following parametric differential equation introducing harmonics filter's current in the GSSA domain as

$$\begin{cases} \langle \dot{v} \rangle_{12k \pm 1} = f(v, I_{DQ0}, V_m, \omega, T, \Psi, \Gamma, K, R_t, L_t) \\ \quad\quad \langle I_{fr} \rangle_{12k \pm 1} = \langle v_1 + v_3 \rangle_{12k \pm 1} \end{cases} \tag{116}$$

where $k = 0, \pm 1, \dots$ depending on the required degree of accuracy.

In Fig. 2.7 the schematic view of the aircraft interconnected power electric system is represented. The scheme depicted in this figure is drawn based on the reduced-order GSSA model. As demonstrated in the diagram, the key features of the system affected by the following/preceding components can be feasibly identified by applying the GSSA technique to obtain the most dominant profiles of the system under study. Therefore, the proposed scheme can be used for design and implementation of a novel Identification and Diagnostic Toolbox for the Advanced Aircraft Electric Power System (IDT-AAEPS) currently is being developed by the author.

IDT-AAEPS is a device that is capable of visualizing the aircraft electric system network in order to check if the entire system operation is within the IEEE/military standards [31]. Shown in Fig. 2.7, one may notice that the state variables (Fourier coefficients) predicted at the following nodes (blocks) are used to approximate the voltage and current waveforms at the preceding nodes. This method of circuit analysis has been employed to reduce the complexity of the system while capturing the key characteristics of the system performance at major nodes (dc and ac buses).

In the block diagram depicted in Fig. 2.7, the Fourier coefficients introduced previously in this Chapter are used to predict the voltage or current waveforms under study at a particular node in the AAEPS network. The Fourier coefficients as state variables of the AAEPS reduced-order system are used to reconstruct the approximated signals in time domain (Eq. (46)), and are given by y_1, y_2, y_3, and y_4, as shown in Fig. 2.7.
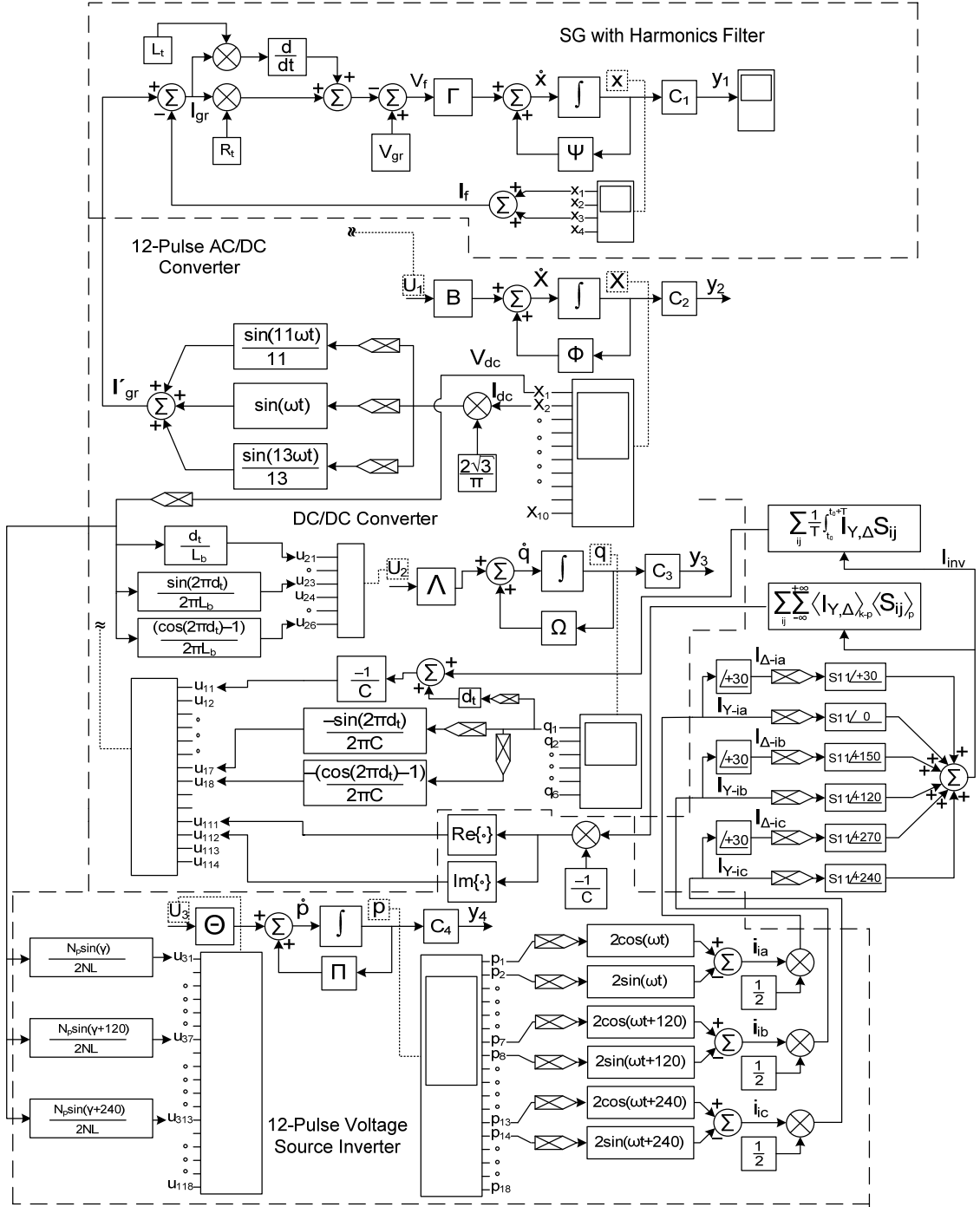
Fig. 2.7: The GSSA representative model for the reduced-order AAEPS.

Section 2.5 of this thesis contains the application of the proposed GSSA model through several case-studies for characterization and performance of the advanced aircraft electric power system under different loading conditions.

2.5 System Analysis with GSSA Models

In this section, the developed models have been utilized to characterize the aircraft electric network performance on both transient and steady-state conditions. The dynamic behaviors of each component have been individually assessed using its corresponding GSSA model. Also, system's responses to changes in power demand are addressed via several case studies. Similarly, the interactions between converters and subsystems are visualized using first-order Fourier-coefficient approximation as time-dependent state variables. It has been demonstrated that the interactions between interconnecting power electronic converters in the aircraft electric system under investigation and the dynamic performance of each converter receiving its voltage source from the preceding converter while supplying outputs to the following load converters can be obtained using generalized average variables with required degree of accuracy.

2.5.1   12-Pulse Voltage Source Inverter (VSI)

The study reported in this section is performed based on a three-phase balanced system assumption, including a 12-pulse VSI with an input voltage of 270V-dc, a tightly regulated ac voltage at 115Vrms per phase. Also, to maintain a constant operating frequency at 400Hz, the sinusoidal PWM control strategy with the modulating frequency of 400Hz and carrier frequency of 25 kHz is employed [34,44,46]. Other parameters used in the simulations are presented in Table 2.1, corresponding to Fig. 2.5.

TABLE. 2.1
AC main bus-system parameters

Quantity	Value	Comment
ω_i	2π*400rad/s	angular operating frequency of VSI
R_f	0.01Ω	filter's series resistance
L_f	20μH	filter's series inductance
C_f	100μF	filter's capacitance
R_L	2Ω	passive load's resistance
L_L	0.4mH	passive load's inductance
R_{lk}	0.001Ω	Y-Y-Δ transformer's leakage resistance
L_{lk}	10μH	Y-Y-Δ transformer's leakage inductance

33

Fig. 2.8 depicts two study models of the switching multi-pulse inverter in the aircraft system. The first column in (a) presents an "exact" switching model, including 3-phase voltage profile at the low-pass harmonic filter terminals, as well as the ac current at the output of 12-pulse bridge inverter before filtering, and after filtering which is the currents through RL loads. This model is developed in the PSIM9 environment. The second figures in column (b) correspond to the developed "averaged" model expressed by Eq. (75). This model is implemented in MATLAB environment.

(a)   (b)
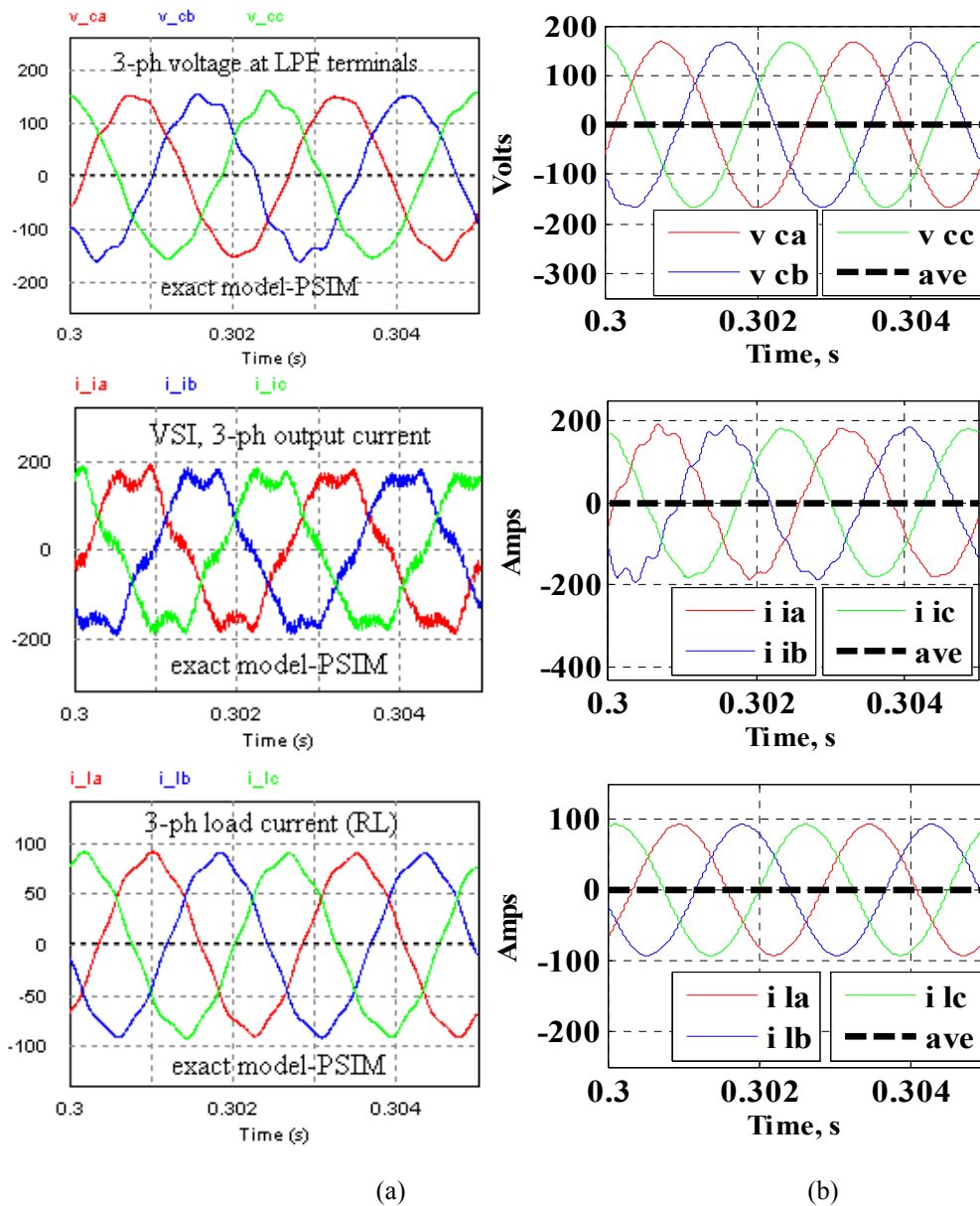
Fig. 2.8: The 12-pulse Voltage Source Inverter with 3-ph passive load, (a) exact time-domain model, (b) averaged model.

As shown in Fig. 2. 8 (a) and (b), the peak value of the ac voltage at low-pass harmonics filter's terminals is set to 165Vpeak/115Vrms and the full load current is approximately 73Apeak/52.5Vrms. Furthermore, the operating frequency is regulated at 400Hz [31]. Fig. 2. 8 (a) also shows the 3-phase output current of the multi-pulse inverter containing the high frequency oscillation contents generated by PWM switching modulation. The simulation is performed for a load power of approximately 18.0kVA [42]. Moreover, the effectiveness of applying the GSSA technique to modeling and characterization of VSI is demonstrated in column (b). As shown in the figures, only the fundamental components of the original signals are considered and terms of higher-order oscillations are omitted. The simulation results obtained from developed model closely agree with that of the exact time-domain models implemented in PSIM9. Fig. 2. 9 (c), (d) depicts the system response to changes in power demand. Correspondingly, the loading configuration is subjected to the following sequence of events. From t_0=0.2s to t_1=0.3s, only 50% of the RL full-load power is activated ($R_L = 4\Omega, L_L = 0.8mH$), while the VSI system is connected to the aircraft electric power system network. At t_1=0.3 the power rating is stepped up to its nominal value at 18.0kVA ($R_L = 2\Omega, L_L = 0.4mH$). It is seen from Fig. 2. 9 that the harmonics filter's voltage remains unaffected as the constant frequency ac bus undergoes the step change in the loading profile.

(a)

(b)
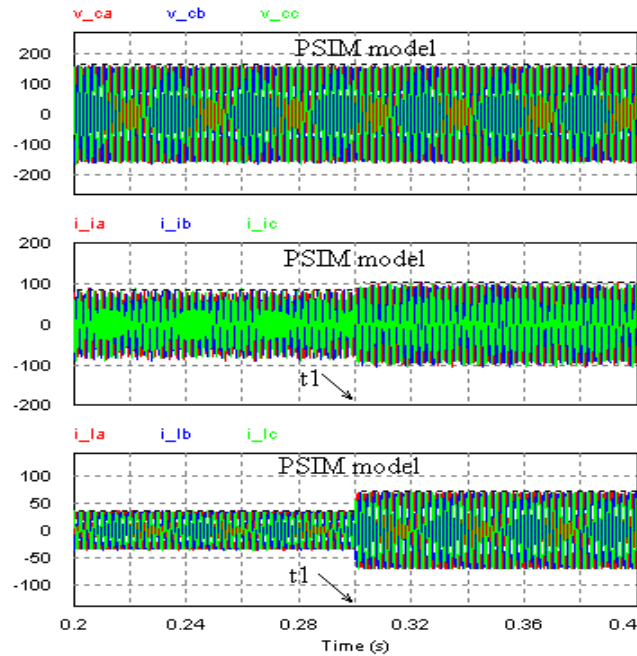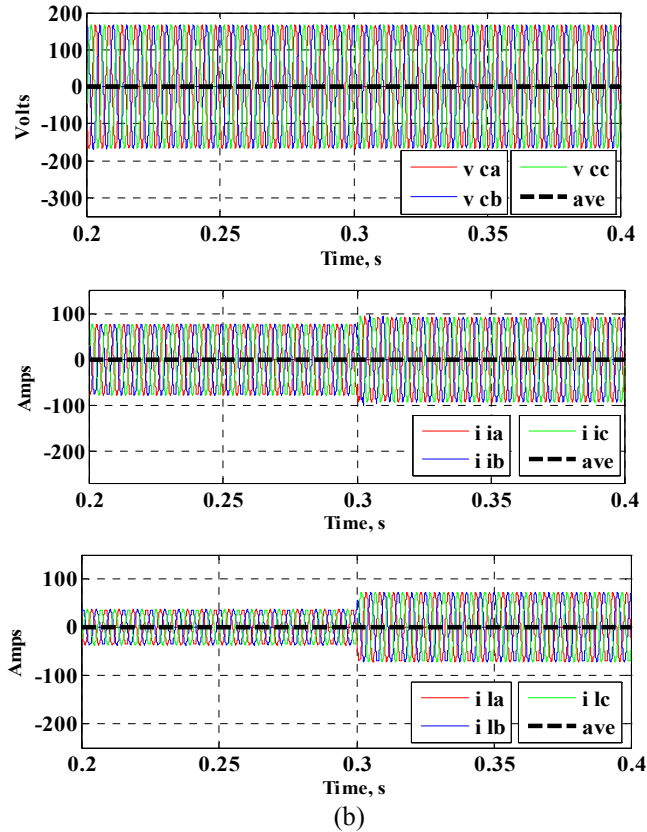
Fig. 2.9: System response to change in power demand, (a) developed by PSIM9 (b) implemented in Matlab using the proposed GSSA model.

Fig. 2. 10 (e), (f) depicts the dc-side current through the 12-pulse bridge inverter. Fig. 2. 10 (f) illustrates that, although the average model does not include the higher-order ripples and harmonics (intentionally are not taken into account in calculation of the generalized average of the input current, for more simplicity), it provides the same pattern of waveform as that of the exact model real-time analysis with PSIM9, in terms of accuracy in the average dc value and fundamental oscillating component.

(e)

(f)
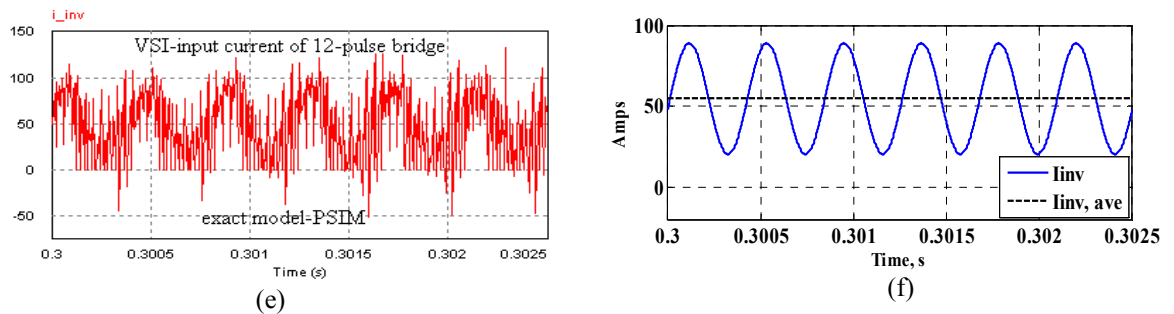
Fig. 2.10: DC-side current profile (e) time-domain exact model by PSIM9 (f) GSSA model implemented in Matlab environment.

As illustrated in Fig. 2.10, the dominant oscillating component appears on the input current of 12-pulse bridge inverter has the frequency of 2.4 kHz which is resulted from the modulation of PWM control signals fundamental component with the 5th order harmonic of the 6-pulse inverter bridge's currents, which has been introduced by Eq. (82) and (83) in this Chapter.

2.5.2 *Constant Voltage Buck Converter (CV-BC) with Time-Varying Load (TVL)*

Based upon the developed model, we will now demonstrate the application of generalized averaging technique to the analysis of CV-BC with time-varying load configuration. Among the dc loads classification of the advanced aircraft electric system proposed by [42, 46], in this section, we have studied the performance of a PWM buck-converter with a tightly regulated output voltage at 28V-dc. The differential state-space matrix equation introduced previously by Eq. (62) is utilized to calculate the averaged Fourier coefficients as representation of the constant voltage buck converter's actual state variables. These variables are then applied to capture the main dynamic characteristics of the converter, considering the average dc values of both voltage and current, as well as their corresponding first-order harmonic components caused by the PWM switching function of the control system. Therefore, the magnitude of transients, along with the steady-state fundamental harmonic may be considered to verify if the system's overshoot and ripple are within the limits of the applicable military standards. The novelty of the proposed model is that the interaction of the multi-converter system is taken into account, by modulating the preceding power supply's output voltage with the switching function of the following buck-converter.

In this effort the transient and steady-state performance of a fully controlled buck-converter with various loading configurations are investigated at different time scales. The modeling of change in power demand is achieved by applying a time-varying dc resistive load, with power ratings of approximately 1.87kW, 3.74kW and 5.6kW for different time intervals. Also, to maintain the output voltage constant at 28V, we have employed a GSSA representative model of the PWM switching function to provide a closed-loop control signal approximation used for voltage regulation. Fig. 2.11 (a), (b) shows the transient performance of the CV-BC, while supplying the full-load power to a dc load. The proposed GSSA model representing the constant voltage main dynamic

characteristics is implemented in MATLAB environment. In fact, we have digitized the continuous state space averaging equations and converted it to a recursive discrete system with a determined sampling time which is much less than the PWM control signal's time period. Also, for real-time analysis and to verify the accuracy of proposed averaging model, a study model is performed with PSIM9. The following parameters are used for simulation purposes: $r_v = 0.002\Omega$, $L_v = 15\text{mH}$, $C_v = 500\mu\text{F}$, $R_t = 0.14\Omega$. The PWM switching frequency is also set to $f_v = 15\text{kHz}$, hence the angular frequency is calculated to be $\omega_v = 2\pi \times 15\text{kHz}$.

(a)   (b)
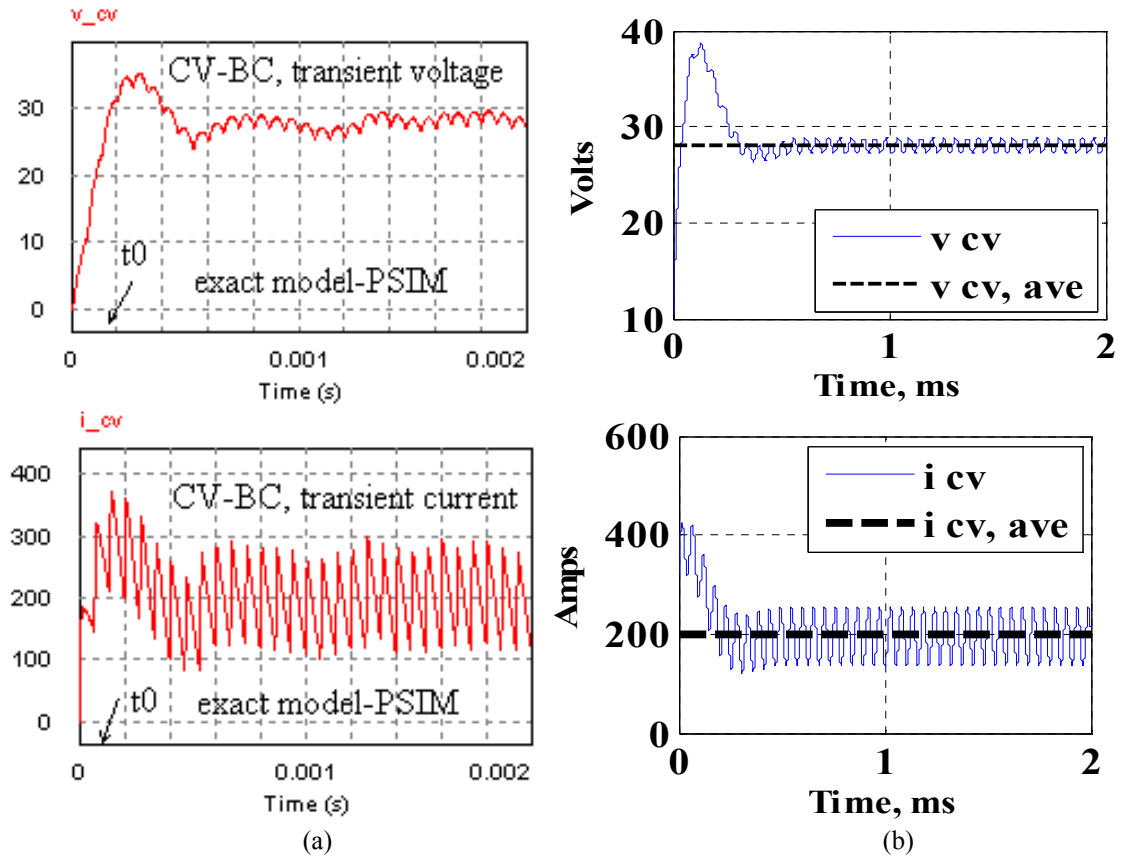
Fig. 2.11: Transient voltage and current profiles (a) exact model developed by PSIM9 (b) the GSSA model implemented in Matlab.

As illustrated, Fig. 2.11 closely compares the results of the "exact" time-domain model with that of the averaged models obtained from generalized state space averaging representation. According to the picture, the rise time of the buck converter's output voltage is approximately calculated at $t_0 = 0.2$ ms which is in good agreement with the rise time obtained from MATLAB® simulation. Fig. 2.12 (b), (d) depicts the magnified

form of top four graphs depicted in Fig. 2.11 (a) and (b). As shown in Fig. 2.12, the ripple corresponding to the regulated constant voltage is approximately 0.5 V or approximately 1.8% which is within the military standard [31]. It should be noted that using first-order approximation approach for the CV-BC system leads to a precise analysis of the system's dynamics and circumvents the necessity of considering higher-order harmonics. Fig. 2.12 (d) also shows that the inductor's current of the buck converter generated by generalized averaging variables precisely follows the current waveform of that has been obtained from "exact" simulation result.

(c)   (d)
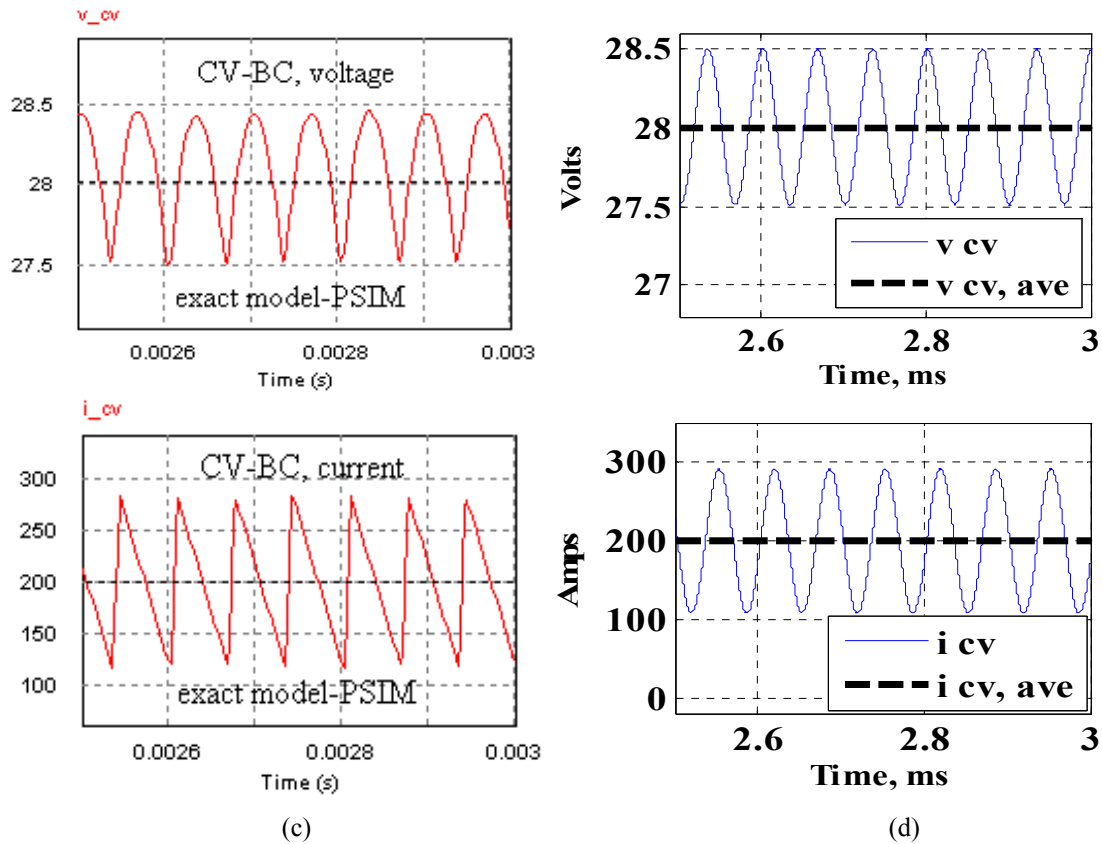
Fig. 2.12: The magnified view of voltage and current profiles (c) exact model developed by PSIM9 (d) the GSSA model implemented in Matlab.

As depicted in Fig. 2.13, the GSSA method is employed to derive the key characteristics of the constant voltage converter where is subjected to a sequence of step changes in the power demand. The simulation results of the exact topological model developed by PSIM9 along with the acquired outcomes of the proposed method are shown in Fig. 2.13 (e) and (f), respectively. The simulations are performed based on the

following steps: initially the system is in a light-load operating condition and the power rating is set to $1.867\ kW$ which is approximately 33% of the full-load power. Accordingly, the average dc current is calculated to be $66.7\ A$. At $t_1 = 0.3\ s$ the load power steps up to $3.73\ kW$($66.6\ \%$ of the nominal power) raising the level of current to $133\ A$. Finally, at $t_2 = 0.32\ s$ the full-load power is applied to the converter, causing another change in the inductor's current (i_cv) to reach its nominal average value at $200\ A$. Modeling the changes in power rating is achieved by selecting three values of dc resistance $R_t(0.42\ \Omega, 0.21\ \Omega\ and\ 0.14\ \Omega)$ for above mentioned time intervals. By comparing the graphs of column (e) with those of column (f) in Fig. 2.13, it can be seen that the proposed GSSA model can closely catch the dynamic characteristics and transient behavior of the converter's output voltage in consideration of the variation in power demand. Also, it is demonstrated that there is a good match between the transient responses corresponding to the current profiles obtained from both models, which confirms the applicability of the proposed model in this types of system. Therefore, first order Fourier approximation of the constant voltage buck converter under study through the GSSA approach provides a very reliable means of system analysis.
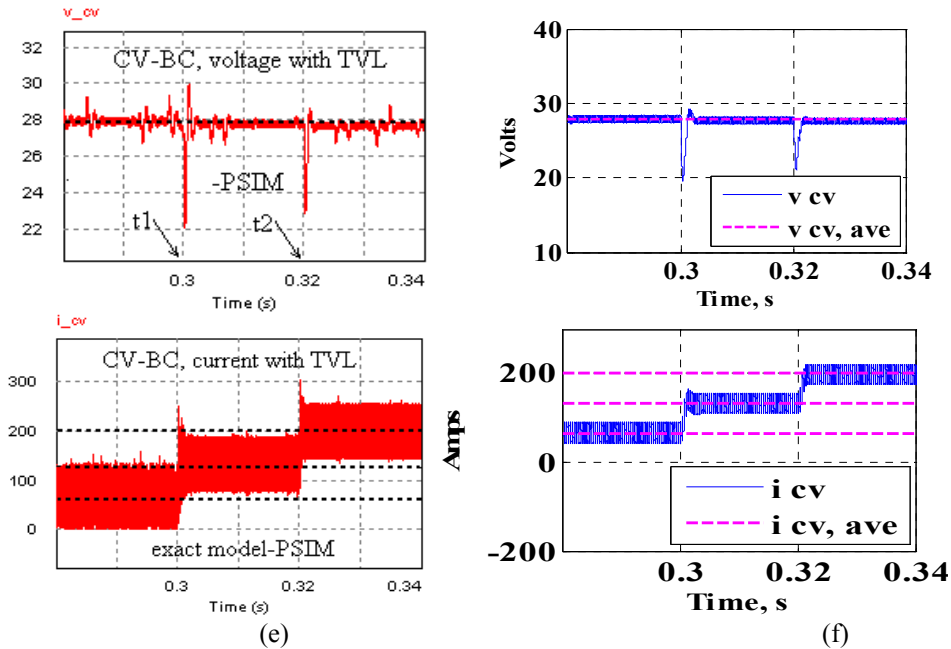
Fig. 2.13: CV-BC dynamic behavior vs step changes in power demand (e) PSIM9 model (f) proposed GSSA model.

40

2.5.3 *Constant Power Buck Converter (CP-BC) with Time-Varying Load (TVL)*

In the proposed VSCF aircraft electric power system model [34,42], the constant power load is connected to the main dc link through a dc/dc buck converter where the load power is kept constant at 10-kW by applying a Proportional-Integral (PI) controller integrated with a PWM switching function generator circuit. In the previous study, we employed the general state-space averaging representation of the buck converter with constant load voltage to model and characterize the circuit's behaviors at different loading conditions. The power rating of the constant-voltage load was subjected to step changes at different time frame, and the dynamic behaviors of the voltage and current waveform due to this variations were recorded. In the similar manner, in this case we have utilized the GSSA technique to obtain the key features of the constant power buck converter with time-variable loads, while interacting with the preceding 12-pulse switching power supplier.

In order to investigate the effectiveness and accuracy of the proposed averaging model, we have captured the system's response to variations in loading configurations by selecting different values of dc load resistances similar to what was done in the previous study for buck converter with constant voltage loads. Also, the representative waveform of the constant load power can be simply estimated using the zeroth-order and first-order Fourier approximation of the original time-domain signal developed in our previous effort.

Let us consider a practical example with the parameters provided in Table 2.2 proposed by [42,44,46] for Boeing 767. aircraft systems. In this table, the PWM operating frequency, representative circuit parameters and load power rating are detailed.

TABLE. 2.2
CP-BC circuit parameters

Parameter	Value	Comment
f_{cp}	20 kHz	PWM frequency
L_p	40 μH	filter inductance
r_p	0.002 Ω	series resistance
C_p	0.5 mF	filter capacitance
P_{o_cp}	10 kW	constant power rating

Fig. 2.14 shows an expanded view of the steady-state profiles of the out voltage and current waveforms at the output of the constant power buck converter. The graphs in the left-hand column are obtained from the topological model developed by PSIM9. These figures are presented to compare with the results shown in the right-hand column derived from the proposed GSSA model. As shown in Fig. 2.14 (b), the ripple of the constant power buck converter output voltage is within $1\,V$ which closely match to that of the real-time simulations obtained by PSIM9 and shown in the left-hand column.

(a)   (b)
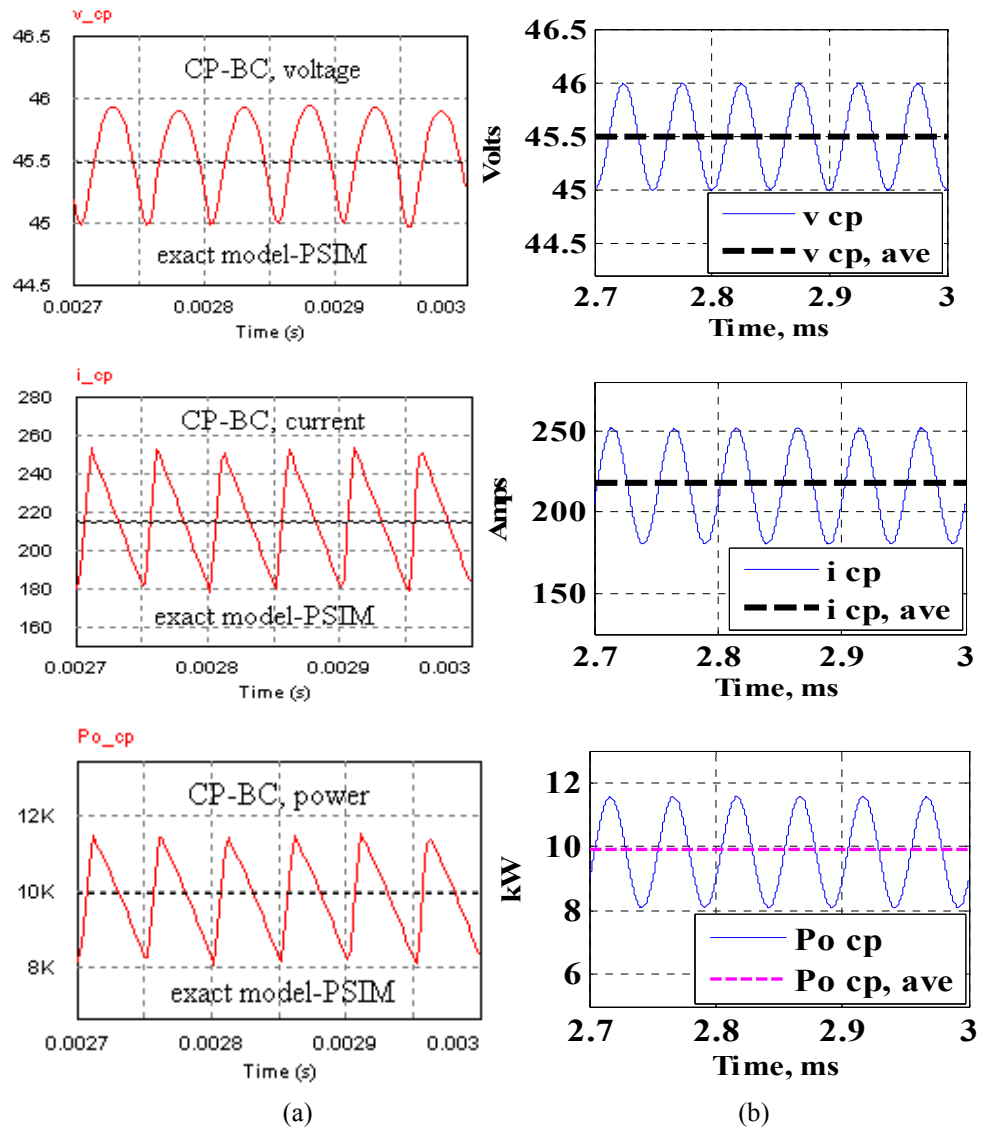
Fig. 2.14: CP-BC magnified view of obtained output voltage, current and constant power consumption (a) PSIM9 model (b) the GSSA model.

This voltage ripple meets the MILSTD- 704F in [31]. Further investigation into the inductor's current and output constant-power waveforms by comparing column (a) and (b), one sees an excellent agreement between the simulation results of the real-time analysis and Fourier-based characterization developed by the GSSA modeling.

Fig. 2.15 (a) and (b) show the dynamic performance of the buck converter with constant power loads, while loading profile changes at different time scales. In column (b), the developed GSSA models are utilized to capture system's response to step decreases in dc load resistances. The procedure of implementing averaging method for time-varying loads is exactly similar to that we performed in the previous section for constant-voltage buck converter with changes in power demand, except the fact that power consumption is kept constant in this case study.

Initially the system is under a steady-state condition while the obtained output voltage v_cp and inductor's current i_cp averaged values are calculated to be $46\ V$ and $219\ A$, respectively. At time $t_1 = 0.3\ s$, the circuit is subjected to a step decrease in the value of load resistance (50% of the initial value at $R_t = 0.21\ \Omega$). As illustrated in Fig. 2.15, the system responds to this variation by a step drop in voltage's average value to approximately $32.5\ V$ (30% voltage drop). Also the averaged value of the inductor's current reaches to $309.5\ A$ at steady-state. At time $t_2 = 0.32\ s$, the load configuration changes to a condition for maximum current demand ($R_t = 0.07\ \Omega$), causing another drop in the averaged value of output voltage ($v_{cp} = 26.5\ V\ DC$). Also, the averaged value of inductor's current is subjected to another step increase and reaches to $i\_cp = 378.5\ A\ DC$ at steady-state. Comparing the figures of column (b) with that of "exact" time-domain simulations in column (a) confirms the fact that the proposed GSSA model for constant power buck converter can accurately describe the system dynamics for large-signal transients. Hence, it can be reliably used for modeling and simulation of such system in which high order harmonics can be possibly neglected.
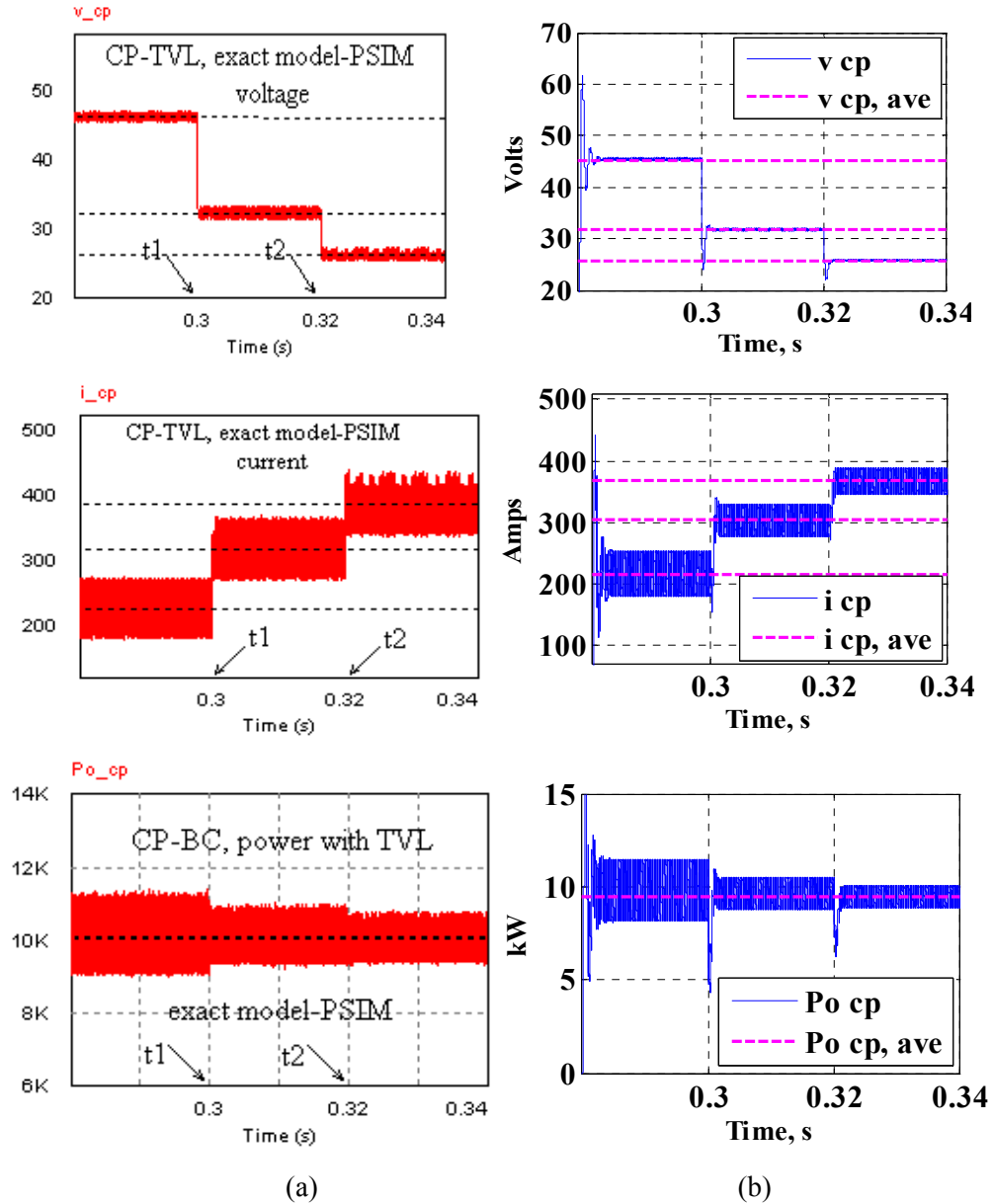
Fig. 2.15: CP-BC dynamics with TVL, voltage, current and constant power profiles (a) PSIM9 model (b) the GSSA model.

2.5.4 *Constant Current Buck Converter (CC-BC) with Time-Varying Load (TVL)*

This section presents transient and steady-state performance of the buck converter with constant-current loads, using the GSSA modeling representation. Quite similar to the previous discussions for constant voltage and constant power dc loads, connected to the main dc link (270 V) are the CC loads, obtained by using a fully controlled buck converter. The load current's average value is regulated and set to 100 *A* with PWM

control strategy. Subsequently, the load voltage at the filter's output is resulted at $200\,V$-dc, hence the load power dissipation is calculated to be $20\,kW$. As an example for a typical model in the aircraft electric system, the parameters are given by Table 2.3 are applied for implementation of the developed averaging equations in Matlab, as well as modeling and simulation of a study model in PSIM9. Fig. 2.16 (a) and (b) show the transient performance of the constant current buck converter where full load current is under consideration. Column (a) presents the voltage and current waveforms captured from real-time simulation. Column (b) illustrates the transient behaviors of the system corresponding to the load's voltage and inductor's current, using the proposed GSSA approach.
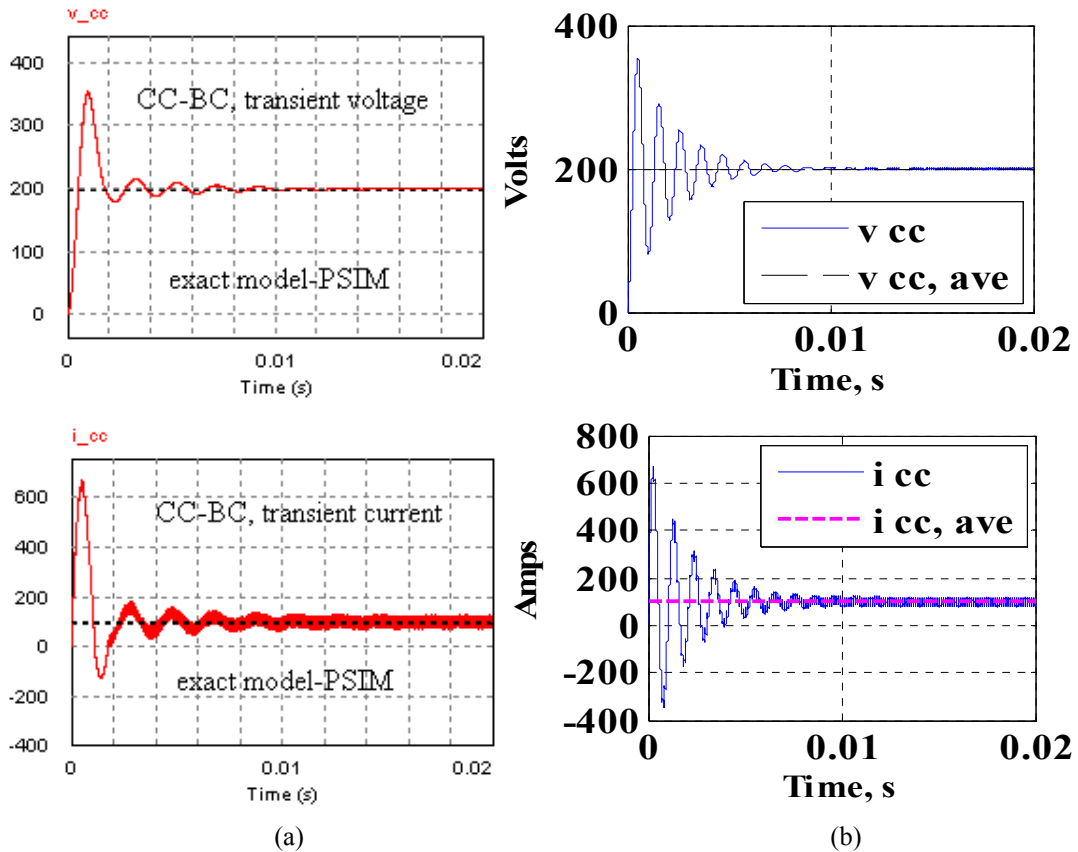
Fig. 2.16: CC-BC voltage and current transient profiles (a) exact model developed by PSIM9 (b) the GSSA model implemented in Matlab.

Comparing the voltage waveform(v_cc) in column (b) with that of in column (a), one notices that, although the average waveforms generated by the GSSA technique

slightly deviates from the corresponding graph resulted from "exact" real-time simulation, the key features between two columns relatively agree. Fig. 2.16 (a) indicates that the voltage and current overshoot percentages are 73 % and 550 %, respectively. On the other hand, the relevant overshoots corresponding to the GSSA constructed voltage and current from column (b) are calculated to be 71 % and 546 %, respectively. Fig. 2.17 (a) and (b) has verified the applicability of the GSSA approach in derivation of the constant current buck converter's key characteristics under steady-state condition of operation. The parameters used for this study are provided in table 2.3.

TABLE. 2.3
CC-BC system parameters

Parameter	Value	Comment
f_{cc}	10 kHz	PWM frequency
L_c	100 μH	filter inductance
r_c	0.002 Ω	series resistance
C_c	1.2 mF	filter capacitance
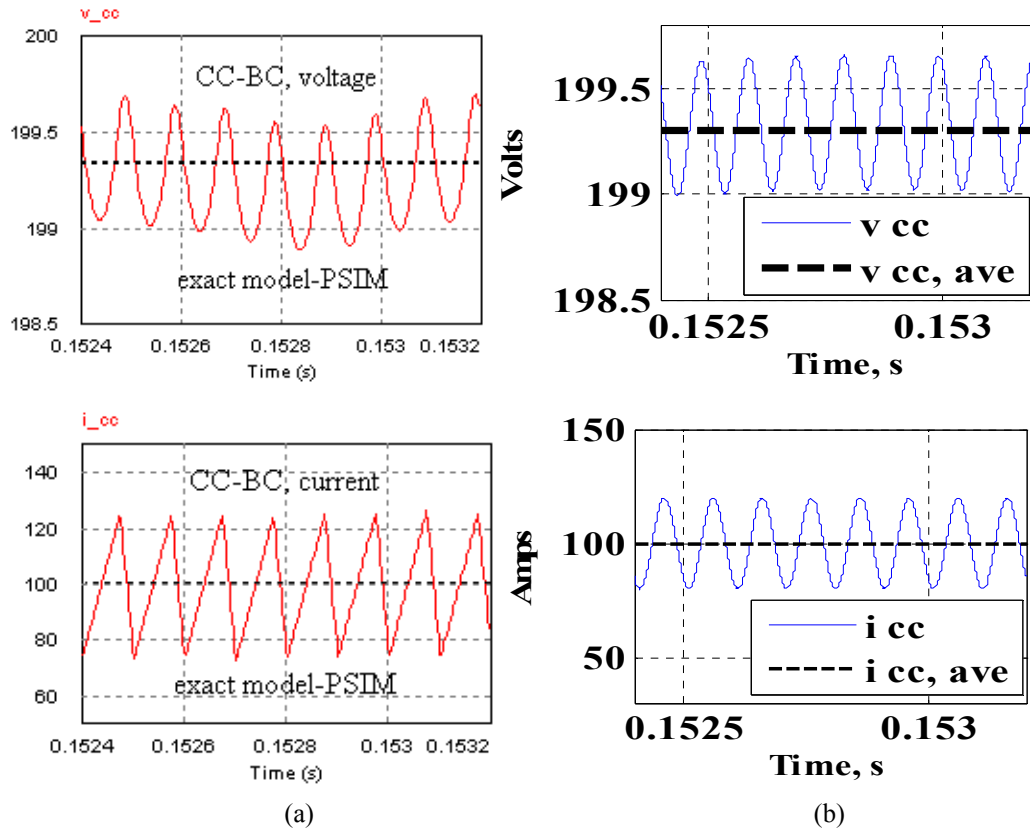
Fig. 2.17: CC-BC voltage and current steady-state performance (a) exact model developed by PSIM9 (b) the GSSA model implemented in Matlab.

46

As depicted in Fig. 2.17, the magnified view of the load voltage and inductor current are presented in (a) obtained from real-time simulation (b) from developed averaging model. As shown in the picture, the voltage ripple corresponding to the reduced-order system with the GSSA modeling is less than $1\,V$ and precisely agrees with the "exact" simulation. Also, measured ripple is within the military standard by [31,42]. The large-signal characteristics analysis for the inductor current is performed in a similar manner as done for the voltage waveforms. As depicted in (a) and (b), the average value for the current is predicted at $100\,A$, also the peak to peak value for the dominant oscillating component is measured to be $49\,A$. By comparing the obtained simulation results from both models, one concludes that the proposed general averaging method provides the same pattern of behavior as that of the PSIM9 time-domain simulation for the constant current buck converter. Therefore, it can be treated as a reliable means for modeling, simulation and analysis of these types of switching converters.

2.5.5 The GSSA Analysis of the Interacting Multi-Converter System

In this section, through the application of generalized state-space averaging, we have investigated the dynamic performance and characteristics of the multi-converter system and subsystems via the GSSA representative models developed in our previous the previous sections. It has been shown that the voltage and current profiles at the following and preceding switching converters main nodes can be described by considering the zeroth and first-order dominant components of the original signals, generated by the modulating frequencies of PWM control signals. Furthermore, the voltage and current waveforms corresponding to the main dc link were constructed following the procedure described previously. Through the application of averaging technique to modeling and simulation of the integrated multi-converter system, this section presents several case studies to demonstrate the effects of switching converters on voltage and current waveforms at dc-side of the 12-pulse rectifier (main dc bus). Moreover, the change in power demand and its effect on both dc and ac side of the rectifier are addressed and supported with several examples. The studies reported in this section were performed using the parameters of Tables 2.1, 2.2 and 2.3 as well as other information provided for modeling and simulation of switching converters in the previous sections. Also, the parameters are provided previously for the GSSA modeling are used

to represent the dynamics of the 12-pulse diode rectifier along with synchronous generator system's main bus connected with harmonics filter. Moreover, the following case studies are conducted to:

- *To demonstrate the effectiveness of the proposed GSSA approach in analysis and characterization of the interacting multi-converter system in the advanced aircraft.*

- *To verify the accuracy of the developed model in duplicating the key features of voltage and current profiles at major nodes, as well as further investigation into applicability of the introduced method to obtain required information to verify whether or not Military/IEEE standards[31] are met.*

A. Case. 1: Interaction between 12-pulse rectifier and CV-BC

This study presents the interaction of 12-pulse diode rectifier with constant voltage buck converter with full-load power rating. In this case, other types of dc loads are disabled and the effects of harmonic component on main dc voltage and current waveforms (V_{dc}, I_{dc}) are considered due to interaction with the CV-BC. Fig. 2.18 (a) and (b) show an expanded view of the simulation results from two study models implemented by PSIM9 and Matlab, as the representation of "exact" time-domain and averaged modeling, respectively. As illustrated in column (b), the output voltage waveform corresponding to low-pass filter connected to the main dc bus ($270\ VDC$) is distorted by first-order harmonic term caused by PWM switching action of the operating CV-BC. It is shown that the averaged dc value for the voltage is predicted to be around $270.4\ V$. Fig. 2.18 (a), (b) also indicates that ripple's variation corresponding to the voltage is less than $1\ V$ which is within the standards by [31]. The peak-to-peak value of ac component corresponding to the dc-side current of 12-pulse rectifier (I_{dc}) is calculated to be $10\ A$. Furthermore, it is demonstrated that I_{dc} remains unaffected while rectifying system is in interaction with CV-BC. By comparing the figures of column (b) with those of column (a) one comes to this fact that there is a good agreement between the results obtained from the developed GSSA modeling and the "exact" real-time simulations captured in PSIM9 environment.

Fig. 2.18: Main dc-link voltage and current profiles, interacting with CV-BC (a) developed by PSIM9 (b) the GSSA model.

B.   *Case. 2: Interaction between 12-pulse rectifier and CV-BC, CP-BC*

In this section, we have analyzed the performance and characteristics of the interconnecting power electronic system including the previously mentioned 12-pulse rectifying system interacting with CV-BC and CP-BC, simultaneously. The operating conditions and system parameters used for two types of switching converters connected to the main dc bus are exactly the same as those studies were performed for different kinds of buck converters in the previous sections. In a similar manner as *Case.1*, in this study the GSSA representation of the energy storage elements corresponding to the 12-pulse diode rectifier's output filter are considered as state variables. Fig. 2.19 demonstrates the voltage and current waveforms at the rectifier's dc-side node, (a) derived from the study model in PSIM9 (b) implemented in Matlab, using the reduced order averaging approximation. Fig. 2.19 indicates that the ac component of the captured voltage waveforms from both models significantly deviate from a pure sinusoidal oscillation. The reason is that the PWM modulating signals of CV-BC and CP-BC have different operating frequencies. Therefore, the merged input currents

through the above mentioned buck converters forms a total distortion appearing on the dc voltage waveform, and this component deviates from a pure sinusoid. Nevertheless, as depicted in column (a) and (b) of Fig. 2.19, the current profile at the main dc bus remains unaffected by distorting component caused by the PWM switching behavior of the CV and CP buck converters, except a step change in the average dc value of the current (compared to Case. 1) due to the contribution of the CP-BC current in this case study. Also, in this study, the simulation results obtained from the proposed averaging technique precisely catch the key features of the system under investigation, resulting to a good correlation between graphs from two study models.
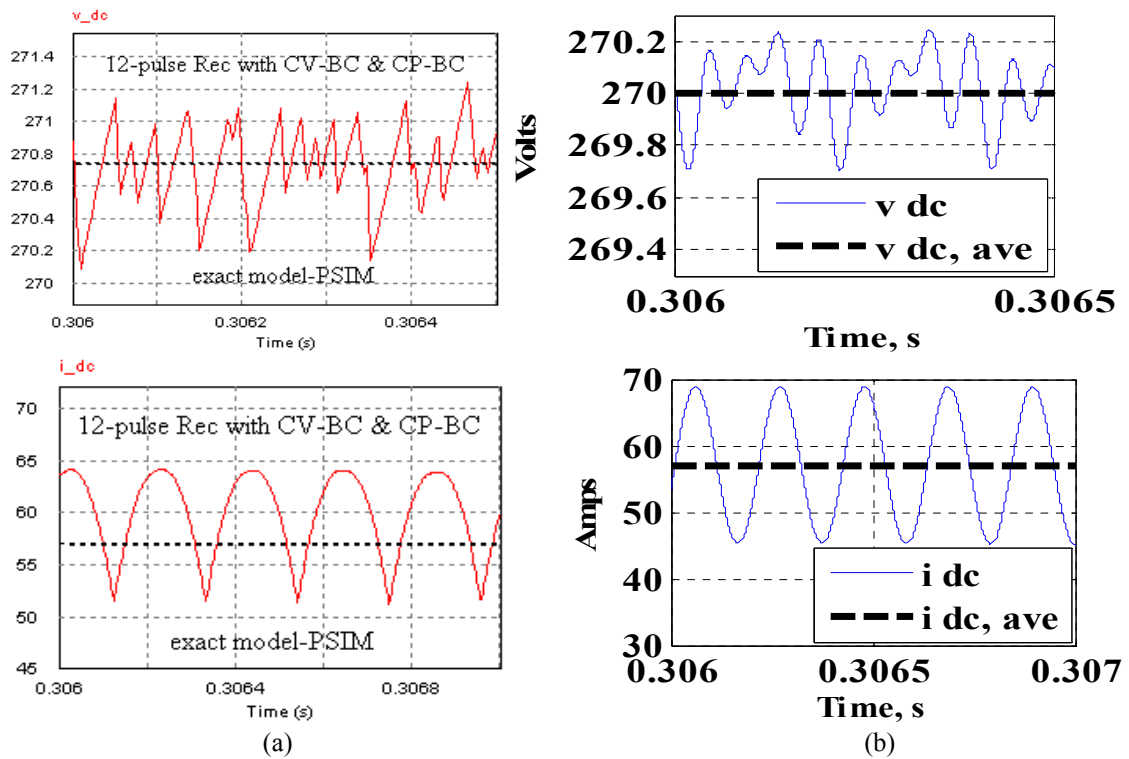
Fig. 2.19: Main dc-link voltage and current profiles, interacting with CV-BC, CP-BC (a) developed by PSIM9 (b) the GSSA model.

C.   *Case. 3: Interaction between 12-pulse rectifier and CV-BC, CC-BC*

This study is performed to characterize the performance of main dc link, where interconnected with the CV-BC and CC-BC at the same time. Exactly same as *Case.2*, the voltage and current profiles are considered for system analysis using two study models as before. Fig. 2.20 (a), (b) closely compares the obtained results from time-domain study model developed by PSIM9 with those simulations implemented in Matlab

using the introduced GSSA model. It is demonstrated in both columns that the voltage waveform (V_{dc}) is subjected to a distortion generated by combination of two input currents of the buck converters. The non-sinusoidal ac component seen in the voltage profile is constructed from the first-order harmonic components due to modulation effects of PWM control signals corresponding to the CV and CC buck converter. As depicted in column (b), the average values for the voltage and current are predicted to be approximately $268.2\,V$ and $94\,A$, respectively. Though the voltage is distorted by switching input currents, the inductor's current profile (I_{dc}) remains unaffected by such high frequency distortion. By comparing the average values and harmonic components of the voltage and current waveforms shown in Fig. 2.20, one sees that there is a relatively good match between the graphs obtained from "exact" modeling and the GSSA approach.
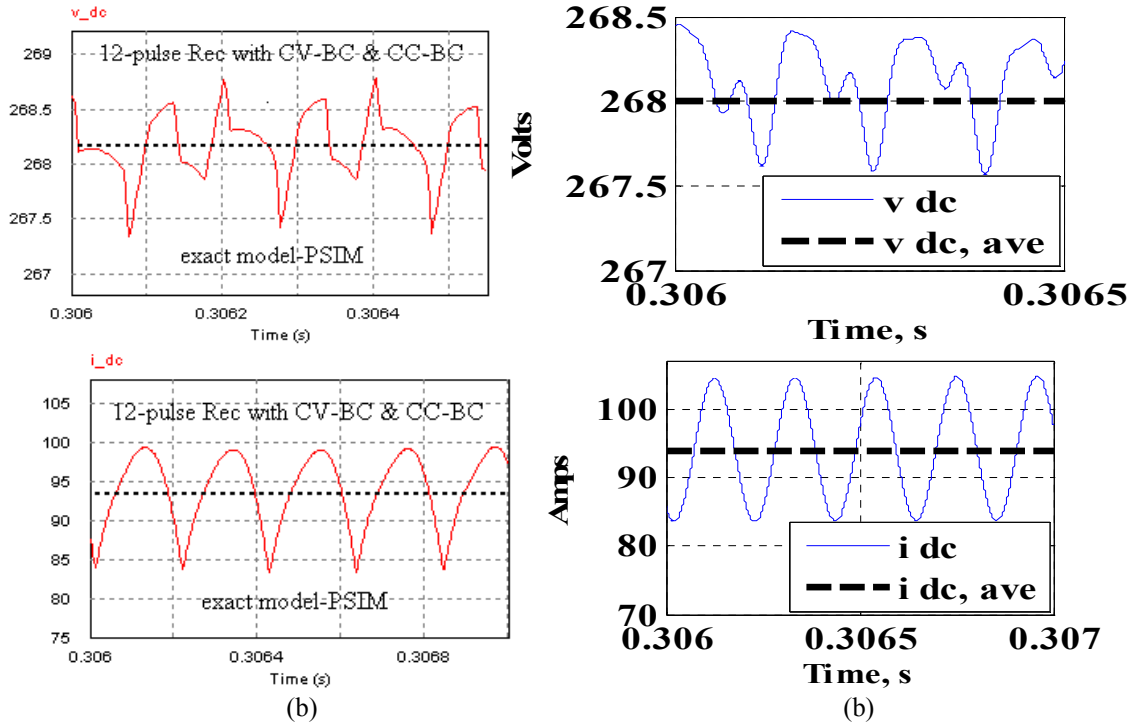
Fig. 2.20: Main dc-link voltage and current profiles, interacting with CV-BC, CC-BC (a) developed by PSIM9 (b) the GSSA model.

D.   *Case. 4: Interaction between 12-pulse rectifier and CP-BC, CC-BC*

Fig. 2.21 (a) and (b) show the interaction among 12-pulse rectifier, constant power and constant current buck converters as distributing devices. The objective of this

section is to demonstrate how the voltage and current waveforms corresponding to the primary dc link is affected by harmonic components exist in the input currents flowing through the mentioned distributing converters (CP-BC, CC-BC). In column (b), we have utilized generalized averaging equation to approximate the voltage and current profiles based on the dc averaged value and first-order harmonic components corresponding to each modulating frequency of PWM buck converters. Also, column (a) presents the same profiles obtained by time-domain simulation. As expected, the voltage waveform is distorted by combination of two types of harmonic components merged together to form a non-sinusoidal waveform consisting of 10 kHz and 20k Hz frequencies. Further investigation into the magnified view of results extracted from averaging model shown in (b), the dc values for voltage and current are predicted to be 268.7 V and 110 A, respectively. Fig. 2.21 also illustrates that the current waveform does not contain the harmonic contents as those appearing on the voltage waveform. Comparing columns (a) and (b) conforms that the GSSA-based generated simulations relatively follow those graphs obtained from the real-time simulations in Matlab environment.
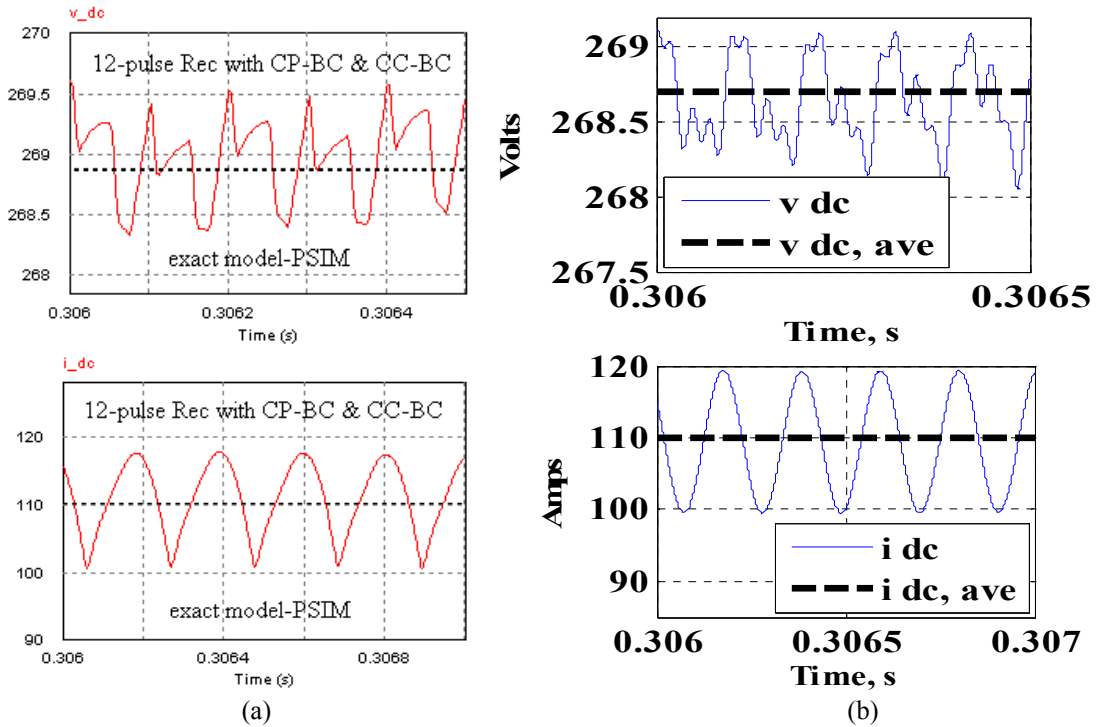
Fig. 2.21: Main dc-link voltage and current profiles, interacting with CP-BC, CC-BC (a) developed by PSIM9 (b) the GSSA model.

52

In this section, we have performed the same procedure as done for the previous studies, except that all three types of distributing converters are interfaced to the grid simultaneously, at the point of 12-pulse rectifier's filter output. The magnified view of simulation results corresponding to the voltage and current waveforms at main dc bus are depicted in Fig. 2.22 (a) and (b). As shown in column (b), the dc averaged values associated with the voltage and current profiles are measured at 268.2 V and 130 A, respectively. Moreover, as previously discussed, the voltage waveform is affected by three different kinds of harmonic components, generated by the PWM modulating frequency corresponding to the distributing buck converters under study. Also, the variation of the mentioned ripple is less than 1 V, which satisfies the standards given by [31].

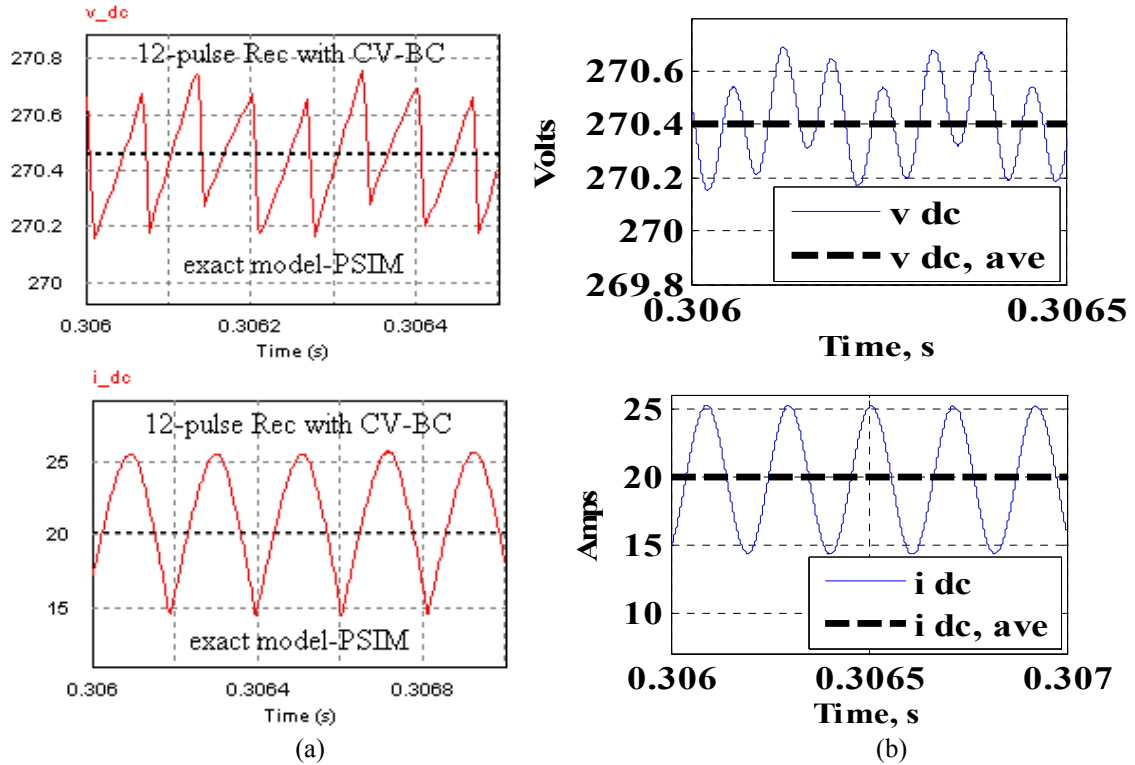(a)   (b)

(a)   (b)
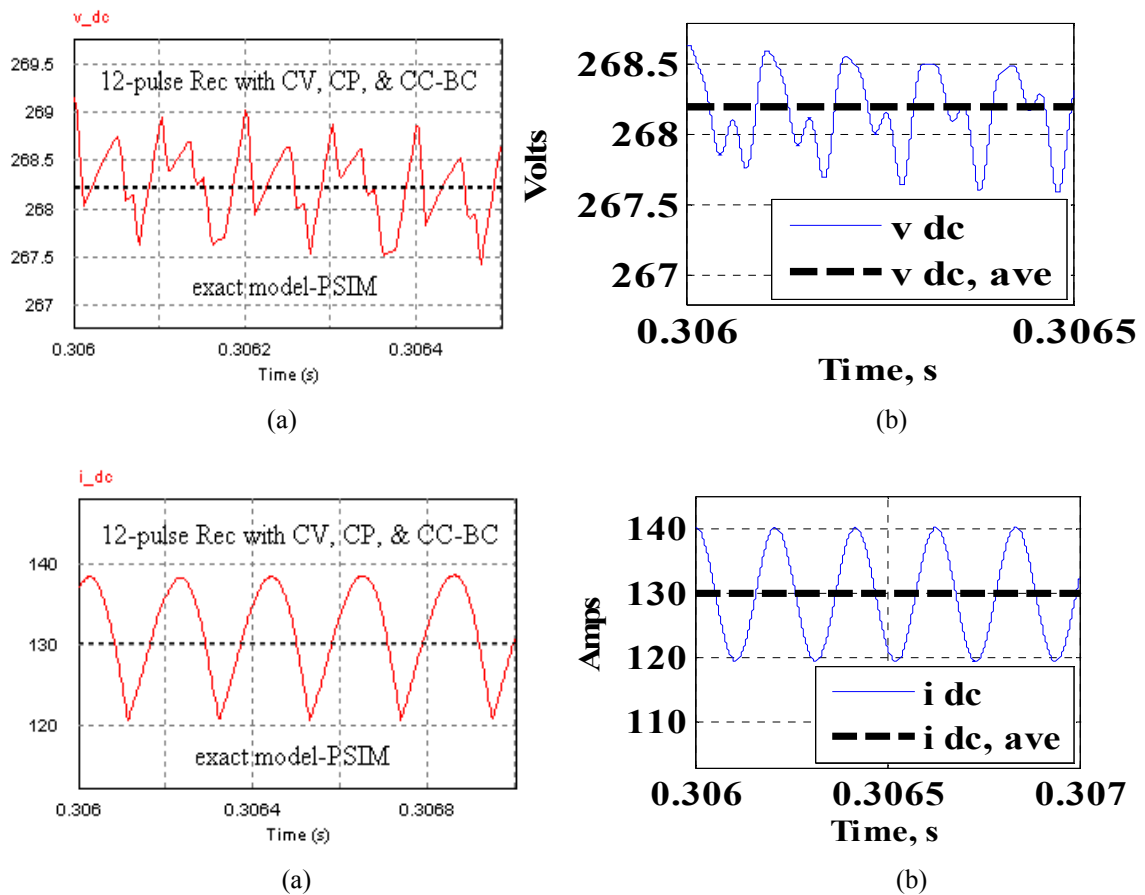
Fig. 2.22: Main dc-link voltage and current profiles, interacting with CV-BC, CP-BC and CC-BC (a) developed by PSIM9 (b) the GSSA developed model.

Though it is seen a slight deviation in oscillating component of the current's waveform obtained by the proposed GSSA modeling and that of the "exact" real-time simulation, the reduced order approximated method is still valid and can be approached as an effective technique for modeling and analysis of such interconnected system with mutual interactions. Furthermore, Fig. 2.22 clearly demonstrates that the developed generalized averaging model precisely catches rapid changes in the voltage profile due to interaction with non-linear switching devices.

F.   Case. 6: Interaction between 12-pulse rectifier and the PWM 12-pulse VSI

This section presents the performance characteristics of the main dc link while interacting with 12-pulse VSI. Fig. 2.23 (a), (b) demonstrates the real-time simulations as representation of exact modeling captured in PSIM9 environment. As shown in the (a), the voltage waveform at the output of HVDC is remarkably distorted by harmonics related to the switching behavior of 12-pulse inverter. Though, the higher-order distortions are absorbed by the filter capacitance, the lower order components still appearing on the voltage waveform. Fig. 2.23 (b) illustrates the current waveform corresponding to the dc-link filter inductor. It is seen from the figure that system is operating in a non-continuous conduction mode.

Also, depicted in Fig. 2.23 (b) and (d) corresponds to the same voltage and current profile which has been obtained from the developed GSSA model. By comparing two sets of figures, one may notice that though there is a good correlating between the averaged dc values of two types of figures, however the reduced-order model implemented in Matlab cannot effectively represent the small oscillatory components appearing on the dc voltage waveform. On the other hand, the current waveform obtained by the GSSA model considerably deviates from that of the "exact" model captured by PSIM9. The reason is because the GSSA models previous developed were based on assuming a continuous conduction mode of operation, while is not valid for this case of operation.
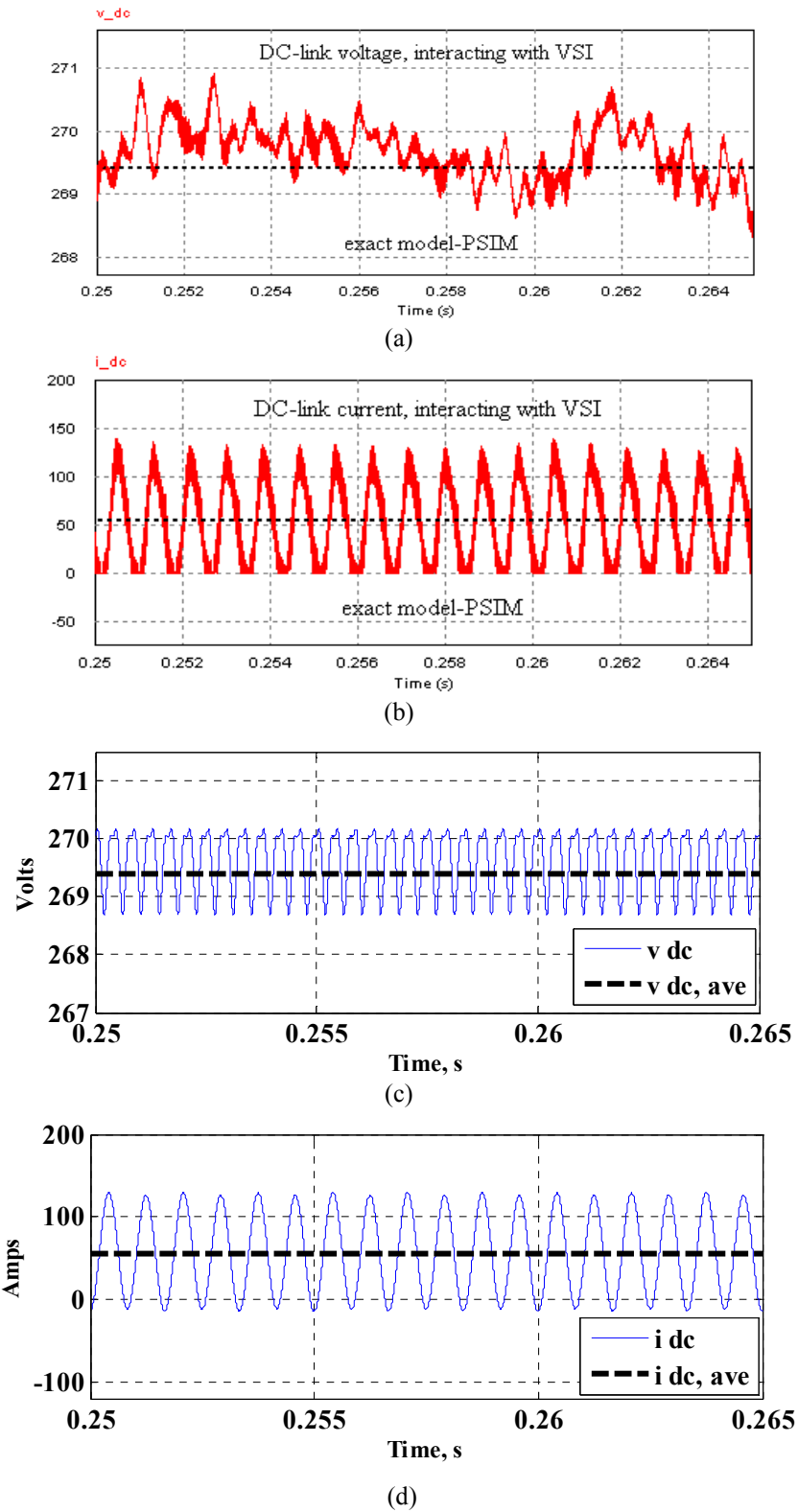
Fig. 2.23: The interaction of HVDC-link with 12-pulse VSI (a) PSIM9 model of dc voltage at HVDC (b) PSIM9 of inductor's dc current (c) dc voltage implemented by Matlab applying the GSSA model (d) corresponding current developed by the GSSA approach.

55

G. *Case. 7: Voltage and current dynamical performance at the VSCF power bus*

This section verifies the accuracy of the GSSA modeling for obtaining the dynamical performance of the aircraft electric system at the SG main ac bus when interacting with dynamic loads at different time scales. As demonstrated in Fig. 2.24 (a) and (b) the system is in normal operation where the CVBC and CPBC are connected to the grid for the total load power of 15.6 kW. At time t_1=0.3s the system is subjected to a step increase in power demand the way that all three types of dc-dc converters are applied to the network, for the total power rating at 35.6 kW. The system continues the operation until the time t_2=0.32s where system undergoes another step change in load power. At that point, the CPBC load is removed from the grid and the network continues operation for the total load power of 25.6 kW which is the power contributed by CVBC and CCBC.

(a)

(b)
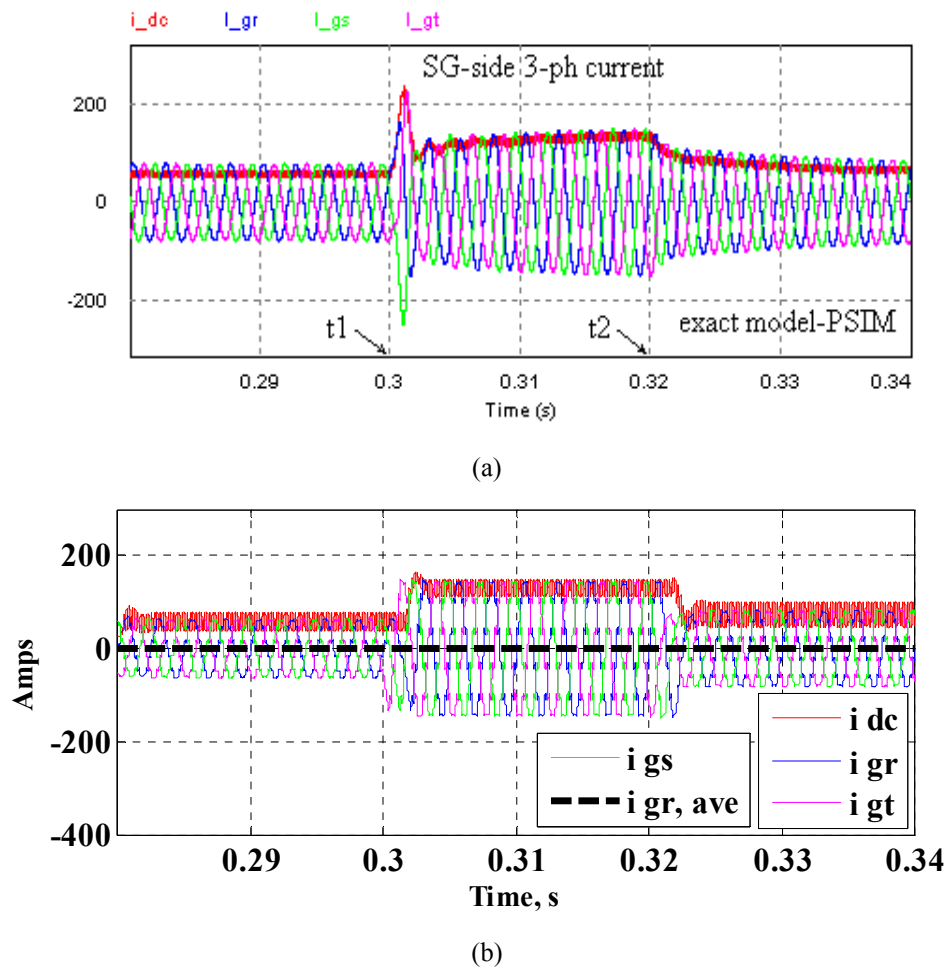
Fig. 2.24: The dynamic performance of the system at SG main ac bus, where supplying power for the ac and dc dynamic loads (a) exact model (b) the GSSA simulation.

Fig. 2.24 (a) represents the time-domain computer simulation, whereas Fig. 2.24 (b) corresponds to the model developed by the GSSA technique. By comparing the figures of two models, one notices that there is an excellent correlation between two results which confirms the applicability of averaging technique to modeling and characterization of the aircraft where the system's dynamical performance is under consideration.

2.6 Summary

In this Chapter, a complete set of mathematical models are proposed to describe the transient and steady-state performance of an Advanced Aircraft Electric Power Distribution System (AAEPDS). Generalized state-space averaging technique has been employed to derive the important mathematical characteristics corresponding to the ac/dc and dc/ac multi-level converters integrated with harmonic filters and ac/dc loads of the system under investigation. The proposed models are then used to simulate the key dynamic behaviors of the system and sub-systems for several case studies. The developed averaging models circumvent the necessity of applying real-time analysis for the aircraft electric power system at major nodes and overcome the difficulties of applying time domain analysis with extra costs of requiring more computer resources. Also, reduction in simulation time is another advantage one can achieve using the GSSA technique.

Chapter Three

Hybrid Auxiliary Power Unit (APU) in Modern Aircraft

3. 1 Chapter Overview

Currently, the electric energy provided to the aircraft system during flight is mostly supplied by the generators that are driven by the core of the main propulsion engines. Electric generators, either driven by an aircraft's main propulsion engines or by a gas turbine auxiliary power unit supply the electric power needs of commercial aircraft. The maximum efficiency of delivered electric power by the main engines and their generators is 40% in flight, whereas on the ground with the engines off, and using the turbine-power APU, the efficiency barely approaches 20%, of course with noise pollution and gaseous emissions [47,48]. Moreover, due to growing demands for electric power capacity on the advanced aircraft, these generators would have to increase in size, which exceeds the space allowed in the aircraft (limitation of space and weight). Therefore, the current design would no longer meet the requirements of emerging more electric aircraft (MEA) with large electric power facilities. One of the best alternative energy resources could be considered as a reliable and more efficient replacement of the conventional heavy structures would be a hybrid battery/fuel cell APU system as a clean source of energy. In recent years, there have been extensive research studies reported on the applicability of fuel cell equipped APU for the transportations systems, as well as aerospace applications [48,50,57,61]

Hybrid energy resources with high power density and efficiency are becoming increasingly attractive for both commercial and military purposes, such as vehicular, aerospace, and marine applications. The hybrid battery/fuel cell-based APU is proposed by many authors [44,48-51] recently and is becoming a reliable source of energy for advanced technology applications. Being environmentally friendly and providing fast response (which is considered as a vital factor for most secure systems) are noteworthy characteristics of the system. The APU system modeled in this Chapter consists of several major components, including: 1) the Proton Exchange Membrane (PEM) fuel

cells 2) the lead-acid battery 3) dc/dc boost converter connected to the PEM-FC output 4) dc/dc buck-boost converter connected to the lead-acid battery package 5) bidirectional switch component used for provide the charging/discharging path between the PEM-FC and battery, as well as between the APU unit and loads 6) control units used for auto regulation of both battery and fuel cell output profile, also controlling the bidirectional switch under different conditions of the system's operation. Fig. 3.1 represents a typical schematic model of the APU-equipped AAEPS proposed for the Boeing 767. aircraft.
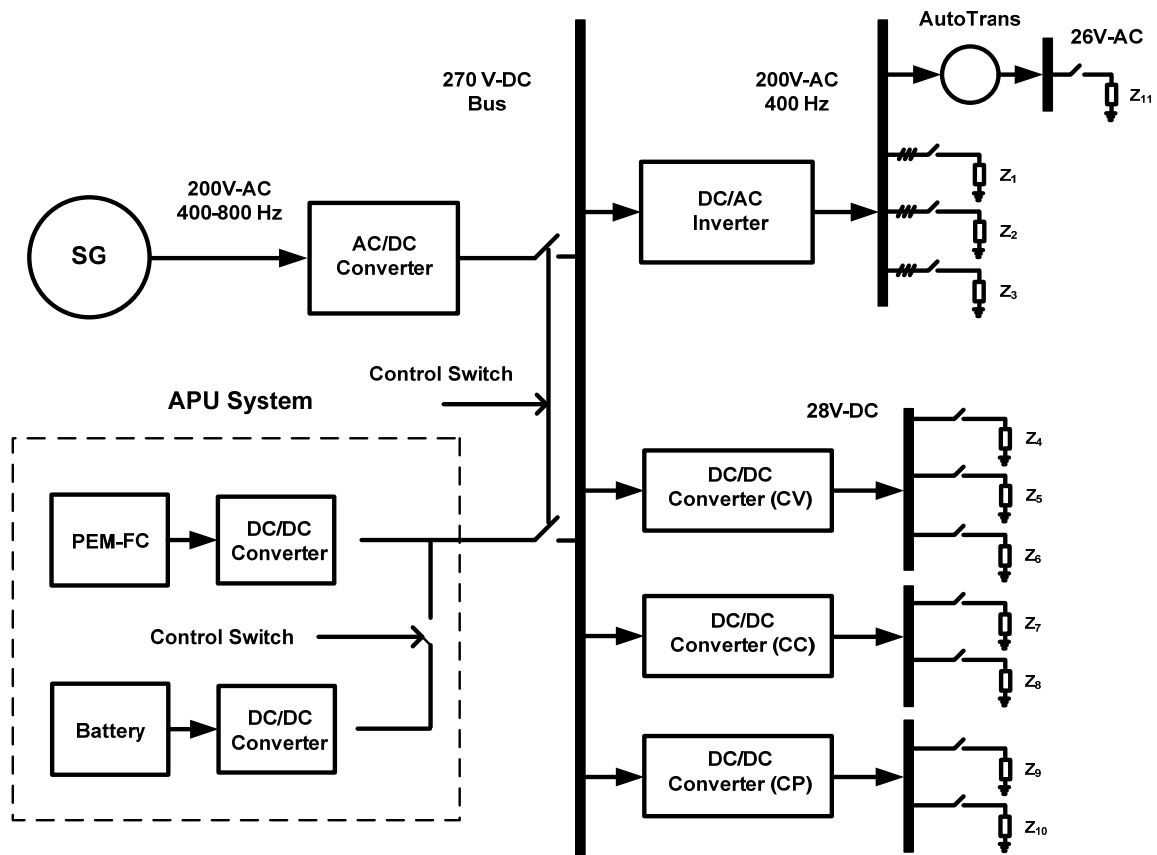
Fig. 3.1: Schematic model of a single channel APU-based AAEPS.

In the literature [44] the similar model is employed, and the performance of the APU system is characterized where the hybrid system is paralleled to the main ac bus via a 12-pulse voltage source inverter (VSI) at the voltage and frequency of 200Vrms and 400Hz. The proposed model demands for an extra 12-pulse inverter which raises the cost

and weight of the design. Also, the voltage and frequency synchronization will be another technical challenge that the proposed method will encounter. In order to avoid the difficulties of implementation exist in the model of [44], we have propose an improved method. In this case, the output of the APU system will be directly connected to the main dc bus of the grid using a power bidirectional switch with an intelligent control system. Therefore, the proposed method will circumvent the necessity of applying extra switching 12-pulse inverter, as well as other hardware for synchronization purposes. This approach would result in better performance.

3. 2 Fuel Cell Equivalent Circuit Modeling

A fuel cell is an electrochemical device that converts the chemical energy stored in fuel into electricity. The Proton Exchange Membrane Fuel Cell (PEMFC) is one of the most promising sources of renewable energy, also considered as a source of "green" power, because it is environmentally friendly, which means having low emissions of polluting gases; such as oxides of nitrogen and sulfur. Fuel cells also operate at very low levels of acoustic noise. In addition, they can provide energy with higher efficiency than conventional power plants. The early PEM fuel cells used to operate with pure oxygen and hydrogen as the reactant gases and were designed for small-scale and for low-power applications. They were neither economically affordable nor commercially viable, also, their efficiency were lower compared to the modern PEM-FCs.

In order to characterize the dynamic performance of the aircraft electric system with a hybrid APU, a representative circuit model of the PEM-FC stack is required. Because of the chemical nature of the fuel cell stack along with a notable complexity, the representative circuit model would facilitate the analysis of system's dynamics under various loading configurations. Hence, different circuit models are found in literatures with concentration on dynamic behavior of the PEM-FC, with consideration of chemical and thermodynamic actions and reactions of the system.

In [52,53] the dynamic models of a practical fuel cell system are developed based on analytical theory and empirical data. Authors of [54,55] have developed electrical circuit models of a typical PEM-FC where both chemical and thermodynamic characteristics inside the fuel cell stacks are included. The author of [56] has proposed an equivalent circuit model of a PEM-FC based on its time-varying impedance

characteristics. The developed model then has been implemented to capture the impedance profile of the fuel cell stack under different operation conditions, also the obtained results are compared with the experimental data. The author of [58] proposes an electrochemical representative model of the PEM-FC, and the developed model is utilized for characterization and analysis of the fuel cell associated with its output voltage, current and power efficiency, with consideration of operational parameters of the cells.

A PEM fuel cell is capable of operating at air temperature for a quick start up performance, and its efficiency may reach up to 60% [48]. Also, the output voltage and power rating of the PEM fuel cell can be designed to meet specific demands for applications, such as; distributed generation power systems and electrical vehicles, as well as in AAEPS. For a low power fuel cell (w≤1-kW), the output voltage is in the range of 25-50V, and the output voltage for above 30-kW power dissipation is estimated in the range of 200-400V [48,49]. In this Chapter, as proposed by the authors of [44] the equivalent circuit model of the PEM-FC is applied to capture the key dynamics of the APU system under investigation. As illustrated in Fig. 3.2, the dynamic circuit model of the fuel cell includes the equivalent capacitances due to "double-layer charging effect", as well as the equivalent resistances of activation, concentration and ohmic voltage drop across the electrodes of FC stacks. Therefore, the second-order circuit model has been employed to derive the dynamic and steady-state behavior of the PEM fuel cell stack under study.

3. 3 Lead-Acid Battery Modeling

The lead acid battery is well recognized for having a relatively large specific power, so they have the ability of supplying high surge currents, which is suitable for systems with large initial power demand. In addition, the cost of the lead acid batteries is low and is economically affordable. Therefore, the mentioned features make them more attractive for use in AAEPS, as they can provide the high current required for step change of power demand in the aircraft electric network. Also, they have fast response time, hence compensating the slow transient response of PWM-FC respect to changes in load power. Therefore, the association of the lead-acid and fuel cell in the hybrid FC/battery-based APU could lead to a promising performance of the system which is economically

61

attractive. In other words, the lead acid battery is widely used and almost considered a least expensive energy storage battery for many applications, while providing reasonable performance and life characteristics [59,60].

Fig. 3.2 depicts the equivalent circuit model of a lead-acid battery in the hybrid APU system used for AAEPS. A commonly used model of lead-acid battery is composed of several basic elements including internal charge and discharge resistances, self-discharging resistance. The forward bias elements (diodes) indicate that the charging and discharging processes of the battery are separated. The capacitance C_b is equivalent to the battery capacitance, and Rp introduces the self-discharging resistance. In addition, the over-potential characteristic of the battery is modeled with a parallel RC branch.
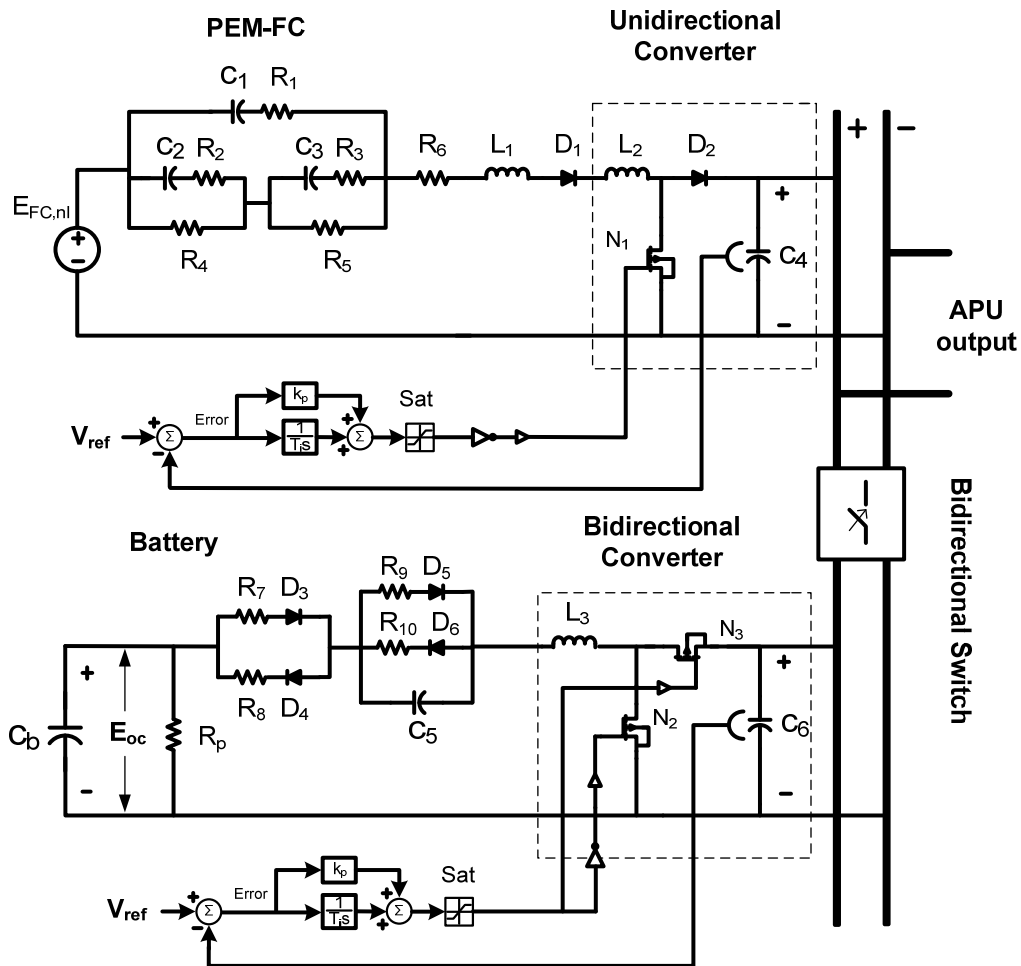
Fig. 3.2: Circuit representation of battery/fuel cell equipped APU in the AAEPS.

Moreover, the corresponding voltage drop for charging and discharging mode is represented with two resistances R_9, R_{10}, whereas C_5 introduces the double layer capacitance characteristic of the battery during charge and discharge mode of operation. Of course, the internal resistances of the lead-acid battery are multi-parameter dependent quantities that vary from one operating status to another. Moreover, the variation of internal impedance respect to change in temperature of operation and electrolyte concentration are not considered in this circuit model.

3. 4 DC/DC Converters

Two types of dc/dc converters are applied to the hybrid battery/fuel cell system in order to regulate the output profile of the APU, as illustrated in Fig. 3.2. In this case study, during transient condition the lead-acid battery supplies electric power for the essential loads of the system until the PEM-FC warms up. Then, the fuel cell provides all required power for the essential loads when the synchronous generator is shut down. Hence, the dc/dc converter of the battery must be designed as a bidirectional device. This means that during transient operation of the system where the battery provides emergency power to the loads, the converter must operate in the "boost-mode", enhancing the output voltage to its standard value at 270V using a feedback control system. Also, during normal operating conditions the PEM-FC should charge the battery, therefore, the converter must turn to the "buck-mode" of operation. On the other hand, a boost-converter is required to be placed between the fuel cell and the main dc-link of the network. This would provide an auto-regulation of voltage at the output of the fuel cell and boost the output voltage to its nominal value at 270V to match the main dc bus. In addition, placing the dc/dc converters between the FC and the battery would substantially improve the performance of the auxiliary power unit and increase the ability of delivering peak output power at start up conditions [44].

3. 5. APU System Performance

The studied aircraft electric network with the PEM fuel cell/battery equipped APU operates in parallel with the main dc-link of the single channel generator. As illustrated in Fig. 3.1, this system consists of two channels, supplying electric power for the main dc load bus; the Synchronous Generator (SG) and the APU system. Also, the

output voltage of the main dc bus is regulated at 270V by controlling the excitation/field current through SG. The studies reported in this section are performed using the parameters of Table.4.1, 4.2. In this effort, the dynamics and steady-state performance of the APU system is analyzed in several case studies. These studies include transient behavior of the hybrid battery/fuel cell system when the APU system is subjected to a sudden change in load power. Also, the duration overlap between the auxiliary unit and AAEPS generating system is considered for another case where both systems contribute electric power to the grid.

3.5.1 Open Circuit (OC) Characteristics of the PEM-FC

Depicted in Fig. 3.3 corresponds to the output profile of the PEM-FC where is disconnected from the electric network. As shown in the picture, the FC output voltage reaches its nominal value at 250V-dc in approximately 220ms. The slow charge-up performance of the PEM-FC terminal voltage is due to time-constant of the double layer capacitance along with other internal resistive components previously introduced in the simulation model.
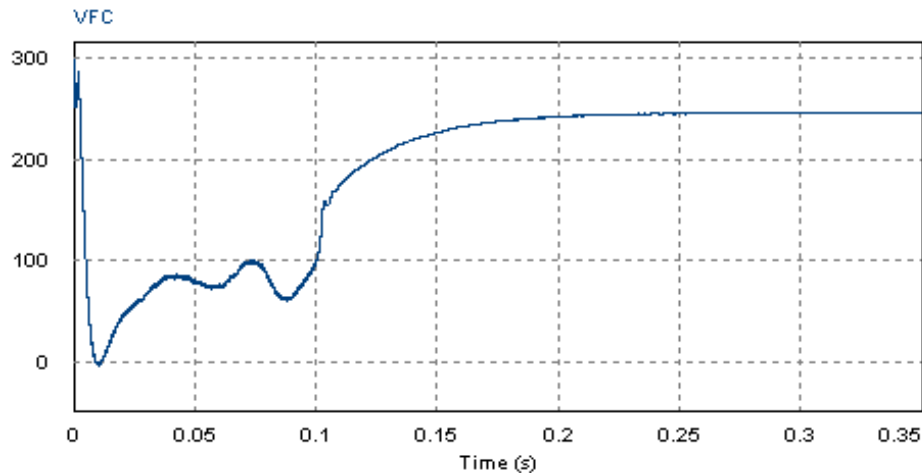
Fig. 3.3: Open-circuit output voltage [Volts] of the PEM-FC during "warm-up" condition.

3.5.2 PEM-FC Dynamic Behavior

In Fig. 3.4 the transient behavior of the fuel cell stack has been obtained while connected to the main dc-link of the AAEPS network via dc/dc converter. In this study, the 12-pulse VSI is interconnected to the main dc bus while supplying power to a three

phase lumped circuit elements of series RL load, with active power dissipation of 36.6kW. By looking at Fig. 3.4, one may notice that the output voltage of the fuel cell drops as its current rises. Also, further investigation into the voltage profile, one concludes that the voltage decrease is due to the compensation of sudden step increase in the load power.
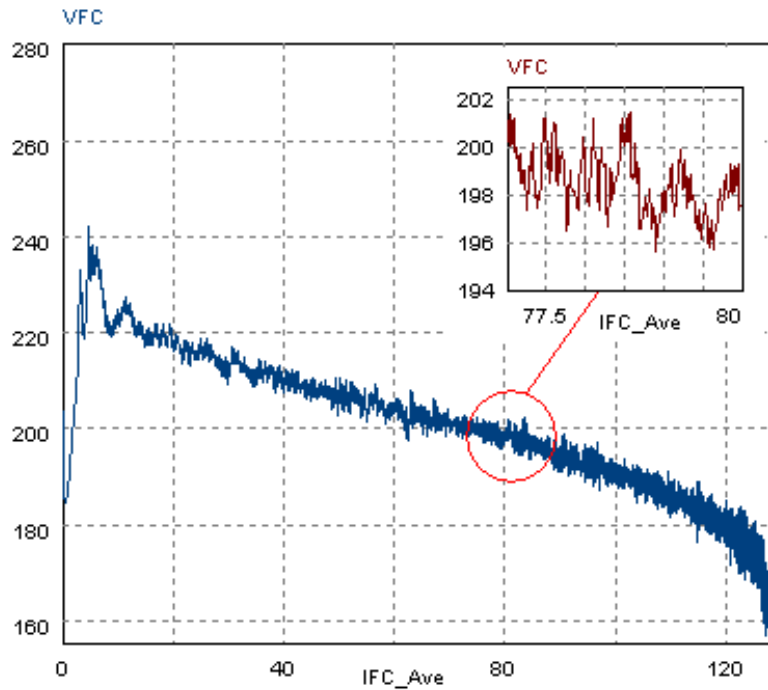
Fig. 3.4: PEM-FC output voltage [Volts] transient performance vs increase in the load current [Amps]

Fig. 3.5 represents a magnified view of the FC's output voltage in steady-state mode of operation when supplying electric power to the switching 12-pulse VSI. Fig. 3.5 clearly shows that the voltage waveform is distorted by some level of harmonics due to interaction of the PEM-FC with the switching inverter. In this figure, VFC represents the PEM-FC output voltage and IFC corresponds to the current. Fig. 3.6 represents the dynamic response of the PEM-FC output voltage to step increase in power demand. As illustrated in the graph, at time t=0.35s the power rating of the RL load connected to the switching VSI has stepped up to 125% of its original power (from 36.6kW to 45.75kW), leading to a voltage drop in the fuel cell output profile. Also, Fig. 3.7 shows the dynamic performance of the FC when interacting with various types of non-linear loads at
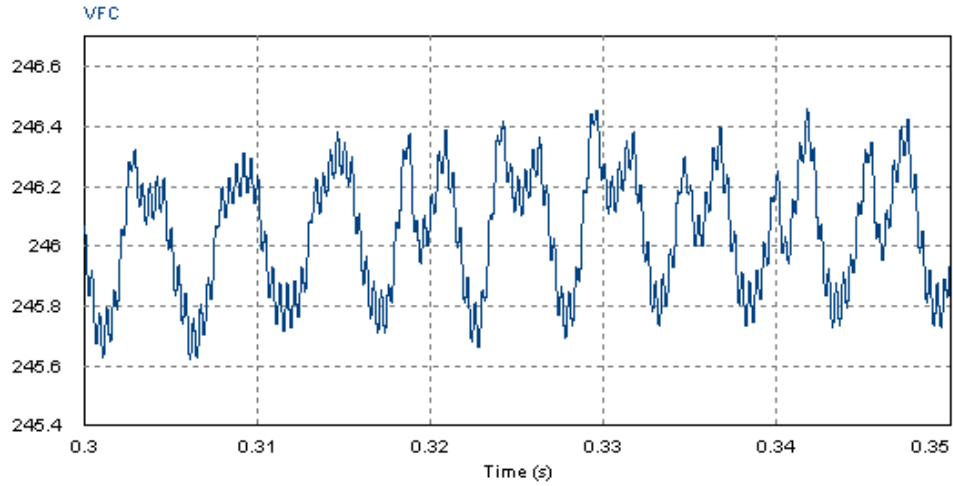
Fig. 3.5: Expanded view of the PEM-FC output voltage [Volts] under normal operation
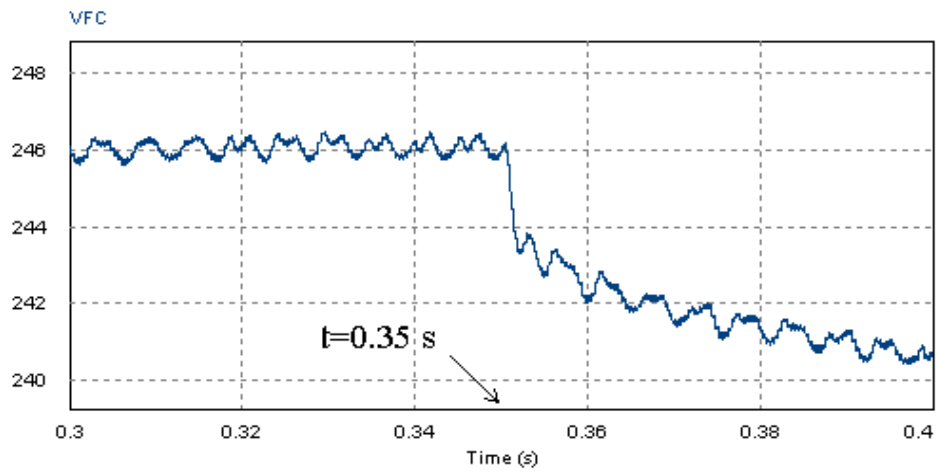
Fig. 3.6: Transient response of the FC voltage [Volts] to step increase in load power
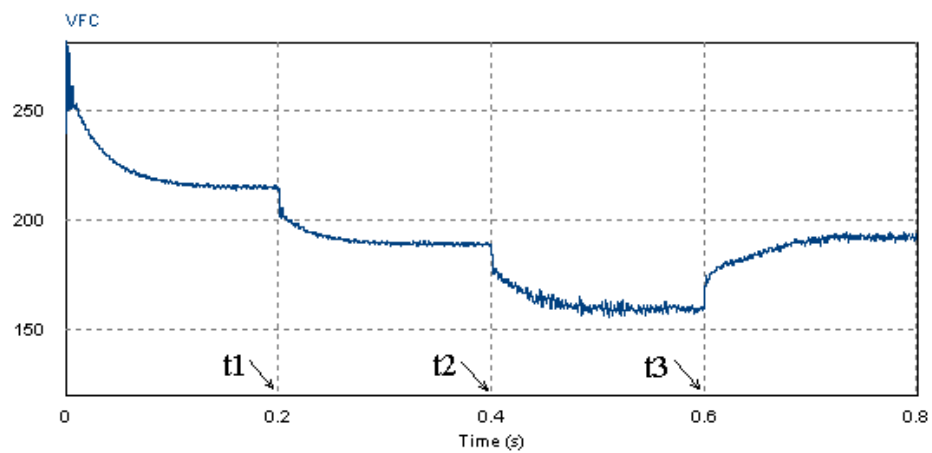
Fig. 3.7: Dynamic characteristics of the FC output voltage [Volts] when subjected to step change in load power

66

different time frame. The FC system is initially supplying power to the main dc-link while the 12-pulse VSI (R=1Ω, L=0.2mH) and a constant voltage buck-converter (CVBC) with resistive load are connected to the HVDC bus. Also, the total power dissipation of the buck-converter is regulated at 5.6 kW and the active power delivered to the RL load through VSI is calculated to be 36.6kW. At t_1=0.2s the system is subjected to a step change in power demand (R=0.5 Ω, L=0.1mH). At t_2=0.4s a constant power buck-converter (CPBC) with total power consumption of 5kW is applied to the main dc network, leading to another voltage drop in the FC's output profile. At t_3=0.6s the CVBC (5.6 kW) is disabled from the grid and the system continues operation with remaining loads. Fig. 3.8 represents the current profile of the PEM-FC when providing power to the
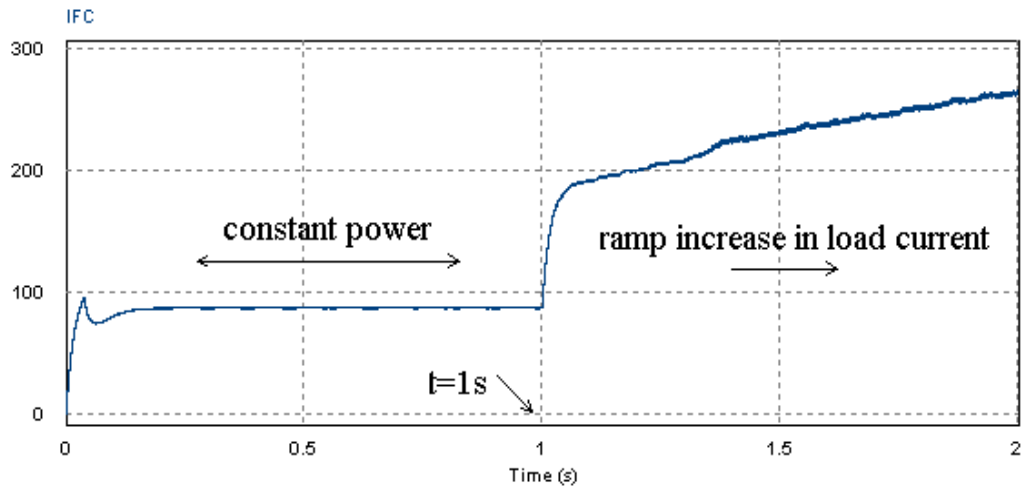
Fig. 3.8: FC Current [Amps] response to a combined step and ramp increase in load current.

main dc bus of the generating system. The PEM FC stack is initially operating while connected to the 12-pulse PWM-VSI with 3-ph RL load (R=2Ω, L=0.4mH). At t=1s the system is subjected to a step increase in load power (22.5 kW) due to interaction with CPBC. At the same time, the fuel cell stack undergoes a ramp increase in the load current due to interaction with another buck-converter with ramp increase in its load current profile. The voltage profile associated with this event is depicted in Fig. 3.9 As seen in the graph, the ramp increase in the load current would result to a pure oscillation in the FC output voltage waveform (as the absorbed current exceeds the stable operating equilibrium of the system's numerical solution). In addition, the phase portrait corresponding to the FC's dynamic behavior is shown in Fig. 3.10.

67
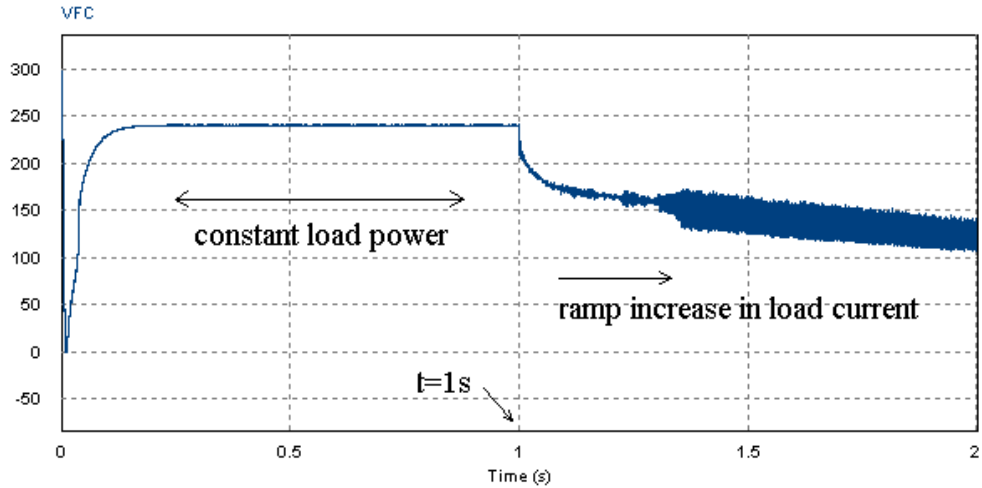
Fig. 3.9: FC voltage [Volts] response to a combined step and ramp increase in load power [kW]
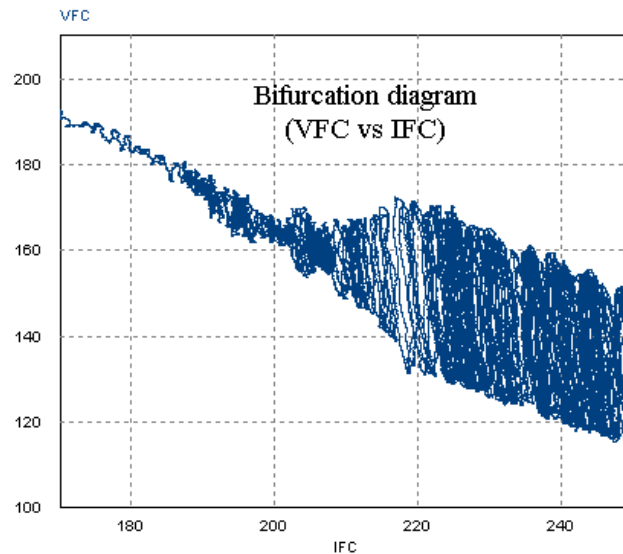
Fig.3.10: Phase plane of the FC output voltage [Volts] vs current [Amps]

It is shown in Fig. 3.10 that continuous increase in the PEM-FC current would result in chaotic behavior in its output voltage profile.

3.5.3 PEM-FC Connected to the Main DC Bus via Boost Converter

In this section, the performance and characteristics of the PEM-FC interconnected to the main dc link at 270V is analyzed through several case studies. The dynamic and steady-state behavior of the system is studied for different loading currents. As mentioned earlier, a dc/dc boost converter with closed-loop PWM switching technique is

applied for output voltage regulation. The PEM fuel cell system modeled in this work is capable of supplying electric power up to 80kW for emergency cases or when the aircraft is on the ground. In Fig. 3.11 the current profile of the PEM fuel cell system is demonstrated for above mentioned case study. In this effort, the fuel cell system is connected to the dc main bus via a dc/dc boost converter at the regulated voltage of 270V-dc. Also, the main dc-link interacts with a fully controlled sinusoidal pulse with modulation (SPWM) 12-pulse voltage source inverter (VSI) with RL passive loads, as well as a PWM dc/dc buck converter with constant power (CP) loads.
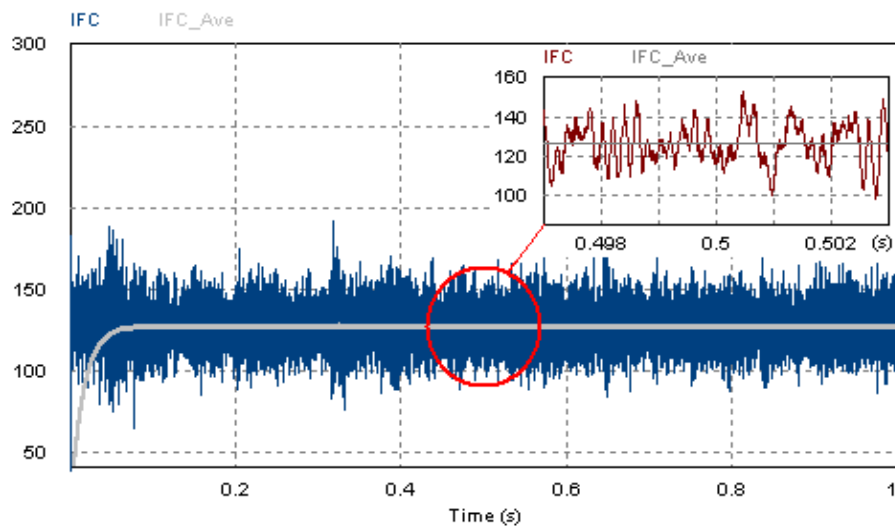
Fig. 3.11: FC output current [Amps] where connected to the dc-dc boost-converter, delivering roughly 35.12-kW load power.
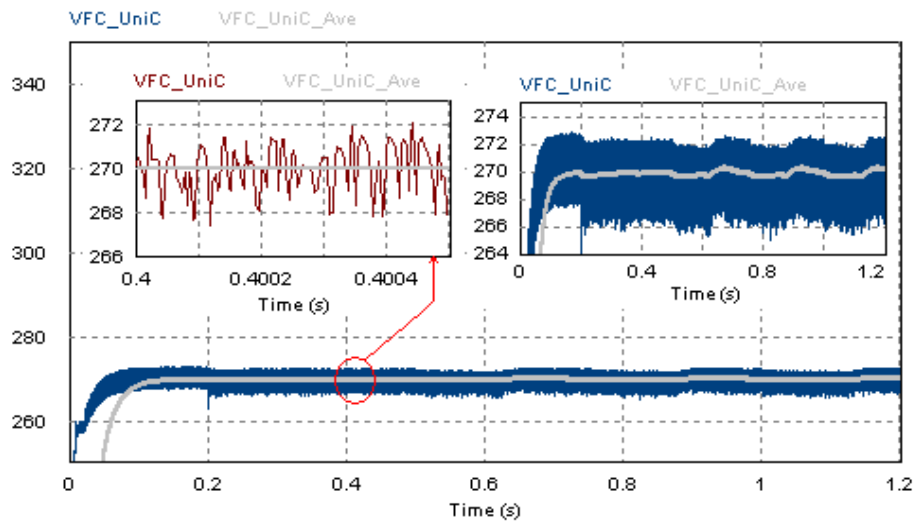
Fig. 3.12: Voltage [Volts] profile at the output of dc-dc boost-converter connected to the PEM-FC

Furthermore, the total power rating of the system is set to 32.8kW. Producing the average load current around 127A, the variation of the current harmonics is bounded within 100 and 150A, as depicted in Fig. 3.11. Also, Fig. 3.12 represents the voltage waveform corresponding to output profile of the unidirectional converter (dc/dc boost-converter) connected to the PEM-FC. The averaged value of the voltage is shown in a magnified view of the same graph. As seen in the picture, variation of the voltage waveform due to the PWM switching behavior of the converter is limited within 268-272V.

3.5.4 APU System Performance Interacting with Dynamic Loads

This section presents the performance and characteristics of the hybrid battery/fuel cell equipped APU where interacting with switching components. In this study, the PWM switching inverter is connected to the RL load. However, in this case study the RL loads have dynamic behavior as illustrated in Fig. 3.13 (a), (b). The 12-pulse switching inverter is initially delivering power to the passive load with 21.56kVA power rating. At time t=0.5s another RL load with same power rating (P_L=21.56kVA), with "on and off" characteristics is connected to the inverter. Therefore, the maximum apparent power dissipation according to this dynamic is calculated to be 43.12kVA at the constant frequency (CF) main ac bus. Also, the constant load power of CP buck converter is set to 10kW.
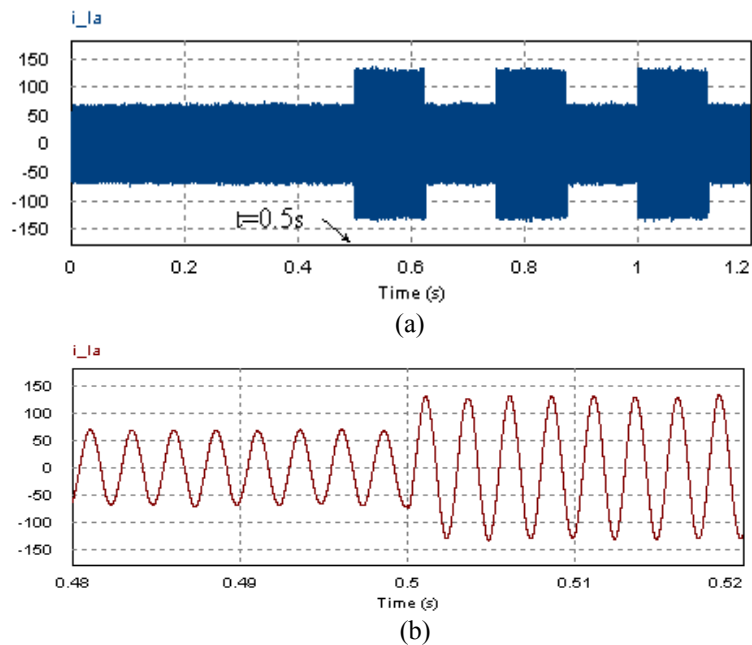
Fig. 3.13: AC load dynamic behavior (a) long-time duration (b) magnified view.

Fig. 3.14 depicts the dynamic performance of the APU system. The IBatt_Bic_Ave and IFC_UniC_Ave correspond to the output average currents of the buck-boost and boost converter, measured in ampere. Also, IL_Ave represents the averaged load current. As shown in the figures, due to the fast response time of the lead-acid battery compensates for the slow performance of the PEM-FC is compensated. In other words, the sudden current demand of the grid is supplied by the battery of the APU system. In this graph, the following legends are used to express system's profiles.

In fact, the graphs shown in Fig. 3.14 are presented to show how the PEM-FC and battery respond to the sudden change in power demand. Both input and output voltage/current waveforms of the dc/dc boost and buck-boost converters are presented to show the applicability and reliability of the control unit designed for output regulation of the APU system under investigation.
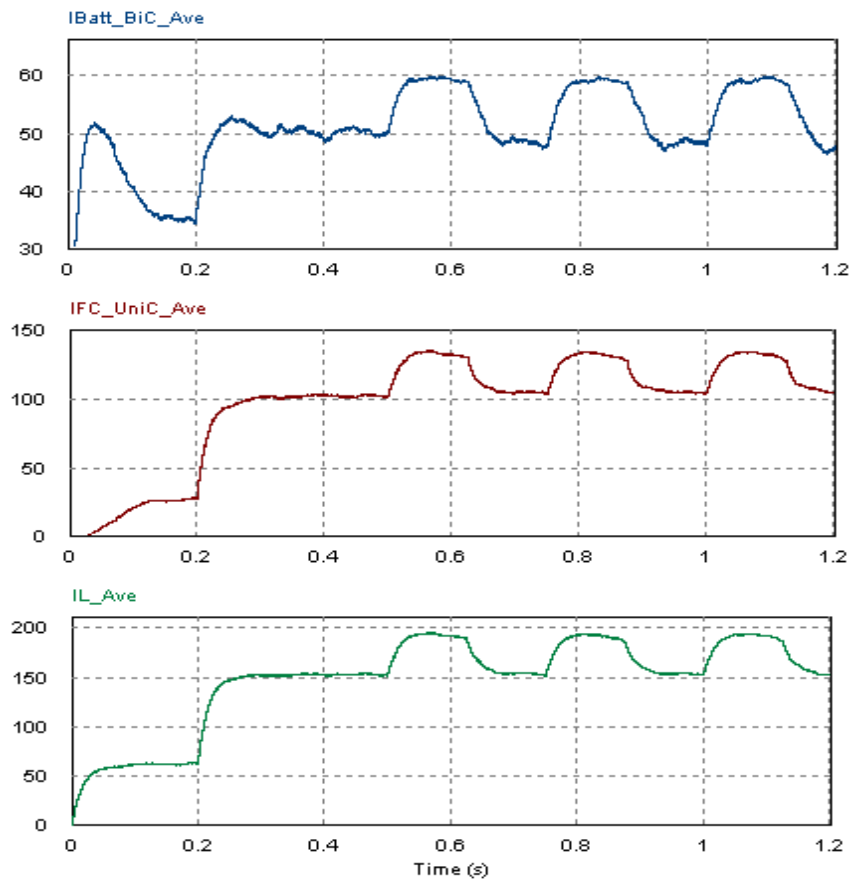
Fig. 3.14: The currents [Amps] corresponding to the buck-boost and boost converters outputs, connected to the battery and PEM-FC output terminals, respectively. The dynamic load current is shown with IL_Ave.

71

Fig. 3.15 represents the averaged voltage (VFC_Ave, VBatt_Ave) and current (IFC_Ave, IBatt_Ave) profiles associated with the fuel cell and battery output terminals for the same scenario (all measured in Volts) as addressed above. These graphs clearly indicate that any rapid increase/decrease in the load current at the VSI ac side due to dynamic behavior of the RL load would lead to the similar periodic variations in the voltage and current waveforms corresponding to the PEM-FC and lead-acid battery. In other words, any instantaneous power demand is supplied by the auxiliary power unit.

(a)

(b)
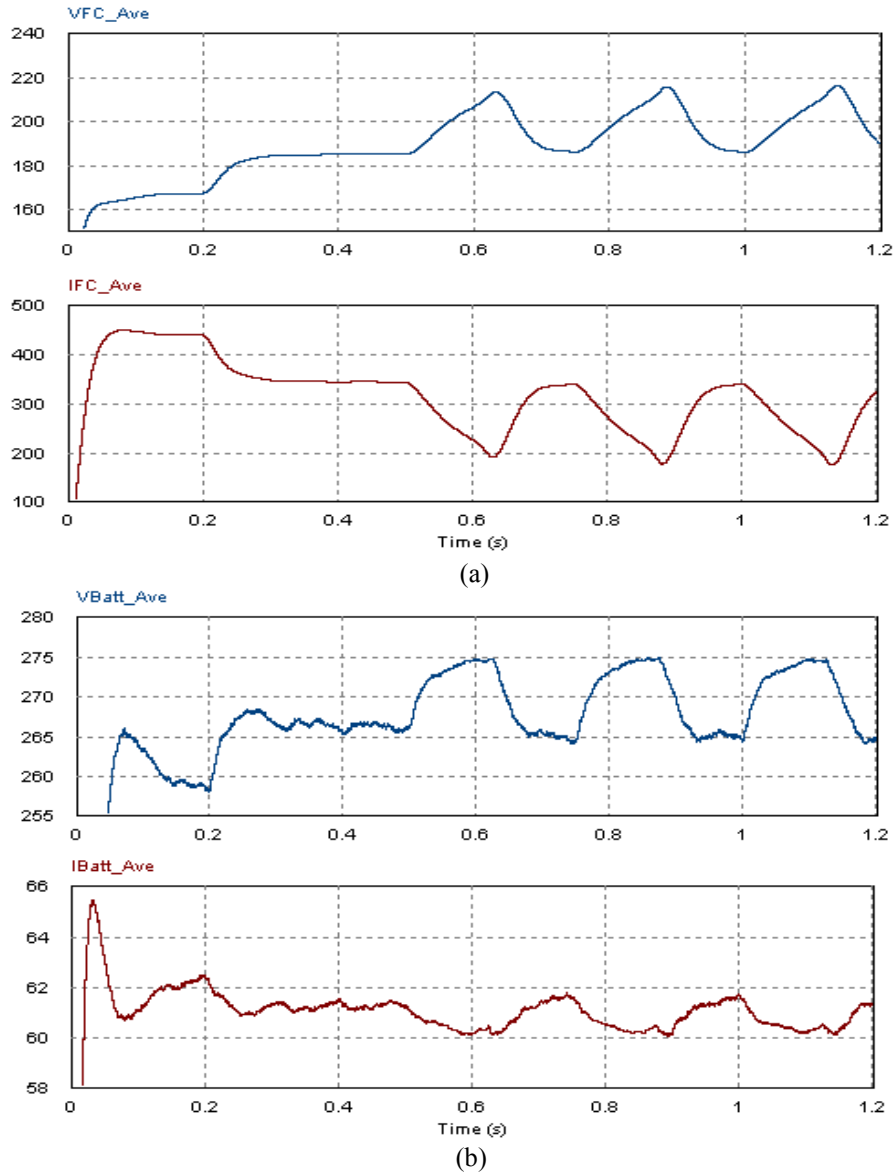
Fig. 3.15: Voltage [Volts] and current [Amps] profiles of the hybrid APU system (a) PEM fuel cell (b) battery. Initially the CP-BC with resistive load of 10-kW and RL load with 21.56-kVA are enabled, at t=0.5 the "on and off" dynamic load is activated.

72

3.5.5 APU Paralleled with Generating System

This section presents modeling and characterization of the hybrid APU system operating in parallel with the synchronous generator system. In [44], Dr. A. Eid proposes a configuration in which the auxiliary unit is directly connected to the ac power bus. As we discussed earlier, the proposed method in [44] has a number of drawbacks, for instance; (1) there is a need for an extra 12-pulse inverter in order to convert the dc voltage at the terminal of the APU system to ac voltage, (2) frequency and phase mismatches between two voltages are considered as a serious challenge.

In this work, the performance of the APU system is characterized for three different operating scenarios. Because of the slow nature of PEM-FC in terms of response to rapid changes in power demand, the hybrid system should be switched on before the generating system shuts down and becomes completely isolated from the aircraft electric network. Therefore, there is an overlap between the operation of the APU system and SG where the auxiliary unit contributes some portion of the required power to the grid (parallel operation). Hence, in the developed simulation model, the generating system initially supplies electric power for the ac and dc loads with total rating of 50.2kW which reflects the system's operation for normal condition. At time t=0.3s the hybrid battery/FC system is connected to the grid, producing power in parallel with the generating system. Since the lead-acid battery is capable of supplying surge current demanded by ac and dc loads, even a sudden disconnection of the main generating system from the grid is well compensated by the APU system. In this regard, at time t=0.4s, the synchronous generator is subjected to an intentional fault and subsequently disconnects from the network, as illustrated in Fig. 3.16. In this figure, v_fr, v_fs and v_ft represent phase voltage at the harmonic filter terminals (at the main ac power bus). Also, Fig. 3.17 represents the transient dynamics of the main dc bus affected by the failure in SG's normal operation. As shown in the same graph, this circumstance is along with an overvoltage occurring at t=0.3s, as well as an undervoltage that the dc bus undergoes when SG shuts down at t=0.4s.

Upon further investigation into Fig. 3.17, one notices that the overvoltage (demonstrated in magnified view) percentage of the main dc-link is around 7% which

exceeds the military standard set by [31]. In addition, the undervoltage error turns out to remain unchanged as depicted in the same figure. Also, this error percentage is calculated to be around 3.5% which is within the standard limit by [31].
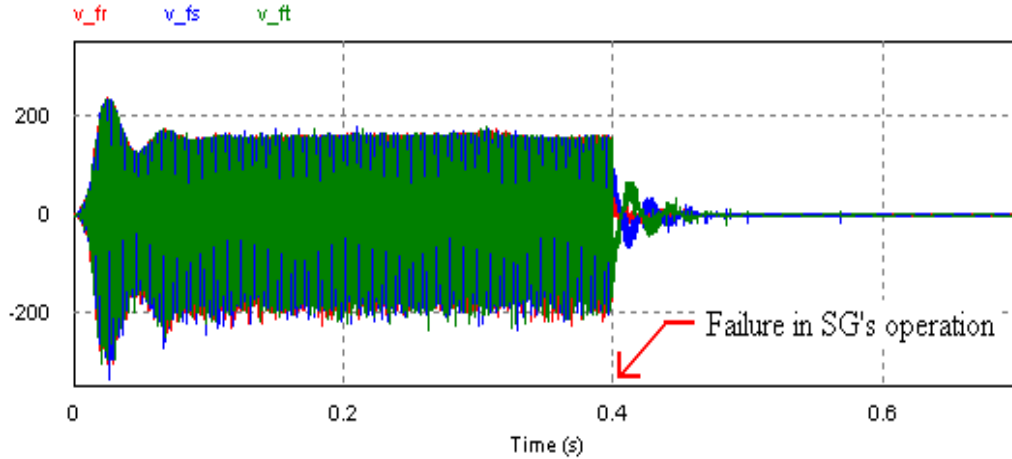
Fig. 3.16: Failure in SG's normal operation, 3-phase voltage [Volts]
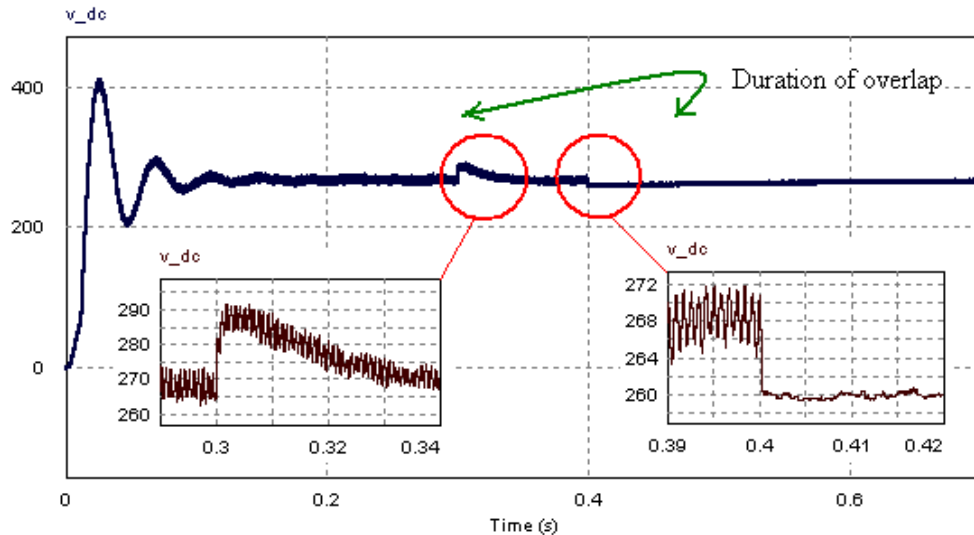
Fig. 3.17: Dynamic behavior of the main dc voltage [Volts] when paralleled with APU system

Fig. 3.18 presents the dynamic performance of the load current corresponding to the three individual scenarios, produced by the generating system and auxiliary power unit. The current through the main dc-link (I_dc_Ave) is supplied by the Synchronous Generator (SG) and measured in Amperes. It is shown in the figure that the absorbed current is initially supplied by the SG. At time t=0.3s, the lead-acid battery's current

74

(IBatt_Bic_Ave) starts rising, therefore, one sees a drop in the averaged current of the main dc-bus terminals, produced by the SG. It is worth mentioning again that the APU system is designed to produce electric power only for essential (emergency) loads, hence in this simulation model only 68% of the original load power is applied to the electric grid at t=0.3s (P_{ess}=33.8kW). At time t=0.45s, the battery system is disabled and PEM-FC produces electric power for the emergency loads. Also, the input current profiles corresponding to the switching converters connected to the AAEPS network are demonstrated in Fig. 3.19.
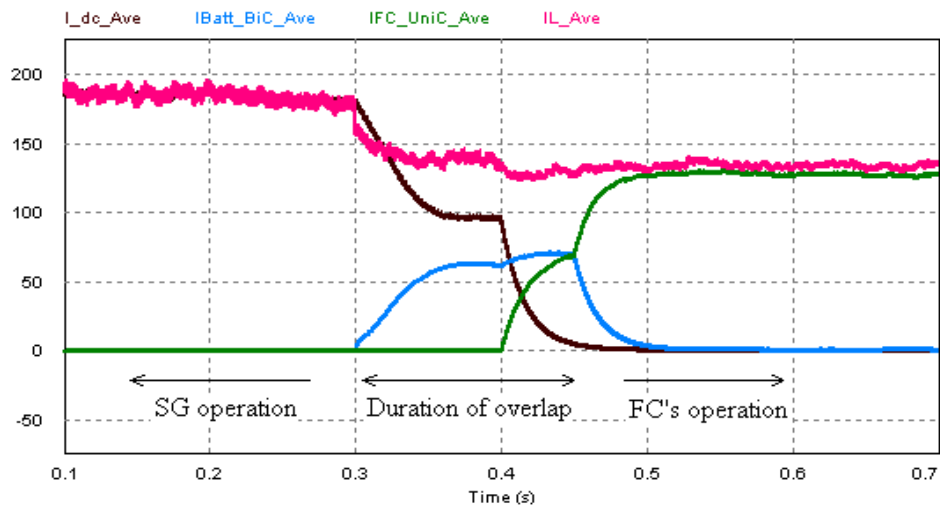
Fig. 3.18: Current [Amps] profiles produced by the SG and APU system at different time scale
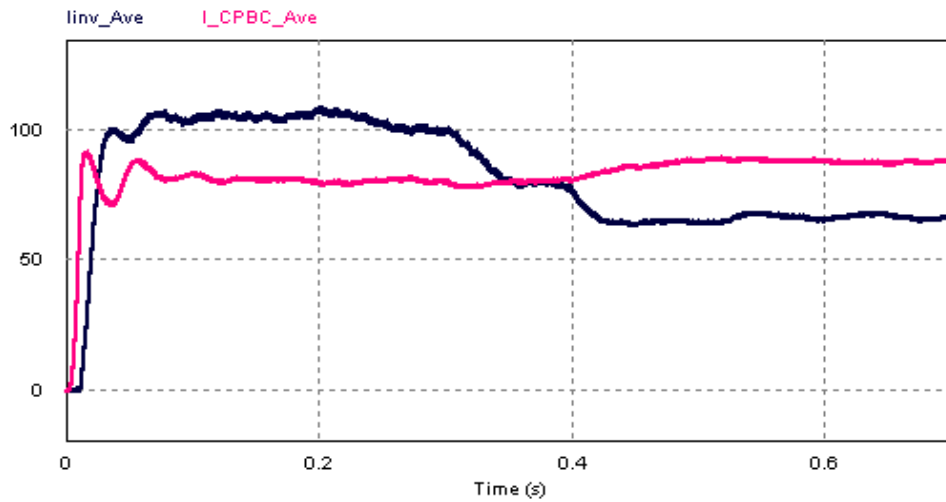
Fig. 3.19: Input currents [Amps] through: 1) the dc/ac PWM VSI supplying a 3-phase RL load (R=2.0Ω and L=0.4mH) of 21.56-kVA rating, 2) constant power buck converter with 12.4-kW resistive load

3.6 Summary

In this Chapter, a circuit model representation of the hybrid battery/FC APU system is developed using PSIM9 package. A comprehensive system analysis of the PEM-FC and lead-acid battery is performed for different loading configurations. The performance of the fuel cell stack is captured where interacting with different kind of static and dynamic loads. Both transient and steady-state behavior of the hybrid system is taken into account via several case studies. Also, the application of the battery/FC-based APU in an AAEPS is investigated under normal and emergency operational conditions. The applicability and effectiveness of using the hybrid system operating in parallel with the main generating bus (interconnected at the main dc-link) is assessed. The paralleled system performance has been analyzed while different scenarios are considered in the developed model. The characterization of the hybrid system is achieved by using the obtained simulation results from PSIM9 environment. The captured results demonstrate that the developed study model closely predicts the behavior and characteristics of a real system under transient and steady-state conditions.

Stability Assessment of AAEPS with Bifurcation Analysis

4. 1 Chapter Overview

Since the electric power system of aircraft is inherently non-linear, maintaining a range of stable operation is of prime concern. In order to address this complication, many nonlinear system analysis techniques have been developed to aid in the comprehension of system stability issues. One method that has come to prominence in recent years for analyzing the stability of power systems is bifurcation theory [62-68, 88].

According to [69-75], extensive research has been conducted on bifurcation theory as it is related to the analysis of ac transmission systems. This research has led to the conclusion that voltage instabilities can be prevented by controlling power system bifurcation. Although much effort has been put forth in analyzing ac transmission systems, little work has been published regarding the analysis of HVDC systems using bifurcation theory [69,76]. Also, much research has been carried out on control and stabilization of power electronic devices for renewable energy applications [89-91]. The stability assessment of the ac system in a typical More Electric Aircraft (MEA) using small signal analysis is addressed in [87]. Based on our knowledge so far, no research has been accomplished on the stability analysis of the aircraft electric system using bifurcation theory. It has been emphasized that increasing power demands, environmental concerns and economic factors are causing power systems to operate very near their stability limits [71,77], the same problem exists in an Advanced Aircraft Electric Power System (AAEPS). A product of increased demand on generation systems is an increase in the presence of dynamic loading. System instability commonly occurs when a load increase causes the generation system to exceed its capacity limits. The authors of [78-82] demonstrate the relevance of bifurcation theory to the application of switching power converters. The linear nature of the circuit topology employed for power converters is complicated by the dynamic behavior of the circuit switching. Each of the preceding factors gives merit to the necessity of system stability analysis for the AAEPS.

Complex conjugate pairs of eigenvalues moving from the LHP to the RHP or vice versa across the imaginary axis characterize Hopf bifurcations, which are indicative of chaotic motions and oscillatory behavior in power systems [71,74,75]. The presence of Hopf bifurcations in the More Electric Aircraft Power System (MEAPS) is determined herein, and their effect on the stability of the system is scrutinized. The investigation of existence of this type of bifurcation is achieved via multi-parameter variations correlated with control parameter changes, alterations in loading conditions and fluctuations in the operating frequency of the SG, which results from variations in the generator's engine speed.

In this article, we have analyzed the dynamic consequences of Hopf bifurcations leading to oscillatory instabilities. Also, the sustainability and robustness of the AAEPS and subsystems under various conditions of operation are investigated. The effects of parameter variations associated with changes in load configuration (changes in power demand, e.g., step change, ramp change), variation in control parameters (e.g., PI control parameters) and variations in operational frequency due to SG engine speed transition are addressed via several case studies. The forecasting of stability margins for bifurcation parameters is obtained from real-time simulations in PSIM9 environment and further supported by analytical discussion.

4. 2 AAEPS Circuit Representative Model

The system analysis reported in this Chapter is based on the single-channel model of the VSCF-AAEPS developed in PSIM9 software environment, represented schematically in Fig. 4.1. The depicted model is equivalent to a Boeing 767. electric power system [34,37,42]. The complex integrated system shown in Fig. 4.1 is composed of several components as follows

I. Generating System

The generating system is comprised of starter/generators, a voltage control unit and a feedback control system from the dc-link. In the VSCF Synchronous Generator (SG), the rated operating frequency is 400 Hz, though the frequency may vary in the range of 400 Hz – 800 Hz due to engine speed changes. A feedback proportional-integral (PI) control strategy regulates the voltage of the 270V-dc bus by appropriately regulating
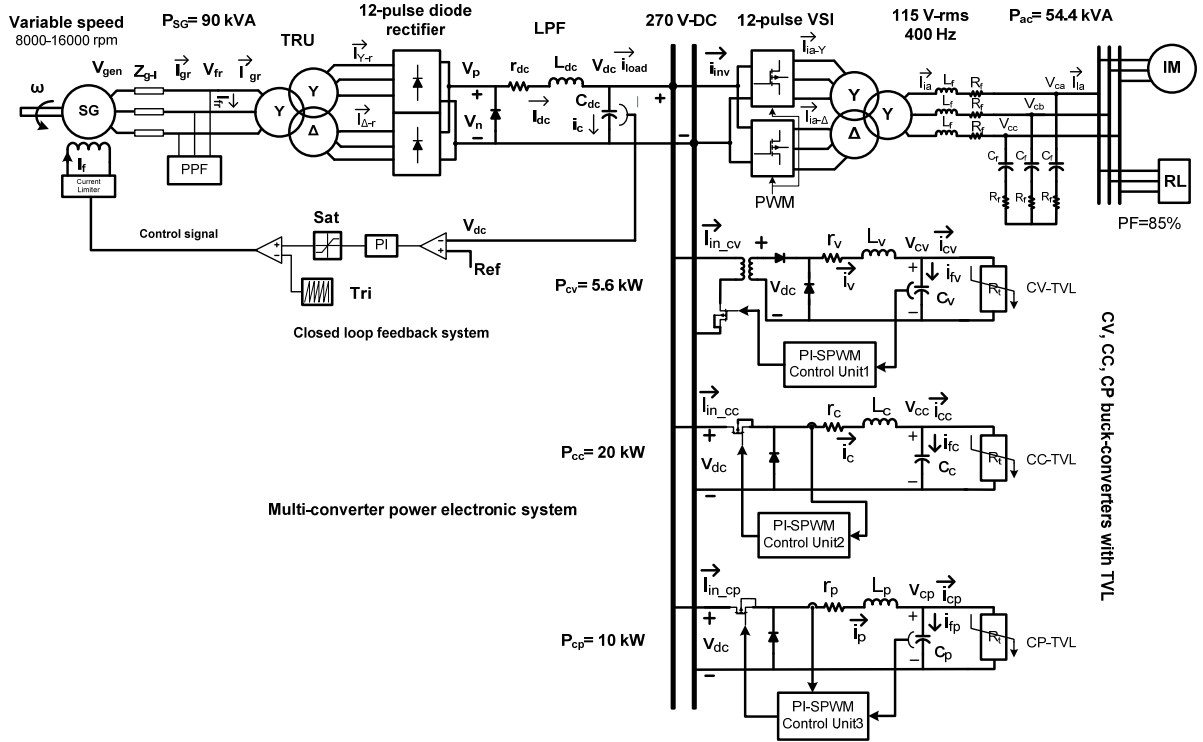
Fig.4.1: Schematic Circuit model of Advanced Aircraft Electric Power System

the field excitation current of the SG using PWM switching technique.

II. Rectifier Unit

Connected to the synchronous generator is a transformer rectifier unit (TRU) with a passive 12-pulse rectifier unit [42]. This configuration ensures the cancellation of low-order harmonics. A Y/Y/Δ transformer is employed to implement the 30° phase shift required to obtain 12-pulse operation.

III. DC/AC Loads

Various types of controlled dc and ac dynamic loads are distributed throughout the aircraft electric network. Depending on the operating conditions (e.g., normal operation or emergency situations), loading configurations may change, producing a time-varying pattern of operation. Load modeling is a critical issue in aircraft electric power system analysis, since the stability properties of the network are strongly dependent on power demands set by loading configuration. Major portions of the loads (ac and dc) have dynamic profiles. The dc non-linear loads are classified as constant

power (CP), constant current (CC), and constant voltage (CV) loads. Also, passive loads are considered in an AAEPS at different power ratings widely distributed throughout ac main bus. In this Chapter, ac passive loads are modeled, with a minimum load power factor of 0.85 lagging [34,37,42] as series RL networks. Also, a three-phase induction machine (IM) as a representation of ac dynamic load is connected to the constant frequency (CF) main ac bus for a separate case study.

IV. Power Inverter

A voltage source inverter (VSI) is also connected to the 270V-dc bus, consisting of two 6-pulse switching bridge inverters. In order to maintain a constant 115V/200V, 400Hz at the main ac bus, a feedback PI controller is utilized to regulate the modulation index of the SPWM inverter. Also, a Y/Y/D transformer applies the necessary 30° phase shift to combine the signals from each output phase of the 6-pulse inverters. The combination of the signals produces the required 115V/200V rms, 400Hz line voltage at the main ac bus.

4. 3 Differential Equations Corresponding to the AAEPS Physical Model

This section exemplifies the dynamics of the physical system with parameter-dependent differential algebraic equations describing the reduced-order aircraft electric system performance at the major node of integrated power electronic system using the Generalized State Space Averaging (GSSA) approach. In the previous Chapter, it was demonstrated that by applying an averaging technique to modeling and simulation of the aircraft system under investigation, the key dynamic features of the system can be obtained. Though the simplified differential equations are utilized to compute the stability region of the system dynamics via eigenvalues extracted from corresponding matrices, stability analysis is also supported with bifurcation diagrams captured from real-time simulations in PSIM9 environment in next sections.

I. Synchronous Generator System

Fig. 4.2 represents a circuit representation of electric system network corresponding to SG with excitation current control method. As shown in Fig. 4.2, a

two-branch passive harmonic filter is connected to the network to reduce harmonic components in the order of 11th and 13th of the fundamental waveform.

Fig.4.2: SG excitation circuit model with closed-loop feedback system

The amplitudes of the voltages at the SG terminals are regulated using a PWM closed-loop control system. The main dc voltage at the output of 12-pulse rectifier is compared to a reference voltage and the error signal is passed through a Proportional Integral (PI) unit. This signal is then compared to a sawtooth wave to construct the switching control signal applied to the field current control circuit. The design parameters used for this study are calculated for a 90-kVA power rating operation and their values are provided in Tables 4.1, 4.2. Furthermore, the state space differential equations representing system dynamics are developed as follow

$$
\begin{cases}
L_{f11}\dfrac{d^2 i_{f11}}{dt} + r_f \dfrac{d i_{f11}}{dt} + \dfrac{1}{C_{f11}} i_{f11} = \dfrac{dV_{fr}}{dt} = \\[2mm]
\quad L_{f13}\dfrac{d^2 i_{f13}}{dt} + r_f \dfrac{d i_{f13}}{dt} + \dfrac{1}{C_{f13}} i_{f13} \\[2mm]
\quad i_{f11} + i_{f13} = I_{fr} = I'_{gr} - I_{gr}
\end{cases}
\tag{117}
$$

$$
V_{fr} = V_{gen} - R_{g-l} I_{gr} + L_{g-l} \dfrac{dI_{gr}}{dt}
\tag{118}
$$

Rearranging Eq. (117) and combining with (118) yields the general form of state-space equation as given by (119)

$$\dot{x} = \Psi x + \Gamma u \qquad (119)$$

where $x_1 = i_{f11}$ and $x_3 = i_{f13}$ are selected as state variables, and the state matrix Ψ is given by

$$x = \begin{bmatrix} x_1 \\ x_2 \\ x_3 \\ x_4 \end{bmatrix}, \quad \Psi = \begin{bmatrix} 0 & 1 & 0 & 0 \\ \dfrac{-1}{L_{f11}C_{f11}} & \dfrac{-R_{f11}}{L_{f11}} & 0 & 0 \\ 0 & 0 & 0 & 1 \\ 0 & 0 & \dfrac{-1}{L_{f13}C_{f13}} & \dfrac{-R_{f13}}{L_{f13}} \end{bmatrix}, \quad \Gamma = \begin{bmatrix} \dfrac{1}{L_{f11}} \\ \dfrac{-R_{f11}}{L_{f11}^2} \\ \dfrac{1}{L_{f13}} \\ \dfrac{-R_{f13}}{L_{f13}^2} \end{bmatrix}, \quad u = V_{fr}(\omega, t) \quad (120)$$

Assuming a 3-phase balanced system for the SG, and further applying the derivative property of the GSSA method to equation (119) one comes to the following expression

$$\begin{cases} \langle \dot{x} \rangle_{12k\pm1} = -j(12k \pm 1)\omega\langle x \rangle_{12k\pm1} + [\Psi\langle x \rangle_{12k\pm1} + \Gamma\langle V_{fr} \rangle_{12k\pm1}] \\ \langle I_{fr} \rangle_{12k\pm1} = \langle x_1 + x_3 \rangle_{12k\pm1} \end{cases} \qquad (121)$$

where the value of integer number $k = 0, \pm1, \dots$ is determined based on the required degree of accuracy for approximation. Also, the filter current can be described by using above state variables as given

$$\langle I_{fr} \rangle_k = \langle x_1 \rangle_k + \langle x_3 \rangle_k \qquad (122)$$
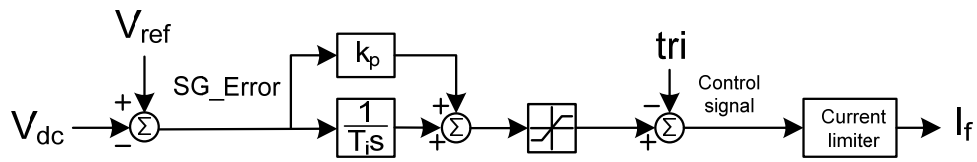
Fig. 4.3: The simplified equivalent control unit for dc voltage regulation

filter terminals, by controlling excitation field current (I$_f$) of the generator. The feedback voltage obtained from the main dc link at the output of 12-pulse diode rectifier system is passed through a low pass filter so that only its dc value is compared to the reference. In Fig. 4.3, V$_{ref}$ represents the reference voltage set to 270 V-dc, and V$_{dc}$ is the dc feedback voltage. K$_p$ and T$_i$ introduce the gain and integral time constant of the PI operator, respectively. I$_f$ corresponds to the excitation current though the generator field winding.

Furthermore, the corresponding switching control signal is constructed as given by equation (123), using a periodic step function in order to provide a fully controlled pattern over I_f for voltage regulation purposes.

$$h(t,T) = U\left\{\left((V_{dc})_0 - V_{ref}\right) * \left(K_p + \frac{1}{T_i s}\right) - Tri\right\} \tag{123}$$

where K_p and T_i are tuned for a desired operating condition. This means that a fully regulated dc voltage can be achieved by controlling the excitation current, and subsequently the ac voltages at the SG's output terminals by controlling over PI parameters (K_p, T_i).

II. DC-Link Dynamic Equations

The dynamic model of the 12-pulse diode bridge rectifier system applied for this study has been described by the following parameterized differential equations. Furthermore, the interaction of the interconnected system corresponds to the multiconverter system of AAEPS modeled via the GSSA approach introduced in Chapter three. Due to the existence of inherent non-linear properties in the system, along with time-varying load configuration, the whole power electronic system is considered as a non-linear system with multi-variable parameters. Assuming a Continuous Conduction Mode (CCM) of operation for the rectifier system, then voltage V_{dc} at the output of dc main bus Low Pass Filter (LPF) can be expressed as

$$\begin{bmatrix} \dot{V}_{dc} \\ \dot{I}_{dc} \end{bmatrix} = \begin{bmatrix} 0 & \frac{1}{C} \\ -\frac{1}{L_2} & -\frac{R_2}{L_2} \end{bmatrix} \begin{bmatrix} V_{dc} \\ I_{dc} \end{bmatrix} + \begin{bmatrix} -\frac{1}{C} & 0 \\ 0 & \frac{1}{L_2} \end{bmatrix} \begin{bmatrix} i_{Load} \\ f_v \end{bmatrix} \tag{124}$$

where the filter capacitance voltage (V_{dc}) and dc link inductor current (I_{dc}) are selected as state variables; also, f_v is identified by the following term

$$f_v = f_v(V_m, \theta, \mu) = h(\theta, \mu)\frac{6+3\sqrt{3}}{7}V_m \sin\left(\theta + \frac{2\pi}{3}\right) + \left(1 - h(\theta, \mu)\right)\frac{\sqrt{3}}{2}\{V_m \cos(\theta) +$$

$$V_m \sin\left(\theta + \frac{2\pi}{3}\right)\} \tag{125}$$

where V_m describes the peak value of voltage at the ac side of the rectifier unit estimated by (1), (2). The commutation angle is represented with μ, which is determined by the loading condition.

$$h(\theta,\mu) = \begin{cases} 1 & if \quad 2n\pi - \frac{\pi}{4} \leq \theta < 2n\pi + \mu - \frac{\pi}{4} \\ 0 & if \quad 2n\pi + \mu - \frac{\pi}{4} < \theta < 2n\pi - \frac{\pi}{12} \\ & n = 0, \pm1, \pm2 \dots \end{cases} \tag{126}$$

The periodic function $h(\theta,\mu)$ repeats every $\frac{\pi}{6}$ radians for the 12-pulse rectifier under study. R_2, L_2 correspond to the summation of leakage resistances and inductances associated with both sides (ac and dc) of the rectifier unit. Moreover, the state-space averaging representation of the system model at the output of rectifier's filter, while interacting with dc/dc, dc/ac switching converters is developed in Chapter three. Based on the proposed model, the simplified state space differential equation describing system dynamics was calculated as (See Appendix A.2)

$$\dot{X} = AX + BY + U_x(\mu, \gamma, \dots) = f(X, Y, U_x) \tag{127}$$

where X contains all the rectifier's averaged state variables (x_1, x_2,...) due to interaction with the following converters, and the state vector Y corresponds to those averaged variables ($y_1, y_2, \dots$) that are utilized to express the dynamics of the following converters interconnected with the dc main bus, also appearing on the preceding 12-pulse power supplier's input profile. Matrix U_x includes the control parameters used for signal regulation purposes and the foreign chaos imposed to system's dynamics which are considered as qualitative changes on system's operation.

III. Buck-Converter

Assuming the CCM of operation, the dynamic performance of the system which has been traditionally used [29,30] can be described by the following differential equations

$$\begin{cases} \frac{dI_v}{dt} = h(t, T_v)\frac{V_{dc(t)}}{L_v} - r_v\frac{I_{v(t)}}{L_v} - \frac{V_{cv(t)}}{L_v} \\ \frac{dV_{cv(t)}}{dt} = \frac{I_{v(t)}}{C_v} - \frac{V_{cv(t)}}{C_v R_t} \\ I_{in\_cv} = h(t, T_v)I_v(t) \end{cases} \tag{128}$$

where I_{in_cv} represents the buck input current. Line current I_v and output voltage of the filter V_{cv} are selected as state variables. r_v, L_v, C_v represent line resistance, inductance and capacitance of the buck converter's filter, respectively. Also, the dc time varying load is introduced by R_t. Also, T_v corresponds to the time period of PWM switching frequency

and may be varied as design requirements change, and the duty cycle d_t is determined according to the loading condition. Communication describes the switching control of the circuit and is defined as

$$h(t, T_v) = \begin{cases} 1 & 0 \leq t \leq d_t T_v \\ 0 & d_t T_v \leq t \leq T_v \end{cases} \tag{129}$$

Also, the dynamics of two other types of buck converter can be identically expressed by Eq. (128). As developed in Chapter three, the interaction of the buck-converter with main dc-link can be addressed by applying the zeroth and first-order terms of Fourier coefficients calculated by the GSSA technique as follows

$$\dot{Y} = \Lambda Y + \phi X + U_y(\tau, \eta, \dots) = g(X, Y, U_y) \tag{130}$$

where the state vectors Y and X consist of averaging state variables developed by [69] to model dynamic behavior of the converter system. The state matrices Λ and ϕ, also the input matrix U_y can be calculated according to the system's dynamics equation (See Appendix A. 2)

IV. Bifurcation-based Characterization of the Interconnected Power Electronic System (An Example)

In this section the bifurcation analysis is given for the interacting multi-converter system of the AAEPS. The dynamics of the integrated physical system discussed in the previous sections can be expressed by the compact form of parameter dependent differential-algebraic equation as following

$$\dot{x} = f(x, y, \mu), \qquad f: \Re^{n+m+p} \longrightarrow \Re^n \tag{131}$$

$$\dot{y} = g(x, y, \mu), \qquad g: \Re^{n+m+p} \longrightarrow \Re^m \tag{132}$$

where $x \in X \subset \Re^n$, $y \in Y \subset \Re^m$, $\mu \in Z \subset \Re^p$; also the solution (X_0, Y_0, U_0) satisfying $f(x, y, \mu) = 0$ and $g(x, y, \mu) = 0$ is called an equilibrium point for the system The values of $n,\ m$ generally depend on the dimension of system under investigation, and p is identified by the number of parameters considered for system operation. In this particular example $n = 10, m = 6$ and $p = 7$. (p is selected according to the number of variable parameters, see Appendix A for more details)

Now, let us consider the standard conditions for Hopf bifurcation [6] and the way that it can be effectively detected by defining the Jacobian matrix of our system. Let us define the related Jacobian matrix as

$$J(X,Y) = \begin{pmatrix} f_X & f_Y \\ g_X & g_Y \end{pmatrix} \tag{133}$$

also, can be rearranged as

$$J = f_X - f_Y g_Y^{-1} g_X \tag{134}$$

the standard eigenvalue condition implied by Hopf bifurcation of (134) and used to detect Hopf bifurcations numerically is that J matrix has eigenvalues $\pm j\omega$ with $\omega \neq 0$. Therefore, by considering Eq. (127) and (130) and using Eq. (134) one gets to Jacobian matrix of the system given by

$$J = A - B\Lambda^{-1}\phi \tag{135}$$

Fig.4.4 represents numerical calculation of the eigenvalues associated with the example discussed previously. In this calculation, the resistance of the dc-dc converter is varied to model a dynamic load power change, considering as bifurcation parameter.

(a)   (b)
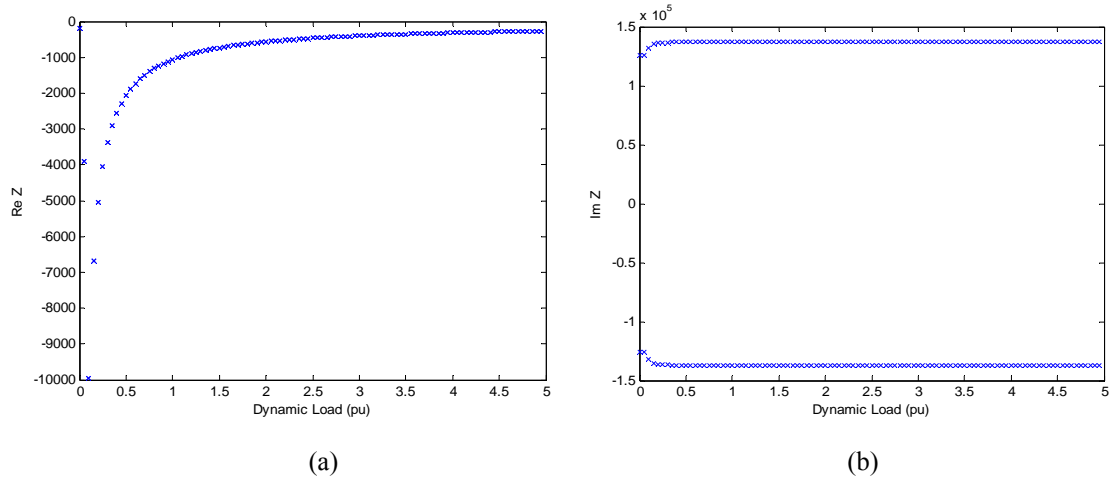
Fig. 4.4: The movement of Jacobian matrix eigenvalues due to variation in load characteristics, (a) real part vs load, (b) imaginary part vs load

The resistance of the constant voltage buck converter is subjected to a continuous decrease, which is equivalent to a continuous increase in the load power. As shown in

Fig. 4.4, the dominant eigenvalues of the Jacobian matrix is approaching to the Imaginary axis as load power increases (by decreasing the load resistance).

4. 4. Bifurcation Analysis of the AAEPS

Several case studies have been developed for the stability analysis of the AAEPS using bifurcation theory. In each case, the dynamics of the aircraft electric system and sub-system are investigated respect to variation in the bifurcation parameters.

4. 4. 1 Bifurcation Analysis for CVBC with Varying Filter Capacitance

Switching buck converters are widely used in the aircraft electric power system, hence in this case study we have performed a stability analysis of this kind of switching component. The circuit under consideration is a dc-dc constant-voltage buck converter with PWM control topology for output voltage regulation. The filter capacitance was the parameter that was varied for this study. Shown in Fig. 4.5(a) is the period-1 phase plane orbit of the system while providing 5.6 kW power for a resistive load. The graph is obtained from a study model implemented in PSIM9 environment, and the output voltage is plotted against the device's inductor current. Fig. 4.5(a) indicates that the system's equilibrium point is located at Hopf bifurcation region because of the pure oscillatory behavior seen in the time-domain computer simulation presented by Fig. 4.6 (a), (b). These plots have been obtained for a filter capacitance of 0.75mF. Fig.4.5 (a) predicts that as the inductor's current oscillates from 160A to 240A, the output voltage maintains stable operation between 26.8V and 28.7V. Fig. 4.5(b) shows a quasi-periodic trajectory in the (v_{cv} ,i_{cv}) space after undergoing a Hopf bifurcation of the stroboscopic map. The difference between diagrams of Fig.4.5 (a) and (b) is resulted from a step change in the filter capacitance C_v from 0.75mF to 1.5mF. The phase plane orbit exhibited in Fig. 4.5(a) and (b) corresponds to the Oscillograms shown in Fig. 4.6 (a), (b). The obtained simulation plots in this study closely agree with the experimental results reported in literature [81]. On the other hand, cost of the design and system's slow response to a change in the input voltage are considered as serious drawbacks of using high filter capacitances for the dc/dc buck converters. Further inspection into the same plots verifies instability problem which is related to the use of high capacitances. In other words, the stable region of the system's operation decreases as the capacitance becomes larger. This

is shown by comparing (a) and (b) in Fig. 4.5, where the stability region in terms of two phase bifurcation diagrams has been plotted for two different capacitor filters. However, further investigation indicates that both the current and voltage remain bounded within acceptable limits of operation satisfying the IEEE/Military standards, though the voltage ripple of Fig. 4.5 (b) exceeds somewhat the standards set by [86].

(a)   (b)
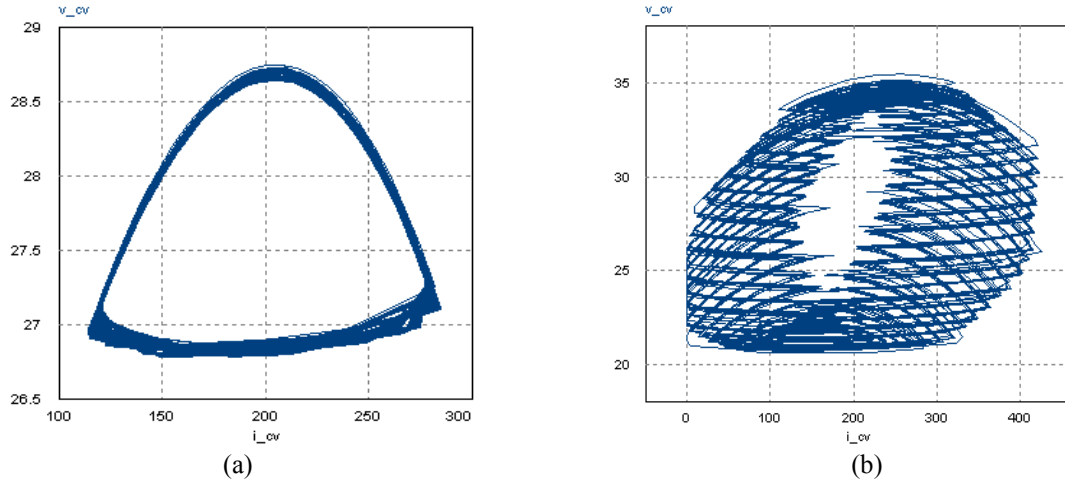
Fig. 4.5: Phase plane orbits for the CVBC voltage [Volts] vs current [Amps] with (a) 0.75mF filter capacitance and (b) 1.5mF filter capacitance

(a)

(b)
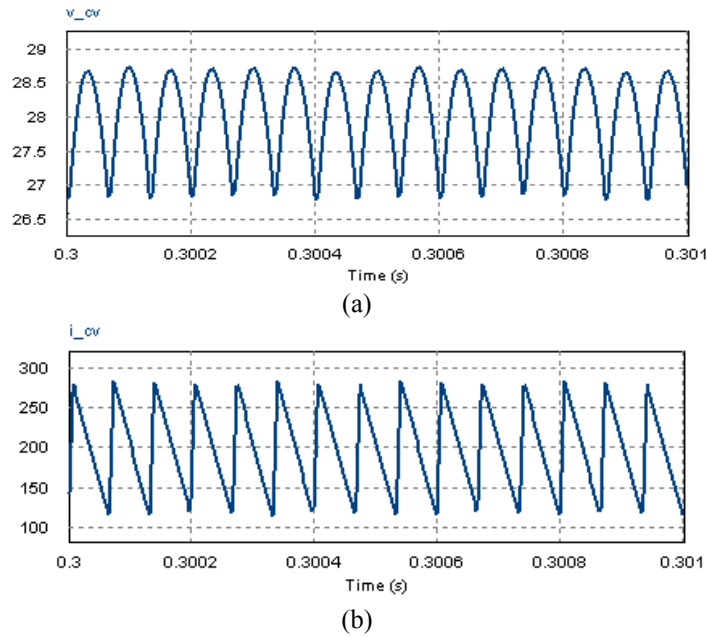
Fig. 4.6: Time-domain graphs of CVBC output (a) voltage [Volts] and (b) current [Amps] with a filter capacitance value of 0.75mF

4. 4. 2 *Stable Region of Operation*

In this case study, the interaction of the 12-pulse diode rectifier and the CVBC was examined. The phase plane orbit diagram in Fig. 4.7 was obtained from the model consisting of the 12-pulse rectifier with the ac and dc loads operating at a power level of 56kW; the HVDC output voltage and current from the rectifier are juxtaposed. It can be seen that the voltage reaches its stable position when the current is near 200A. A plot of the generator voltage superimposed on the generator current is shown in Fig. 4.8(a). The voltage appears to remain stable with current oscillations. This result can be confirmed with the phase plane diagram in Fig. 4.8 (b). As illustrated in Fig. 4.8 (b), the phase angle between SG voltage and its line current is near zero degree which confirms the applicability and effectiveness of TRU (connected to the 12-pulse diode bridge rectifier) in improving the power factor (PF) of the system. According to the graphs (a) and (b) of Fig. 4.8, one notices that the equilibrium solution of the system's non-liner characteristics equations are hyperbolic fixed points which are located at a stable node, hence we call them Stable Node Bifurcation (SNB).
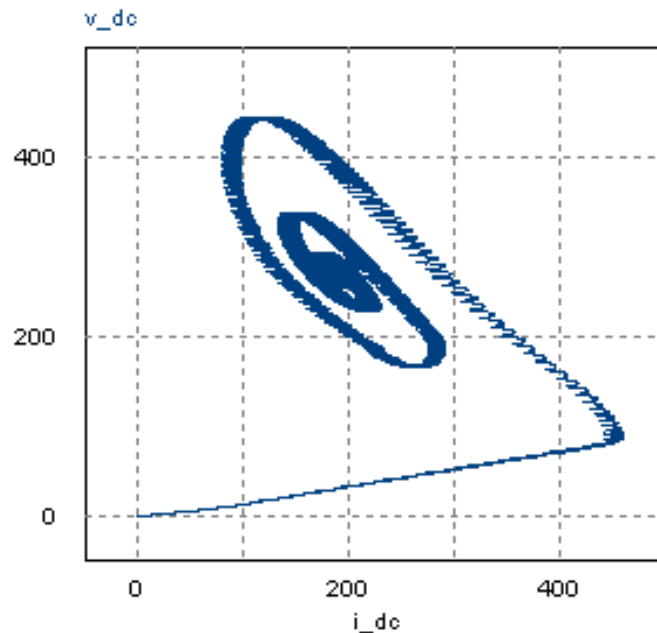
Fig. 4.7: Stable operating point of 12-pulse rectifier, voltage [Volts] vs current [Amps]

(a)

(b)
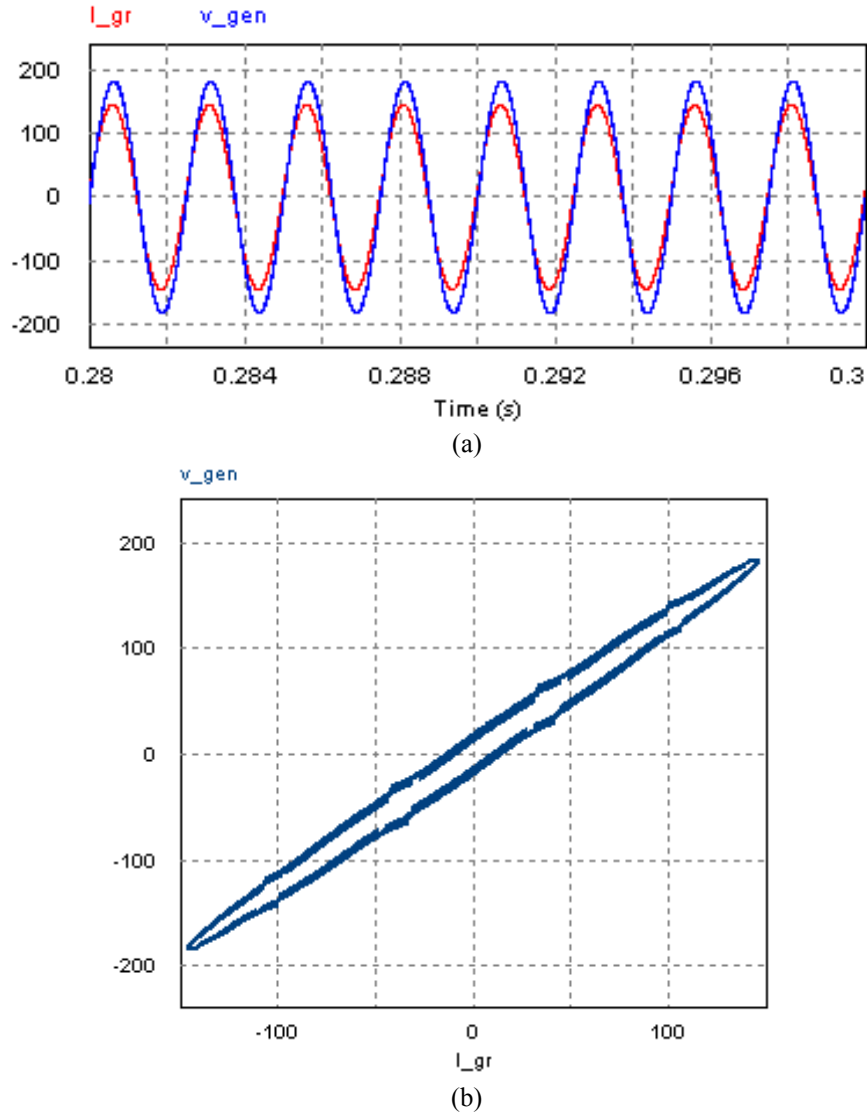
Fig. 4.8: SG voltage [Volts] and current [Amps] (a) oscillogram and (b) phase plane orbit

4. 4. 3 *Stability Analysis for SG and AC/DC Loads With Variations in PI Control Parameter (K_p)*

The second case study involved the performance characteristics of the non-linear system while analyzing the interaction of the SG, the 12-pulse diode rectifier and the dynamic ac and dc loads of the entire system. Fig. 4.9 reveals the system's operation under variation of the control parameter. The proportional coefficient corresponds to PI block applied for excitation current control was gradually ramped up. Fig. 4.9 (a), (b) show the computer simulations obtained for the output voltage and line current of the rectifier at the HVDC node. According to the figures, It can be seen that by continually

increasing the value of proportional (K_p) the equilibrium points of the system move toward an unstable region. In fact, the eigenvalues of the Jacobian matrix corresponds to system's inherent non-linear equations experience crossing the imaginary axis, later the real parts of the dominant poles obtain positive values which causes the system fall into a total unstable node of operation. Also, the voltage profile at harmonics filter's terminal is depicted in Fig. 4.9 (c). Its shown in the figure that the ac voltage V_{fr} resists against instability due to increase in K_p until it's value reaches a critical point (around K_p=0.168). Then, the system dynamics demonstrate to be unstable as time proceeds. In this case study, the power demand at the output dynamic loads model is set to 81.2kW in total, for the current loading condition. Furthermore, by looking at Fig. 4.9 (a), (b), (c), one sees that as the Proportional parameter is subjected to a ramp increase, the HVDC voltage (V_{dc}) and the corresponding inductor's current (I_{dc}) remain stable until t=0.49s, at approximately 270V and 302A, respectively. Nevertheless, a Hopf bifurcation occurs near that time and the location of dominant eigenvalues moves to an unstable region, leading the voltage and current to begin oscillatory behavior. The complex pair of eigenvalues remains in the RHP, precluding the return of the dc output voltage to stability. The oscillograms shown in Fig. 4.9 (a) and (b) confirm that the occurrence of the voltage instability of the rectifier coincides with instability in the rectifier line dc current. This is manifested in the time-domain figure of the current for the instances where the current value drops to zero.

Also, the movement of the eigenvalues associated with parameterized differential equations corresponding to the dynamic behaviors of major nodes of the system under study can be interpreted as following: initially all real-parts of the complex-pair eigenvalues are located at the left half plane (LHP) of the complex plane. Continuing the increase in K_p leads to a gradual movement of some of the real-parts (but not all) to the right half plane (RHP). The speed of eigenvalues displacement is dependent on the speed of variation in the proportional coefficient (K_p). As shown in Fig. 4.9 (a) and (b), the voltage and current waveforms undergo a rapid oscillation and then fall into unstable region of operation. According to this event, it turns out that one pair of eigenvalues crosses the imaginary axis rapidly due to fast change in the K_p parameter.
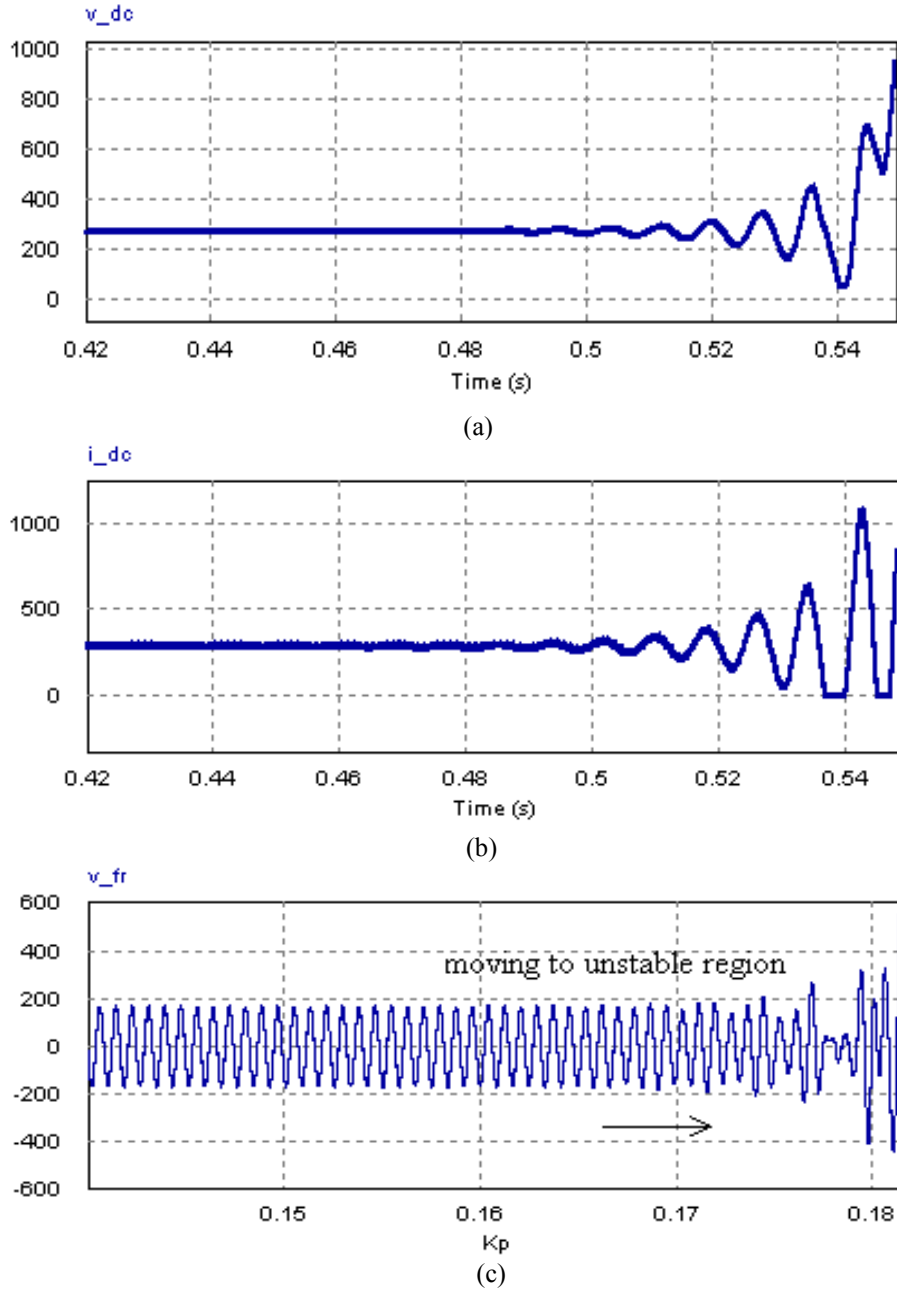
Fig. 4.9: Time-domain plots corresponding to (a) voltage at the main dc-link [Volts] (b) current at the main dc-link [Amps] (c) AC phase voltage at the harmonic filter terminals [Volts]

The phase plane orbit diagrams for various nodes of the SG ac and dc system are also captured for varying the proportional gain parameter K_p of the PI controller and are shown in Fig. 4.10. The graph in Fig. 4.10(a) indicates that voltage collapse occurs as the current deviates from the operating point of 302A. The SG filter voltage in Fig. 4.10(b) also experiences collapse as the filter current becomes chaotic, which is analogous to the

case for the generator voltage and current in (c). The diagram of the rectifier output voltage in (d) indicates that the collapses are concurrent with the deviation of the SG error from zero to nonzero values.
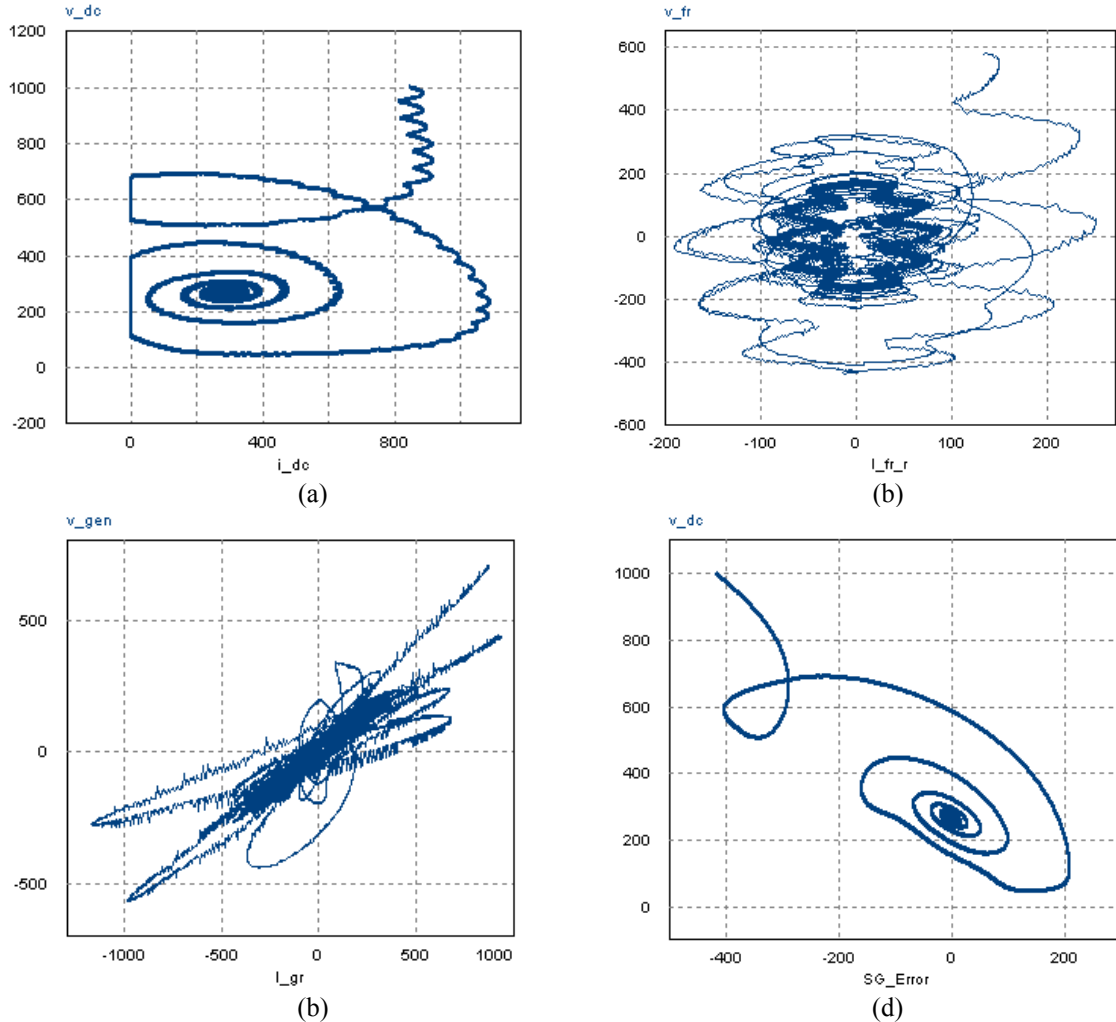
Fig. 4.10: Phase plane orbit diagrams corresponding to the SG ac and dc system for (a) the dc voltage [Volts] vs the dc current [Amps], (b) the filter voltage [Volts] vs current [Amps], (c) the generator voltage [Volts] vs current [Amps] and (d) the dc voltage [Volts] vs SG error

4. 4. 4 *Stability Analysis of the SG and AC/DC Loads With Variations in PI Control Parameter (K$_i$)*

In this section, the performance characteristics of the aircraft power electronics system under variations of integral gain K_i are studied. It has been demonstrated that by increasing the Integrator coefficient K_i (Integrator's time constant) parameter, the variation would lead to emerge of two regions of instability in the system's profiles, including HVDC and SG main bus nodes. Neglecting the transient performance, the

operation of the system can be divided into three regions of operation; as the parameter K_i is increased, the voltages at both dc and ac side of the grid undergo a pure oscillatory responses that complies with Hopf bifurcation phenomena as seen in Fig. 4.11(a). According to the same picture, further increase in the value of K_i causes the dominant eigenvalues of the system's Jacobian matrix, moving to an unstable region, gaining positive real values. In fact crossing the imaginary axis has no return to the LHP and the system becomes completely unstable. The oscillogram in Fig. 4.11(a), (b), (c) verifies this result.
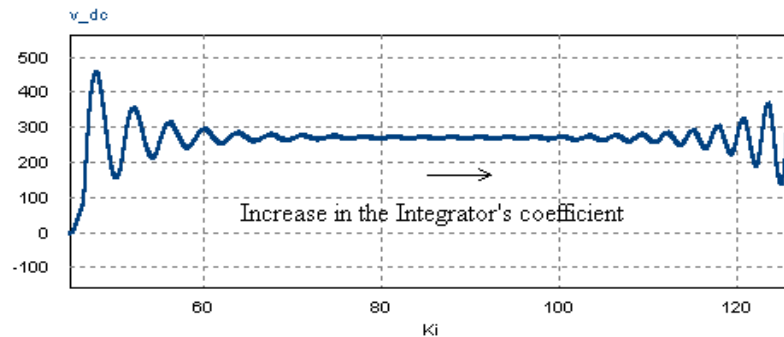
(a)
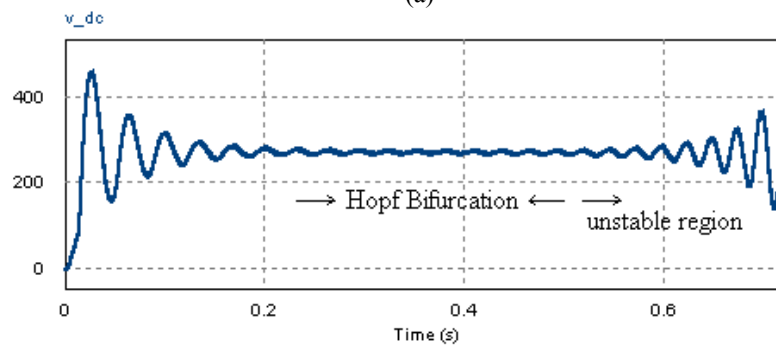
(b)
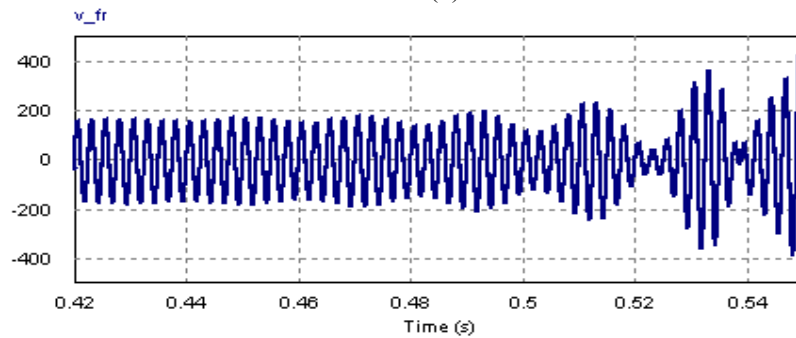
(c)

Fig. 4.11: The rectifier output voltage (a) output dc voltage [Volts] vs K_i (b) time-domain response vs varying K_i parameter in PI controller (c) time-domain simulation of the filter's voltage

The phase plane orbit for the SG filter voltage and the filter current and the corresponding oscillogram also reflect the shift from stability equilibria to to chaos exhibited at the ac main bus of the synchronous generator system with increasing control parameter value. The oscillations in the filter voltage begin to resonate as the parameter is incrementally increased beyond a certain value ($K_i \geq 96$ or $T_i \leq 0.0104$). The graphs that complement this are illustrated in Fig. 4.11(c) and Fig. 4.12.
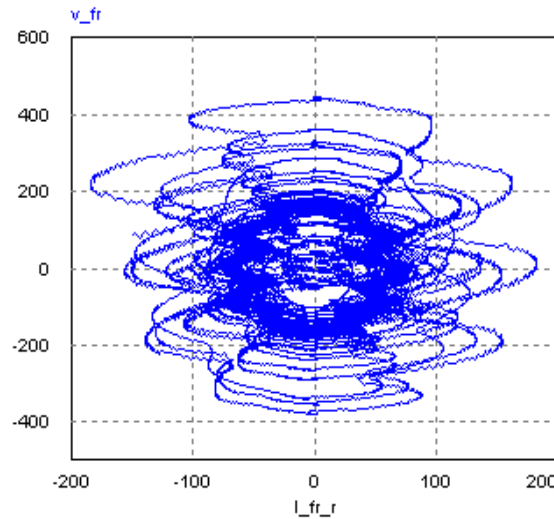
Fig. 4.12: SG filter phase plane diagram (Harmonic filter voltage [Volts] vs current [Amps])

4. 4. 5 *Stability Assessment Versus Change in Loading Condition*

In this study, bifurcation analysis for the AAEPS is performed to investigate the stability of the system when subjected to sudden change in power demand. This section is divided into two efforts. In the first one, the system operating at a normal condition for the power level at 20.2 kW has experienced a step increase in the load power to 45.6 kW at time $t_1=0.3s$. The time-domain simulation of voltage profiles at both HVDC and SG harmonics filter terminals are shown in Fig. 4.13 (a) and (b), respectively. As seen in both figures, the effect of sudden increase in power demand is compensated by a transient oscillatory response. Subsequently, the equilibrium solution of the system's characteristics equation may be identified as a hyperbolic stable node. By further investigation into the figures, one notices that the dominant eigenvalues of the system's Jacobian matrix should be located at a stable region on the LHP with negative real parts,

hence, the system under study maintains its stability against these kinds of variations in power level. In the second effort, we performed the same procedure as done before, except that the aircraft power system was subjected to a larger step increase in load power at the time t_2=0.2s, where the system has experienced a load power of 81.4kW. The phase plane orbit of the rectifier output voltage was captured for two periods of operation. The following graph in Fig. 4.14 (a), (b) shows that the system reached its first stability point near 270V and 80A. At time t_2=0.2s a sudden step increase in load power occurs, causing the system undergoes a transient periodic solution of oscillation, which damps down as time goes on. In that sense, dominant roots of the Jacobian matrix of the system's implicit equations achieve a new locations at LHP that guarantees returning of the system to another normal condition of operation at another equilibrium point at V_{dc}=270 V and I_{dc}=302 A. The oscillograms shown in part (a) and (b) of Fig. 4.14 validate this assessment.

(a)

(b)
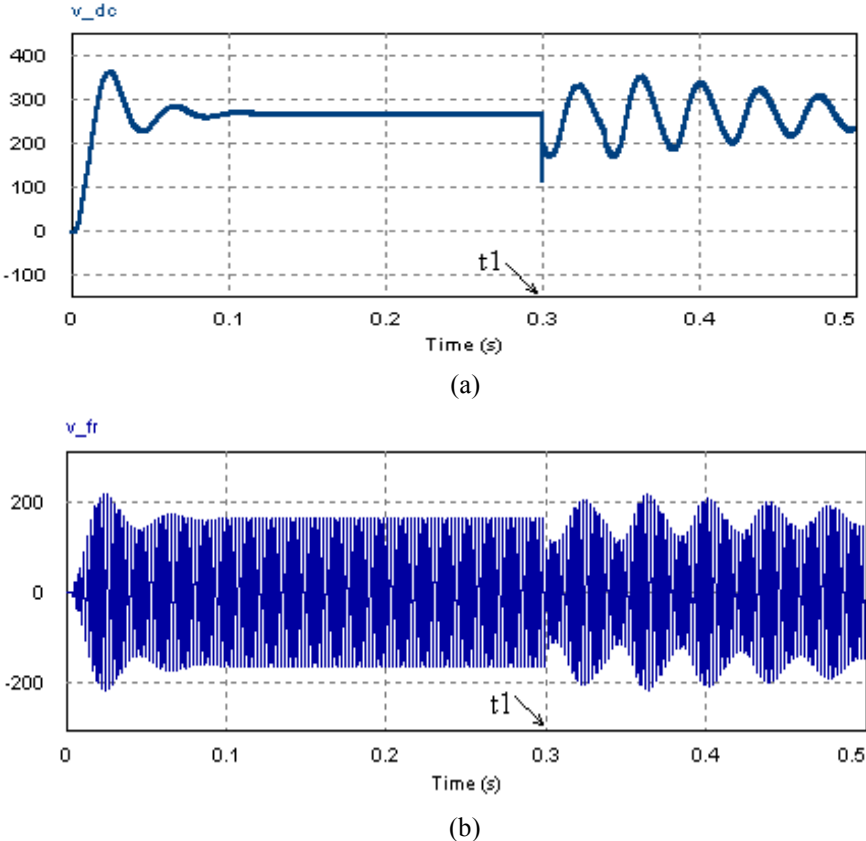
Fig. 4.13: System response to step change in load power (a) voltage at HVDC [Volts] (b) AC voltage at SG harmonic filter terminals [Volts]

96

The phase plane corresponding to the step increase in the power demand of the system is portrayed in Fig. 4.14 (c), (d), where in (c) dc voltage at the output ac/dc rectifier is plotted versus inductor's current at the same link.
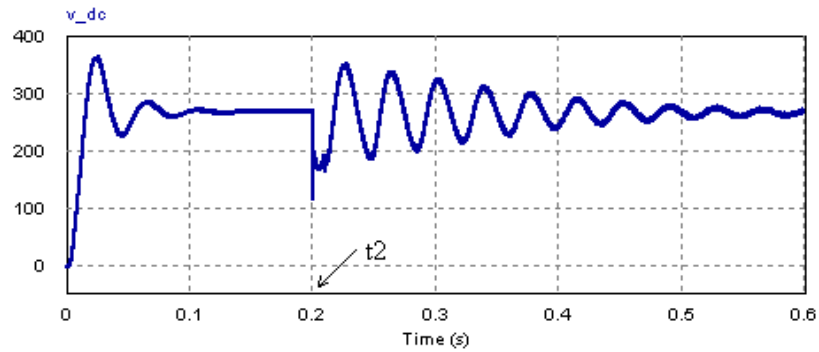
(a)
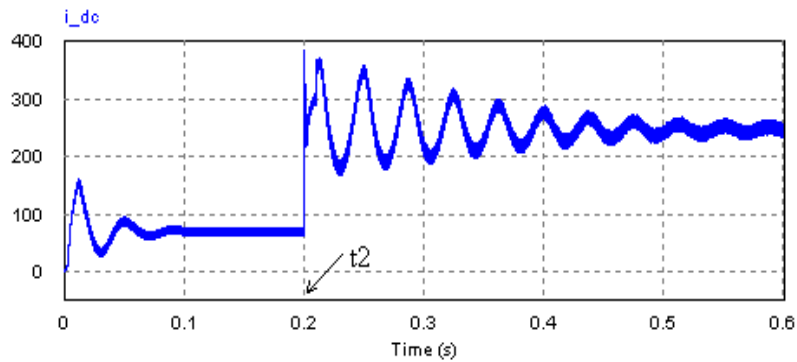
(b)
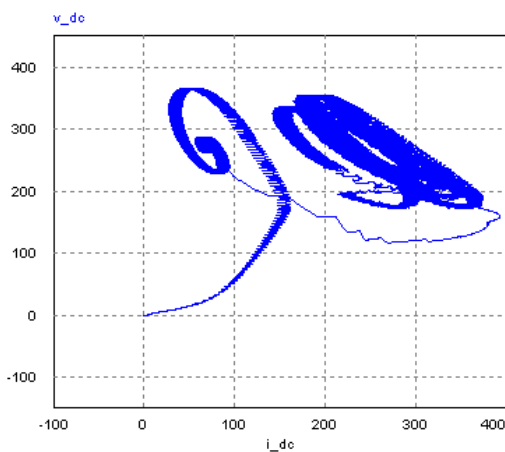
(c)
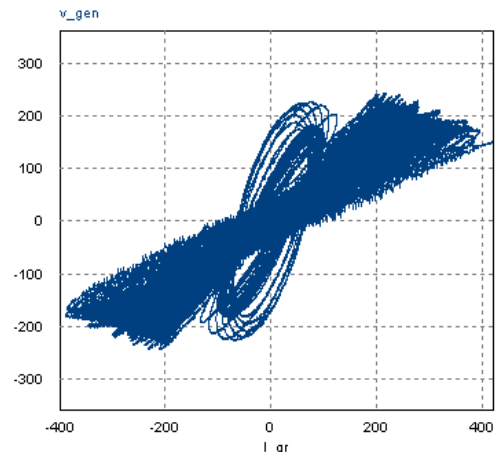
(d)

Fig. 4.14: System dynamics for the step change in power demand (a) voltage at HVDC link [Volts] (b) inductor's current at HVDC [Amps] (c) bifurcation diagram voltage vs current phase plane at HVDC (d) bifurcation diagram corresponding to phase plane at the SG harmonic filter terminal.

4. 4. 6 Bifurcation Analysis with Consideration of Ramp Increase in Load Power

This section presents a comprehensive analysis of the system considering a ramp increase in the loading profile as the bifurcation parameter. The time-domain computer simulations are obtained from PSIM9, and are presented in Fig. 4.15. As depicted in (a), the filter voltage at SG-side tolerates the ramp increase in power demand until the load power reaches the level of around 0.95pu (the base power is considered 110kW) where the system gradually falls into a pure oscillatory behavior. This means that by increasing the load power some eigenvalues in the system Jacobian matrix approach the imaginary axis, cross it and goes into the RHP. The emergence of pure imaginary components in the corresponding Jacobian matrix eigenvalues is translated as Hopf bifurcation in the system dynamics.

However, further increase in power rating may lead to total instability of the system as the dominant poles may move to unstable node regions in the RHP. The phase plane orbits for the rectifier output voltage against the output current and power are shown in Fig. 16. The voltage reaches a stability point after the transition where the current reaches around 200A. As time elapses, a transient period of oscillation occurs with a further increase in the current, indicating a region of purely imaginary complex roots. The voltage again reaches a new stability point, but later becomes completely chaotic. The four oscillograms corresponding to the system's dynamics under variation of load power in a form of ramp increase are illustrated in Fig. 4.16.

The voltage instability at both ac and dc side of the aircraft electric network can be attributed to the magnetic core saturation of the 3-phase synchronous generator. In other words, to compensate the voltage drop at the main ac power bus due to over drawn of the load power, the excitation current should magnify the magnetization property of the SG's stator. Since, the hysteresis graph corresponding to the SG's stator has two region of operation (linear and saturation), increasing in power demand may cause the generating system to fall into saturation region, leading the instability as we discussed earlier and the related graphs are presented in Fig. 4.15 and Fig. 4.16.
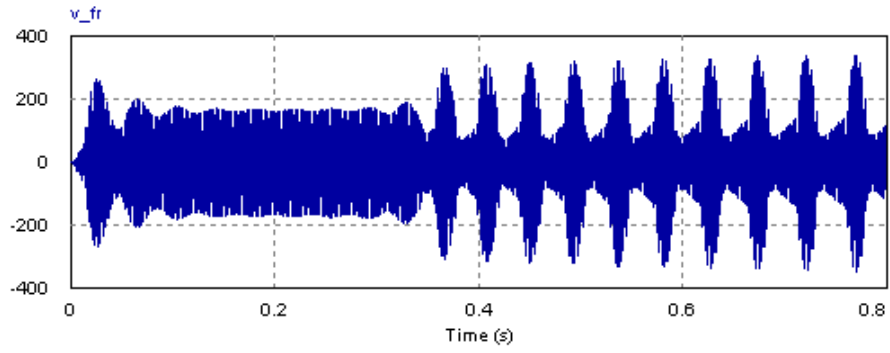
(a)
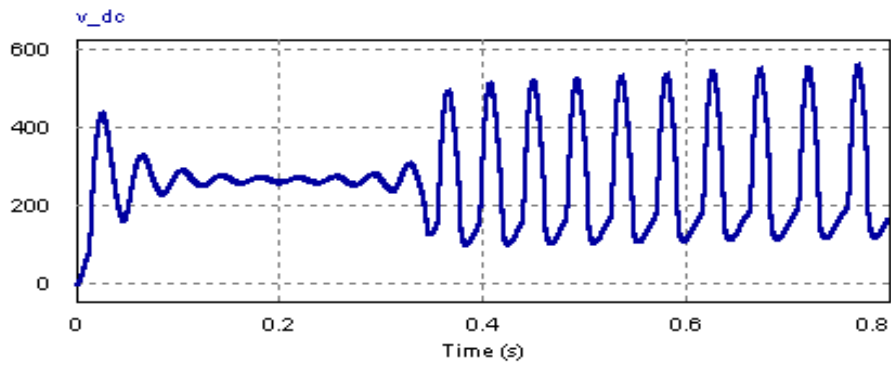
(b)
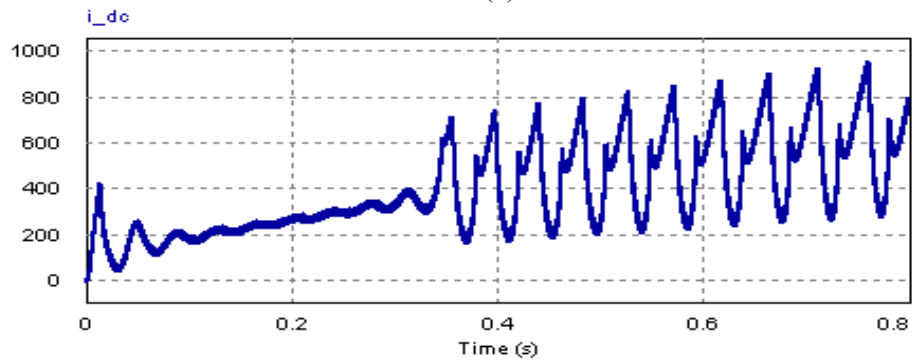
(c)
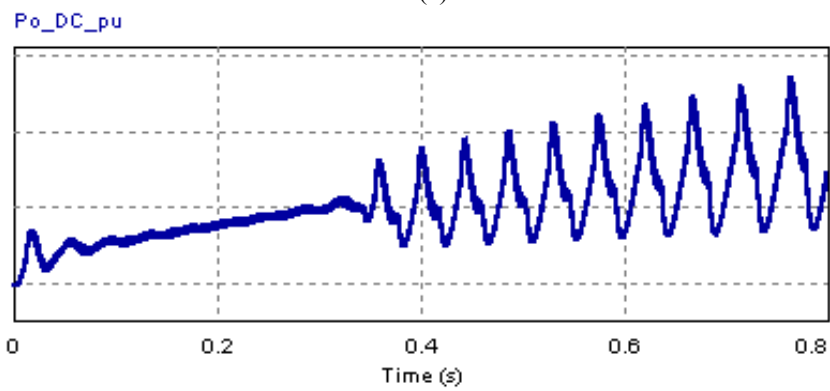
(d)

Fig. 4.15: Computer simulation in PSIM9 environment (a) SG filter's voltage (b) voltage at HVDC (c) inductor's current at HVDC link (d) load power delivered by 12-pulse power supplier.

(e)   (f)

(g)   (h)
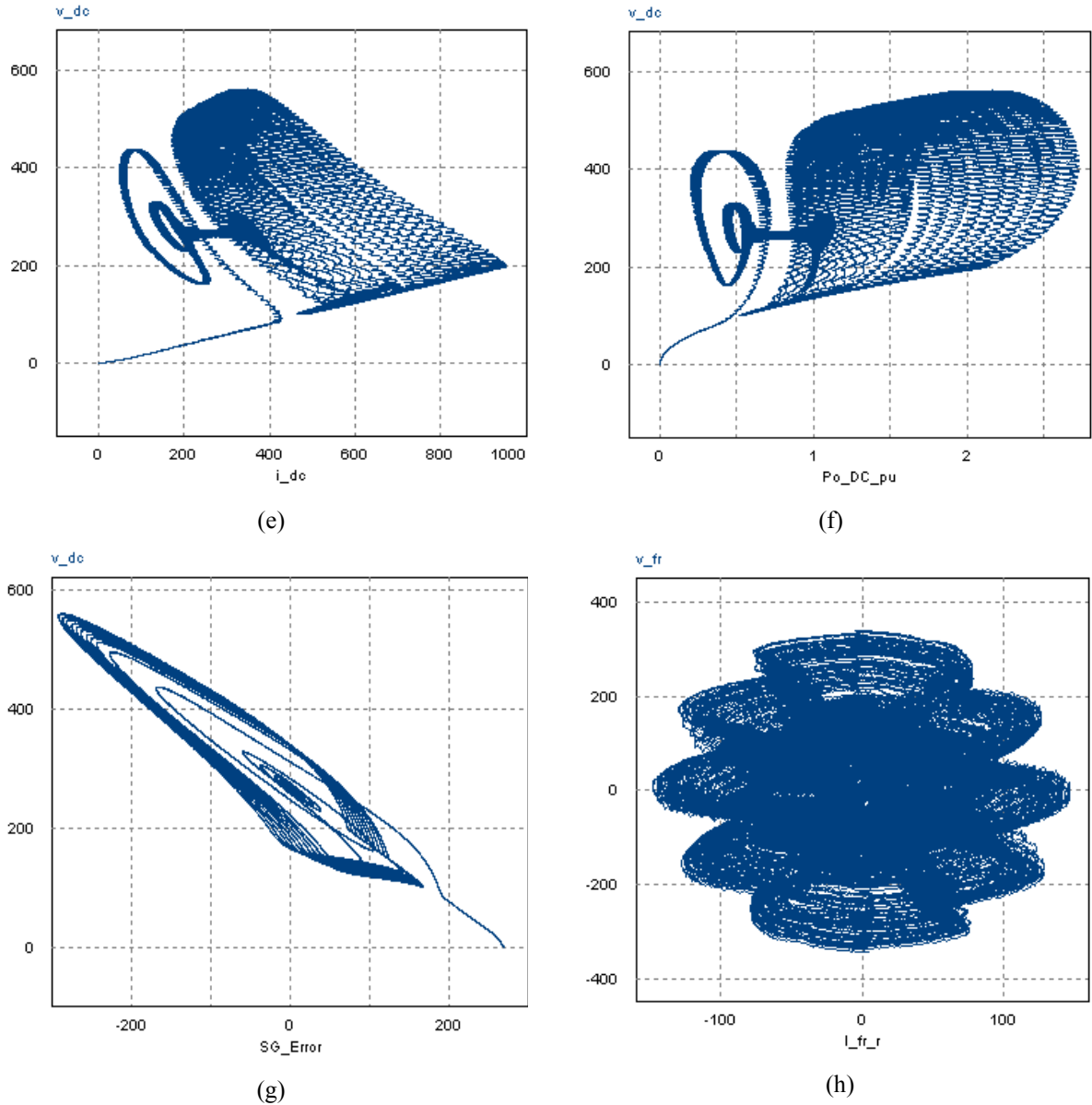
Fig. 4.16: Bifurcation diagrams for 12-pulse rectifier dc output voltage [Volts] versus (e) dc-link current [Amps] and (f) power demand [pu] (g) SG error signal. The phase diagram corresponding to the SG harmonic filter voltage [Volts] versus current [Amps] is illustrated in (h).

4.4.7 *Variation in the Main AC Bus Frequency Due to Change in the SG Engine Speed*

In this section, we investigated the performance characteristics of the aircraft system when subjected to a ramp variation in the operating frequency. Because of passive filters used at the SG main ac bus which are tuned for cancellation of harmonic components with particular values, there is a possibility of system's instability due to

change in the fundamental operating frequency, which causes the system to fall into resonance or even collapse. Fig. 4.17 (a), (b) demonstrates system stability under the consideration of SG frequency as a varying parameter. As shown in the figures, due to ramp increase in SG frequency, the voltage at both dc and ac side remains stable until the frequency reaches around 2.385 kHz. Since then we notice that voltage collapse occurs in the system, leading to a full instability in the aircraft electric network.
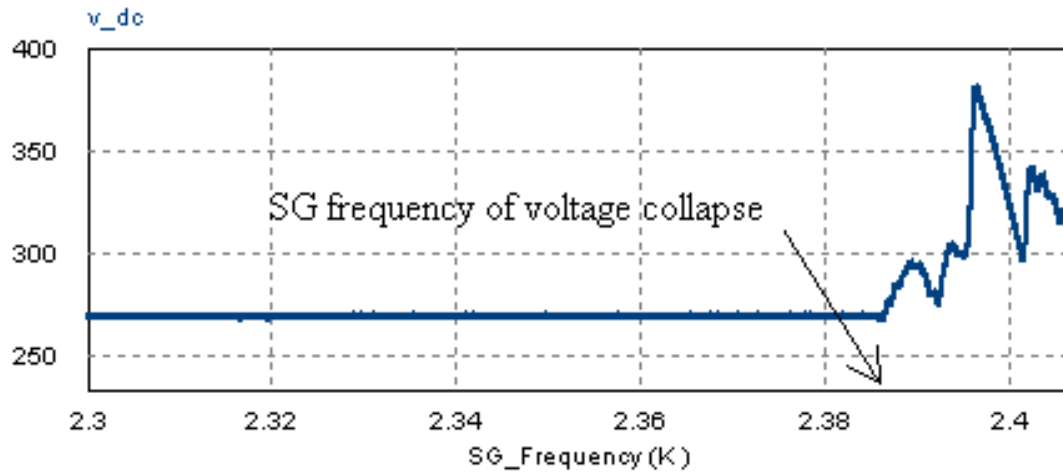
(a)
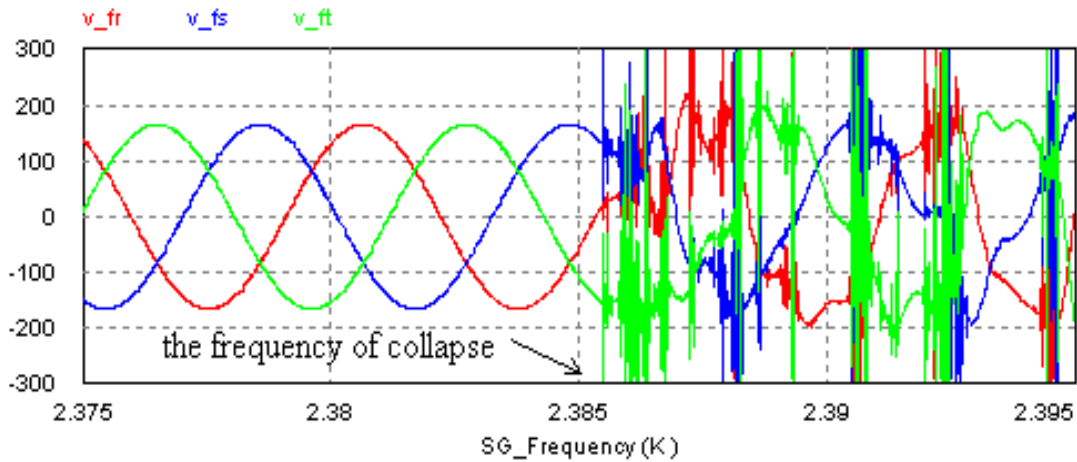
(b)

Fig. 4.17: System stability respect to variation in the operating frequency [kHz] (a) voltage [Volts] at the main dc-link (b) three-phase voltage [Volts] profile at the harmonics filter terminals

4.4.8 *Stability Problem of the 12-Pulse VSI Interacting with AC Dynamic Load*

In this section, the stability problem of the 12-pulse Sinusoidal Pulse Width Modulation (SPWM) inverter interconnected with a three-phase induction machine (IM), as representative of an ac dynamic load is addressed. The transient and steady-state performance of the system at Constant Frequency (CF) main ac bus (main load bus with 115Vrms/400Hz) is addressed. In modeling and control of the 12-pulse inverter under investigation, the sinusoidal pulse width modulation (SPWM) technique is widely used for output voltage and frequency regulation of the system at ac bus. In this case study a simple PI control approach has been employed for the voltage and frequency regulation purposes. In order to measure the stability margin of the system for secure operation, we have considered the proportional coefficient (K_p) of the PI unit as a variable parameter or bifurcation parameter. The dynamic behavior of the system when interconnected with an ac dynamic load (IM) is assessed for two case studies.

In the first case, the stability analysis is performed while no variation is considered for the PI parameters (K_p and K_i remain unchanged). As shown in Fig. 18, the system is initially operating in its stable region where the dominant pole of the system is located at the imaginary axis. Since the IM has a dynamic nature, the input/phase current undergoes a transient change, which is equal to gradual decrease in the input current's amplitude, as depicted in the same figure in column (b). This transition also results to an improvement in the power factor (PF) of the new operating point, where the system has reached a steady-state. The phase plane demonstrated in Fig. 4.18 (a) would better picture the mentioned transition.

As depicted in Fig. 18 (b), the IM input current during transition is apparently higher than the absorbed current during steady-state operation. Also, the initial absorbed power turns out to be more reactive. Though as time elapses, the delivered power turns to be active and the corresponding factor (PF) of the system approaches to unity (shown in the phase plane graph in Fig. 18 (a)
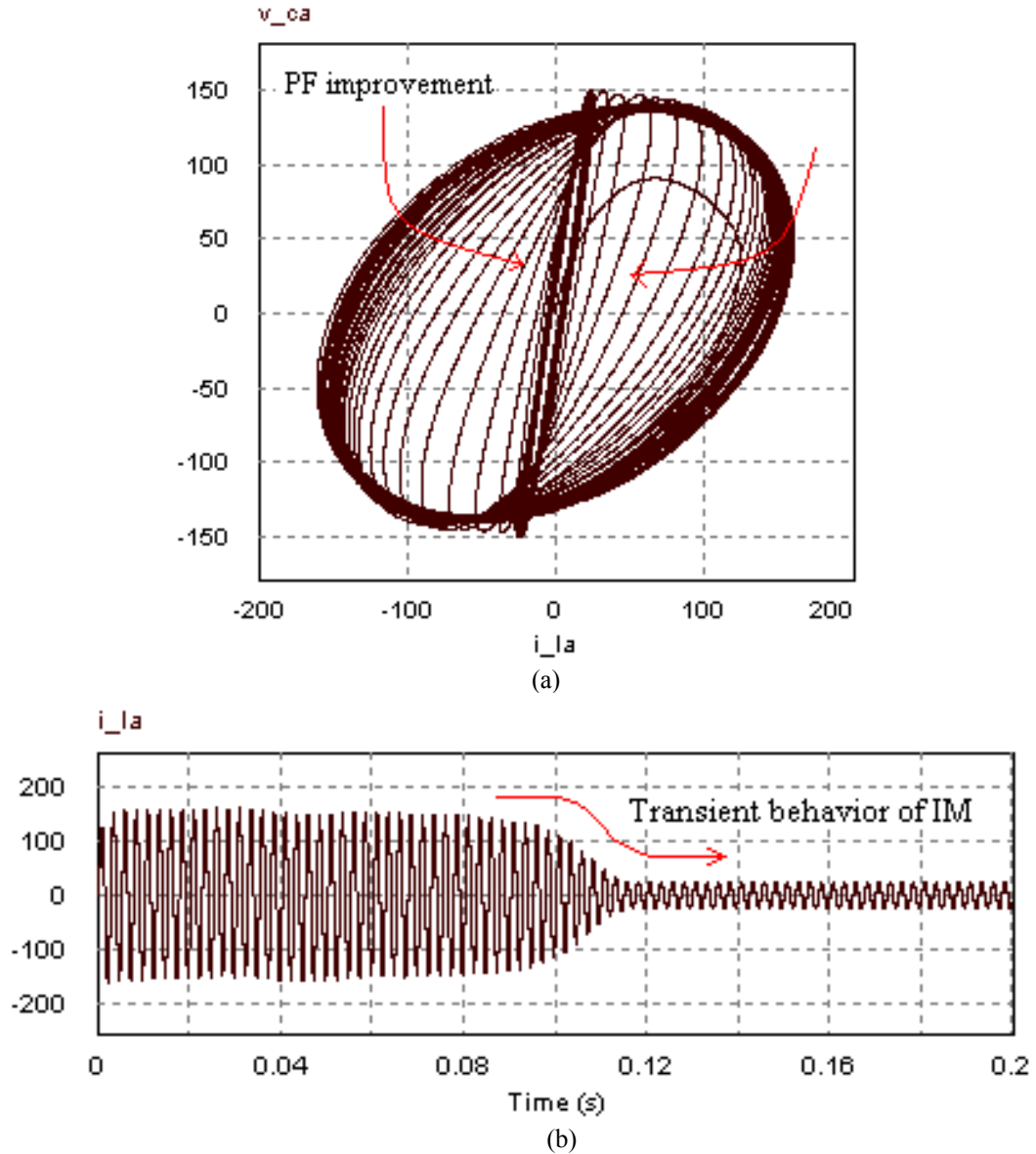
Fig. 4.18: The transient performance of the inverter system (a) phase portrait corresponding to the main CF ac bus, voltage [Volts] vs current [Amps] (b) time-domain waveform associated with input current of the IM [Amps]

Fig. 4.19 (a), (b) represents the performance characteristics of the system where the proportional coefficient (K_p) is subjected to a ramp increase. Depicted in Fig. 4.19 (a) is the phase input current of the IM. Further investigation into the magnified view of the same graph, it is noted that the system is initially operating in a normal condition where the equilibrium solution of the system's eigenvalues are located in a stable region with a pure oscillatory characteristic. As K_p increases, it turns out that the dominant eigenvalue of the Jacobian matrix corresponding to the inverter system moves to an unstable region

in RHP, leading to a sub-synchronous resonance in the voltage and current profile of the ac main bus, as demonstrated by the phase portrait in Fig. 4.19 (b).
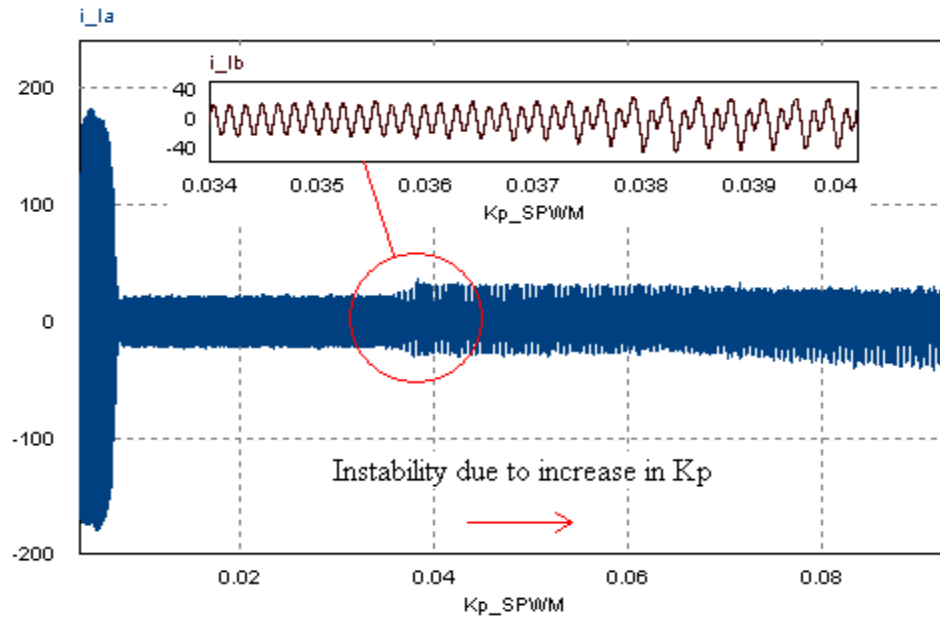
(a)
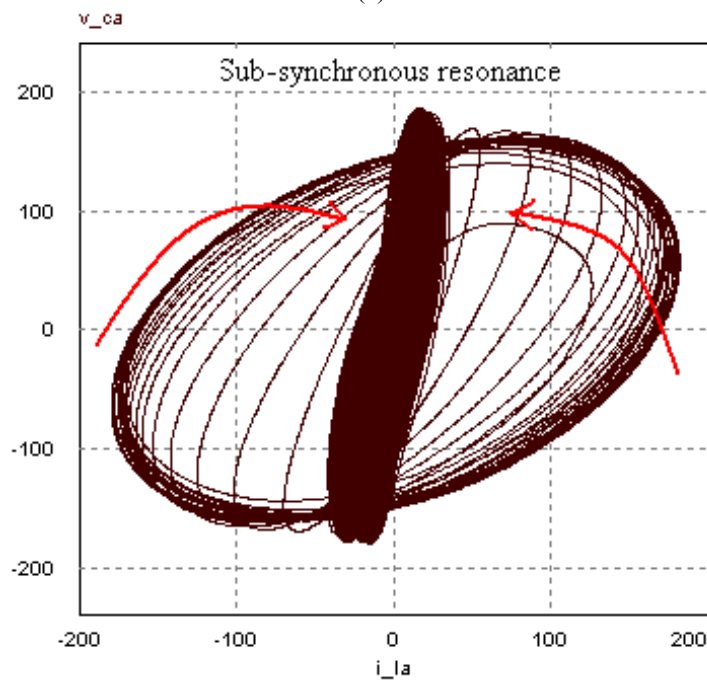
(b)

Fig. 4.19: System dynamic vs change in the bifurcation parameter (a) current waveform associated with input profile of the IM [Amps] (b) phase portrait corresponding to phase voltage [Volts] vs current [Amps] at the main ac bus

TABLE. 4.1
VSCF-main generating system parameters

Description	Parameter	Value
Synchronous Generator		
stator resistance	R_s	0.001Ω
stator inductance	L_s	$0.0051mH$
d-axis mag. inductance	L_{dm}	$0.1mH$
q-axis mag. inductance	L_{qm}	$0.1mH$
field resistance	r_f	0.05Ω
field leakage inductance	L_{fl}	$0.1mH$
damping cage resistance	R_{dr}	0.1Ω
damping cage inductance	L_{drl}	$0.05mH$
damping cage resistance	R_{qr}	0.01Ω
damping cage inductance	L_{qrl}	$0.05mH$
transformation ratio	N_s/N_f	3
parasitic resistance	r	0.05Ω
parasitic inductance	l	$46pH$
parasitic capacitance	c	$46pF$
operating frequency	f_{SG}	400-800Hz
shaft speed	ω_{sh}	8000-16000rpm
moment of inertia	J	$0.1kg.m^2$
number of poles	N_{SG}	6
Transmission Line		
line resistance	R_{g-l}	0.081Ω
line inductance	L_{g-l}	$10\mu H$
Transformer Rectifier Unit (TRU)		
primary resistance	R_p	0.001Ω
secondary resistance	R_s	0.001Ω
tertiary resistance	R_t	0.001Ω
primary leakage inductance	L_p	$10\mu H$
secondary leakage inductance	L_s	$10\mu H$
tertiary leakage inductance	L_t	$10\mu H$
magnetizing inductance	L_m	$0.1H$
primary turns ratio	N_p	1.0
secondary turns ratio	N_s	1.0
tertiary turns ratio	N_t	1.73205
bridge diode resistance	R_d	0.001Ω
Synchronous Generator-side Harmonics Filter		
filter resistance	r_f	0.05Ω
filter inductance	L_{fl1}	$15.915\mu H$
filter capacitance	C_{fl1}	$82.373\mu F$
filter inductance	L_{fl3}	$15.915\mu H$
filter capacitance	C_{fl3}	$58.977\mu F$

TABLE. 4.2
AC/DC dynamic loads parameters

Description	Parameter	Value
Constant Voltage Buck Converter		
filter series resistance	r_v	0.002Ω
filter series inductance	L_v	$15\mu H$
filter capacitance	C_v	$1.5mF$
power rating	P_{CV}	$5.6kW$
PWM frequency	f_{CV}	$15kHz$
PI parameters	K_p, K_i	0.005, 0.0001
Constant Current Buck Coverter		
filter series resistance	r_c	0.005Ω
filter series inductance	L_c	$100\mu H$
filter capacitance	C_c	$1mF$
power rating	P_{CC}	$20kW$
PWM frequency	f_{CC}	$10kHz$
PI parameters	K_p, K_i	1.5, 0.0001
Constant Power Buck Converter		
filter series resistance	r_p	0.002Ω
filter series inductance	L_p	$25\mu H$
filter capacitance	C_p	$0.5mF$
power rating	P_{CP}	$10kW$
PWM frequency	f_{CP}	$20kHz$
PI parameters	K_p, K_i	1.5, 0.0001
12-pulse Voltage Source Inverter		
operating frequency	ω_i	$400Hz$
filter series resistance	R_f	0.01Ω
filter series inductance	L_f	$20\mu H$
filter capacitance	C_f	$100\mu F$
passive load resistance	R_L	2Ω
passive load inductance	L_L	$0.4mH$
Y-Y-Δ transformer leakage resistance	R_{lk}	0.001Ω
Y-Y-Δ transformer leakage inductance	L_{lk}	$10\mu H$

4. 5 Summary

In this article a comprehensive analysis of the detailed AAEPS dynamics was studied using bifurcation theory, using a multi-variable parameter approach. The combination of mathematical concepts associated with the system's stability profile along with the real-time simulation give improved knowledge of the system dynamic performance under various conditions, as well as possible problems coming from the variation of system parameters. For instance, by applying bifurcation analysis and using the corresponding diagrams, it is possible to determine the specific values of the

parameters where the system equilibrium becomes unstable due to Hopf bifurcation, and also to determine the stability margins of the associated oscillation.

Furthermore, the state space averaging variables as representation of the reduced-order system are utilized to characterize the stability performance of the system via differential algebraic equations. Also, it was demonstrated that bifurcation analysis with consideration of varying parameters brings additional information such as the location of system equilibrium points which is required for a highly reliable design. Finally, the robustness of the system profiles against variations of control parameters was reported in this thesis.

Chapter Five

Power Quality of AAEPS with Non-linear Loading

5. 1 Chapter Overview

This Chapter outlines power quality assessment of the aircraft electric power system. In this study, a comprehensive model of variable-speed, constant-frequency (VSCF) aircraft electric power system (AEPS) with a number of nonlinear loads is developed. The model is used to study the performance of the system under different nonlinear loading conditions. The performance of the VSCF AEPS is studied over the entire range of the aircraft electric power system operating frequency. Moreover, the model is extended to study the performance of the AEPS under nonlinear loading along with harmonic cancellation. Both transient and steady-state performance characteristics of the system are obtained and investigated. The effect of nonlinear loading on power quality of the AEPS is also investigated and compared to applicable aircraft electric power system's IEEE and military standards.

Due to a widespread use of computerized and power electronic components in modern aircraft, the quality of delivered power is becoming increasingly important, hence considered as a major concern in reliable systems [92]. The quality of electric power supply in an AEPS is considered as a significant issue in relation with the loads that are sensitive to power quality. In fact, poor power quality causes undesired disturbances leading to malfunction of the electric grid, or even loss of some loads which is not acceptable in aerospace applications. Hence, there are some commercial pressures to ensure adequate power quality (where minimum requirements are met). Also, IEEE/military standards are set in place to define the maximum permissible distortion levels [31].

As mentioned earlier, switching-mode power suppliers, also defined hereby as multi-converter power electronics in the VSCF-AAEPS are the main source of distortion or harmonics in the system. Conventional aircraft power systems use constant frequency (CF) 400 Hz ac power distribution produced by so-called integrated drive-generators (IDG) [93].

The CF system has been replaced on new commercial passenger airplanes by VSCF electric structures in order to eliminate the maintenance-intensive IDG. Currently, More Electric Aircraft (MEA) technology is also being adopted, in which many functions that are traditionally operated by hydraulic, pneumatic, or mechanical power are electrified in order to reduce size and weight and improve fuel efficiency [94]. This has resulted in the use of large number of motor drives for such functions as fuel pumping, cabin pressurization and air conditioning, engine start, and flight control actuation, making power electronics an indispensable part of MEA technologies [94]. In order to obtain constant frequency voltage and current waveforms from the variable-speed drives, the use of multi-converter becomes mandatory. A significant portion of the modern aircraft system power is composed of power electronic circuits. Therefore, harmonic distortion on the main power bus of the synchronous generator (SG), as well as other switching terminals turns out to be a critical problem for MEA. Fig. 5.1 represents a schematic view of a single-channel interconnected power electronic system in the AAEPS model proposed by [45]
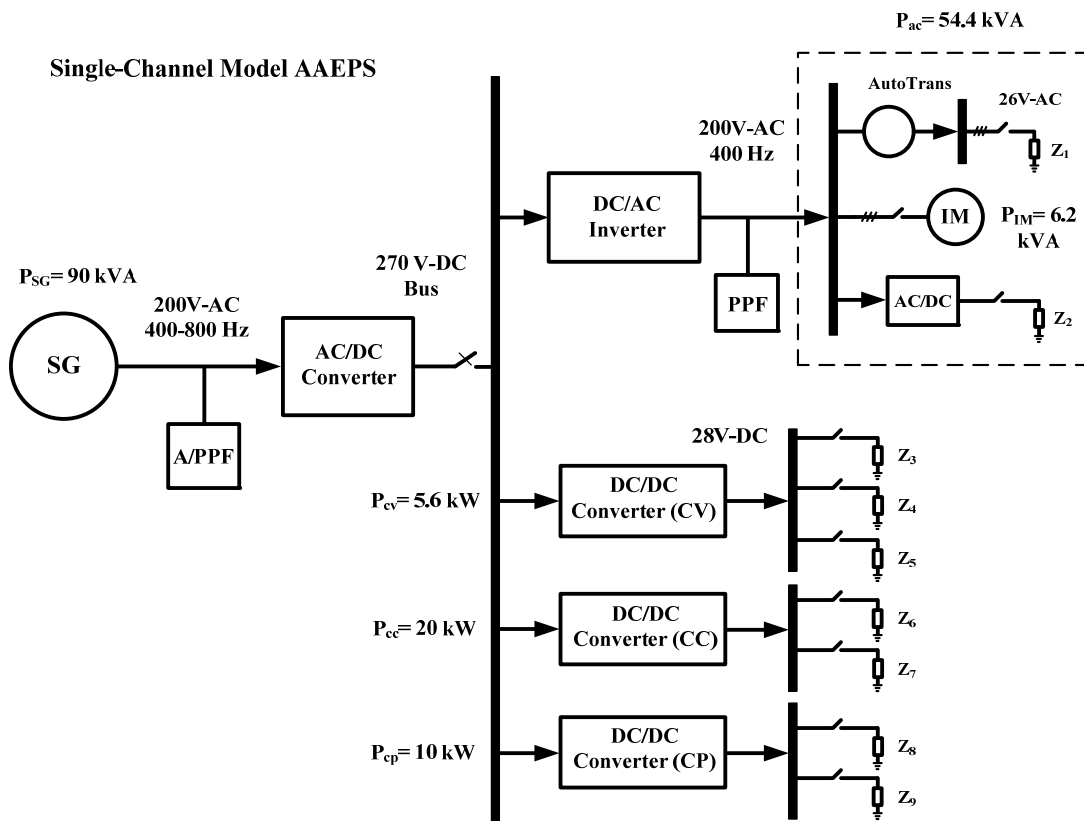
Fig. 5.1: Circuit representation model of the MEA integrated power electronic system.

Fig. 5.1 demonstrates a conceptual VSCF power system highlighting the use of various kinds of rectification power electronics at different major nodes on the power bus. This electric structure would better demonstrate the main source of harmonic components in the AAEPS.

5. 2. Power Quality Measurement in Terms of Total Harmonic Distortion

Multi-pulse switching converters act as non-linear loads, drawing a distorted current waveform that contains harmonics. Harmonic waveforms are recognized as Fourier representations of the original signal at one fundamental frequency. Subsequently, the amplitude and frequency of the distorting signals can be estimated based on the number of switching pulses and harmonic order. Due to a broad application of switching mode power supplier in the AAEPS, the generated harmonic distortion caused by those non-linear components is of major concern. These harmonics can cause problems ranging from communication transmission interference to degradation of conductors and insulating material in motors and transformers. Therefore it is important to gauge the total effect of these harmonics. The summation of all harmonics in a system is known as total harmonic distortion (THD). This Chapter will attempt to investigate the level of THD in the developed aircraft electric network. Moreover, the performance of the aircraft electric grid is studied in this section while using harmonic filter under different loading condition. It has been demonstrated that active filtering (AF) can be used to more effectively reduce the level of distortion in the grid. Let us first define the basic concept of THD (or THD%) as follows

Assume a voltage/current waveform with the fundamental component H_1 at the frequency f_1. Now harmonics have frequencies that are integer multiplies of the waveform's fundamental frequency. Hence, 2nd, 3rd, 4th,…order harmonics (if available) are given as H_2, H_3, H_4, …Therefore, total harmonic distortion, or THD, is the summation of all harmonic components of the voltage or current waveform compared against the fundamental component of the voltage or current waveform as follows:

$$THD\% = \sqrt{\frac{H_2{}^2 + H_3{}^2 + H_4{}^2 + \cdots}{H_1{}^2}} \qquad (136)$$

Harmonics have existed in power systems from the time of the first generators have been invented. However, less attention was paid to harmonic distortion, because the distortion components were so small that their effects on systems were negligible. This was due to the lack of non-linear loads before the 1960s [103].

5. 3 Importance of Harmonic Mitigation in AAEPS

Harmonic distortion can have some potentially negative effects on aircraft electrical equipment. Unwanted distortion in the current through power system can result in higher temperature in neutral conductors and distribution transformers. Also, high frequency distortion may cause additional core loss in motors due to "eddy effect" currents, which result in excessive heating. Increased temperatures can substantially shorten the life of electronic equipment and cause serious damage to power systems. Additionally, these higher-order harmonics may interfere with communication systems.

5. 4 Methods of Harmonics Cancellation in AAEPS

In order to reduce the level of harmonics generated by non-linear loads two methods of filtering have been conventionally suggested: 1) passive power filtering (PPF), and: 2) active power filtering (APF). Depending on application and level of sensitivity of the system, each of these mentioned techniques may be utilized. In our study model developed in this Chapter both methods have been employed for power quality improvement. For harmonic suppression at the variable frequency (VF) main ac bus, we have installed both shunt PPF and APF for separate case studies and the level of distortion with and without harmonic filters have been measured. Also, the collected data have been used to provide a comparison between two methods of filtering and assess the effectiveness of each method in reducing harmonic level in the grid.

5. 4. 1 Harmonics Reduction using PPF

Depicted in Fig. 5.2 is the circuit representation of a single-channel VF main bus corresponding to AAEPS under study. In this picture, a band pass filter (BPF) is tuned to the current harmonics generated by 12-pulse diode rectifier for the harmonics of 11th and 13th order of the fundamental component.
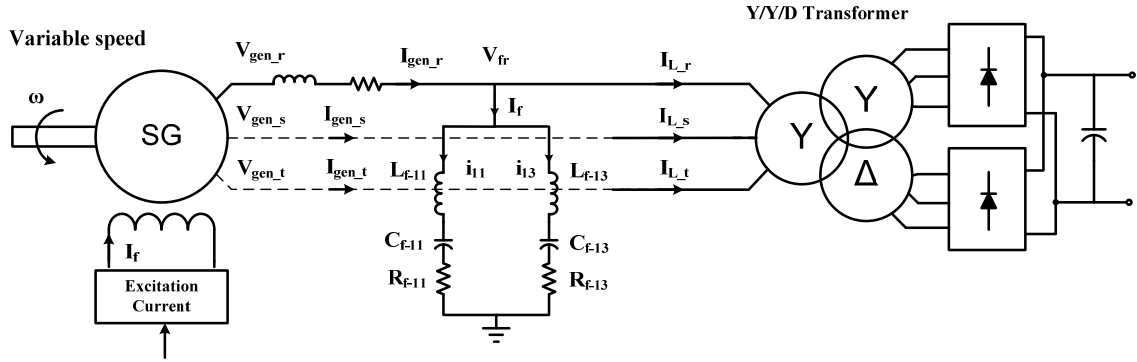
Fig. 5.2: Schematic view of the VF synchronous generator main bus with shunt PPF.

The shunt passive filter shown in above figure performs based on tuned reactance elements (LC) to filter distortion contents at the 11th and 13th of the fundamental frequency. A switching converter with P pulses per switching cycle can generate harmonics with following multiplies of the fundamental frequency (in Fig. 5.2 P=12 and k=1, 2, 3…).

$$h = kP \pm 1 \tag{137}$$

To remove distortion generated by switching rectifier and dynamic loads, we have designed a second-order BPF (RLC type). For a variable-frequency operating system, we have considered all distortion components that are multiplies of fundamental frequencies in a range of 400-800Hz. Hence, we have calculated the values for L and C in each branch of shunt passive filter considering corner frequency for each particular case, so that it guarantees all harmonics components (multiplies of 11th and 13th of fundamental frequency) and even higher orders will be mitigated. We have installed a modular package of BPF including five branches where each has been regulated to neutralize the 11th order harmonic of the fundamental frequency (400, 500, 600, 700 and 800Hz). We have also designed a low pass filter to be connected at the output terminals of the 12-pulse voltage source inverter (VSI) at the 200-Vrms main bus (before ac loads) to mitigate harmonic generation by PWM switching action of the inverter. The following differential equations describe the dynamics of the band pass filter designed for harmonics cancellation of the main ac generating bus.

$$\begin{cases} L_{f11}\dfrac{d^2 i_{f11}}{dt} + R_{f-11}\dfrac{d i_{f11}}{dt} + \dfrac{1}{C_{f11}} i_{f11} = \dfrac{dV_{fr}}{dt} = \\[2mm] \qquad L_{f13}\dfrac{d^2 i_{f13}}{dt} + R_{f-13}\dfrac{d i_{f13}}{dt} + \dfrac{1}{C_{f13}} i_{f13} \\[2mm] \qquad i_{f11} + i_{f13} = I_{fr} = I_{gen-r} - I_{L-r} \end{cases} \qquad (138)$$

where L_{f11}, C_{f11} and L_{f13}, C_{f13} represent the inductors and capacitors of each branch in the BPF tuned for harmonic mitigation. Currents i_{f11}, i_{f13} are the filter currents correspond to the order of 11th and 13th of the reference current. Also, R_{f-11} *and* R_{f-13} represent the filter's resistances tuned for each branch. Eq. (138) can be rearranged in the form of a differential state-space equation given by (139)

$$\begin{bmatrix} \dot{x}_1 \\ \dot{x}_2 \\ \dot{x}_3 \\ \dot{x}_4 \end{bmatrix} = \begin{bmatrix} 0 & 1 & 0 & 0 \\ \dfrac{-1}{L_{f11}C_{f11}} & \dfrac{-R_{f11}}{L_{f11}} & 0 & 0 \\ 0 & 0 & 0 & 1 \\ 0 & 0 & \dfrac{-1}{L_{f13}C_{f13}} & \dfrac{-R_{f13}}{L_{f13}} \end{bmatrix} \begin{bmatrix} x_1 \\ x_2 \\ x_3 \\ x_4 \end{bmatrix} + \begin{bmatrix} \dfrac{1}{L_{f11}} \\ \dfrac{-R_{f11}}{L_{f11}^2} \\ \dfrac{1}{L_{f13}} \\ \dfrac{-R_{f13}}{L_{f13}^2} \end{bmatrix} V_{fr} \qquad (139)$$

where $x_1 = i_{f11}$ and $x_3 = i_{f13}$ represent the state variables describing the system dynamics. Eq. (139) also can be represented in the form of a general state-space equation describing the harmonic filter characteristics as follows

$$\dot{x} = \Psi v + \Gamma u \qquad (140)$$

Where the state vector x is given by (141), and I_{fr} can be approximated accordingly

$$v = \begin{bmatrix} x_1 \\ x_2 \\ x_3 \\ x_4 \end{bmatrix}, I_{fr} = x_1 + x_3 \qquad (141)$$

In Table 5.1 we have represented filter parameters for each corner frequency. The values are chosen based on the fact that in one hand harmonic distortions for that particular operating frequency should be suppressed, on the other hand, filter branches would never go into resonance or instability region in regards of the ac bus transmission line parameters (R, L).

Table. 5.1: PPF parameters

Filter Parameters	Corner Frequencies									
	$f_{c1\text{-}11}$	$f_{c1\text{-}13}$	$f_{c2\text{-}11}$	$f_{c2\text{-}13}$	$f_{c3\text{-}11}$	$f_{c3\text{-}13}$	$f_{c4\text{-}11}$	$f_{c4\text{-}13}$	$f_{c5\text{-}11}$	$f_{c5\text{-}13}$
	4400	5200	5500	6500	6600	7800	7700	9100	8800	10400
$R_f (\Omega)$	0.02	0.018	0.019	0.017	0.016	0.015	0.015	0.014	0.014	0.013
$L_f (uH)$	15.91									
$C_f (uF)$	82.37	58.88	52.63	37.68	36.55	26.17	26.85	19.23	20.56	14.72

5. 4. 2 Harmonics Reduction with Shunt APF

Passive filters have traditionally been utilized to attenuate the harmonic distortion and compensate reactive power. They are economically efficient and, because of their simplicity in design and operation, they are alternative to electrical engineers. However, passive filters are bulky, detune with age, and can resonate with the supply impedance if not properly designed. Fixed compensation is also considered as another drawback of this type of filter [95]. The use of active power filters (APF) is widely recommended and practically employed as a more flexible and dynamic means of power conditioning. Though APFs were introduced in 1970, extensive literature has recently appeared on developing new algorithms for reference signal generation and controlling of the device. Active power filters are expected to generate the appropriate compensating signals that cancel out the existing harmonics and reactive power components in the voltage/current waveforms from the mains. The reference compensation signals are also generated by making use of a control algorithm. There are several methods used for reference signal generation, including;

A. **Analog Filters**: Passive filters such as band-pass filters and low-pass filters are used to detect the harmonics (reference signal) [96,97]. The issue with applying this technique is that the obtained components have magnitude and phase errors.

B. **Fourier Transform Technique**: By development of digital signal processors (DSPs) and microcontrollers, the use of discrete algorithms became more and more popular. Fast Fourier Transform (FFT) and Discrete Fourier Transform

(DFT) methods were studied and used accordingly by designers [98,99,100]. However, the delay of one complete cycle is unavoidable in these algorithms, hence leading to instability in some cases. Therefore, these methods are suitable for slowly-conditions.

C. **Other Methods:** Fuzzy control approach, adaptive technique, and Kalman filtering are the other methods of reference signal generation that have better dynamic performance compared to FFT or DFT, however, these types of algorithm demand a considerable amount of calculation which reduces the operational speed of the filter. Also, software implementation of digital signal filters is recommended as a replacement for analog filters, however, the instability issue due to delay in reference signal generation with analog filters still remains.

5. 4. 3 Perfect Harmonics Cancellation (PHC) Method

In order to avoid the concerns of using above mentioned strategies for harmonic mitigation at the main ac bus of the AAEPS, the PHC control method is adopted in this study to generate the required compensation current for the shunt APF. This control strategy is divided in two separate stages, in the first stage, the reference current is predicted in a manner that the generator current be in phase with the fundamental positive sequence voltage component at the point of common coupling (PCC). This can be achieved by using the mathematical equations as following

Assuming the load power P_L provided by the synchronous generator (SG) of the advanced aircraft (shown in Fig. 5.2) is given by

$$P_L = V_{gen-r}(t)I_{L-r}(t) + V_{gen-s}(t)I_{L-s}(t) + V_{gen-t}(t)I_{L-t}(t) \qquad (142)$$

where the set of voltages at PCC are V_{gen-r}, V_{gen-s}, V_{gen-t} and I_{L-r}, I_{L-s}, I_{L-t} introduce the loading line currents (either for a balance or unbalance system) through the transformer rectifier unit (TRU). Hence, the calculated power can be represented with mean and oscillatory components as follows

$$P_L = \overline{P_L} + \widetilde{P_L} \qquad (143)$$

In Eq. (143), if a 3-phase balanced system is under consideration, then the oscillatory part of the power ($\widetilde{P_L}$) will be set to zero. Moreover, bringing the reference current in phase with the positive sequence of voltage component (V) at PCC yields

$$I_{ref} = K * V \tag{144}$$

rearranging the load power supplied by the SG in (142), one comes to Eq. (145) as follows

$$P_L = K * V^2 \tag{145}$$

also, the constant K can be determined by using the mean value of the instantaneous active power of (145) given by

$$K = \frac{\overline{P_L}}{V^2{}_r + V^2{}_s + V^2{}_t} \tag{146}$$

where V_r, V_s, V_t are the positive sequence of the voltage components at PPC derived by Phase Lock Loop (PLL) technique [101].
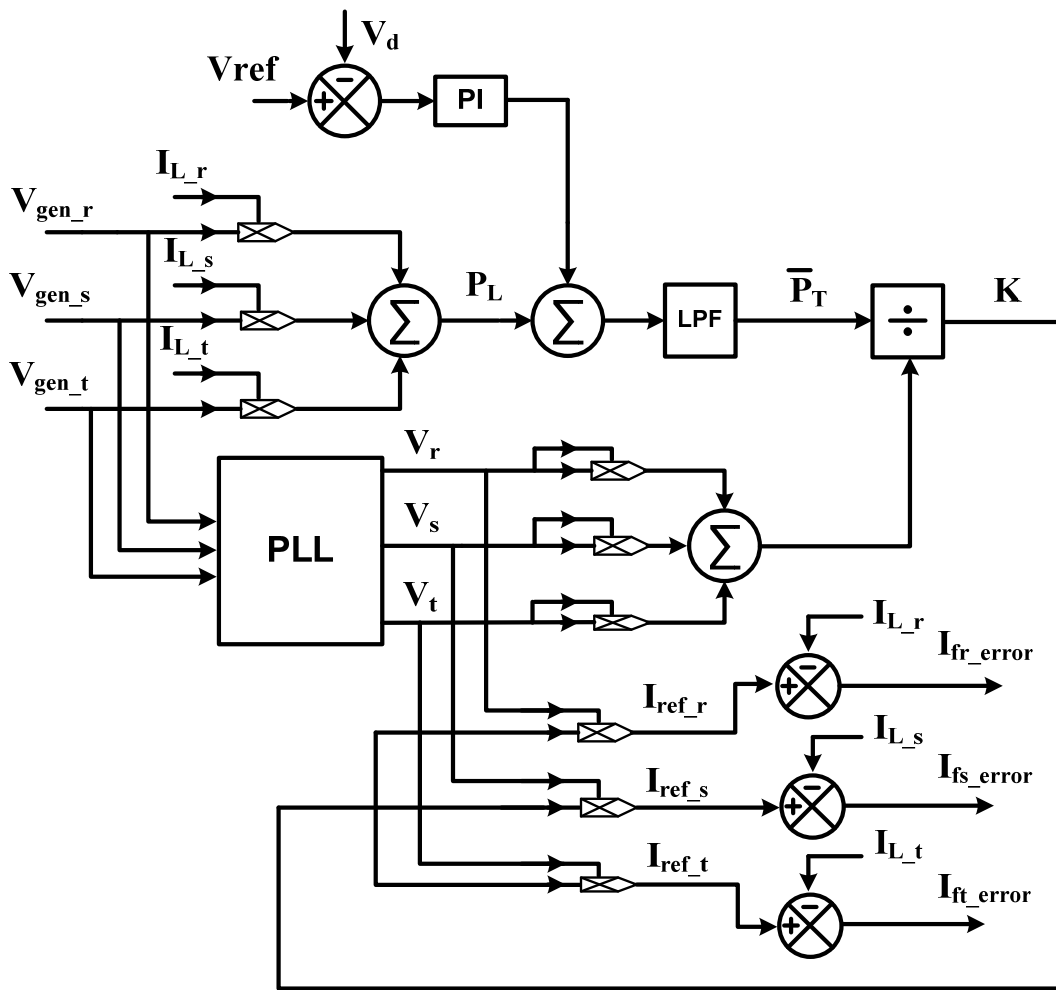
Fig. 5.3: Source current generation with PHC method [5].

115

Also, Fig. 5.3 represents a simple view of the 3-phase reference current generation corresponding to the APF using the PHC method. As depicted in the block diagram of Fig. 5.3, the error signal can be generated by subtracting the 3-ph load currents from the predicted reference currents. Furthermore, the dc value of the calculated active power may be obtained by applying a LPF as depicted in the same diagram. Illustrated in Fig. 5.4 is the circuit configuration of the shunt APF installed to the main power bus of the generating system. Its shown that the circuit model consists of a six-pulse bridge voltage source inverter, the smoothing inductors L_f which damp the high frequency distortion current caused by the PWM switching action, the filter capacitors C_f which are designed for the same purpose to cancel out high-frequency distortion contents injected to PCC.
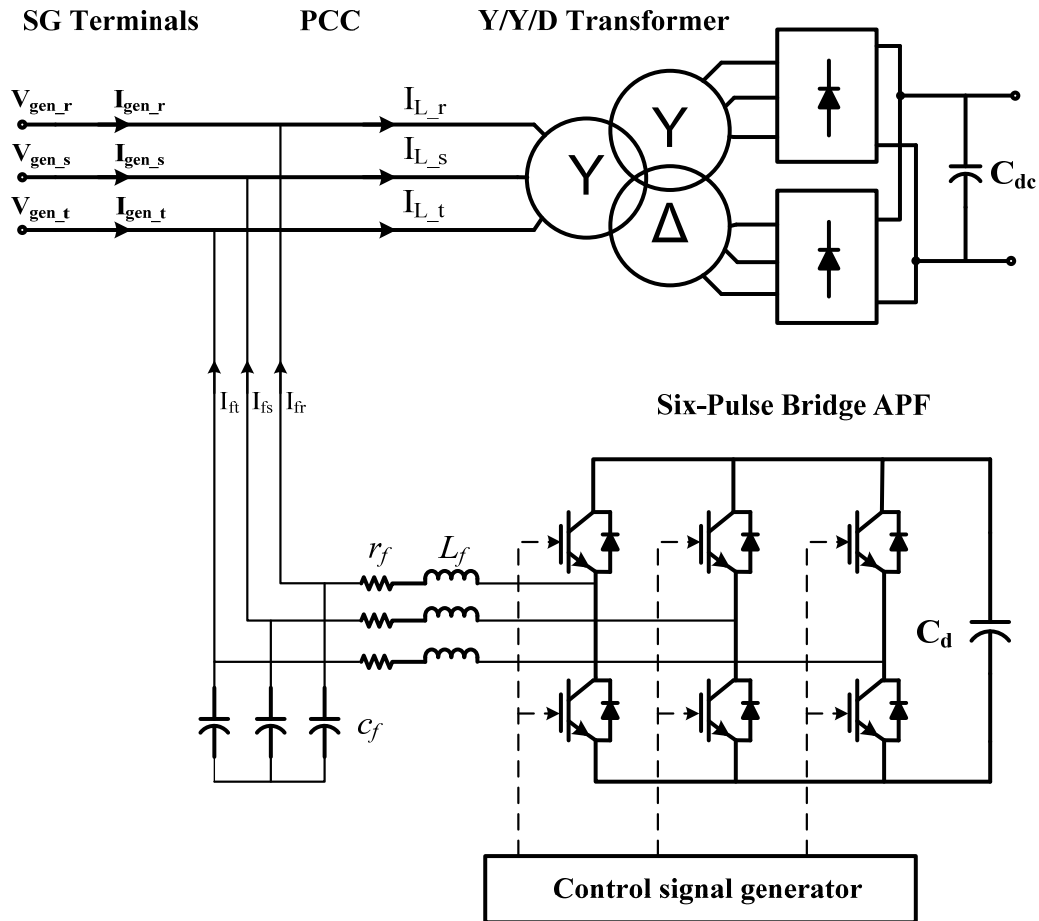
Fig. 5.4: Six-pulse VSI as active power filter [5].

116

Moreover, the second major stage of the proposed APF model deals with the strategy has been employed for generation of the control signals in order to govern the switching behavior of IGBTs in the six-pulse bridge inverter. The hysteresis band PWM current control [101,102] has been utilized to control the switches of the six-pulse VSI so that its output currents follow the opposite of effort signal/harmonic currents. Also, the parameters are provided in Table. 5.2 have been utilized for modeling of the developed APF with PHC control approach.

Table. 5.2: APF parameters

APF Parameters	
SG L-L voltage	200 V(rms)
SG operating frequency	400-800 Hz
Filter inductance (L_f)	0.1 mH
Filter inductance resistance (r_f)	0.01 Ω
Filter capacitance (C_f)	25 μF
Filter dc capacitance (C_{dc})	2 mF
Filter dc voltage	700 V

5. 5 Discussion and Simulation Results

This section presents simulation results obtained from developed model in PSIM9 environment. In order to consider the performance and characteristics for the AAEPS under various loading conditions, the model has been studied for different loading scenarios. The study model has been broken into several case studies where in each case only certain portion of full load power is connected to the grid to investigate the effects on a system's performance and power quality at major nodes. In order to measure the effectiveness of each power filter previously introduced, the same studies have been repeated while both types of the proposed filters have been applied to the grid in separate simulations.

117

The characterization and performance of Active Power Filtering (APF) on power quality of the developed study model (Boeing 767.) AAEPS with non-linear loading is achieved via several case studies. In this work, the quality of delivered power to the ac static/dynamic loads via a 12-pulse PWM voltage source inverter (VSI) is investigated at the main constant frequency (CF) ac bus (400 Hz). Passive loads are simulated by using lumped circuit elements of series RL with a minimum load power factor of 0.85 lagging as recommended by aircraft electrical standards [2,31]. A 12-pulse PWM dc/dc rectifier is also connected to the main Constant Frequency (CF) ac bus as a representation switching non-linear load Also, the performance of the electric grid at the presence of a 3-phase induction motor (IM) as a representation of ac dynamic load is studied. The level of distortion in terms of total harmonic distortion (THD) content in both voltage and current profiles is measured under various loading conditions, as summarized in Table. 5.3. Moreover, the information corresponding to power ratings of the modeled loads is provided in Table. 5.4.

Table. 5.3: Power flow management for different loading scenarios

Case No.	12-Pulse Switching Rectifier at CF-AC bus	IM	DC/DC Dynamic Loads	RL Load at CF-AC bus
CS.1	X			
CS.2	X	X	X	X
CS.3		X		
CS.4	X		X	
CS.5			X	X
CS.6		X	X	
CS.7				X

Table. 5.4 Load characteristics used for power quality analysis

Load	S (kVA)	R(Ω)	L (mH)	I (A)
RL	18	2.0	0.4	52.0
36.4-kVA 12-Pulse Converter (200 V-ac/ 28 V-dc)				
6.2-kVA current constant induction motor				
DC/DC Dynamic Loads				
CP	46V-dc, 220A-dc		10.2-kW	
CC	200V-dc, 100 A-dc		20-kW	

5. 5. 1 Power Quality without Harmonics Cancellation

In this section, power quality of the system under various operating frequencies is addressed. Harmonic contents in both voltage and current profiles are measured at major nodes where no compensation is applied to the system. As mentioned earlier, the system performance analysis is performed for several case studies with different loading profiles as provided in the Tables 5.3, 5.4. Also, variation of the operating frequency due to change in the SG engine speed is modeled by considering a variable frequency in the PSIM9 simulation model within the following frequency range: 400, 500, 600, 700 and 800 Hz. The collected data have been plotted versus operating frequency as shown in the graphs corresponding to THD measurement below. It is clearly seen from the graphs that the THD% is a frequency-dependent quantity and varies as the operating frequency changes.

Also, Fig. 5.9 and Fig. 5.10 represent the 3-phase voltage and current profiles at the VS-SG, as well as the CF main ac bus terminals. These figures correspond to the system's operation when no filtering device is applied.
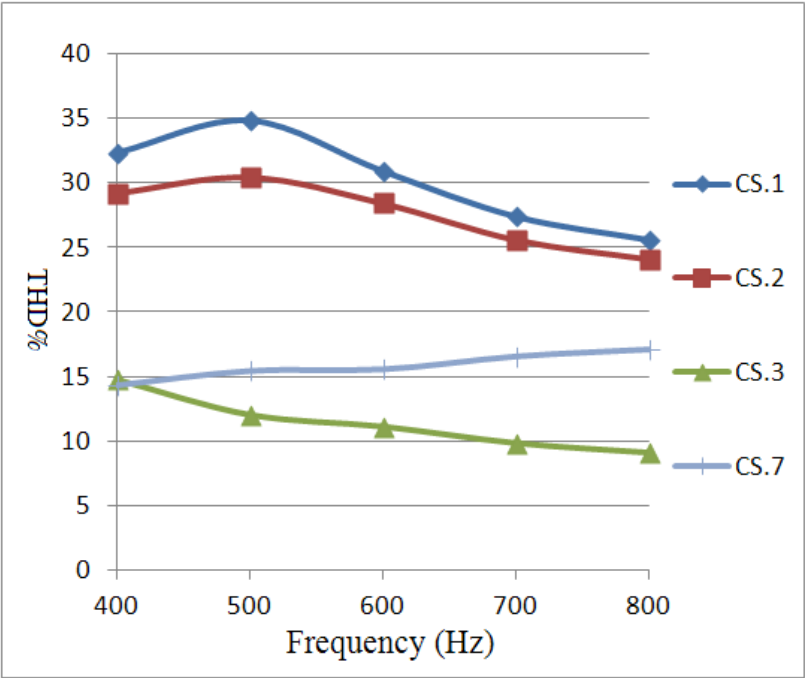
Fig. 5.5: THD% related to the current at CF ac load, without filtering. Cases 1, 2, 3 and 7
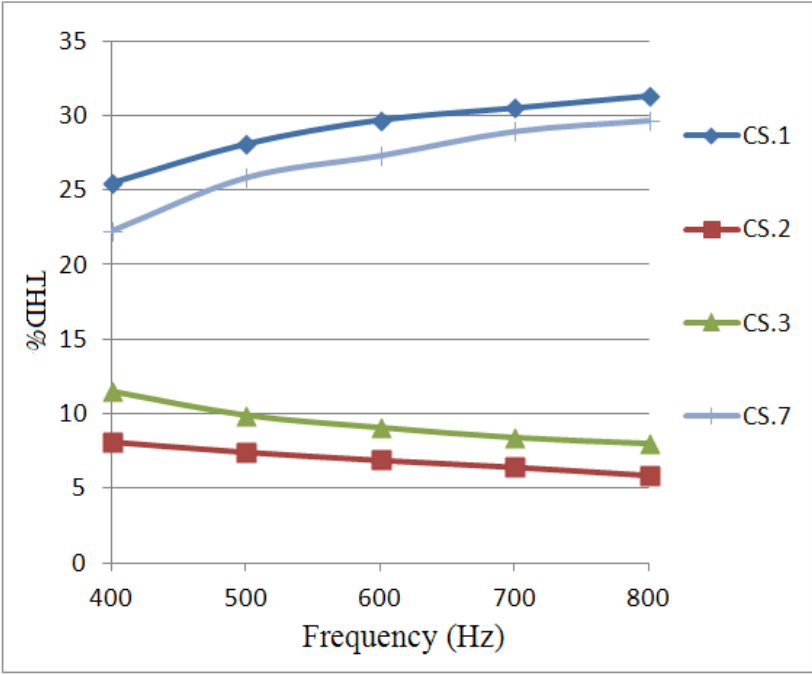
Fig. 5.6: THD% related to the voltage at CF ac load bus, without filtering. Cases 1, 2, 3 and 7
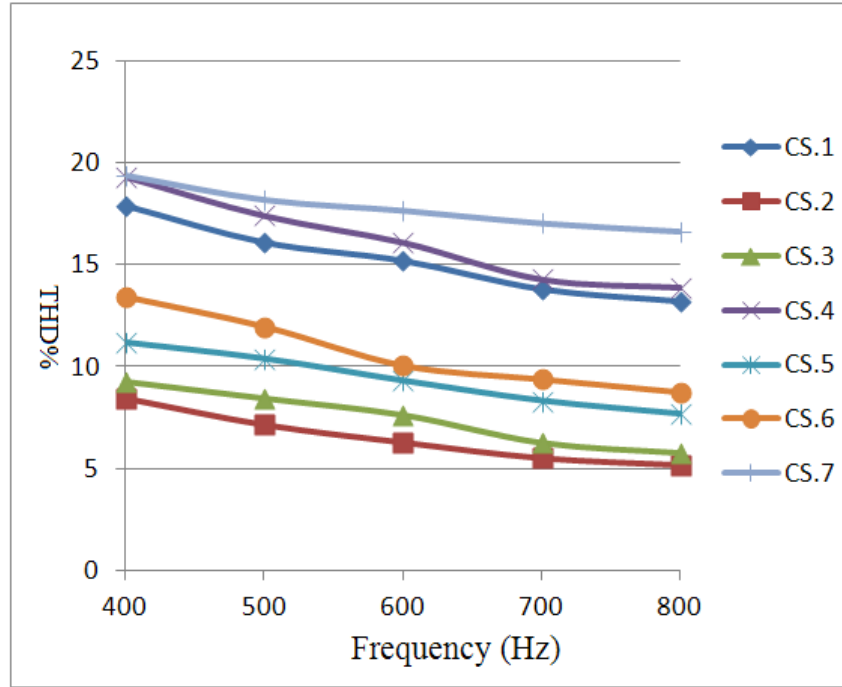
Fig. 5.7: THD% related to the VS-SG line current, without filtering. Cases1- 7
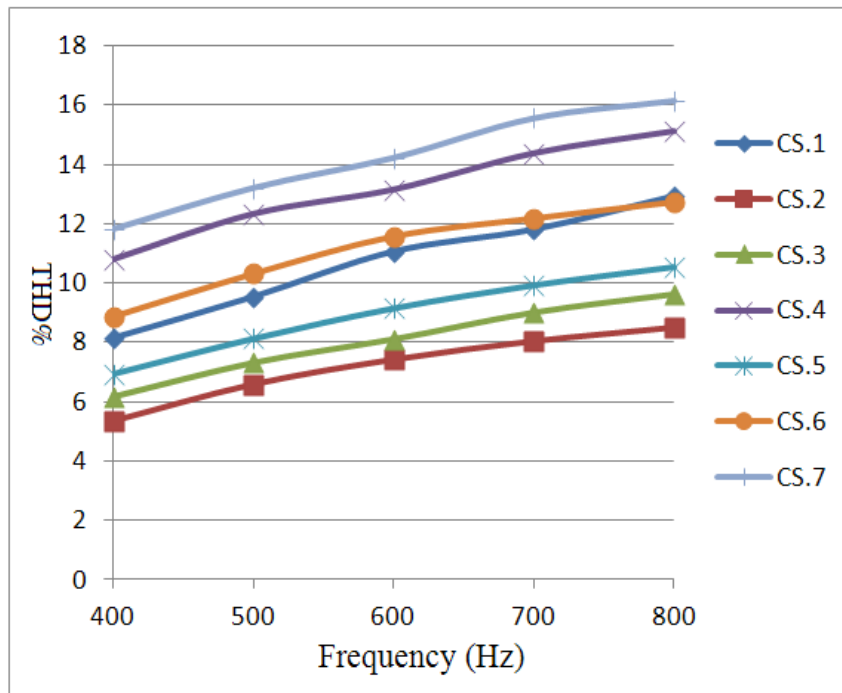
Fig. 5.8: THD% related to phase voltage at the SG terminals without harmonics mitigation. Cases 1- 7
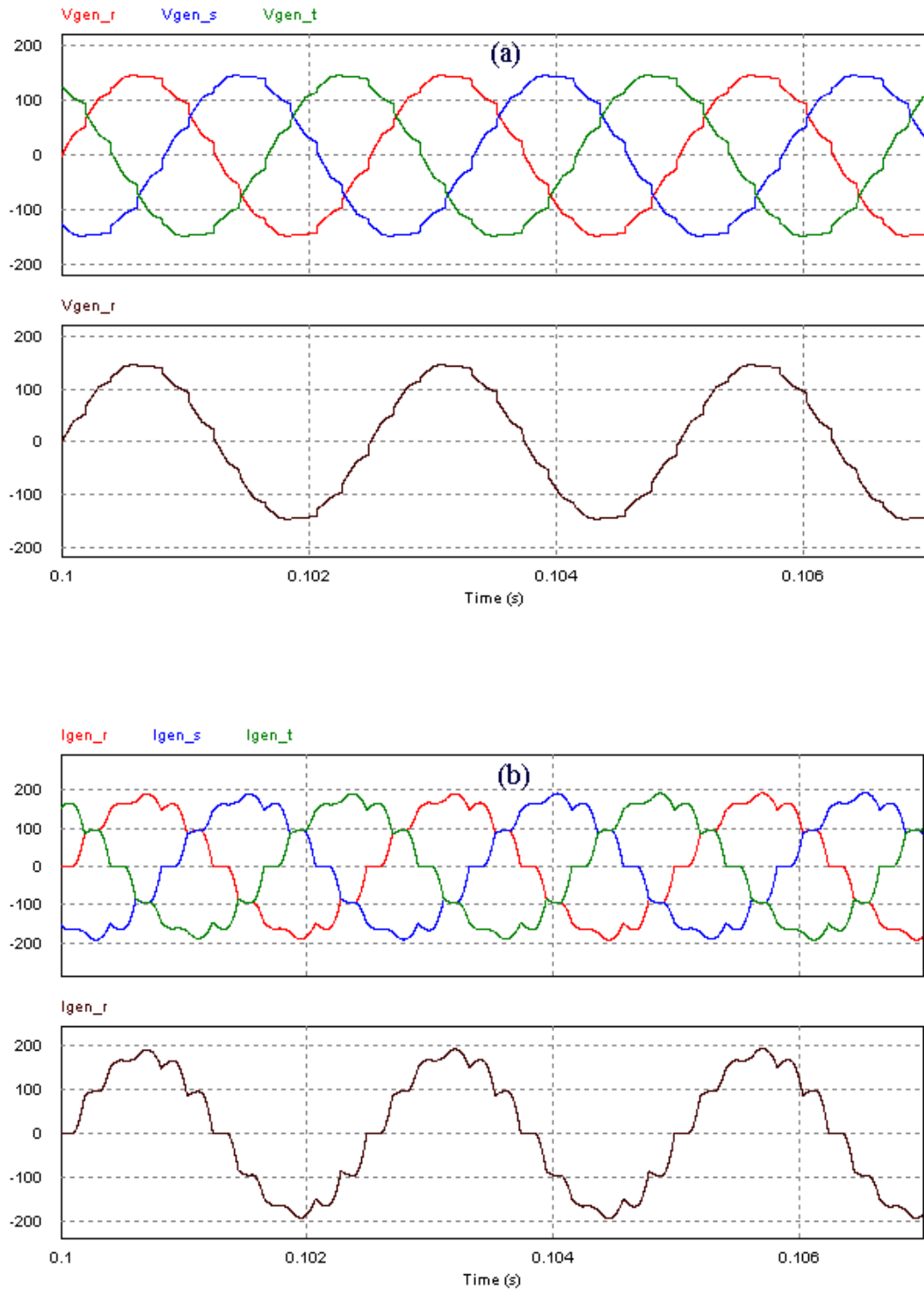
Fig. 5.9: (a) Phase voltage [Volts] and (b) current [Amps] profiles at the SG terminals, without harmonic compensation (CS.4).
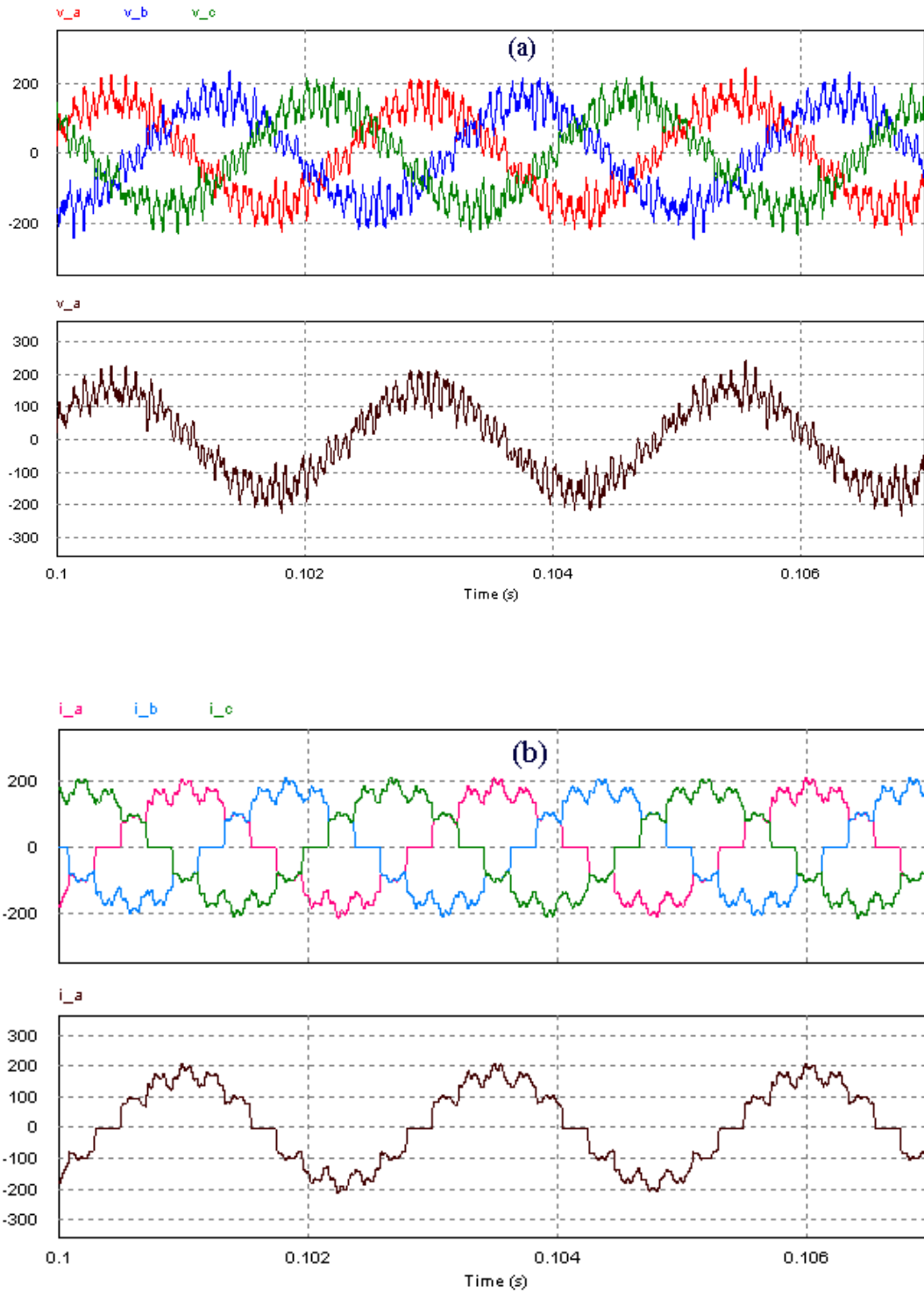
Fig. 5.10: (a) phase voltage [Volts] and (b) current [Amps] profiles at the main CF ac bus, without harmonic compensation (CS.4).

5. 5. 2 Power Quality Analysis with APF

In this section, the performance characteristics of the aircraft electric network are studied where APF is applied to the electric grid. The use of active filtering and its effect on reduction the level of harmonic distortion is studied through same case studies as performed in the previous section. Also, the dynamic and steady-state behavior of the APF is obtained from simulation model in the PSIM9 environment. It has been demonstrated that active filtering introduces a flexible method of harmonics mitigation and its performance on reducing harmonic contents from the VS-CF aircraft system is far better than the fixed compensation by PPF. Also, Fig. 5.16 and Fig. 5.17 represent the transient and steady-state performance of the PHC-based APF at synchronous generator terminals where CS. 6 is under investigation.
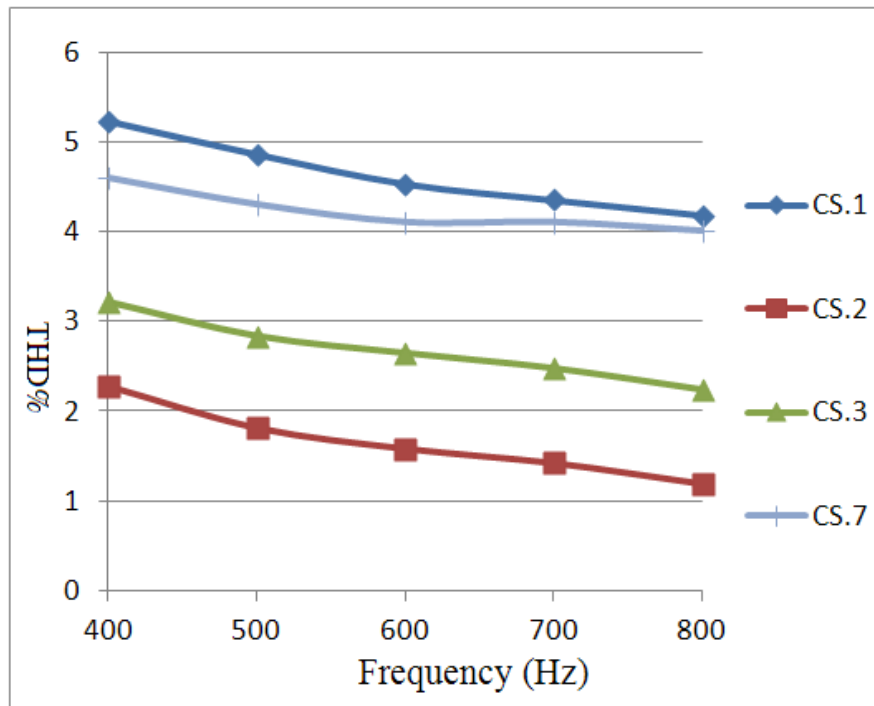
Fig 5.11: THD% related to the current harmonics at the CF ac load bus with APF.
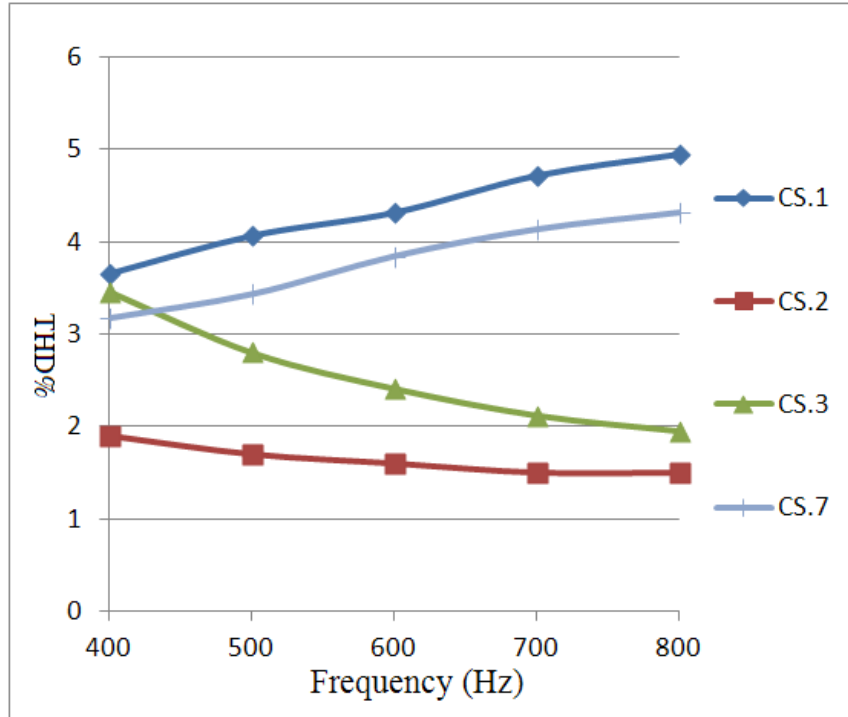
Fig. 5.12: THD% related to the phase voltage harmonics at CF ac load bus with APF.
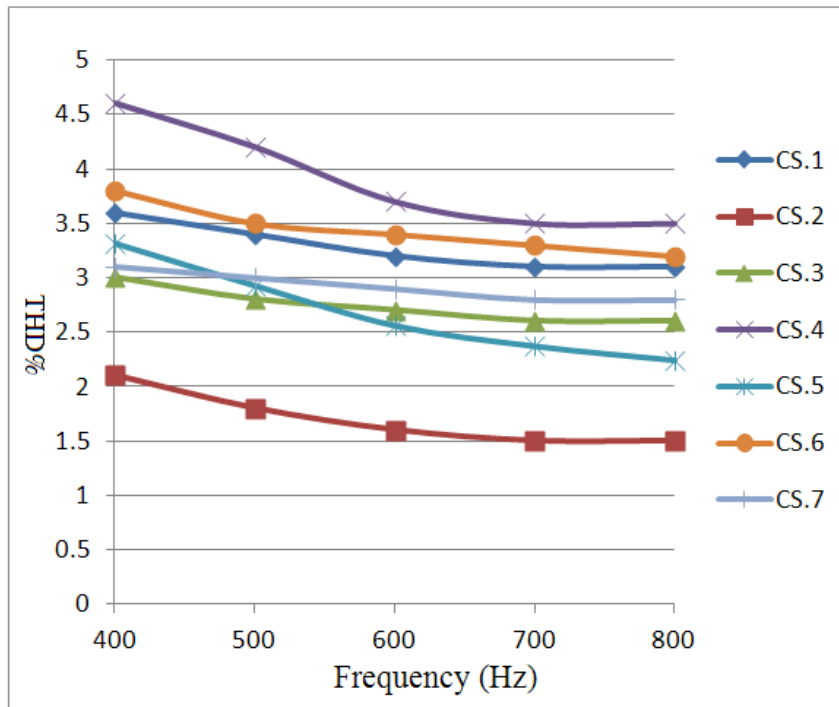
Fig. 5.13: THD% related to the SG current with APF.
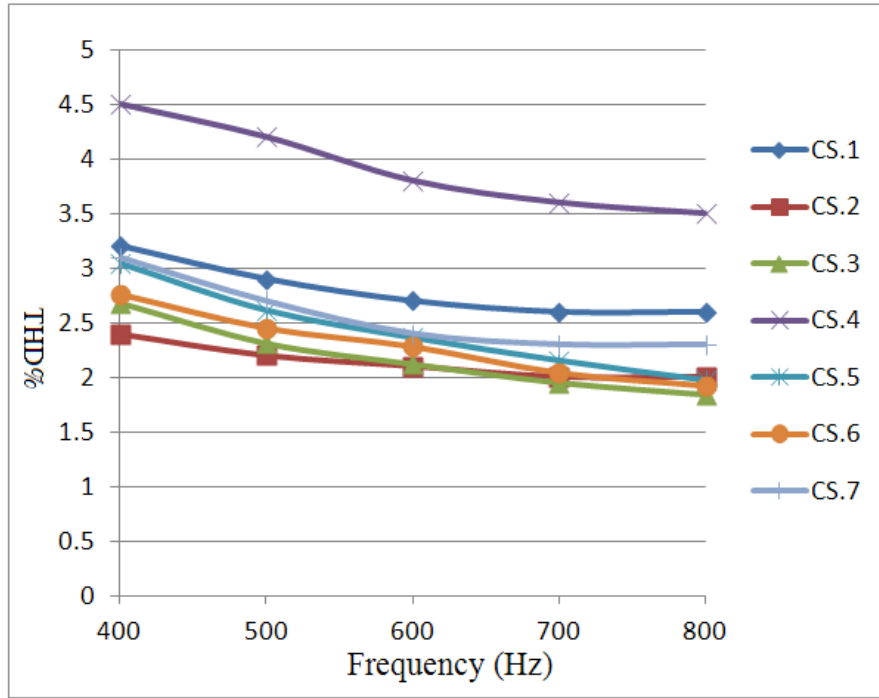
Fig. 5.14: THD% related to the SG voltage with APF.
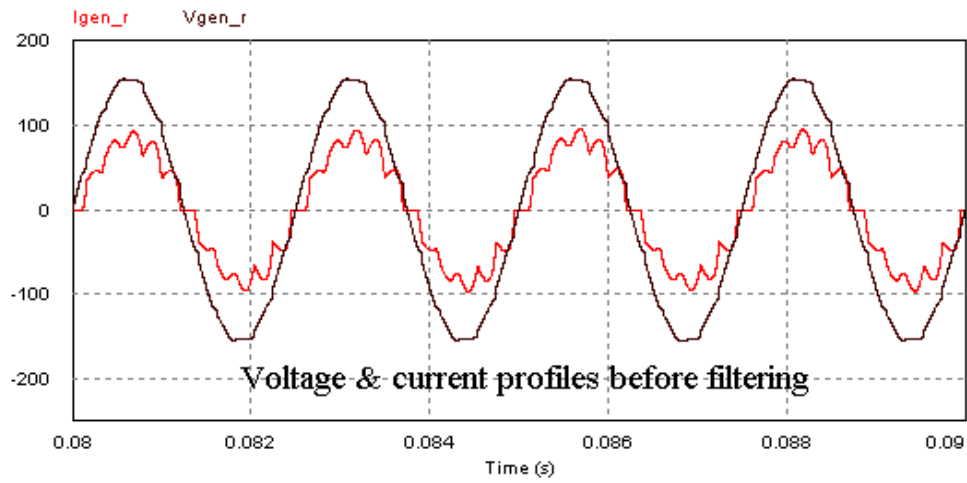
Fig. 5.15: Voltage [Volts] and current [Amps] profiles at the SG terminals without APF (CS. 6)
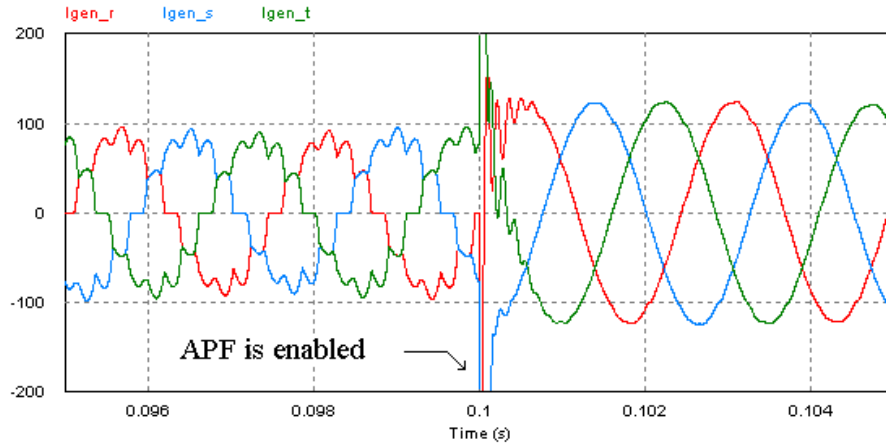
(a)
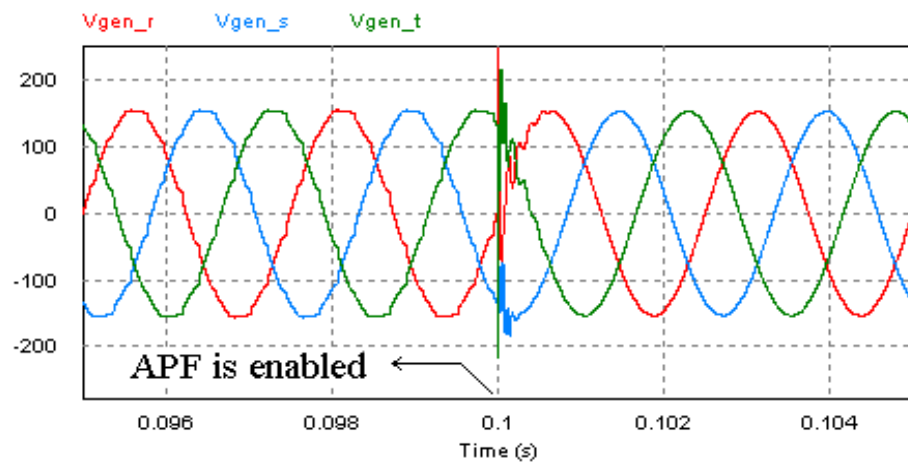
(b)

Fig. 5.16: Transient performance of the SG terminals when APF is activated (a) 3-ph currents [Amps] (b) 3-ph voltage [Volts] (CS. 6)
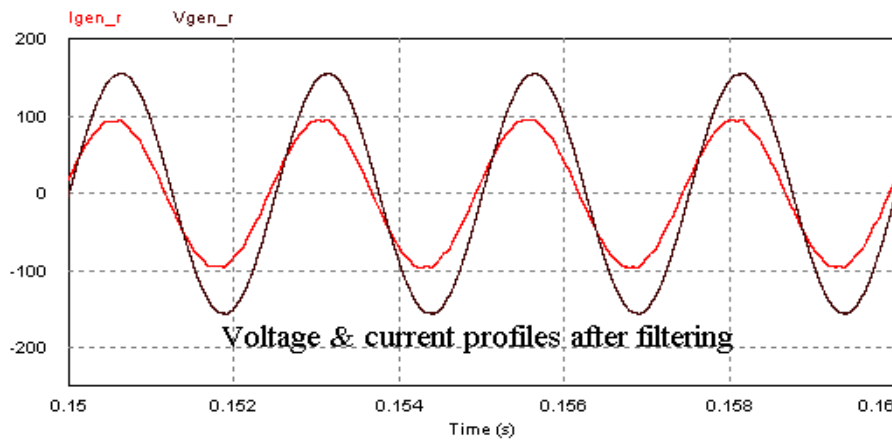
Fig. 5.17: Harmonics compensation with APF, voltage [Volts] and current [Amps] waveforms at the SG terminals (CS. 6)
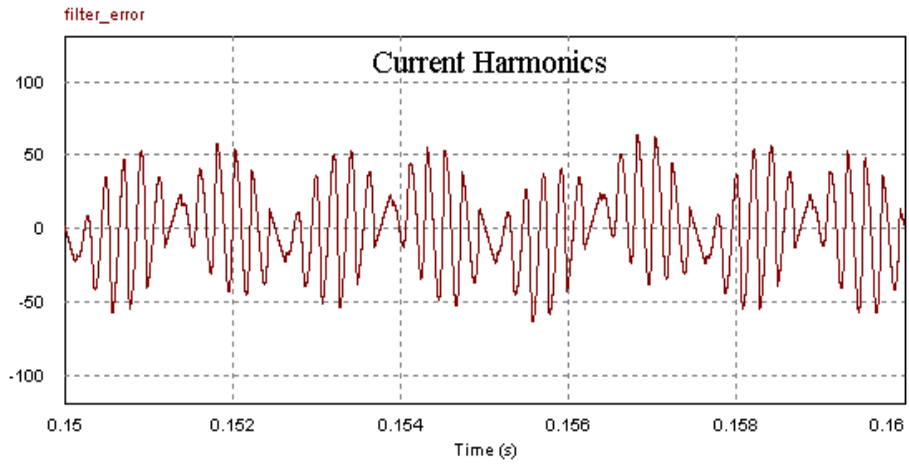
(a)
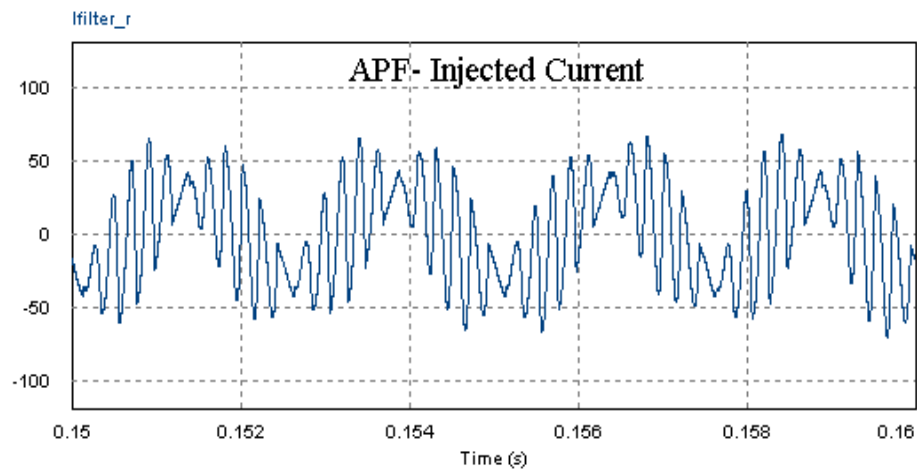
(b)

Fig. 5.18: (a) the inverse form of harmonic current [Amps] (b) current generated by APF, injected into the PCC.
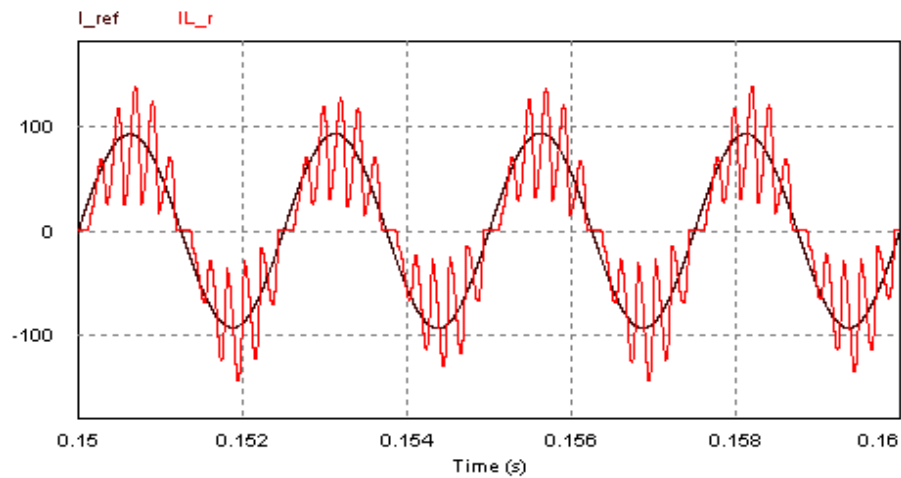
Fig. 5.19: The generated reference current [Amps] and non-linear load current through TRU by PHC technique.

Fig. 5.20-5.24 represent the dynamic and steady-state behavior of the aircraft electric grid profiles at major nodes when APF is enabled. In this effort, CS. 1 is considered as a loading scenario and the applicability and effectiveness of APF is studied.
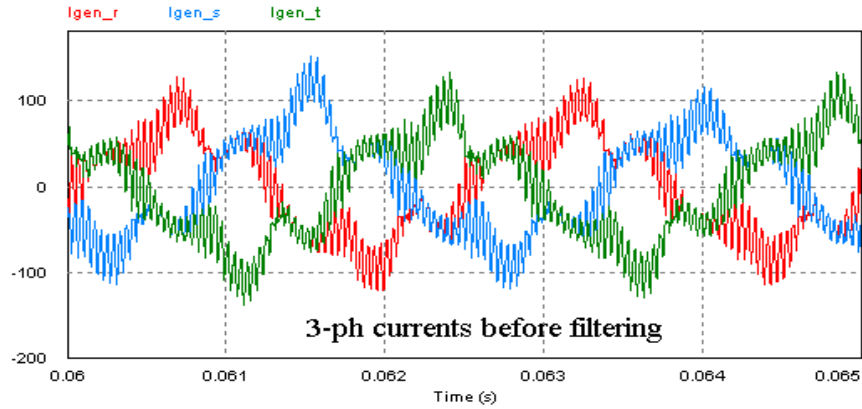
Fig. 5.20: The 3-ph line currents [Amps] at the SG terminals, before filtering (CS. 1).

(a)

(b)
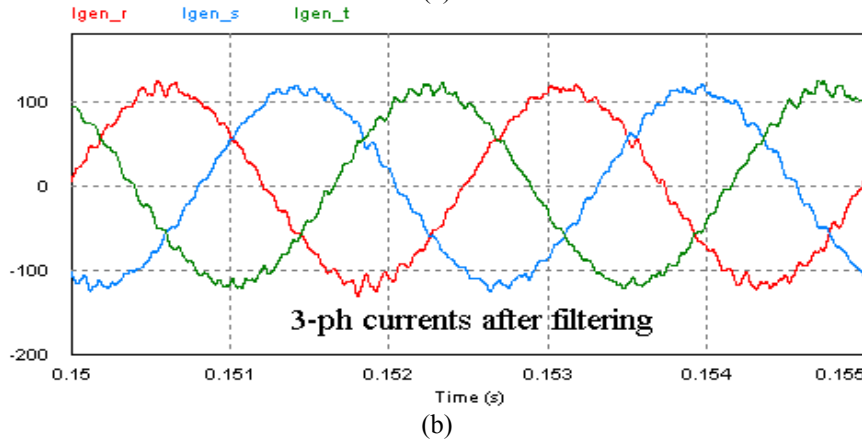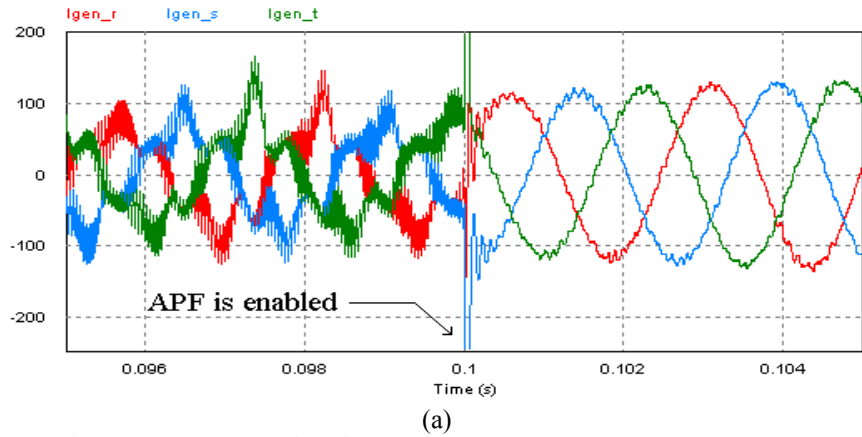
Fig. 5.21: (a) the dynamic (b) steady-state behavior of 3-ph line currents [Amps] at the SG terminals when APF is enabled (CS. 1).

129
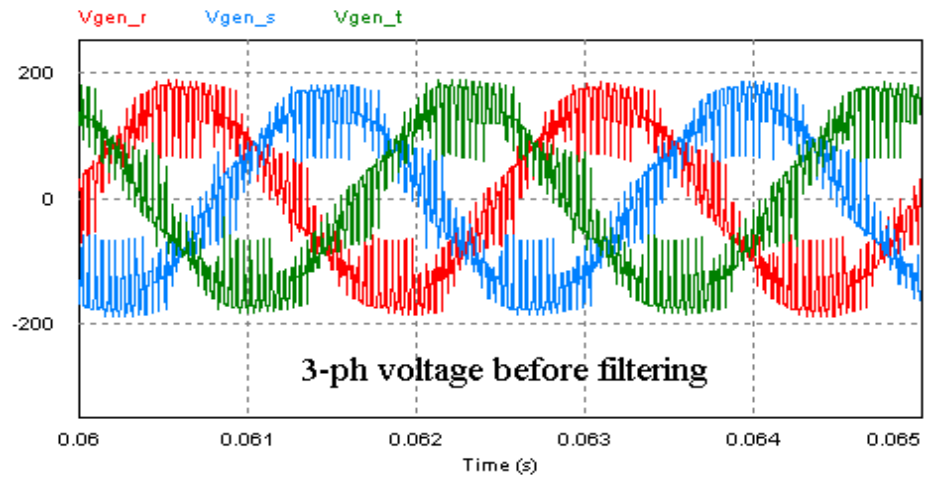
Fig. 5.22: The 3-ph line voltage [Volts] at the SG terminals, before filtering (CS. 1).
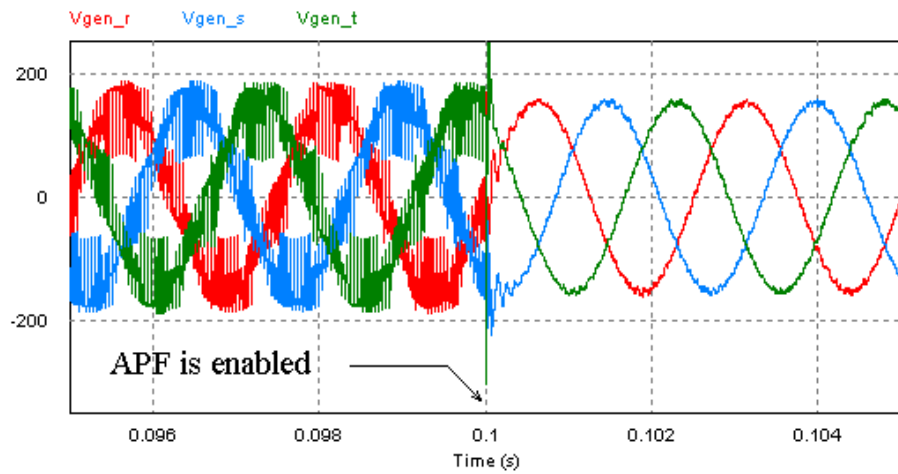
(a)
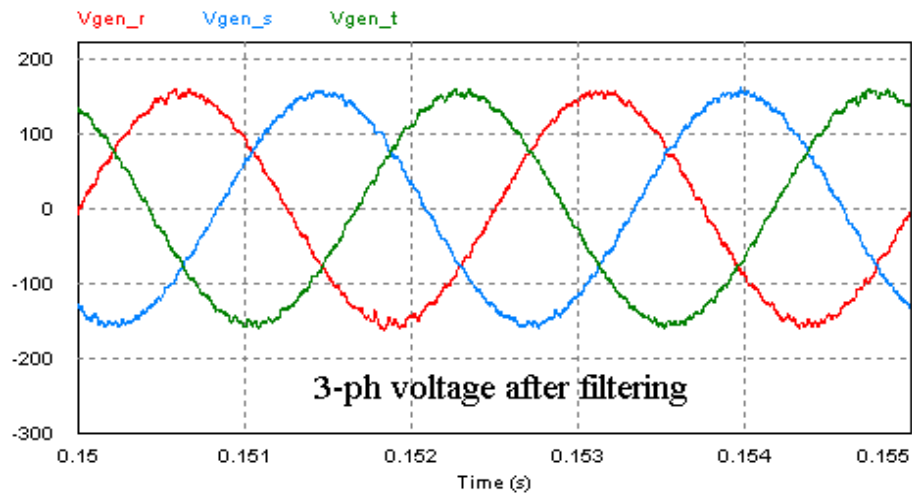
(b)

Fig. 5.23: (a) the dynamic (b) steady-state behavior of 3-ph line voltage [Volts] at the SG terminals when APF is enabled (CS. 1).

130
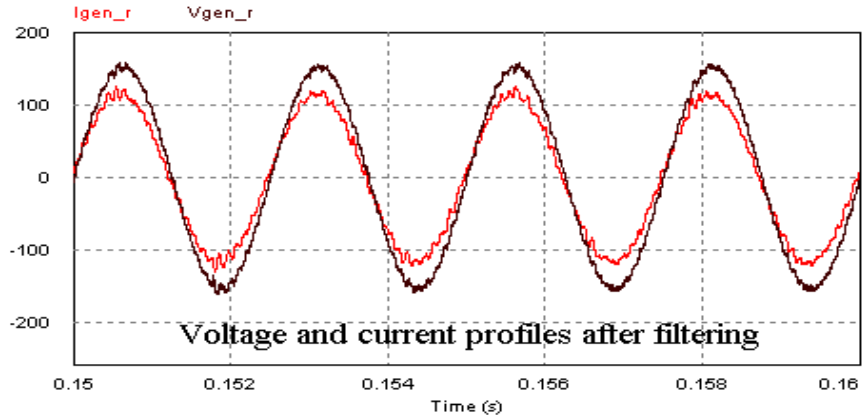
Fig. 5.24: The voltage [Volts] and current [Amps] waveforms at the SG terminals, harmonics compensation using APF (CS. 1).

Fig.5.25 and Fig.5.26 represent the error signal (harmonic components) and the compensation current generated by APF, respectively.
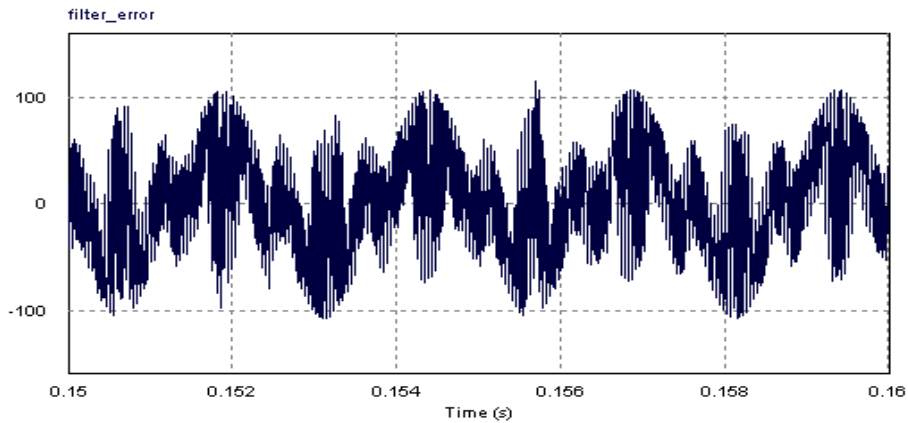
Fig. 5.25: The error signal or harmonics current [Amps] through the SG transmission line.
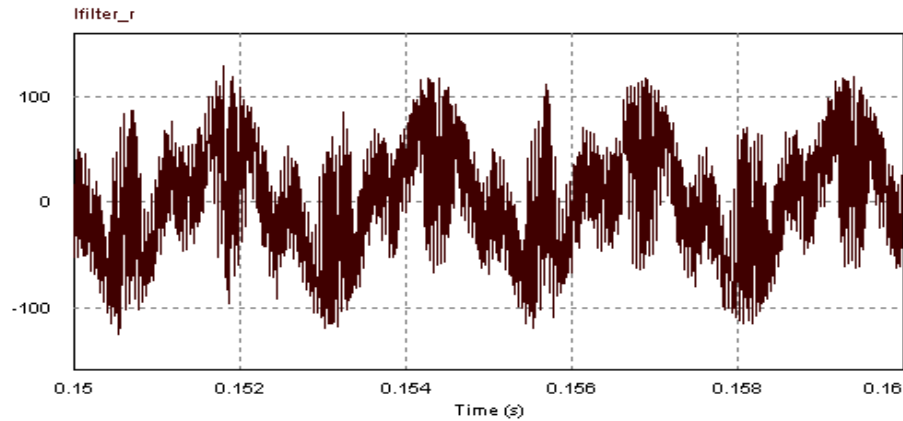
Fig. 5.26: The filter current [Amps] generated by APF injected to the PCC.

131

5. 5. 3 Power Quality Analysis with PPF

This section presents the performance characteristics of the advanced aircraft electric system where harmonics mitigation is achieved by applying the PPF to the major nodes. For more simplicity, the continuous range of the SG's operating frequency 400-800Hz has been divided into five fundamental frequencies, considered as separate case studies. In each case, the 11th and 13th order harmonic components are regarded as corner frequencies and the filter parameters corresponding to each branch are tuned to resonate out the harmonic components at that particular corner frequency. The main ac generating system with PPF is shown in Fig. 5.2. In order to avoid the possible instability due to interaction between PPF and the generating system's impedances, the filter's parameters are carefully chosen for a stable region of operation. By looking at the graphs representing THD% of the currents it is evident that increasing in the operating frequency reduces harmonic components in the current profiles. Also, increasing the load power would lead to a substantial improvement in power quality delivered to the loads.
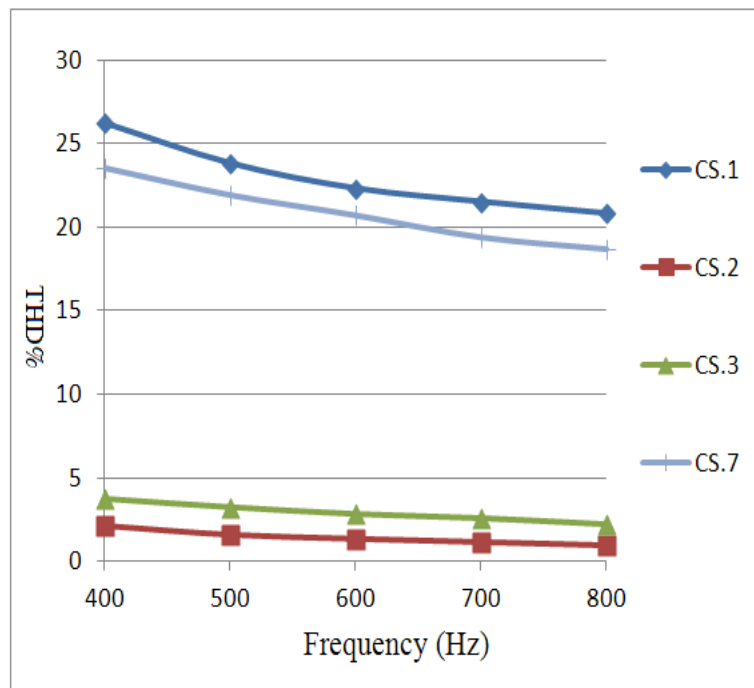
Fig. 5.27: THD% related to the current harmonics at the CF ac bus with PPF. CS.1, CS.2, CS.3 and CS.7
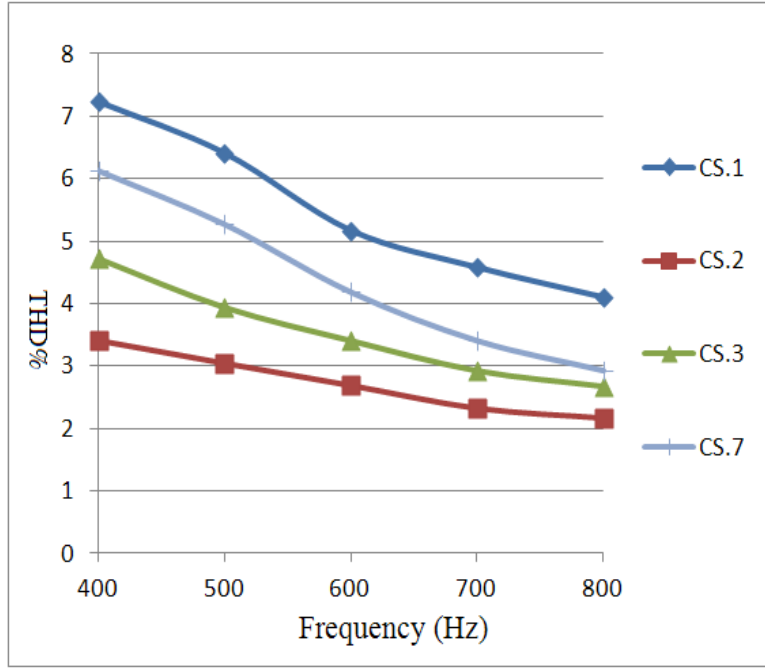
Fig. 5.28: THD% related to the voltage harmonics at the CF ac bus with PPF. CS.1, CS.2, CS.3 and CS.7
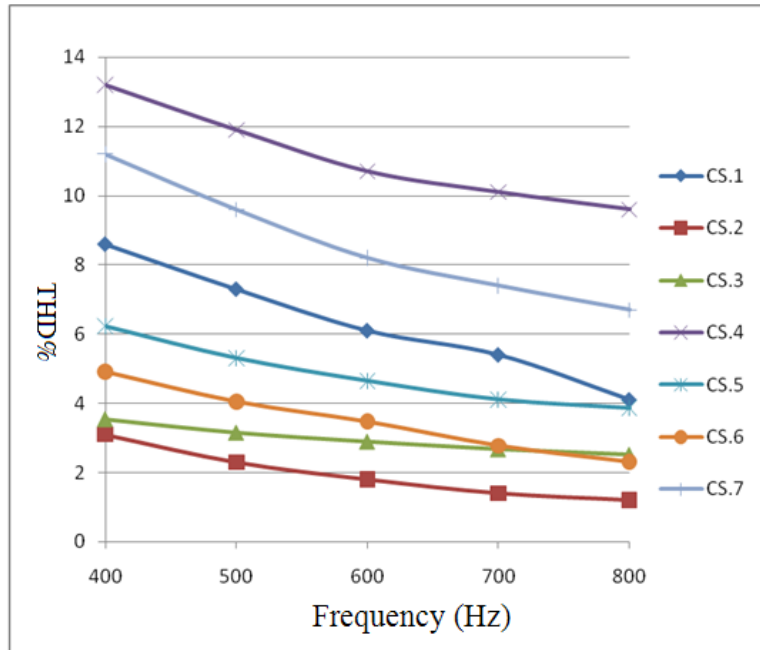
Fig. 5.29: THD% related to the SG terminals current with PPF CS.1-CS.7

133
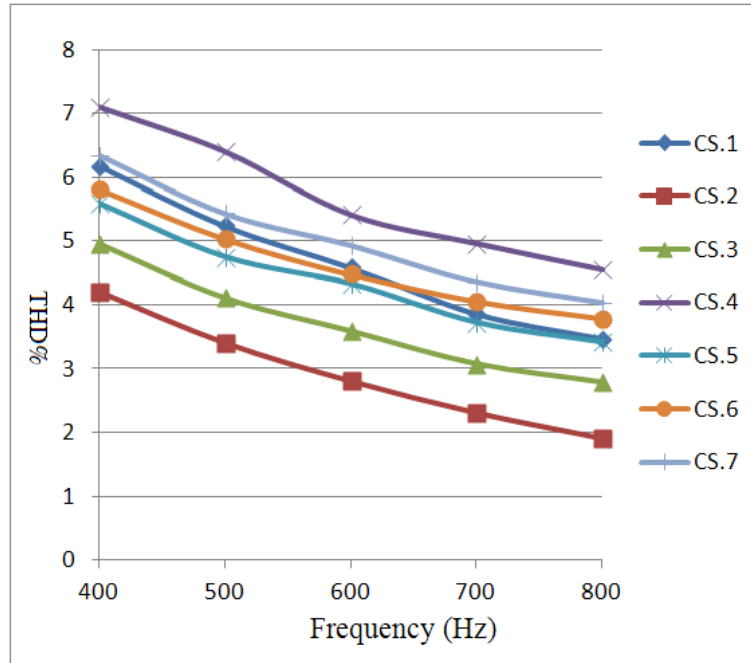
Fig. 5.30: THD% related to the SG terminals voltage with PPF CS.1-CS.7

(a)

(b)
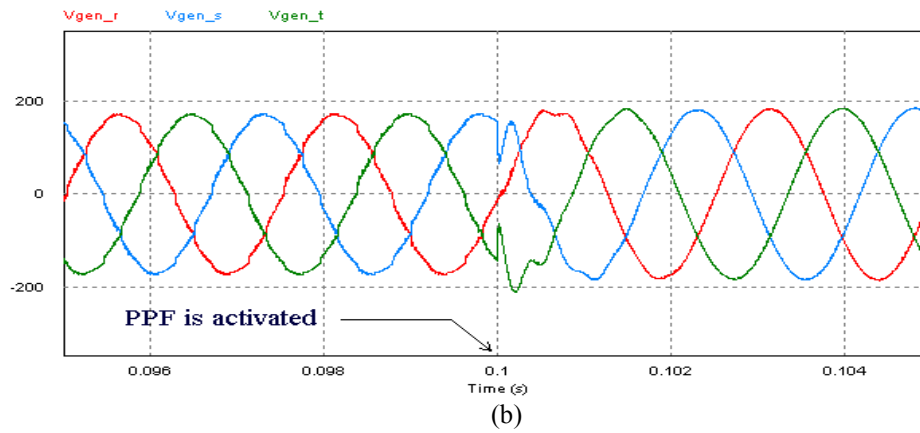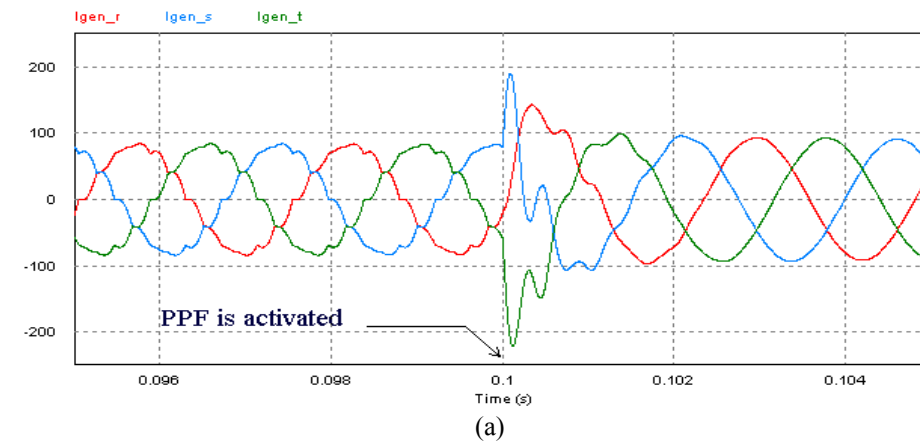
Fig. 5.31: Transient performance of the SG terminals when PPF is activated (a) 3-phase currents [Amps]
(b) 3-phase voltage [Volts] (CS. 6)

134
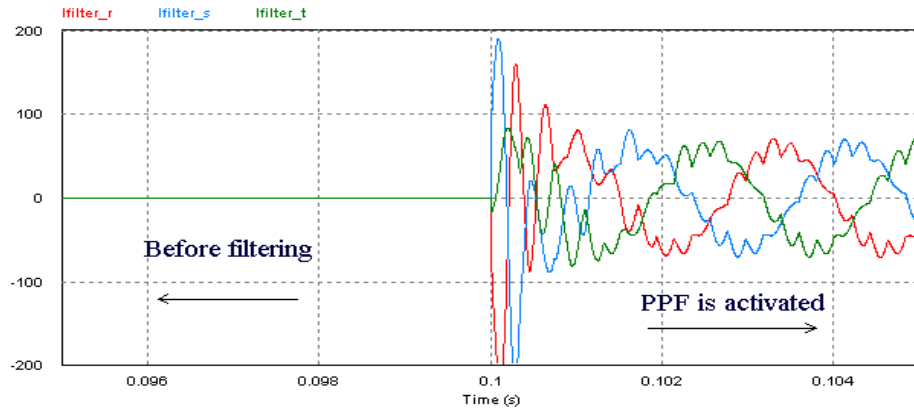
Fig. 5.32: 3-phase filter current [Amps] (CS. 6)

5.6 Summary

A comprehensive circuit model of the VS-CF electric power system (EPS) for Boeing 767. aircraft was developed in this Chapter. Performance characteristics of the entire system were studied while different loading configurations were applied. The power quality analysis is performed over a wide range of operating frequencies (400-800Hz). Moreover, the effects of loading condition on power quality of the aircraft EPS were investigated with various types of ac/dc active/passive loads are considered as different case studies. The level of harmonic contents in terms of THD% was measured at major nodes. It has been demonstrated that the overall power quality of the system varies according to change in the SG's operating frequency, as well as the load power under study.

In order to mitigate the harmonics distortion in the grid, a fully controlled APF was designed based on the PHC method. Using this method of harmonic cancellation, an effective voltage regulation, correction of the supply power factor (PF), elimination of the THD contents and minimization the effects of unbalanced loads are achieved. To better investigate the effectiveness and applicability of the APF method studied, a shunt passive power filter (SPPF) was designed and integrated into the studied aircraft electric network. Also, THD% measurements were achieved for a wide range of operating frequency by applying two methods of harmonic elimination. By comparing the collected data from two efforts, it has been shown that the inductive nature of the system harmonic

135

impedance of the modeled VSCF aircraft EPS contributes considerably to lowering the current harmonic contents and particularly at higher frequencies. Generally, effective harmonic compensation and the overall improvement in power quality of the modeled VSCF aircraft EPS may be attributed to the effective PHC control scheme of the proposed fast-switching, real-time APF. Further investigation into the collected data, one sees that the power quality characteristics and PF improvement achieved by the proposed PHC-APF is compliance with the most recent military aircraft electrical standards MIL-STD-704F [31], as well as the common IEEE-Std. 519.

Chapter Six

Conclusions and Future Work

6.1 Research Summary

In this research a complete set of mathematical models are obtained to describe the transient and steady-state performance of an Advanced Aircraft Electric Power Distribution System (AAEPDS). Generalized state-space averaging technique has been employed to derive the important mathematical characteristics corresponding to the ac-dc/dc-ac multi-level converters integrated with harmonics filters and ac/dc loads of the system under investigation. The proposed models are then used to simulate the key dynamic behaviors of the system and sub-systems for several case studies. The developed averaging models circumvent the necessity of applying real-time analysis for the aircraft electric power system at major nodes and overcome the difficulties of applying time domain analysis with extra costs of requiring more computer resources. Also, saving in simulation time is another advantage one can achieve using the GSSA technique.

In addition, a circuit model representation of the hybrid battery/FC APU system is developed using PSIM9 software. A comprehensive system analysis of the PEM-FC and lead-acid battery is performed for different loading configurations. The performance of the fuel cell stack is captured where interacting with different kind of static and dynamic loads. Both transient and steady-state behavior of the hybrid system is taken into account via several case studies. Also, the application of the battery/FC-based APU in an AAEPS is investigated under normal and emergency operational conditions. The applicability and effectiveness of using the hybrid system operating in parallel with the main generating bus (interconnected at the main dc-link) is assessed. The paralleled system performance has been analyzed while different scenarios are considered in the developed model. The characterization of the hybrid system is achieved by using the obtained simulation results from PSIM9 environment. The captured results demonstrate that the developed study model closely predicts the behavior and characteristics of a real system under transient and steady-state conditions.

In order to investigate the stability problem of the system under study, a comprehensive analysis of the detailed AAEPS dynamics was studied using bifurcation theory, using multi-variable parameters approach. The combination of mathematical concept associated with the system's stability profile along with the real-time simulation analysis give an improved knowledge of the system dynamic performance under various conditions, as well as the possible problems coming from the variation of system parameters. For instance, by applying the bifurcation analysis and using the corresponding diagrams it is possible to determine the specific values of the parameters where the system equilibrium becomes unstable due to a Hopf bifurcation, and also find out the stability margins of the associated oscillation.

Furthermore, the state space averaging variables as representation of the reduced-order system are utilized to characterize the stability performance of the system via differential algebraic equations. Also, it was demonstrated that bifurcation analysis with consideration of varying parameters brings additional information such as the location of system equilibrium points which is required for a high secure design. Finally, the robustness of the system profiles against variations of control parameters was reported in this thesis.

Also, the power quality of the operating system has been considered as a remarkable concern. Hence, the performance characteristics of the entire system are studied while different kinds of loading configuration are taken into account. The power quality analysis is performed over a wide range of operating frequency (400-800Hz). Moreover, the effects of loading condition on power quality of the aircraft EPS is investigated where various types of ac/dc active/passive loads are considered as different case studies. Also, the level of harmonics contents in terms of THD% is measured at major nodes. It has been demonstrated that the overall power quality of the system varies according to change in the SG's operating frequency, as well as the load power under study.

In order to mitigate the harmonics distortion in the grid, a fully controlled APF is designed based on PHC method. Using this method of harmonics cancellation, an effective voltage regulation, correction of the supply power factor (PF), elimination of the

THD contents and minimization the effects of unbalanced loads are achieved. To better investigate the effectiveness and applicability of the studied APF method, a shunt passive power filter (SPPF) is designed and integrated into the studied aircraft electric network. Also, THD% measurement is achieved for a wide range of operating frequency by applying two methods of harmonics elimination. By comparing the collected data from two efforts, it has been shown that the inductive nature of the system harmonic impedance of the modeled VSCF aircraft EPS considerably contributes to lowering the current harmonic contents and particularly at higher frequencies. Generally, the effective harmonic compensation and the overall improvement in power quality of the modeled VSCF aircraft EPS may be attributed to the effective PHC control scheme of the proposed fast-switching, real-time APF. Further investigation into the collected data, one sees that the power quality characteristics and PF improvement achieved by the proposed PHC-APF is in compliance with the most recent military aircraft electrical standards MIL-STD-704F [31], as well as the common IEEE-Std. 519.

6.2 Future Work

An immediate extension of this research may be a scaled-down lab model design and implementation of the AAEPS with APU system. In order to ensure the security of operation and performance reliability of the entire system, developing an Identification and Diagnostic Toolbox (IDT) may be suitable to monitor the system's operation under various conditions. The significance of the proposed device can be better understood by further investigation into it's applicability in fault detection of the electric grid when the aircraft is on the ground. Also, the effectiveness of installing other types of FACTs devices and active filtering, such as; Modulated Power Filters (MPF), may be examined in this research to improve the power quality of the system.

References

[1] K.W.E. Cheng, "Comparative study of AC/DC converters for more electric aircraft," IEE Power Electronics and Variable Speed drives Conference, pp. 299-304, Sep. 1998.

[2] Richard E. Quigley, Jr., "More electric aircraft", Proc. IEEE Applied Power Electronics Conference, San Diego, pp. 906-911, 1993.

[3] Lester Faleiro; "Beyond the more electric aircraft", AIAA, 2005.

[4] Eid, A.; El-Kishky, H.; Abdel-Salam, M.; El-Mohandes, T.; "Constant frequency aircraft electric power systems with harmonic reduction," *Industrial Electronics, 2008. IECON 2008, 34th Annual Conference of IEEE*, pp.623-628, 10-13 Nov. 2008.

[5] Eid, A.; El-Kishky, H.; Abdel-Salam, M.; El-Mohandes, M.T., "On Power Quality of Variable-Speed Constant-Frequency Aircraft Electric Power Systems," *Power Delivery, IEEE Transactions on*, vol.25, no.1, pp.55-65, Jan. 2010.

[6] Segrest, J.D.; "Advanced Aircraft Electric System," *Aerospace and Electronic Systems, IEEE Transactions on*, vol.AES-20, no.3, pp.213-216, May1984.

[7] Izquierdo, D.; Azcona, R.; del Cerro, F.; Fernandez, C.; Delicado, B.; "Electrical power distribution system (HV270DC), for application in more electric aircraft," *Applied Power Electronics Conference and Exposition (APEC), 2010 Twenty-Fifth Annual IEEE*, pp.1300-1305,21-25, Feb.2010.

[8] Chen, Z.; Luo, Y.; Chen, M.; "Control and Performance of a Cascaded Shunt Active Power Filter for Aircraft Electric Power System," *Industrial Electronics, IEEE Transactions on*, vol. PP, no.99, pp.1.

[9] "Aircraft Electric Power Characteristics", Military Standard, MILSTD- 704F, 2004.

[10]   Eid, A.; El-Kishky, H.; Abdel-Salam, M.; El-Mohandes, T.; "VSCF aircraft electric power system performance with active power filters," *System Theory (SSST), 2010 42nd Southeastern Symposium on*, pp.182-187, 7-9 March 2010.

[11]   Eid, A.; El-Kishky, H.; Abdel-Salam, M.; El-Mohandes, T.; "Modeling and characterization of an aircraft electric power system with a fuel cell-equipped APU connected at HVDC bus," *Power Modulator and High Voltage Conference (IPMHVC), 2010 IEEE International*, pp.639-642, 23-27 May 2010.

[12]   Tao Lei; Xiao-Bin Zhang; Yan-Jun Dong; Jing-Hui Zhao; Hui Lin; "Study of high power factor rectifiers based on one cycle control in aircraft electric power system," *Power System Conference, 2008. MEPCON 2008. 12th International Middle-East*, pp.325-329, 12-15 March 2008.

[13]   Shanshan Wu; Yongdong Li; "Application and challenges of power electronics for variable frequency electric power system of more electric aircraft," *Electrical Machines and Systems (ICEMS), 2011 International Conference on*, pp.1-4, 20-23 Aug. 2011.

[14]   Lavopa, E.; Sumner, M.; Zanchetta, P.; Ladisa, C.; Cupertino, F.; "Real-time estimation of fundamental frequency and harmonics for active power filters applications in aircraft electrical systems," *Power Electronics and Applications, 2007 European Conference on* , pp.1-10, 2-5 Sept. 2007.

[15]   Lavopa, E.; Zanchetta, P.; Sumner, M.; Cupertino, F.; "Real-Time Estimation of Fundamental Frequency and Harmonics for Active Shunt Power Filters in Aircraft Electrical Systems," *Industrial Electronics, IEEE Transactions on*, vol.56, no.8, pp.2875-2884, Aug. 2009.

[16]   Wu, T.; Bozhko, S.V.; Asher, G.M.; Thomas, D.W.P.; "Accelerated functional modeling of aircraft electrical power systems including fault scenarios," *Industrial Electronics, 2009. IECON '09. 35th Annual Conference of IEEE*, pp.2537-2544, 3-5 Nov. 2009.

[17] Wu, T.; Bozhko, S.V.; Asher, G.M.; "High speed modeling approach of aircraft electrical power systems under both normal and abnormal scenarios," *Industrial Electronics (ISIE), 2010 IEEE International Symposium on*, pp.870-877, 4-7 July 2010.

[18] Liqiu Han; Jiabin Wang; Howe, D.; "State-space average modeling of 6- and 12-pulse diode rectifiers," *Power Electronics and Applications, 2007 European Conference on*, pp.1-10, 2-5 Sept. 2007.

[19] K.W.E. Cheng, "Comparative study of AC/DC converters for more electric aircraft," IEE Power Electronics and Variable Speed drives Conference, pp. 299-304, Sep. 1998.

[20] A. Emadi and A**.** Abur, "Real time state estimation of multi-converter DC power electronic systems using generalized state space averaging method,**"** IEEE Power Electronics Specialists Conf.*, 2002. PESC**, 2002, pp. 881-886.

[21] Sanders, S.R.; Noworolski, J.M.; Liu, X.Z.; Verghese, G.C.; "Generalized averaging method for power conversion circuits," Power Electronics Specialists Conference, 1990. PESC '90 Record., 21st Annual IEEE, pp.333-340, 11-14 Jun 1990.

[22] J. Mahdavi, A. Emaadi, M. Bellar, and M. Ehsani; "Analysis of power electronic converters using the generalized state-space averaging approach,"IEEE Trans. Circuits Syst. I, vol. 44, no. 8, pp. 767–770, Aug. 1997.

[23] V. Caliscan, G. Verghese, and A. Stankovic´; "Multi-frequency averaging of dc/dc converters," IEEE Trans. Power Electron., vol. 14, no. 1, pp.124–133, Jan. 1999.

[24] Jianping Xu; Long, D.Z.; Lee, C.Q.; "Generalized state space averaging approach and its application to the analysis of quasi-resonant converters," Power Electronics Specialists Conference, PESC '94 Record., 25th Annual IEEE, pp.1046-1052 vol.2, 20-25 Jun 1994.

[25]   Arulselvi, S.; Uma, G.; Kalaranjini, B.; "Design and simulation of model based controllers for quasi resonant converters using neural networks," Power Electronics, 2006. IICPE 2006. India International Conference on, pp.197-202, 19-21 Dec. 2006.

[26]   Sun, J.; Grotstollen, H.; "Averaged 143odeling of switching power converters: reformulation and theoretical basis," Power Electronics Specialists Conference, 1992. PESC '92 Record., 23rd Annual IEEE, pp.1165-1172 vol.2, 29 Jun-3 Jul 1992.

[27]   Yazdani, A.; Iravani, R.; "A generalized state-space averaged model of the three-level NPC converter for systematic DC-voltage-balancer and current-controller design," Power Delivery, IEEE Transactions on , vol.20, no.2, pp. 1105- 1114, April 2005.

[28]   Krein, P.T.; Bentsman, J.; Bass, R.M.; Lesieutre, B.L.; "On the use of averaging for the analysis of power electronic systems," Power Electronics, IEEE Transactions on, vol.5, no.2, pp.182-190, Apr 1990.

[29]   R. D. Middlebrook and S. Cuk, "A general unified approach to modeling switching converter power stages," in *Proc. IEEE PESC'76*, June 1976, pp. 18–34.

[30]   Eid, A.; El-Kishky, H.; Abdel-Salam, M.; El-Mohandes, M.T.; "On Power Quality of Variable-Speed Constant-Frequency Aircraft Electric Power Systems," Power Delivery, IEEE Transactions on , vol.25, no.1, pp.55-65, Jan. 2010.

[31]   "Aircraft Electric Power Characteristics", Military Standard, MILSTD-704F, 2004.

[32]   T. M. Jahns and M. A. Maldonado, "A new resonant link aircraft power generating system," IEEE Trans. Aerosp. Electron. Syst., vol. 29, no. 1, pp. 206–214, Jan. 1993.

[33] M. H. Taha, D. Skinner, S. Gami, M. Holme, and G. Raimondi, "Variable frequency to constant frequency converter (VFCFC) for aircraft applications," in Proc. Inst. Elect. Eng. Int. Conf. Power Electronics, Machines and Drives, Jun. 2002, pp. 235–240.

[34] El-Kishky, H.; Ibrahimi, H.; Abu Dakka, M.; Eid, A.; Abdel-Akher, M.; "Modeling and characterization of VSCF aircraft electric power systems with nonlinear loading," *Pulsed Power Conference (PPC), 2011 IEEE*, pp.1482-1485, 19-23 June 2011.

[35] Liqiu Han; Jiabin Wang; Howe, D.; "State-space average modeling of 6- and 12-pulse diode rectifiers," Power Electronics and Applications, 2007 European Conference on, pp.1-10, 2-5 Sept. 2007.

[36] Baghramian, A.; Forsyth, A.J.; "Averaged-value models of twelve-pulse rectifiers for aerospace applications," Power Electronics, Machines and Drives, 2004. (PEMD 2004). Second International Conference on (Conf. Publ. No. 498*)*, vol.1, no., pp. 220- 225 Vol.1, 31 March-2 April 2004.

[37] Eid, A.; El-Kishky, H.; Abdel-Salam, M.; El-Mohandes, T.; "Modeling and characterization of an aircraft electric power system with a fuel cell-equipped APU connected at HVDC bus," Power Modulator and High Voltage Conference (IPMHVC), 2010 IEEE International, pp.639-642, 23-27 May 2010.

[38] Chrin, P.; Trakuldit, S.; Polmai, S.; Bunlaksananusorn, C.; "Improvement of output dynamic performance of an Average Current Mode Controlled buck converter with a parallel controller," Power Electronics Conference (IPEC), 2010 International, pp.1916-1922, 21-24 June 2010.

[39] Xiong Du; Luowei Zhou; Heng-Ming Tai; "Double-Frequency Buck Converter," Industrial Electronics, IEEE Transactions on , vol.56, no.5, pp.1690-1698, May 2009.

[40]   Premalatha, L.; Vanajaranjan, P.; "Spectral Analysis of DC-DC Buck Converter with Chaotic Dynamics," INDICON, 2005 Annual IEEE, pp. 605- 608, 11-13 Dec. 2005.

[41]   Lee, B.K.; Ehsani, M.; "A simplified functional model for 3-phase voltage source inverter using switching function concept," Industrial Electronics Society, 1999. IECON '99 Proceedings. The 25th Annual Conference of the IEEE, pp.462-467 vol.1, 1999.

[42]   Eid, A.; El-Kishky, H.; Abdel-Salam, M.; El-Mohandes, M.T.; "On Power Quality of Variable-Speed Constant-Frequency Aircraft Electric Power Systems," Power Delivery, IEEE Transactions on , vol.25, no.1, pp.55-65, Jan. 2010.

[43]   Liqiu Han; Jiabin Wang; Howe, D.; "State-space average modeling of 6- and 12-pulse diode rectifiers," Power Electronics and Applications, 2007 European Conference on, pp.1-10, 2-5 Sept. 2007.

[44]   Eid, A.; El-Kishky, H.; Abdel-Salam, M.; El-Mohandes, T.; "Modeling and characterization of an aircraft electric power system with a fuel cell-equipped APU connected at HVDC bus," Power Modulator and High Voltage Conference (IPMHVC), 2010 IEEE International, pp.639-642, 23-27 May 2010.

[45]   Krein, P.T.; Bentsman, J.; Bass, R.M.; Lesieutre, B.L.; "On the use of averaging for the analysis of power electronic systems," Power Electronics, IEEE Transactions on, vol.5, no.2, pp.182-190, Apr 1990.

[46]   A. Eid, M. Abdel-Salam, H. El-Kishky, and T. El-Mohandes, "Simulation and transient analysis of conventional and advanced aircraft electric power systems with harmonic mitigation," *Elect. Power Syst. Res.*, vol. 79, no. 4, pp. 660–668, Apr. 2009.

[47]   Rajashekara, K.; Grieve, J.; Daggett, D.; "Hybrid fuel cell power in aircraft," *Industry Applications Magazine, IEEE*, vol.14, no.4, pp.54-60, July-Aug. 2008.

[48] Rajashekara, K.; "Hybrid fuel cell strategies for clean power generation," *Industry Applications Conference, 2004. 39th IAS Annual Meeting. Conference Record of the 2004 IEEE*, vol.3, no., pp. 2077- 2083 vol.3, 3-7 Oct. 2004.

[49] Zhenhua Jiang; Dougal, R.A.; "A hybrid fuel cell power supply with rapid dynamic response and high peak-power capacity," *Applied Power Electronics Conference and Exposition, 2006. APE '06. Twenty-First Annual IEEE*, pp. 6 pp., 19-23 March 2006.

[50] Miller, A.R.; Peters, J.; "Fuel cell hybrid locomotives: applications and benefits," *Rail Conference, 2006. Proceedings of the 2006 IEEE/ASME Joint*, pp.287-293, 4-6 April 2006.

[51] Bontour, S.; Hissel, D.; Gualous, H.; Harel, F.; Kauffmann, J.M.; "Design of a parallel fuel cell-supercapacitor auxiliary power unit (APU)," *Electrical Machines and Systems, 2005. ICEMS 2005. Proceedings of the Eighth International Conference on*, vol.2, no., pp.911-915 Vol. 2, 29-29 Sept. 2005.

[52] Lee, J.M.; Cho, B.H.; "A Dynamic Model of a PEM Fuel Cell System," *Applied Power Electronics Conference and Exposition, 2009. APEC 2009. Twenty-Fourth Annual IEEE*, pp.720-724, 15-19 Feb. 2009.

[53] Caisheng Wang; Nehrir, M.H.; Shaw, S.R.; "Dynamic models and model validation for PEM fuel cells using electrical circuits,"*Energy Conversion, IEEE Transactions on*, vol.20, no.2, pp. 442- 451, June 2005.

[54] Page, S.C.; Anbuky, A.H.; Krumdieck, S.P.; Brouwer, J.; "Test Method and Equivalent Circuit Modeling of a PEM Fuel Cell in a Passive State," *Energy Conversion, IEEE Transactions on*, vol.22, no.3, pp.764-773, Sept. 2007.

[55] Dhirde, A.M.; Dale, N.V.; Salehfar, H.; Mann, M.D.; Han, T.H.; "Equivalent Electric Circuit Modeling and Performance Analysis of a PEM Fuel Cell Stack Using Impedance Spectroscopy," *Energy Conversion, IEEE Transactions on*, vol.25, no.3, pp.778-786, Sept. 2010.

[56]   Xu Qingshan; Wang Nianchun; Ichiyanagi, K.; Yukita, K.; "PEM Fuel Cell modeling and parameter influences of performance evaluation," *Electric Utility Deregulation and Restructuring and Power Technologies, 2008. DRPT 2008. Third International Conference on*, vol., no., pp.2827-2832, 6-9 April 2008.

[57]   Ke Jin; Xinbo Ruan; Mengxiong Yang; Min Xu; "A Hybrid Fuel Cell Power System,"*Industrial Electronics, IEEE Transactions on*, vol.56, no.4, pp.1212-1222, April 2009.

[58]   Choi, W.; Enjeti, P.N.; Howze, J.W.; "Development of an equivalent circuit model of a fuel cell to evaluate the effects of inverter ripple current," *Applied Power Electronics Conference and Exposition, 2004. APEC '04. Nineteenth Annual IEEE*, vol.1, no., pp. 355- 361 Vol.1, 2004.

[59]   Hongyan Wang; Guangkai Li; Mu Li; Zhengxin Jiang; Xintao Wang; Quanxin Zhao; , "Third-order dynamic model of a lead acid battery for use in fuel cell vehicle simulation, "*Mechatronic Science, Electric Engineering and Computer (MEC), 2011 International Conference on*, pp.715-720, 19-22 Aug. 2011.

[60]   Salameh, Z.M.; Casacca, M.A.; Lynch, W.A.; "A mathematical model for lead-acid batteries," *Energy Conversion, IEEE Transactions on*, vol.7, no.1, pp.93-98, Mar 1992.

[61]   El-Kishky, H.; Ibrahimi, H.; Abu Dakka, M.; Eid, A.; Abdel-Akher, M.; "Transient performance of battery/fuel cell-based APU on aircraft electric power systems with nonlinear loading, "*Pulsed Power Conference (PPC), 2011 IEEE*, pp.1486-1489, 19-23 June 2011.

[62]   Zhou, Y.; Ajjarapu, V.; "A Fast Algorithm for Identification and Tracing of Voltage and Oscillatory Stability Margin Boundaries,"*Proceedings of the IEEE*, vol.93, no.5, pp.934-946, May 2005.

[63]   H. G. Kwatny, A. K. Pasrija, and L. Y. Bahar, "Static bifurcations in electric power networks: Loss of steady-state stability and voltage collapse," *IEEE Trans. Circuits Syst.*, vol. CAS 33, no. 5, pp. 981–991, Oct. 1986.

[64]   H. D. Chiang, "Application of bifurcation analysis to power systems," in
        Bifurcation Control. Lecture Notes in Control and Information Sciences, G. Chen,
        D. J. Hill, and X. Yu, Eds. Berlin, Germany: Springer-Verlag, 2003, vol. 293, pp.
        1–28.

[65]   H. O.Wang, E. H. Abed, and A. M. Hamdan, "Bifurcations, chaos, and crises in
        voltage collapse of a model power system," *IEEE Trans. Circuits Syst. I, Fundam.
        Theory Appl.*, vol. 41, pp. 294–302, Mar. 1994.

[66]   C. Guoyun, D. J. Hill, and R. Hui, "Continuation of local bifurcations for power
        system differential-algebraic equation stability model," *IEE Proc.-Gener. Transm.
        Distrib.*, vol. 152, no. 4, pp. 575–580, Jul. 2005.

[67]   J. L. Moiola and G. Chen*, Hopf Bifurcation Analysis—A Frequency Domain
        Approach*. Singapore: World Scientific, 1996, vol. 21.

[68]   C.-W. Tan, M. Varghese, P. Varaiya, and F. F. Wu, "Bifurcation, chaos, and
        voltage collapse in power systems," *Proc. IEEE*, vol. 83, pp. 1484–1496, Nov.
        1995.

[69]   Yang, X.; Chen, Y.; Shu, H.L.; "Stability analysis of AC/DC power transmission
        system based on bifurcation theories," *Sustainable Power Generation and Supply,
        2009. SUPERGEN '09. International Conference on*, pp.1-7, 6-7 April 2009.

[70]   Dobson, I.; Chiang, H.-D.; Thorp, J.S.; Fekih-Ahmed, L.; "A model of voltage
        collapse in electric power systems," *Decision and Control, 1988., Proceedings of
        the 27th IEEE Conference on*, vol., no., pp.2104-2109 vol.3, 7-9 Dec 1988.

[71]   Abed, E.H.; Alexander, J.C.; Wang, H.; Hamdan, A.M.A.; Lee, H.-C.; "Dynamic
        bifurcations in a power system model exhibiting voltage collapse," *Circuits and
        Systems, 1992. ISCAS '92. Proceedings., 1992 IEEE International Symposium on*,
        vol.5, no., pp.2509-2512 vol.5, 10-13 May 1992.

[72]   Ma You-jie; Wen Hu-long; Zhou Xue-song; Li Ji; Yang Hai-shan; "Bifurcation
        Analysis on Power System Voltage Stability," *Intelligent Computation*

Technology and Automation, 2009. ICICTA '09. Second International Conference on, vol.3, no., pp.26-29, 10-11 Oct. 2009.

[73]   Rajesh K G and Padiyar K R. "Bifurcation analysis of a three node power system with detailed models," *Electrical Power and Energy Systems*, vol.21, pp.375-393, May 1999.

[74]   Ma You-jie; Li Xiao-shuang; Zhou Xue-song; Li Ji; "The Comments on Dynamic Bifurcation of Voltage Stability in Power System," *Information Engineering (ICIE), 2010 WASE International Conference on*, vol.4, no., pp.272-275, 14-15 Aug. 2010.

[75]   Kwatny, H.G.; Fischl, R.F.; Nwankpa, C.O.; "Local bifurcation in power systems: theory, computation, and application," *Proceedings of the IEEE*, vol.83, no.11, pp.1456-1483, Nov 1995.

[76]   Denis Lee Hau Aik; Andersson, G.; "Nonlinear dynamics in HVDC systems," *Power Delivery, IEEE Transactions on*, vol.14, no.4, pp.1417-1426, Oct 1999.

[77]   Revel, G.; Leon, A.E.; Alonso, D.M.; Moiola, J.L.; "Bifurcation Analysis on a Multimachine Power System Model, "*Circuits and Systems I: Regular Papers, IEEE Transactions on*, vol.57, no.4, pp.937-949, April 2010.

[78]   Dai, D.; Tse, C.K.; Ma, X.; "Symbolic Analysis of Switching Systems: Application to Bifurcation Analysis of DC/DC Switching Converters, "*Circuits and Systems I: Regular Papers, IEEE Transactions on*, vol.52, no.8, pp. 1632-1643, Aug. 2005.

[79]   El Aroudi, A.; Rodriguez, E.; Leyva, R.; Alarcon, E.; "A Design-Oriented Combined Approach for Bifurcation Prediction in Switched-Mode Power Converters, "*Circuits and Systems II: Express Briefs, IEEE Transactions on*, vol.57, no.3, pp.218-222, March 2010.

[80]   Taborda, J.A.; Angulo, F.; Olivar, G.; "Smooth bifurcations in 3D-parameter space of Digital-PWM Switched Converter, "*Circuits and Systems (LASCAS), 2011 IEEE Second Latin American Symposium on*, pp.1-4, 23-25 Feb. 2011.

[81]   Chakrabarty, K.; Poddar, G.; Banerjee, S.; "Bifurcation behavior of the buck converter, "*Power Electronics, IEEE Transactions on*, vol.11, no.3, pp.439-447, May 1996.

[82]   Fossas, E.; Olivar, G.; "Study of chaos in the buck converter," *Circuits and Systems I: Fundamental Theory and Applications, IEEE Transactions on*, vol.43, no.1, pp.13-25, Jan 1996.

[83]   Yue Ma; Kawakami, H.; Tse, C.K.; "Bifurcation analysis of switched dynamical systems with periodically moving borders," *Circuits and Systems I: Regular Papers, IEEE Transactions on*, vol.51, no.6, pp. 1184- 1193, June 2004.

[84]   A. Emadi and A**.** Abur, "Real time state estimation of multi-converter DC power electronic systems using generalized state space averaging method,**"** IEEE Power Electronics Specialists Conf.*,* 2002. PESC**,** 2002, vol. 2, pp. 881-886.

[85]   Xiong Du; Luowei Zhou; Heng-Ming Tai; "Double-Frequency Buck Converter," Industrial Electronics, IEEE Transactions on, vol.56, no.5, pp.1690-1698, May 2009.

[86]   "Aircraft Electric Power Characteristics", Military Standard, MILSTD- E461.

[87]   Han, L.; Wang, J.; Griffo, A.; Howe, D.; "Stability assessment of AC hybrid power systems for 'more electric' aircraft," *Vehicle Power and Propulsion Conference, 2008. VPPC '08. IEEE*, pp.1-6, 3-5 Sept. 2008.

[88]   Kwasinski, A.; Onwuchekwa, C.N.; "Dynamic Behavior and Stabilization of DC Microgrids with Instantaneous Constant-Power Loads, "*Power Electronics, IEEE Transactions on*, vol.26, no.3, pp.822-834, March 2011.

[89]   Molina, M.G.; Mercado, P.E.; "Power Flow Stabilization and Control of Microgrid with Wind Generation by Superconducting Magnetic Energy Storage," *Power Electronics, IEEE Transactions on*, vol.26, no.3, pp.910-922, March 2011.

[90]   Molina, M.G.; Mercado, P.E.; "Power Flow Stabilization and Control of Microgrid with Wind Generation by Superconducting Magnetic Energy Storage," *Power Electronics, IEEE Transactions on*, vol.26, no.3, pp.910-922, March 2011.

[91]   Cespedes, M.; Lei Xing; Jian Sun; "Constant-Power Load System Stabilization by Passive Damping," *Power Electronics, IEEE Transactions on*, vol.26, no.7, pp.1832-1836, July 2011.

[92]   Ise, T.; Hayashi, Y.; Tsuji, K.; "Customized power quality supply system by use of power electronics and its realization using three phase four wire AC system," *Power Electronics and Motion Control Conference, 2000. Proceedings. IPEMC 2000. The Third International*, vol.3, no., pp.1025-1030 vol.3, 2000.

[93]   J. Weimer, "Electrical power technology for the more electric aircraft," in *Conference Proceedings of IEEE DASC*"93, pp. 445-450, 1993.

[94]   Kamiar J. Karimi, "The role of power electronics in more electric airplanes (MEA)," presentation at 2006 *IEEE Control and Modeling for Power Electronics (COMPEL) Workshop*, July 2006.

[95]   Hongyu Li; Fang Zhuo; Zhaoan Wang; Lei, W.; Wu, L.; "A novel time-domain current-detection algorithm for shunt active power filters," *Power Systems, IEEE Transactions on*, vol.20, no.2, pp. 644- 651, May 2005.

[96]   W. M. Grady, M. J. Samotj, and A. H. Noyola, "Survey of active power line conditioning methodologies," *IEEE Trans. Power Del.*, vol. 5, no.3, pp. 1536–1542, Jul. 1990.

[97]   L. A. Moran, J. W. Dixon, and R. R. Wallace, "A three-phase active power filter operating with fixed switching frequency for reactive power and current harmonic

compensation," *IEEE Trans. Ind. Electron.*, vol. 42, no. 4, pp. 402–408, Aug. 1995.

[98]   Hsiung Cheng Lin; "Inter-Harmonic Identification Using Group-Harmonic Weighting Approach Based on the FFT, "*Power Electronics, IEEE Transactions on*, vol.23, no.3, pp.1309-1319, May 2008.

[99]   Zuhua Ren; Bolin Wang; "Estimation Algorithms of Harmonic Parameters Based on the FFT, "*Power and Energy Engineering Conference (APPEEC), 2010 Asia-Pacific*, pp.1-4, 28-31 March 2010.

[100]   A. A. Girgis, W. B. Chang, and E. B. Makram, "A digital recursive measurement scheme for on-Line tracking of power system harmonics,"*IEEE Trans. Power Del.*, vol. 3, pp. 1153–1160, Jul. 1991.

[101]   Eid, A.; El-Kishky, H.; Abdel-Salam, M.; El-Mohandes, T.; "VSCF aircraft electric power system performance with active power filters," *System Theory (SSST), 2010 42nd Southeastern Symposium on*, pp.182-187, 7-9 March 2010.

[102]   G.W. Chang; Chia-Ming Yeh; Wei-Cheng Chen; "Meeting IEEE-519 current harmonics and power factor constraints with a three-phase three-wire active power filter under distorted source voltages," *Power Delivery, IEEE Transactions on*, vol.21, no.3, pp.1648-1654, July 2006.

[103]   Lundquist, Johan. On Harmonic Distortion in Power Systems. Chalmers University of Technology: Department of Electrical Power Engineering, 2001.

Appendix A

A.1:

The matrix equation representing the averaged voltage and current profile at the main DC bus due to interaction of the 12-pulse diode rectifier and three different types of DC-DC buck converters, as well as 12-pulse PWM VSI is derived as (using the GSSA method)

$$\dot{X}_{22\times1} = A_{22\times22}X_{22\times1} + U_{22\times1}$$

where the state matrix A

$$
A=
\begin{bmatrix}
0 & \frac{1}{C} & 0 & 0 & 0 & 0 & 0 & 0 & 0 & 0 & 0 & 0 & 0 & 0 & 0 & 0 & 0 & 0 & 0 & 0 & 0 & 0\\
\frac{-1}{L_2} & \frac{-R_2}{L_2} & 0 & 0 & 0 & 0 & 0 & 0 & 0 & 0 & 0 & 0 & 0 & 0 & 0 & 0 & 0 & 0 & 0 & 0 & 0 & 0\\
0 & 0 & 0 & \omega_1 & \frac{1}{C} & 0 & 0 & 0 & 0 & 0 & 0 & 0 & 0 & 0 & 0 & 0 & 0 & 0 & 0 & 0 & 0 & 0\\
0 & 0 & -\omega_1 & 0 & 0 & \frac{1}{C} & 0 & 0 & 0 & 0 & 0 & 0 & 0 & 0 & 0 & 0 & 0 & 0 & 0 & 0 & 0 & 0\\
0 & 0 & \frac{-1}{L_2} & 0 & \frac{-R_2}{L_2} & \omega_1 & 0 & 0 & 0 & 0 & 0 & 0 & 0 & 0 & 0 & 0 & 0 & 0 & 0 & 0 & 0 & 0\\
0 & 0 & 0 & \frac{-1}{L_2} & -\omega_1 & \frac{-R_2}{L_2} & 0 & 0 & 0 & 0 & 0 & 0 & 0 & 0 & 0 & 0 & 0 & 0 & 0 & 0 & 0 & 0\\
0 & 0 & 0 & 0 & 0 & 0 & 0 & \omega_2 & \frac{1}{C} & 0 & 0 & 0 & 0 & 0 & 0 & 0 & 0 & 0 & 0 & 0 & 0 & 0\\
0 & 0 & 0 & 0 & 0 & 0 & -\omega_2 & 0 & 0 & \frac{1}{C} & 0 & 0 & 0 & 0 & 0 & 0 & 0 & 0 & 0 & 0 & 0 & 0\\
0 & 0 & 0 & 0 & 0 & 0 & \frac{-1}{L_2} & 0 & \frac{-R_2}{L_2} & \omega_2 & 0 & 0 & 0 & 0 & 0 & 0 & 0 & 0 & 0 & 0 & 0 & 0\\
0 & 0 & 0 & 0 & 0 & 0 & 0 & \frac{-1}{L_2} & -\omega_2 & \frac{-R_2}{L_2} & 0 & 0 & 0 & 0 & 0 & 0 & 0 & 0 & 0 & 0 & 0 & 0\\
0 & 0 & 0 & 0 & 0 & 0 & 0 & 0 & 0 & 0 & 0 & \omega_3 & \frac{1}{C} & 0 & 0 & 0 & 0 & 0 & 0 & 0 & 0 & 0\\
0 & 0 & 0 & 0 & 0 & 0 & 0 & 0 & 0 & 0 & -\omega_3 & 0 & 0 & \frac{1}{C} & 0 & 0 & 0 & 0 & 0 & 0 & 0 & 0\\
0 & 0 & 0 & 0 & 0 & 0 & 0 & 0 & 0 & 0 & \frac{-1}{L_2} & 0 & \frac{-R_2}{L_2} & \omega_3 & 0 & 0 & 0 & 0 & 0 & 0 & 0 & 0\\
0 & 0 & 0 & 0 & 0 & 0 & 0 & 0 & 0 & 0 & 0 & \frac{-1}{L_2} & -\omega_3 & \frac{-R_2}{L_2} & 0 & 0 & 0 & 0 & 0 & 0 & 0 & 0\\
0 & 0 & 0 & 0 & 0 & 0 & 0 & 0 & 0 & 0 & 0 & 0 & 0 & 0 & \omega_4 & \frac{1}{C_{dc}} & 0 & 0 & 0 & 0 & 0 & 0\\
0 & 0 & 0 & 0 & 0 & 0 & 0 & 0 & 0 & 0 & 0 & 0 & 0 & 0 & -\omega_4 & 0 & 0 & \frac{1}{C_{dc}} & 0 & 0 & 0 & 0\\
0 & 0 & 0 & 0 & 0 & 0 & 0 & 0 & 0 & 0 & 0 & 0 & 0 & 0 & \frac{-1}{L_2} & 0 & \frac{-R_2}{L_2} & \omega_4 & 0 & 0 & 0 & 0\\
0 & 0 & 0 & 0 & 0 & 0 & 0 & 0 & 0 & 0 & 0 & 0 & 0 & 0 & 0 & \frac{-1}{L_2} & -\omega_4 & \frac{-R_2}{L_2} & 0 & 0 & 0 & 0\\
0 & 0 & 0 & 0 & 0 & 0 & 0 & 0 & 0 & 0 & 0 & 0 & 0 & 0 & 0 & 0 & 0 & 0 & 0 & \omega_5 & \frac{1}{C_{dc}} & 0\\
0 & 0 & 0 & 0 & 0 & 0 & 0 & 0 & 0 & 0 & 0 & 0 & 0 & 0 & 0 & 0 & 0 & 0 & -\omega_5 & 0 & 0 & \frac{1}{C_{dc}}\\
0 & 0 & 0 & 0 & 0 & 0 & 0 & 0 & 0 & 0 & 0 & 0 & 0 & 0 & 0 & 0 & 0 & 0 & \frac{-1}{L_2} & 0 & \frac{-R_2}{L_2} & \omega_5\\
0 & 0 & 0 & 0 & 0 & 0 & 0 & 0 & 0 & 0 & 0 & 0 & 0 & 0 & 0 & 0 & 0 & 0 & 0 & \frac{-1}{L_2} & -\omega_5 & \frac{-R_2}{L_2}
\end{bmatrix}
$$

also the state vector X and the input matrix U are defined as

$$
X = \begin{bmatrix} \dot{X}_1 \\ \dot{X}_2 \\ \dot{X}_3 \\ \dot{X}_4 \\ \dot{X}_5 \\ \dot{X}_6 \\ \dot{X}_7 \\ \dot{X}_8 \\ \dot{X}_9 \\ \dot{X}_{10} \\ \dot{X}_{11} \\ \dot{X}_{12} \\ \dot{X}_{13} \\ \dot{X}_{14} \\ \dot{X}_{15} \\ \dot{X}_{16} \\ \dot{X}_{17} \\ \dot{X}_{18} \\ \dot{X}_{19} \\ \dot{X}_{20} \\ \dot{X}_{21} \\ \dot{X}_{22} \end{bmatrix} \quad and \quad U = \begin{bmatrix} -\dfrac{1}{C_{dc}}\langle I_{Load}\rangle_0 \\[2mm] \dfrac{1}{L_2}\langle f_v\rangle_0 \\[2mm] -\dfrac{1}{C_{dc}}\Re\langle I_{Load}\rangle_{1(rec)} \\[2mm] -\dfrac{1}{C_{dc}}\Im\langle I_{Load}\rangle_{1(rec)} \\[2mm] \dfrac{1}{L_2}\Re\langle f_v\rangle_{1(rec)} \\[2mm] \dfrac{1}{L_2}\Im\langle f_v\rangle_{1(rec)} \\[2mm] -\dfrac{1}{C_{dc}}\Re\langle I_{Load}\rangle_{1(cv\_bc)} \\[2mm] -\dfrac{1}{C_{dc}}\Im\langle I_{Load}\rangle_{1(cv\_bc)} \\[2mm] \dfrac{1}{L_2}\Re\langle f_v\rangle_{1(cv\_bc)} \\[2mm] \dfrac{1}{L_2}\Im\langle f_v\rangle_{1(cv\_bc)} \\[2mm] -\dfrac{1}{C_{dc}}\Re\langle I_{Load}\rangle_{1(cc\_bc)} \\[2mm] -\dfrac{1}{C_{dc}}\Im\langle I_{Load}\rangle_{1(cc\_bc)} \\[2mm] \dfrac{1}{L_2}\Re\langle f_v\rangle_{1(cc\_bc)} \\[2mm] \dfrac{1}{L_2}\Im\langle f_v\rangle_{1(cc\_bc)} \\[2mm] -\dfrac{1}{C_{dc}}\Re\langle I_{Load}\rangle_{1(cp\_bc)} \\[2mm] -\dfrac{1}{C_{dc}}\Im\langle I_{Load}\rangle_{1(cp\_bc)} \\[2mm] \dfrac{1}{L_2}\Re\langle f_v\rangle_{1(cp\_bc)} \\[2mm] \dfrac{1}{L_2}\Im\langle f_v\rangle_{1(cp\_bc)} \\[2mm] -\dfrac{1}{C_{dc}}\Re\langle I_{Load}\rangle_{1(inv)} \\[2mm] -\dfrac{1}{C_{dc}}\Im\langle I_{Load}\rangle_{1(inv)} \\[2mm] \dfrac{1}{L_2}\Re\langle f_v\rangle_{1(inv)} \\[2mm] \dfrac{1}{L_2}\Im\langle f_v\rangle_{1(inv)} \end{bmatrix}
$$

A.2:

The matrix A introduces the state matrix for the 12-pulse diode rectifier where interacting with the CVBC.

$$
A = \begin{bmatrix}
0 & \dfrac{1}{C_{dc}} & 0 & 0 & 0 & 0 & 0 & 0 & 0 & 0 \\[2mm]
\dfrac{-1}{L_2} & \dfrac{-R_2}{L_2} & 0 & 0 & 0 & 0 & 0 & 0 & 0 & 0 \\[2mm]
0 & 0 & 0 & \omega_1 & \dfrac{1}{C_{dc}} & 0 & 0 & 0 & 0 & 0 \\[2mm]
0 & 0 & -\omega_1 & 0 & 0 & \dfrac{1}{C_{dc}} & 0 & 0 & 0 & 0 \\[2mm]
0 & 0 & \dfrac{-1}{L_2} & 0 & \dfrac{-R_2}{L_2} & \omega_1 & 0 & 0 & 0 & 0 \\[2mm]
0 & 0 & 0 & \dfrac{-1}{L_2} & -\omega_1 & \dfrac{-R_2}{L_2} & 0 & 0 & 0 & 0 \\[2mm]
0 & 0 & 0 & 0 & 0 & 0 & 0 & \omega_2 & \dfrac{1}{C_{dc}} & 0 \\[2mm]
0 & 0 & 0 & 0 & 0 & 0 & -\omega_2 & 0 & 0 & \dfrac{1}{C_{dc}} \\[2mm]
0 & 0 & 0 & 0 & 0 & 0 & \dfrac{-1}{L_2} & 0 & \dfrac{-R_2}{L_2} & \omega_2 \\[2mm]
0 & 0 & 0 & 0 & 0 & 0 & 0 & \dfrac{-1}{L_2} & -\omega_2 & \dfrac{-R_2}{L_2}
\end{bmatrix}
$$

The multiplication of the vectors B and U_X produces the input matrix for the interaction of the 12-pulse rectifier and the CVBC.

$$
B = \begin{bmatrix}
\dfrac{-d}{C_{dc}} & 0 & \dfrac{-\sin(2\pi d)}{\pi C_{dc}} & \dfrac{1-\cos(2\pi d)}{2\pi C_{dc}} & 0 & 0 \\[2mm]
0 & 0 & 0 & 0 & 0 & 0 \\[1mm]
0 & 0 & 0 & 0 & 0 & 0 \\[1mm]
0 & 0 & 0 & 0 & 0 & 0 \\[1mm]
0 & 0 & 0 & 0 & 0 & 0 \\[1mm]
0 & 0 & 0 & 0 & 0 & 0 \\[1mm]
\dfrac{-\sin(2\pi d)}{2\pi C_{dc}} & 0 & \dfrac{-d}{C_{dc}} & 0 & 0 & 0 \\[2mm]
\dfrac{1-\cos(2\pi d)}{2\pi C_{dc}} & 0 & 0 & \dfrac{-d}{C_{dc}} & 0 & 0 \\[2mm]
0 & 0 & 0 & 0 & 0 & 0 \\[1mm]
0 & 0 & 0 & 0 & 0 & 0
\end{bmatrix}
$$

Appendix: A. 2 (Continued)

$$U_X = \begin{bmatrix} 0 \\ \dfrac{1}{L_2}\left\{0.7905V_m - 1.4V_m\cos\left(\mu + \dfrac{5\pi}{12}\right) - 1.654V_m\sin\left(\mu - \dfrac{\pi}{4}\right)\right\} \\ 0 \\ 0 \\ \hline \left\{\dfrac{1}{L_2}\{-0.0538V_m\cos\left(13\mu - \dfrac{31\pi}{12}\right) + 0.0636V_m\cos\left(-11\mu + \dfrac{41\pi}{12}\right) - \right. \\ \left. 0.0636V_m\sin\left(13\mu - \dfrac{13\pi}{4}\right) + 0.0751V_m\sin\left(11\mu - \dfrac{11\pi}{4}\right) + 0.0055V_m\right\} \\ \hline \left\{\dfrac{1}{L_2}\{-0.0637V_m\sin\left(-11\mu + \dfrac{41\pi}{12}\right) - 0.0539V_m\sin\left(13\mu - \dfrac{31\pi}{12}\right) + \right. \\ \left. 0.0636V_m\cos\left(13\mu - \dfrac{13\pi}{4}\right) + 0.0752V_m\cos\left(11\mu - \dfrac{11\pi}{4}\right) + 0.0204V_m\right\} \\ \hline 0 \\ 0 \\ 0 \\ 0 \end{bmatrix}$$

TABLE. 1: SYSTEM PARAMETERS

Description	Parameter	Value
Rectifier with CVBC Load		
total series resistance	R_2	0.135Ω
total series inductance	L_2	$40\mu H$
filter capacitance	C_{dc}	2.5mF
duty cycle of modulated signal	d	28/270
twelve times the generator frequency	ω_1	12*2*π*400
PWM frequency	ω_2	15k*2*π
CVBC		
total series resistance	R_t	0.14Ω
total series inductance	L	$15\mu H$
filter capacitance	C_v	0.5mF
duty cycle of modulated signal	d	28/270
PWM frequency	ω	15k*2*π
series resistance	r	0.002Ω

The matrix Λ is the state matrix for the CVBC. Also, the matrix Φ represents the input matrix for the CVBC.

$$\Lambda = \begin{bmatrix} \dfrac{-r}{L} & \dfrac{-1}{L} & 0 & 0 & 0 & 0 \\[2mm] \dfrac{1}{C_v} & \dfrac{-1}{R_t C_v} & 0 & 0 & 0 & 0 \\[2mm] 0 & 0 & \dfrac{-r}{L} & \omega & \dfrac{-1}{L} & 0 \\[2mm] 0 & 0 & -\omega & \dfrac{-r}{L} & 0 & \dfrac{-1}{L} \\[2mm] 0 & 0 & \dfrac{1}{C_v} & 0 & \dfrac{-1}{R_t C_v} & \omega \\[2mm] 0 & 0 & 0 & \dfrac{1}{C_v} & -\omega & \dfrac{1}{R_t C_v} \end{bmatrix}$$

$$\Phi = \begin{bmatrix} \dfrac{d}{L} & 0 & 0 & 0 & 0 & 0 & \dfrac{\sin(2\pi d)}{2\pi L} & \dfrac{\cos(2\pi d)-1}{2\pi L} & 0 & 0 \\[2mm] 0 & 0 & 0 & 0 & 0 & 0 & 0 & 0 & 0 & 0 \\[2mm] \dfrac{\sin(2\pi d)}{2\pi L} & 0 & 0 & 0 & 0 & 0 & \dfrac{d}{L} & 0 & 0 & 0 \\[2mm] \dfrac{\cos(2\pi d)-1}{2\pi L} & 0 & 0 & 0 & 0 & 0 & 0 & \dfrac{d}{L} & 0 & 0 \\[2mm] 0 & 0 & 0 & 0 & 0 & 0 & 0 & 0 & 0 & 0 \\[2mm] 0 & 0 & 0 & 0 & 0 & 0 & 0 & 0 & 0 & 0 \end{bmatrix}$$